5-2023

Large-scale volcanism on the terrestrial planets

Keenan Ben Golder
kgolder@vols.utk.edu

To the Graduate Council:

I am submitting herewith a dissertation written by Keenan Ben Golder entitled "Large-scale volcanism on the terrestrial planets." I have examined the final electronic copy of this dissertation for form and content and recommend that it be accepted in partial fulfillment of the requirements for the degree of Doctor of Philosophy, with a major in Geology.

Bradley Thomson, Major Professor

We have read this dissertation and recommend its acceptance:

Harry Y. McSween, Linda C. Kah, W. Brent Garry

Accepted for the Council:

Dixie L. Thompson

Vice Provost and Dean of the Graduate School

(Original signatures are on file with official student records.)

Large-scale volcanism on the terrestrial planets

A Dissertation Presented for the
Doctor of Philosophy
Degree
The University of Tennessee, Knoxville

Keenan Ben Golder
May 2023

DEDICATION

To my mother, Sandra Lesch, and to Erin, Candence, and Ethan. All have been a constant source of love, strength, and encouragement without whom I would not have been able to reach the goals I set out to achieve.

ACKNOWLEDGEMENTS

Funding for portions of the work in this dissertation was provided by the Mars Data Analysis Program, grant NNX12AJ45G. The University of Tennessee and Department of Earth and Planetary Sciences provided graduate assistantship support. Dr. Laszlo Keszthelyi generously shared his early mapping linework of Athabasca Valles. Dr. Joseph Panzik contributed to the early interpretations of the gravity anomaly data. The pi-group scaling calculations were derived in part from a similar crater count age dating spreadsheet developed by Dr. Caleb Fassett. The lava flow model developed by Mr. Gislason served as a base model which was modified to accomplish the desired lava flow modeling in this work. Dr. Lillian Ostrach-Toborek provided insightful discussion and suggestions for the Mercury investigations. Two anonymous reviewers provided thoughtful comments and suggestions during the review and revision of the Chapter 1 manuscript.

I want to thank my committee chair and faculty advisor, Brad Thomson, for his concerted efforts and support while I completed this dissertation. I want to thank the members of my dissertation committee, Drs. Linda Kah, Hap McSween, and Brent Garry for their support. I would also like acknowledge Drs. Devon Burr, Josh Emery, and Liem Tran for their support as previous members of my dissertation committee. I would also like to acknowledge and thank my friends in the Department of Earth and Planetary Sciences, especially Miles Henderson, Ashley Manning-Berg, Jason Muhlbauer, Rachel Kronyak, Robert Jacobsen, and countless others. I want to thank my mother, Sandra Lesch, for everything and without whom I would not have been able to pursue my dreams. Finally, I would especially like to thank Erin, Cadence, and Ethan for their love, support, patience, and strength as I worked to complete this degree.

ABSTRACT

Evidence for mafic volcanism has been identified on all the planets in the inner Solar System. Lava flows on these planets have varying extents, ranging in length from 10s to 1000s of kilometers, and areas ranging from 100s to 100,000s of square kilometers. This dissertation investigates large-scale lava flows on Mercury, Earth, and Mars with the intent of deciphering emplacement mechanisms and the evolution of lava under conditions that occur on various planets. Ultimately, this work aids in constraining the factors that affect the overall extent and potential source areas of the planetary lavas and provides a mechanism to enhance our understanding of lava flows found on the terrestrial planets.

Chapter 1 investigates large-scale lava flows in the Cerberus region of Mars, specifically to understand their emplacement history, material properties, and potential magma sources. I use geological mapping and crater counting techniques to investigate the age and areal extent of these flows. The absolute age estimates derived from crater counting suggest an unexpected trend of decreasing ages with increasing distance from the flow source. Using pi-group scaling, I identify changes within the material properties of the lavas during emplacement as a potential cause for this unusual age distribution, wherein increased strength and decreased vesicularity of the lava result in changes to both crater size and retention. I then use these absolute age estimates to infer that the source of the magma feeding these young and extensive lava flows developed at the base of the crust below the Cerberus region.

Chapter 2 focuses on the comparison of long and areally extensive lava flows on Earth and Mars, to determine the effect of viscosity on the emplacement of flows >1000 km in length and areas >100,000 km^2. I hypothesize that on both planets low viscosity lavas are necessary to generate such long and areally extensive lava flows. In this chapter, computer simulations are used to determine the range of viscosity that is consistent with the observed lava flows. The results of this work support the inference that low bulk viscosities, which generally correspond to a basaltic magma composition with minimal phenocrysts and/or gas bubbles, generate the best reproductions of the terrestrial and martian lava flows. Using these data, I suggest that extensive terrestrial and martian lava flows were likely emplaced rapidly, with their final extents limited by the total erupted volume of lava. These results, coupled with the derived ages from chapter one, suggest that the internal conditions of Mars have been conducive to the formation of hot, low viscosity lavas in the very recent geologic past.

Chapter 3 investigates volcanism on Mercury. Mercury hosts broad smooth plains in three localities that have emplacement mechanisms variously attributed to impact-related ejecta and melt, as well as volcanic processes. The smooth plains units are located in the annulus surrounding the Caloris impact basin and contain intermingled high-reflectance red and low-reflectance blue materials. Geologic mapping, crater counting, and spectral analyses are used to infer the emplacement mechanism for these smooth plains. The results of this work support a volcanic origin, though impact related processes cannot be discounted.

TABLE OF CONTENTS

LIST OF TABLES

LIST OF FIGURES

INTRODUCTION

Volcanism on the Terrestrial Planets

Evidence for mafic volcanism has been found on each of the bodies of the inner Solar System, including Mercury, Venus, Earth, the Moon, and Mars (e.g., Head and Coffin, 1997; Zimbelmann, 1998; Head et al., 2009). Many of the lava flows identified on these bodies are categorized as flood basalts, which inundate large areas and result in relatively smooth, low relief (<100 m relief) plains (e.g., Geikie 1880; Washington 1922; Tyrrell 1937; Keszthelyi et al., 2000). Smaller-scale lava flows, categorized as plains-style volcanism, have similar emplacement mechanisms as flood basalts (Greeley, 1976; Greeley and King, 1977; Greeley, 1982; Sakimoto et al., 2003; Vaucher et al., 2009). These smaller lava flows can be used as analogues to better understand the emplacement of larger scale flood basalt eruptions. On Earth and Mars, flood basalts are commonly associated with multiple lava flows that form thick units that are a primary component of ancient large igneous provinces (LIPs). On Earth, such areally extensive accumulations of lavas are primarily attributed to voluminous emplacements of basaltic rock (e.g., Coffin and Eldholm, 1994; Keszthelyi et al., 2006). This dissertation investigates various lava flows on Mercury, Earth, and Mars, each within this wide range of sizes and with varying interpretations for their emplacement mechanism(s).

Starting on the innermost planet, the surface of Mercury hosts vast expanses of what have been described as “smooth plains”. Such plains include the Caloris interior plains (CIP), the circum-Caloris exterior plains (CEP), and the northern smooth plains (NSP), which have variously been interpreted to have formed from impact ejecta, volcanism, or a mixture of the two (e.g., Wilhelms, 1976; Kiefer and Murray, 1987; Spudis and Guest, 1988; Strom et al., 2008,

2011; Fassett et al., 2009; Head et al., 2009, 2011; Denevi et al., 2009, 2013; Whitten et al., 2014; Byrne et al., 2013, 2016; Ostrach et al., 2015; Klima et al., 2018). The morphological characteristics that unite these regions include sparse cratering, distinct boundaries with adjacent terrain, embayment of older units, lowland ponding, and low relief gently rolling features (e.g., Trask and Guest, 1975; Denevi et al., 2009, 2013). The emplacement of the CEP has been variously interpreted to have been emplaced either through impact or volcanic processes, or a combination of the two. Impact-related emplacement is based on apparent stratigraphic relationships and their geospatial proximity to Caloris (Wilhelms, 1976; Oberdeck et al., 1977; Schaber and McCauley, 1980; McCauley et al., 1981; Guest and Greeley, 1983). By contrast, a volcanic origin for these smooth plains is based upon their smooth morphology, wide distribution, relative youth compared to the largest impact basins, color characteristics, and embayment relationships (e.g., Trask and Guest, 1975; Kiefer and Murray, 1987; Strom et al., 2008, 2011; Fassett et al., 2009; Head et al., 2009, 2011; Prockter et al., 2010; Byrne et al., 2013; Hurwitz et al., 2013; Ostrach et al., 2015). The formation mechanism, however, is not clearly identifiable and requires further investigation.

Farther out among the terrestrial planets is Mars. Despite its small size, Mars has been volcanically active through much of its geologic history. The majority of volcanic emplacement occurred during the Noachian and early Hesperian, with volcanism persisting, although with decreasing intensity, well into the Amazonian (e.g., Werner, 2009). An excellent example of young volcanism is found within the Cerberus region, which is located between the Olympus-Tharsis Volcanic Province and the Elysium Volcanic Province. The Cerberus plains consist of complex overlapping lava flows and low shield volcanoes that were emplaced over a period of ~250 Ma (Plescia, 1990, 2003; Vaucher et al., 2009; Thomas, 2013). Distinct lava flows stretch

for 100s of km within the plains and >1000 km within three circum-Cerberus aqueously-carved flood channels, Athabasca, Grjótá, and Marte Valles (Plescia, 1990; Burr et al., 2002a, 2002b; Berman and Hartmann, 2002; Plescia, 2003; Keszthelyi, et al., 2004; McEwen et al., 2005; Burr et al., 2009; Vaucher et al., 2009; Jaeger et al., 2010; Golder et al., 2020). With the rapid interior cooling expected for Mars and its corresponding crustal thickening (e.g., Montesi and Zuber, 2003; McGovern et al., 2002, 2004), the generation and eruption of high-volume lavas there would appear to be unlikely, but the young Cerberus volcanism suggest geologically very recent magma formation.

Interpretations of large-scale planetary flood basalts often rely on the study of terrestrial lava flows (e.g., Keszthelyi et al., 2000, 2004), which are assumed to be analogous and therefore can inform our understanding of extraterrestrial volcanic sites. Terrestrial examples of lava flows that range from plains-style lava flows to flood basalts include the McCartys basalt flow within the Zuni-Bandera volcanic field (Nichols, 1946; Ander et al., 1981; Crumpler and Aubele, 2001; Zimbelman and Johnston, 2002), Icelandic Eldgá and Laki basalt flows (e.g., Thordarson and Self, 1993; Keszthelyi et al., 2000; Thordarson et al., 2001), and large igneous provinces, which are typified by the Deccan Basalt Group (DBG; e.g., Self et al., 2008) and the Columbia River Basalt Group (CRBG; e.g., Self et al., 1996). The McCartys basalt flow, at ~3 ky and 50 km long, is one of the youngest and longest lava flows within the continental United States. It consists of primarily of rubbly, fractured plates of pahoehoe that were sourced from a single vent (e.g., Nichols, 1946; Ander et al., 1981; Crumpler and Aubele, 2001; Zimbelman and Johnston, 2002). The Eldgá and Laki lava flows in Iceland are fissure-fed lava flows that were emplaced in 934 C.E. and 1783-85 C.E., respectively, and have a platy-ridged surface texture (Thordarson and Self, 1993; Thordarson et al., 2001). The voluminous DBG and CRBG are comprised of

stacks of inflated pahoehoe, where lava continued flowing underneath and lifted a chilled crust, producing a distinct surface morphology of tumuli, inflation plateau, and inflation pits (Keszthelyi et al., 2006). These sheet flows were then emplaced over a long period of time, ~3 Ma, with some individual flows formed rapidly during a single pulse, and others during more prolonged eruptions that involved multiple pulses of activity (e.g., Walker et al., 1971; Self et al., 1996, 2008; Keszthelyi et al., 2006; Ernst, 2014). The investigation of each of these terrestrial flows, including the various parameters that affect their overall extent, can be used to better understand similar lava flows on other planetary bodies.

Overview of the Present Study

These studies aim to better understand how lava flows on the terrestrial planets were emplaced, how changes to their material properties during emplacement affected their final extent, the conditions required for their emplacement, and their magmatic sources in the subsurface.

Chapter 1: Investigation of target property effects on crater populations in long lava flows: A study in the Cerberus region, Mars, with implications for magma source identification.

This chapter investigates the extent to which the material properties of lava flows affect crater populations and the age determinations derived from these populations. Derived ages are used to determine the emplacement timing of each lava in the Cerberus region and to infer the location of the magma source for the youngest regional-scale lava flows on Mars.

In this chapter, I investigate the channelized lavas surrounding the Cerberus plains. The goals of this investigation are to: (1) derive their emplacement sequence; (2) explore potential magma migration patterns; and (3) constrain likely magma sources. In this analysis, I perform geomorphological mapping, crater counting, and crater-scaling to quantify the effect of target

properties on the final CSFDs. During these analyses, I identify why a decreasing age trend was observed in these large late-Amazonian lava flows, and explore implications for lavas elsewhere on Mars and within the Solar System. The results of this work offer new insights into rheological changes that take place during the emplacement of long lava flows, and how these rheological changes affect crater retention, as well as to suggest the likely magma source for these eruptions. This study was published in the journal Icarus (Golder et al., 2020).

Chapter 2: Emplacement of widespread lavas: Investigating the effect of bulk viscosities on martian lava flows through modeling.

This chapter investigates, through geologic mapping and computer modeling, the effect of various parameters on the emplacement of long and areally extensive lava flows on Earth and Mars. In particular, it explores the effect of changes to the bulk viscosities of lava, and how the corresponding changes to yield strength affect the flow of lava across a surface. The viscosity and yield strength both relate to the internal resistance to flow of a fluid. Fluids with high viscosity and yield strength cannot flow great distances, while those fluids with low viscosity and yield strength can propagate across a surface to great lateral distances. I use terrestrial analogues to provide data for the calibration and validation of modeling, as well as to provide a reasonable input range for the parameter values to be applied to the martian flows. These terrestrial values constrain the parameter space and can lead to reasonable reproductions of observed lava flows, from which inferences on the effect of viscosity can be made. I then focus the investigations onto two channelized lava flows on Mars, Athabasca and Grjótá Valles, to constrain the bulk viscosity values required for their formation. By better understanding the inherent qualities of the terrestrial and martian lava flows, inferences can be made regarding recent lava emplacement on Mars.

<u>Chapter 3:</u> Source(s) of the circum-Caloris smooth plains on Mercury: Mapping, remote analyses, and scenarios for future testing with BepiColombo data.

This chapter investigates enigmatic smooth plains surrounding the Caloris impact basin to constrain the geologic processes that resulted in their emplacement. Understanding the emplacement process(es) of these plains, which could have multiple steps, sheds light on regional late-stage volcanism and impact effects. The region northwest of the Caloris basin is explored using geomorphological and color-based mapping, crater counting, and spectral analyses, with the goal of placing constraints on the emplacement mechanisms and identifying the source of the observed units. I develop hypothetical scenarios, focused primarily on volcanic or impact process, while also including the potential for post-emplacement modification by volatile release, to explain the observations in the region. I find that volcanism is the most likely explanation for the formation of these plains units, but this result is not conclusive. Follow-up observations from ESA's BepiColombo mission will potentially provide data to address the outstanding questions from this work.

References

Ander, M. E., Heiken, G., Eichelberger, J., Laughlin, A. W., & Huestis, S. (1981). Geologic and geophysical investigations of the Zuni-Bandera volcanic field, New Mexico (No. LA-8827-MS). Los Alamos National Lab., NM (USA); Sandia National Labs., Albuquerque, NM (USA); New Mexico Univ., Albuquerque (USA). Dept. of Geology.

Berman, D. C., & Hartmann, W. K. (2002). Recent fluvial, volcanic, and tectonic activity on the Cerberus plains of Mars. Icarus, 159(1), 1-17.

Burr, D. M., McEwen, A. S., et al. (2002a). Recent aqueous floods from the Cerberus Fossae, Mars. Geophys. Res. Letters, 29(1), 13-1.

Burr, D. M., Grier, J. A., et al. (2002b). Repeated aqueous flooding from the Cerberus Fossae: Evidence for very recently extant, deep groundwater on Mars. Icarus, 159(1), 53-73.

Burr, D.M., L. Wilson, and A.S. Bargery (2009) Floods from Fossae: a review of Amazonian-aged extensional tectonic megaflood channels on Mars. In Megaflooding on Earth and Mars, D.M. Burr, V.R. Baker and P.A. Carling (eds), Cambridge University Press, Cambridge, UK. Pp. 194-208.

Byrne, P. K., Klimczak, C., Williams, D. A., Hurwitz, D. M., Solomon, S. C., Head, J. W., Preusker, F., Oberst, J. (2013). An assemblage of lava flow features on Mercury. Journal of Geophysical Research: Planets, 118(6), 1303-1322.

Byrne, P. K., Ostrach, L. R., Fassett, C. I., Chapman, C. R., Denevi, B. W., Evans, A. J., et al. (2016). Widespread effusive volcanism on Mercury likely ended by about 3.5 Ga. Geophysical Research Letters, 43, 7408–7416.

Coffin, M.F. & Eldholm, O. (1994). Large igneous provinces: crustal structure, dimensions, and external consequences. Reviews of Geophysics, 32, 1–36.

Crumpler, L. S., & Aubele, J. C. (2001). Volcanoes of New Mexico: an abbreviated guide for non-specialists. Volcanology in New Mexico. New Mexico Museum of Natural History and Science Bulletin, 18, 5-15.

Denevi, B. W., Robinson, M. S., Solomon, S. C., Murchie, S. L., Blewett, D. T., et al., (2009). The evolution of Mercury's crust: A global perspective from MESSENGER. Science, 324(5927), 613-618.

Denevi, B. W., Ernst, C. M., Meyer, H. M., Robinson, M. S., Murchie, S. L., Whitten, J. L., et al., (2013). The distribution and origin of smooth plains on Mercury. Journal of Geophysical Research: Planets, 118(5), 891-907.

Ernst, R. E. (2014). Large igneous provinces. Cambridge University Press.

Fassett, C. I., Head, J. W., Blewett, D. T., Chapman, C. R., Dickson, J. L., Murchie, S. L., et al., (2009). Caloris impact basin: Exterior geomorphology, stratigraphy, morphometry, radial sculpture, and smooth plains deposits. Earth and Planetary Science Letters, 285(3), 297-308.

Geikie, A. (1880). The lava-fields of North-western Europe. Nature, 23, 3–5.

Golder, K. B., Burr, D. M., & Kattenhorn, S. A. (2020). Investigation of target property effects on crater populations in long lava flows: A study in the Cerberus region, Mars, with implications for magma source identification. Icarus, 113388.

Greeley, R. (1976). Modes of emplacement of basalt terrains and an analysis of mare volcanism in the Orientale Basin. In Lunar and Planetary Science Conference Proceedings (Vol. 7, pp. 2747-2759).

Greeley, R., & King, J. S. (1977). Volcanism of the Eastern Snake River Plain, Idaho: A comparative planetary geology-guidebook. http://www. sti. nasa. gov/RECONselect. html.

Greeley, R. (1982). The Snake River Plain, Idaho: Representative of a new category of volcanism. Journal of Geophysical Research: Solid Earth, 87(B4), 2705-2712.

Head, J. W., and Coffin, M. F. (1997). Large igneous provinces: A planetary perspective. Geophysical Monograph-American Geophysical Union, 100, 411-438.

Head, J. W., Murchie, S. L., Prockter, L. M., Solomon, S. C., Chapman, C. R., Strom, R. G., Watters, T.R., Blewett, D.T., Gillis-Davis, J.J., Fassett, C.I., Dickson, J.L., Morgan, G.A., Kerber, L. (2009). Volcanism on Mercury: Evidence from the first MESSENGER flyby for extrusive and explosive activity and the volcanic origin of plains. Earth and Planetary Science Letters, 285(3), 227-242.

Head, J. W., Chapman, C. R., Strom, R. G., Fassett, C. I., Denevi, B. W., Blewett, D. T., et al., (2011). Flood volcanism in the northern high latitudes of Mercury revealed by MESSENGER. Science, 333(6051), 1853-1856.

Hurwitz, D. M., Head, J. W., Byrne, P. K., Xiao, Z., Solomon, S. C., Zuber, M. T., Smith, D.E., Neumann, G. A. (2013). Investigating the origin of candidate lava channels on Mercury with MESSENGER data: Theory and observations. Journal of Geophysical Research: Planets, 118(3), 471-486.

Jaeger, W. L., Keszthelyi, L. P., Skinner, J. A., Milazzo, M. P., McEwen, A. S., Titus, T. N., Rosiek, M.R., Galuszka, D.M., Howington-Kraus, E., Kirk, R. L., the HiRISE Team (2010). Emplacement of the youngest flood lava on Mars: A short, turbulent story. Icarus, 205(1), 230-243.

Keszthelyi, L., McEwen, A. S., Thordarson, T. (2000). Terrestrial analogs and thermal models for Martian flood lavas. Journal of Geophysical Research: Planets (1991–2012), 105(E6), 15027-15049.

Keszthelyi, L., Thordarson, T., McEwen, A., Haack, H., Guilbaud, M. N., Self, S., Rossi, M. J. (2004). Icelandic analogs to Martian flood lavas. Geochemistry, Geophysics, Geosystems, 5(11).

Keszthelyi, L., Self, S., & Thordarson, T. (2006). Flood lavas on earth, Io and Mars. Journal of the geological society, 163(2), 253-264.

Kiefer, W. S., & Murray, B. C. (1987). The formation of Mercury's smooth plains. Icarus, 72(3), 477-491.

Klima, R. L., Denevi, B. W., Ernst, C. M., Murchie, S. L., & Peplowski, P. N. (2018). Global distribution and spectral properties of low-reflectance material on Mercury. Geophysical Research Letters, 45(7), 2945-2953.

McEwen, A. S., Preblich, B. S., et al. (2005). The rayed crater Zunil and interpretations of small impact craters on Mars. Icarus, 176(2), 351-381.

Nichols, R. L. (1946). McCartys basalt flow, Valencia County, New Mexico. Geological Society of America Bulletin, 57(11), 1049-1086.

Ostrach, L. R., Robinson, M. S., Whitten, J. L., Fassett, C. I., Strom, R. G., Head, J. W., Solomon, S. C. (2015). Extent, age, and resurfacing history of the northern smooth plains on Mercury from MESSENGER observations. Icarus, 250, 602-622.

Plescia, J. B. (1990). Recent flood lavas in the Elysium region of Mars. Icarus, 88(2), 465-490.

Plescia, J. B. (2003). Cerberus Fossae, Elysium, Mars: A source for lava and water. Icarus, 164(1), 79-95.

Prockter, L. M., Ernst, C. M., Denevi, B. W., Chapman, C. R., Head, J. W., Fassett, C. I., ... & Cremonese, G. (2010). Evidence for young volcanism on Mercury from the third MESSENGER flyby. Science, 329(5992), 668-671.

Sakimoto, S. E. H., Gregg, T. K. P., Hughes, S. S., & Chadwick, J. (2003). Re-assessing plains-style volcanism on Mars. In Sixth International Conference on Mars.

Self, S., Thordarson, T., Keszthelyi, L., Walker, G. P. L., Hon, K., Murphy, M. T., Long, P., Finnemore, S. (1996). A new model for the emplacement of Columbia River basalts as large, inflated pahoehoe lava flow fields. GRL, 23(19), 2689-2692.

Self, S., Jay, A. E., Widdowson, M., Keszthelyi, L. P. (2008). Correlation of the Deccan and Rajahmundry Trap lavas: Are these the longest and largest lava flows on Earth? Journal of Volcanology and Geothermal Research, 172(1), 3-19.

Spudis, P. D., and Guest, J. E. (1988). Stratigraphy and geologic history of Mercury. Mercury, University of Arizona Press, 1, 118-164.

Strom, R. G., Chapman, C. R., Merline, W. J., Solomon, S. C., Head, J. W. (2008). Mercury cratering record viewed from MESSENGER's first flyby. Science, 321(5885), 79-81.

Strom, R. G., Banks, M. E., Chapman, C. R., Fassett, C. I., Forde, J. A., Head, J. W., Merline, W.J., Prockter, L.M., Solomon, S. C. (2011). Mercury crater statistics from MESSENGER flybys: Implications for stratigraphy and resurfacing history. Planetary and Space Science, 59(15), 1960-1967.

Thomas, R. J. (2013). Identification of possible recent water/lava source vents in the Cerberus plains: stratigraphic and crater count age constraints. Journal of Geophysical Research: Planets, 118(4), 789-802.

Thordarson, T., and Self, S. (1993). The Laki (Skaftár Fires) and Grímsvötn eruptions in 1783-1785. Bulletin of Volcanology, 55, 233-263.

Thordarson, T., Miller, D.J., Larsen, G., Self, S., Sigurdsson, H. (2001). New estimates of sulfur and atmospheric mass-loading by the 934 AD Eldgjá eruption, Iceland. Journal of Volcanology and Geothermal Research, 108, 33-54.

Trask, N. J., and Guest, J. E. (1975). Preliminary geologic terrain map of Mercury. Journal of Geophysical Research, 80(17), 2461-2477.

Tyrrell, G.W. (1937). Flood basalts and fissure eruption. Bulletin of Volcanology, 1, 87–111.

Vaucher, J., Baratoux, D., et al. (2009). The volcanic history of central Elysium Planitia: Implications for martian magmatism. Icarus, 204(2), 418-442.

Walker, G. P. L. (1971). Compound and simple lava flows and flood basalts. Bulletin Volcanologique, 35(3), 579-590.

Washington, H.S. (1922). Deccan Traps and the other plateau basalts. Bulletin of the Geological Society of America, 33(4), 765-804.

Werner, S. C. (2009). The global martian volcanic evolutionary history. Icarus, 201(1), 44-68.

Whitten, J. L., Head, J. W., Denevi, B. W., Solomon, S. C. (2014). Intercrater plains on Mercury: Insights into unit definition, characterization, and origin from MESSENGER datasets. Icarus, 241, 97-113.

Wilhelms, D.E., (1976). Mercurian volcanism questioned. Icarus 28, 551–558.

Zimbelman, J. R. (1998). Emplacement of long lava flows on planetary surfaces. Journal of Geophysical Research: Solid Earth (1978–2012), 103(B11), 27503-27516.

Zimbelman, J. R., & Johnston, A. K. (2002). New precision topographic measurements of Carrizozo and McCartys basalt flows, New Mexico. Geology of white sands.

CHAPTER 1
INVESTIGATIONS OF TARGET PROPERTY EFFECTS ON CRATER POPULATIONS IN LONG LAVA FLOWS: A STUDY IN THE CERBERUS REGION, MARS, WITH IMPLICATIONS FOR MAGMA SOURCE IDENTIFICATION

A version of this chapter was originally published by Keenan B. Golder, Devon M. Burr, and Simon A. Kattenhorn. “Investigation of target property effects on crater populations in long lava flows: A study in the Cerberus region Mars, with implications for magma source identification.” *Icarus* 355 (2020): 113388. https://doi.org/10.1016/j.icarus.2019.113388

I wrote this article based on geomorphological mapping and crater counting performed on image data collected by the Context Camera instrument aboard the Mars Reconnaissance Orbiter. The co-authors guided me during the interpretation of the data and helped me revise and edit the entire manuscript prior to submission. This article underwent two rounds of reviews by 2 anonymous reviewers for the journal *Icarus*, was accepted for publication in July, 2019, and published in January, 2020.

Abstract

Young volcanism on Mars is exemplified within the Cerberus region, which enables examination of relatively pristine lava flow surfaces. In this investigation, I derived model ages within the circum-Cerberus channelized lavas for sites proximal, medial, and distal to the lava flow sources, finding that these ages decrease with increasing distance from the inferred source. Investigating multiple possible explanations for this downstream decrease in model ages, I concluded that the most likely cause is changes in the rheological properties of the lava during emplacement. Analogous terrestrial lava flows exhibit rheological changes along their length during emplacement, supporting the hypothesis that target properties affect crater size frequency distributions (CSFDs) on extraterrestrial bodies. Using scaling methods, I investigated how possible material property changes in the Cerberus channelized lavas affected CSFDs. To derive a single model age for each channel, I arithmetically size-scaled the distal and proximal crater sizes. I also used pi-group scaling to estimate the effect of material strength and porosity on the final CSFDs. I infer that the Athabasca, Grjótá, and Marte Valles lavas underwent minor, moderate, and major rheological changes, respectively, to account for the progressively larger age discrepancies along their respective flow lengths. The arithmetic size-scaling yields relative lava emplacement ages, from oldest to youngest, respectively, as Grjótá, Marte, and Athabasca.

This lack of a consistent progressive directional emplacement (east-to-west or west-to-east) of lava model ages implies that the magma source was spatially distributed beneath the Cerberus region, although magma contributions from the two bordering volcanic provinces cannot be ruled out. The results of this study support the findings of previous lunar and martian studies that inferred target property changes affected CSFDs, which may have some bearing on age dating of young lava surfaces across the inner Solar System.

Introduction

Evidence for mafic volcanism has been found on numerous bodies in the inner Solar System, including Mercury, Venus, Earth, the Moon, and Mars (e.g., Head and Coffin, 1997; Zimbelmann, 1998; Head et al., 2009). Despite its small size, Mars has been volcanically active throughout much of its geologic history. The majority of volcanic emplacement occurred during the Noachian and early Hesperian, with volcanism persisting, although with decreasing intensity, well into the Amazonian (e.g., Werner, 2009). The areal distribution of volcanic landforms combined with crater count model ages indicates that martian volcanic activity decreased over time from wide-spread activity in the Noachian to more localized events in the late-Amazonian, concentrated around the Tharsis and Elysium volcanic provinces (Werner, 2009; Grott et al., 2013), particularly within the calderas and along the flanks of Olympus and Elysium Mons (e.g., Platz and Michael, 2011; Isherwood et al., 2013). Another example of late-Amazonian regional volcanism is found in Kasei Valles, where lava fills a large outflow channel (e.g., Chapman et al., 2010). An excellent example of this young regional volcanism is located within the Cerberus region, which is located between the Olympus-Tharsis Volcanic Province (OTVP) and the Elysium Volcanic Province (EVP; Fig. 1A).

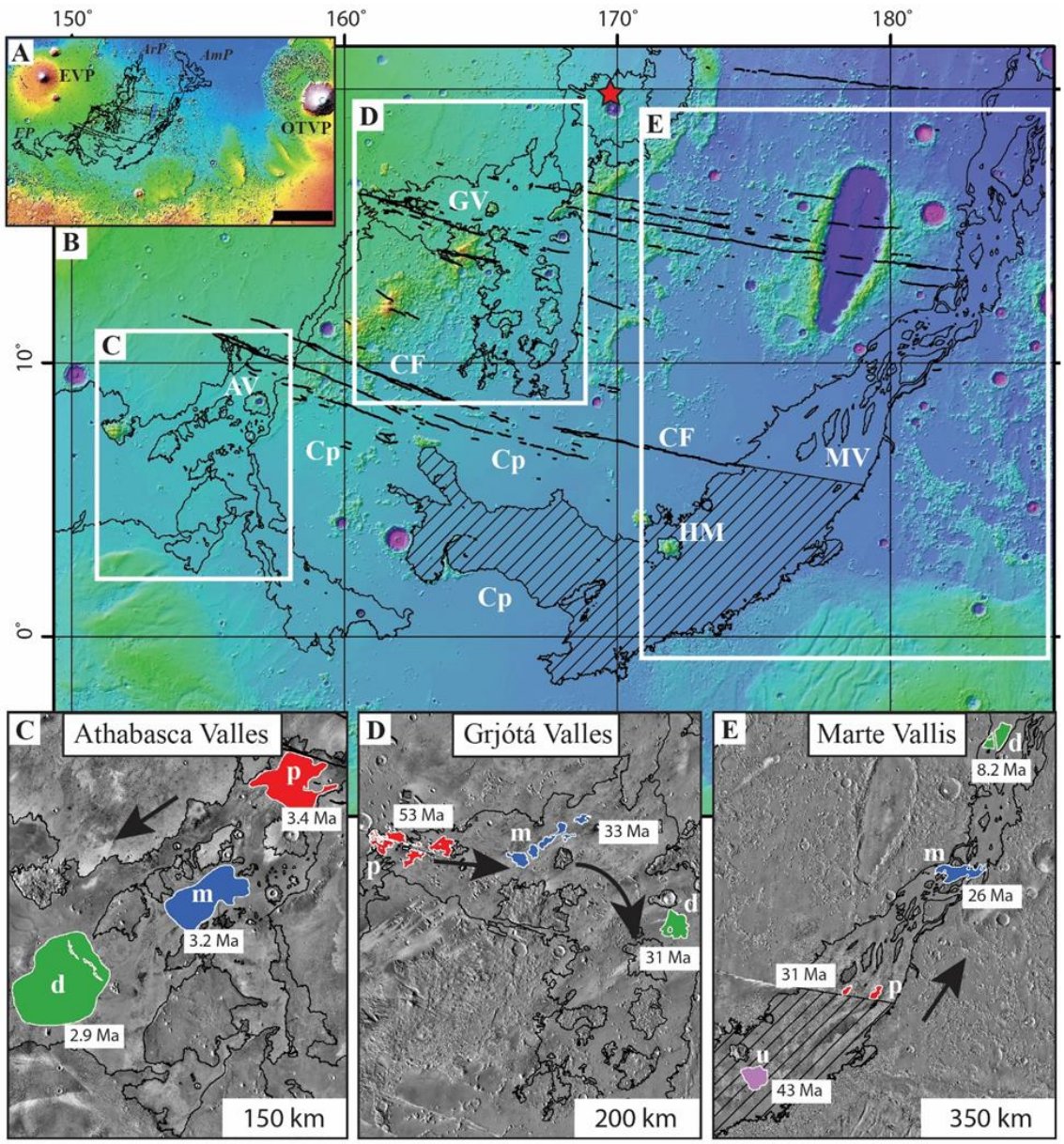

Figure 1. A: Regional context image, centered at 170° E, 10° N, scale bar equals 1000 km. The mapped extent of the three lava-filled channels, Athabasca (AV), Grjótá (GV), and Marte Valles (MV), is overlain on a shaded-relief basemap (image credit: MOLA science team). These lava flows extend into the surrounding Elysium Planitia (*EP*), Arcadia Planitia (*ArP*), and Amazonis Planitia (*AmP*). Warm colors denote higher elevations, and cool colors denote lower elevations. B: A zoomed portion of the channelized lavas encompassing the study areas, including the Cerberus plains (Cp). The NW-SE trending features are the regional Cerberus Fossae (CF) fissure network. The red star denotes the location of Kotka crater. The hachured area corresponds to the portion of the latest lava that filled MV, which is upstream of the now-buried CF segment that may have sourced the aqueous flow that incised MV. the hachured and non-hachured portions represent the same flow but were delineated based on whether the observed lavas were within the Cerberus plains or within MV proper. This latest lava flow originated within the Cerberus plains. Images C, D, E, corresponding to the white bounding boxes, show the proximal (p, red), medial (m, blue), and distal (d, green) crater count locations and their matching crater count model ages for each of these lava flows. Black arrows denote the general flow direction of lava within the channels. Marte Vallis has an additional count area (u, purple), upstream of the buried Cerberus fossa segment, and located directly south of Hibes Montes (HM).

The ages of the lavas within the Cerberus region have been calculated based on crater count derived model ages, but crater characteristics (e.g., size and population) can be affected by the material they are formed in. Previous analyses of crater populations from comets (Holsapple and Housen, 2007), adjacent cogenetic lunar geologic units (van der Bogert et al., 2010, 2017), and within platy-ridged lava flows on Mars (Murray et al., 2005; Page et al., 2009; Chapman et al., 2010; Dundas et al., 2010) show geospatial variation within geologic units in the final diameters of impact craters and crater size frequency distributions (CSFDs). These geospatial variations in both crater size and distribution are unexpected within single geologic units and suggest that properties of the target materials affect the final crater diameters and population distributions (e.g., Murray et al., 2005; Holsapple and Housen, 2007; Page et al., 2009; Chapman et al., 2010; Dundas et al., 2010; Housen and Holsapple, 2011; Dundas and Keszthelyi, 2014; van der Bogert et al., 2017). Data for terrestrial sites support the suggested influence of target properties on crater diameters on extraterrestrial bodies. These data indicate rheological changes occur during lava emplacement, with observations in Hawai'i and Iceland showing clear changes in vesicularity, porosity, density, and crystallinity with increasing distance from the eruption source (e.g., Swanson, 1973; Wilmoth and Walker, 1993; Flóvenz and Sæmundsson, 1993; Polacci et al., 1999; Keszthelyi et al., 2004).

Martian lava flows in the Cerberus region are an ideal extraterrestrial site to investigate target property effects on crater diameter and population distribution. These lavas are young, have undergone little apparent surface modification, and stretch for more than 1000 km from their sources (Plescia, 1990; Burr et al., 2002a, 2002b; Berman and Hartmann, 2002; Plescia, 2003; Keszthelyi, et al., 2004; McEwen et al., 2005; Burr et al., 2009; Vaucher et al., 2009; Jaeger et al., 2010). They also have wide-spread coverage by visible imaging at high resolutions.

The surface of these lava flows exhibits crater count model age discrepancies, with downstream decreasing age trends identified in Marte and Athabasca Valles (Vaucher et al., 2009), consistent with differences in strength of the target material (Murray et al., 2005; Page, 2009, Dundas et al., 2010). This downstream decreasing age trend was later found in Kasei Valles (Chapman et al., 2010; Dundas and Keszthelyi, 2014). In addition, a difference in CSFDs was identified in the Cerberus region between the plates and interplate troughs in the platy-ridge textured locales (Murray et al., 2005; Page et al., 2009; Dundas et al., 2010).

In this study, I analyzed the Cerberus lava flows to address the question of why the observed decreasing age trends exist in these large late-Amazonian lava flows, and derive implications for lavas elsewhere on Mars and within the Solar System. In this analysis, I performed geomorphological mapping, crater counting, and crater-scaling to quantify the effect of target properties on the final CSFDs. The results of this work offer new insights into changes that take place during the emplacement of long lava flows, and how these rheological changes affect crater retention. Lastly, I reduced the crater count model ages to single ages for each channel in order to explore potential magma migration patterns and to infer likely magma sources.

Background

Cerberus Region Volcanism

The Cerberus plains consists of complexly overlapping lava flows and low shield volcanoes that were emplaced over a period of ~250 Ma (Plescia, 1990; Plescia, 2003; Vaucher et al., 2009; Thomas, 2013). Distinct and pristine-looking lava flows stretch for 100s of km within the plains and >1000 km within three circum-Cerberus aqueously-carved flood channels, Athabasca, Grjótá, and Marte Valles (Fig 1B; Plescia, 1990; Burr et al., 2002a, 2002b; Berman

and Hartmann, 2002; Plescia, 2003; Keszthelyi, et al., 2004; McEwen et al., 2005; Burr et al., 2009; Vaucher et al., 2009; Jaeger et al., 2010). Typical thicknesses measured from topographic data of lava flow fronts are ~20 m within the Cerberus plains and Athabasca Valles (Vaucher et al., 2009; Jaeger et al., 2010), and up to ~30 m in Grjótá Valles (Burr and Parker, 2006); in Marte Vallis, estimated thickness are up to ~100 m, based on Shallow Radar (SHARAD) channel depth measurements and observations that the channel is entirely filled (Morgan et al., 2013). This value for Marte Vallis is greater than the typical range for terrestrial inflated pahoehoe lobe thicknesses of 15-30 m (Self et al., 1998) and may be the result of multiple stacked lava flows, similar to the Columbia River Basalt Group (e.g., Self et al., 1996). Athabasca and Grjótá Valles originate from separate points that remain discernable along the Cerberus Fossae fissure network (Fig. 1B), as do their infilling lava flows (Plescia, 1990; Tanaka et al., 1992; Burr et al., 2002a, 2002b; Berman and Hartmann, 2002; Plescia, 2003; Keszthelyi et al., 2004; Burr and Parker, 2006). Although the surface source for Marte Vallis is obscured, topography (Burr et al., 2002b; Plescia, 2003; Vaucher et al., 2009) and subsurface radar (Morgan et al., 2013) indicate the source is an eastern segment of the Cerberus Fossae, buried by post-flooding lava emplacement.

In Athabasca and Grjótá Valles, the lavas are interpreted to have been emplaced as single flow units based on their morphologies and mapped extents (Jaeger et al., 2010; Hamilton, 2013), though emplacement as multiple stacked lava flows (cf. Self et al., 1996) cannot be excluded on these bases. The emplacement of the channelized lavas during a single eruption, possibly at high flow rates and low viscosities (e.g., Jaeger et al., 2007, 2010), is consistent with modeled flow rates and viscosities associated with the eruptions that built small shield volcanoes in the Cerberus plains (Baratoux et al., 2009). The latest lava flow unit in Marte Vallis also appears to have been emplaced as a single flow unit (Vaucher et al. 2009), though there are

indications earlier eruptive events may have infilled the channel, such as the older volcanic ACo unit mapped as underlying the latest volcanic unit filling the channel (e.g., Vaucher et al., 2009). A lava flow in Kasei Valles, in the opposite hemisphere, was also inferred to have been emplaced during a single eruptive event (Chapman et al., 2010; Dundas and Keszthelyi, 2014). Due to the similar extent, flow morphology, and surface textures, this flow provides a morphological analogue to the Athabasca, Grjótá, and Marte Valles lava flows. A rapid, turbulent emplacement has been suggested for the lavas in Athabasca (Jaeger et al., 2010) and Kasei Valles (Dundas and Keszthelyi, 2014). Grjótá and Marte Valles have surface textures and areal extents that are comparable to those found in both Athabasca (Fig. 2) and Kasei Valles. If the inference of rapid emplacement is valid for Athabasca and Kasei Valles, then the similarity in surface textures suggests these other two Cerberus lava flows were also emplaced geologically rapidly. This emplacement might have spanned days or weeks (Jaeger et al., 2010) or have been more gradual over the course of months, years, or decades, as observed in analogous terrestrial systems (e.g., Columbia River Basalts; Self et al., 1996).

The interpretation of the channel-filling material as lava is supported by multiple lines of observational evidence. This evidence includes the embayment of streamlined plateaus and craters, platy-ridged surface textures comparable to rafted lava plates on Earth, marginal levees, and knobs interpreted as rootless cones (Fig. 2; e.g., Plescia, 1990; Keszthelyi et al., 2000; Burr et al., 2002b, Plescia, 2003; Keszthelyi et al., 2004; Burr and Parker, 2006; Jaeger et al., 2007; Burr et al., 2009; Hamilton and Fagents, 2009; Vaucher et al., 2009; Keszthelyi et al., 2010; Jaeger et al., 2010). The presence of rootless cones in Athabasca Valles, which form during the emplacement of lava on a water/ice-rich surface leading to phreatomagmatic eruptions and

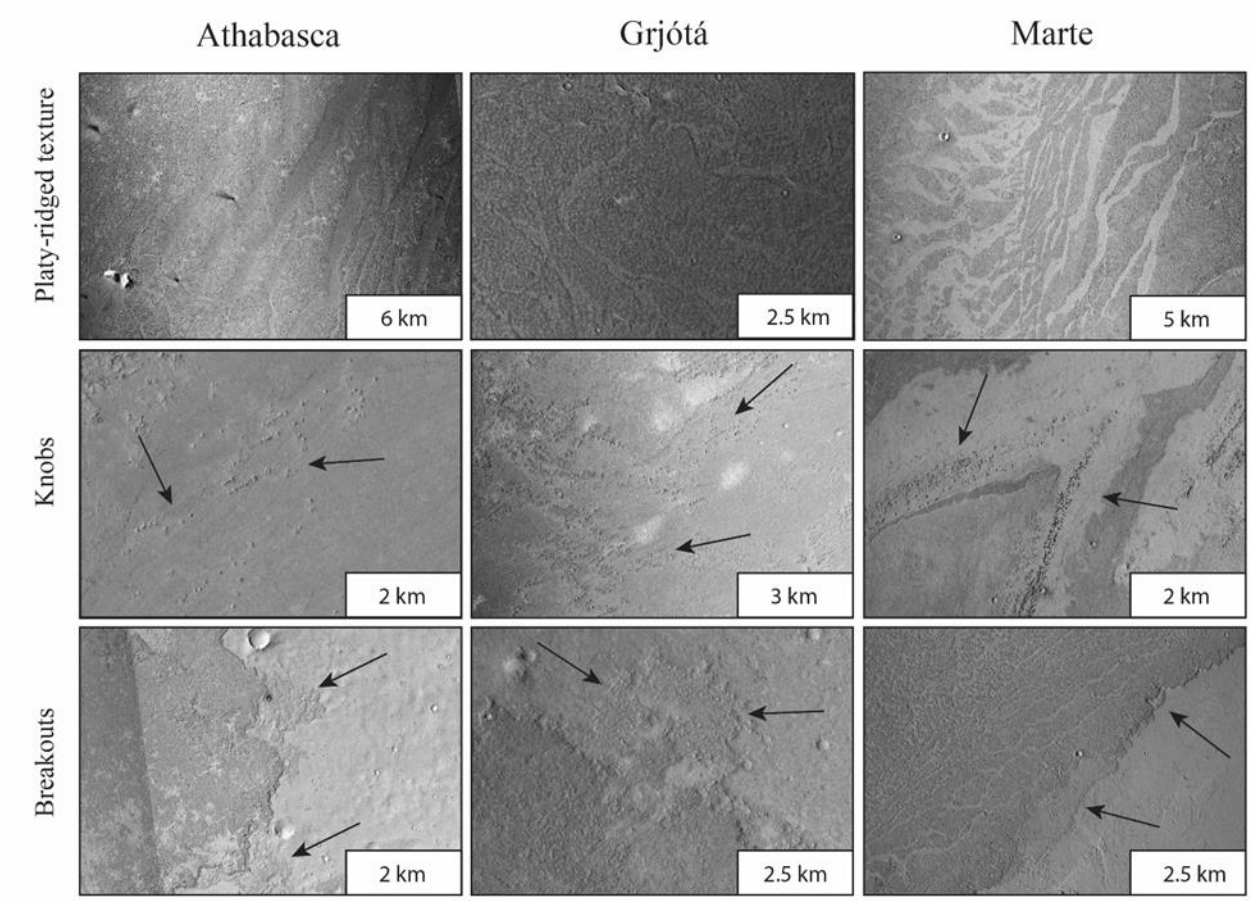

Figure 2. Typical surface textures identified in the three channelized lavas, including platy-ridges, knobs, and breakouts. The interplate regions of the platy-ridged texture are dark in Athabasca Valles, unlike in Grjótá and Marte Valles. These plates and ridges are smaller and extremely muted in Grjótá Valles. Each flow contains populations of knobs (black arrows), often found in curvilinear concentrations. The margins of the flows may also exhibit limited breakouts (black arrows) from beneath their coherent crusts. These breakouts are generally small, with the exception of those found along the eastern margin of Marte Vallis.

resultant cone construction, is strongly indicative of interactions between lava and ground-ice or groundwater (e.g., Lanagan et al., 2001; Burr et al., 2005). Additionally, the observed signal loss rate, or attenuation, of the Mars Advanced Radar for Subsurface and Ionosphere Sounding (MARSIS) instrument observations of Athabasca Valles is higher than that expected for an ice-rich environment and is consistent with a volcanic origin for this infilling material (Boisson et al., 2009). Gamma Ray Spectrometer (GRS) data indicates the materials in the Cerberus region are very dry (Feldman et al., 2004), consistent with a lava composition. Alternative proposed origins for these surface features include: 1) an ice-rich fluvial origin (Rice et al., 2002); 2) ponded flood waters which later froze (Murray et al., 2005); and 3) thermal contraction of an ice-rich regolith (Page and Murray, 2006; Page, 2007, 2008). Smaller, dark lobate deposits within the Cerberus plains have been interpreted as mudflows (Wilson and Mouginis-Mark, 2014). However, the morphology and texture of the material, the interpretation of the pitted cones in the channels as rootless cones, and the relevant MARSIS and GRS data all support the prevailing interpretation of the infilling material as lava, and I accept that interpretation as a foundation for this work.

Intrusive volcanism in the region is suggested by tectonic landforms that are analogous to volcanotectonic landforms on Earth. Terrestrial graben overlie giant radiating dike swarms, such as the Ottawa Graben and the Grenville dike swarm (e.g., Ernst et al., 1995; Ernst et al., 2001), and the shallow dike intrusions around the Krafla caldera in Iceland and Kilauea volcano in Hawai'i (e.g., Ernst et al., 1995; Rubin, 1995). Fissure networks on Mars, including the Cerberus Fossae which are the source for both water and lava (e.g., Burr et al., 2002a, 2002b; Plescia, 2003), have been interpreted to be graben that are the surface expression of underlying dike systems (Wilson and Head, 2002; Head et al., 2003; Schultz et al., 2004; Vetterlein and Roberts,

2010; Klimczak, 2014). Pits and pit chains along and at the ends of many Cerberus Fossae segments are further evidence for the presence of dikes, as such features are commonly associated with dilation and subsequent collapse related to dike intrusions (Wyrick et al., 2004; Ferrill et al., 2004; Patterson et al., 2016).

Crater Counting and Cerberus Region Age Estimates

The craters in the channelized Cerberus lava flows are all simple craters, consisting of shallow, bowl-shaped depressions, occasionally hosting small ejecta blankets. Most of these craters are <100 m in diameter (e.g., Dundas et al., 2010). These craters form when a projectile impacts the surface and excavates a transient crater, and they are later modified by collapse or subsequent processes to attain its final morphology (e.g., Melosh, 1989; Ivanov and Hartmann, 2007; Melosh, 2011). The surfaces of each of the lava flows in the Cerberus region host crater populations of varying densities, which can be used to infer the history and timing of processes in the region. Estimation of planetary surface ages relies on CSFDs, a statistical approach in which craters of various diameters within a given area are counted. Surfaces which contain higher densities of impact craters are inferred to be older than surfaces with lower densities of craters (e.g., Neukum and Ivanov, 1994; Hartmann and Neukum, 2001; Ivanov, 2001; Neukum et al., 2001; Hartmann, 2005; Werner and Tanaka, 2011).

Secondary craters, which originate as ejecta from primary impacts, may skew crater counting results through contamination and subsequent overestimation of small crater populations (e.g., McEwen and Bierhaus, 2006; Werner and Tanaka, 2011). Within the Cerberus plains, secondary craters from the young impact sites Zunil (~1 Ma; McEwen et al., 2005; Williams et al., 2014) and Corinto (~3 Ma; Golombek et al., 2014) overlap Athabasca and Grjótá Valles, although observations of ejecta patterns indicate secondaries from these impacts

do not affect Marte Vallis (McEwen et al., 2005; Williams et al., 2014). Recognizing the potential for secondary crater contamination in the region, I chose locations for crater counting that avoided locales containing obvious clustered secondaries.

Crater counts have been used to age-date overlapping lavas and volcanic structures in the Cerberus region, including low shield volcanoes, to the very late Amazonian (Vaucher et al., 2009). According to these data, the volcanic activity within the plains was episodic, with the lava flows emplaced between 2.5-173.4 Ma and the shield volcanoes emplaced between 9.2-234 Ma. The lavas within the Cerberus channels are similarly young. The derived emplacement ages (Table 1) for the inferred single lava unit (e.g., Jaeger et al., 2010) in Athabasca Valles are late Amazonian (Burr et al., 2002b). Following the discovery of the Zunil impact crater and associated secondaries, McEwen et al. (2005) revised the age estimates for the lava in that channel, deriving an age range from 1.5-200 Ma. That maximum age estimate is based on the presence of a single 500 m crater not embayed or filled with lava, with a factor of two uncertainty. Vaucher et al. (2009) performed crater counts in several locations in Athabasca Valles, which suggested a minor increasing age trend with distance from the source, although the uncertainties of these derived ages overlap. Grjótá Valles is interpreted to consist of a single lava flow (Hamilton, 2013), with age estimates that suggest it was emplaced between 10-40 Ma (Burr et al., 2002b) or 62-250 Ma (Hamilton et al., 2010). The lava in Grjótá has also been interpreted to be a part of a unit that was emplaced ~500 Ma (Vaucher et al., 2009). This disparity in age estimates may be a result of the lack of clear unit and contact identification between Grjótá Valles and the surrounding older volcanic terrain. Marte Vallis age estimates range from 8-200 Ma (Berman and Hartmann, 2002; Burr et al., 2002b; Vaucher et al., 2009).

Table 1. Previously derived crater count model ages for the lava-infilled channel systems and Cerberus plains. *Vaucher et al. (2009) only performed crater counts in one location within their *ACo* unit, of which they determined Grjótá Valles was a part.

Location	Age estimate	Reference
Athabasca	2-8 Ma	Burr et al., 2002b
	1.5-200 Ma	McEwen et al., 2005
	2.5-2.81 Ma	Vaucher et al., 2009
Grjótá	10-40 Ma	Burr et al., 2002b
	~62-250 Ma	Hamilton et al., 2010
	500* Ma	Vaucher et al., 2009
Marte	35-140 Ma	Burr et al., 2002b
	~10-200 Ma	Berman & Hartmann, 2002
	8-24 Ma	Vaucher et al., 2009
Cerberus Plains	2.5-234 Ma	Vaucher et al., 2009

Crater counts performed in Marte Vallis show a trend of decreasing model ages downstream from the source (Vaucher et al., 2009).

Material Properties of Lava Flows and Possible Effects on Crater Retention

Small, simple impact craters, as are found on the Cerberus channelized lavas, are formed within the strength regime where the material properties of the target govern the final crater sizes, morphologies, and total population densities (e.g., Ivanov, 2001; Housen and Holsapple, 2011). Lab and field experiments of craters formed by explosives, and numerical modeling of crater formation processes, suggest stronger targets (i.e., of more crystalline or less porous material) yield smaller craters, due to the greater cohesive strength restricting crater expansion during the excavation stage (e.g., Schmidt and Housen, 1987; Holsapple, 1993; Wünnemann et al., 2011; Housen and Holsapple, 2011). This greater material strength also restricts overall crater formation, yielding fewer and smaller craters (Dundas et al., 2010; Wünnemann et al., 2011). Whereas more crystalline, denser, less porous material is inferred to produce smaller craters due to strength effects, this previous research into target properties also suggests that highly porous target material (~30-40%) restricts crater sizes and results in fewer craters due to the dissipation of the impactor energy in the crushing of vesicles or pore space, although not to the same degree as crystalline target materials (e.g., Holsapple and Housen, 2007; Wünnemann et al., 2011; Housen and Holsapple, 2011; van der Bogert et al., 2017). In summary, a stronger and less porous target will exhibit smaller craters and a lower overall population for a given impactor population than will a weaker and more porous target.

On Earth, the observed decrease in porosity, directly related to lava vesicularity, and increase in crystallinity with increasing distance from the eruption source, has been directly attributed to the lava degassing during emplacement (e.g., Wilmoth and Walker, 1993; Polacci et

al., 1999). Highly vesicular lavas (~70%) in Hawai'i have been identified near their sources and exhibit a trend of decreasing vesicularity as distance from the source increased (Swanson, 1973; Wilmoth and Walker, 1993; Polacci et al., 1999). Decreasing porosity with increasing distance from the source has also been identified in Icelandic lava flows (e.g., Flóvenz and Sæmundsson, 1993). In Hawai'i, this decreasing porosity trend, identified in two flows, is coupled with an increase in overall crystallinity (Polacci et al., 1999), which leads to a denser and stronger whole rock in the distal reaches of the flow (Keszthelyi et al., 1998). High porosities (40-50%) have been inferred within a few hundred kilometers of the Athabasca Valles source on the basis of SHARAD permittivity analyses (Alberti et al., 2012). These porosity values are consistent with vesicular basalt and brecciated crusts, and resultant low densities (Keszthelyi et al., 2004; Dundas and Keszthelyi, 2014). A downstream decrease in vesicularity and increase in crystallinity, and corresponding increase in strength, are suggested to have occurred during the emplacement of the Kasei Valles lava as an explanation for the decrease in crater count model ages with increasing distance downstream (Dundas and Keszthelyi, 2014). Quantification of the effect of these properties on final crater diameters and CSFDs is shown in my discussion of Crater Scaling (see *Size-scaling of Channelized Lava Crater Counts to Derive a Single Model Age* section).

Hypotheses

The driving question for this work concerns why age discrepancies exist within geologic units, such as lava units on Mars (Page et al., 2009; Dundas et al., 2010) and impact melt deposits on the Moon (van der Bogert et al., 2017), that are inferred to have been emplaced contemporaneously or within a geologically short time span. Previous crater count derived ages for the channelized lavas in the Cerberus region show significant variations (Table 1), possibly

influenced by disparate count locations. These variations in age, and specifically decreasing age trends in Marte Vallis, suggest either lava emplacement at different times or changes to crater populations during their formation by target properties effects. Although secondary craters can affect derived ages, and non-obvious secondary craters may have been overlooked, the consistent trend derived within all three Cerberus channels suggests that such omissions are unlikely to be significant. With these data, I developed hypotheses to explain previous trends and seek to test them within the Cerberus channelized lavas.

Based on previous age estimates derived from the Cerberus lava surfaces, particularly Marte Vallis (e.g., Burr et al., 2002b; McEwen et al., 2005; Vaucher et al., 2009), and Kasei Valles in the opposite hemisphere (Chapman et al., 2010; Dundas and Keszthelyi, 2014), I consider the hypothesis that *rheological changes occurred within the lavas during their emplacement.* I test this hypothesis with new crater counts spatially distributed in the channelized lavas. A wide range of model ages, particularly decreasing ages downstream from the source, on a single flow would suggest changes occurred to the lava during emplacement, resulting in changes in crater production and retention at different locations downstream from the source.

Alternatively, based on the narrow age range previously identified in Athabasca Valles, and the lack of a clear pattern to the other ages identified in the Cerberus region, I also consider the competing hypothesis that *no rheological changes occurred within the lavas during their emplacement.* For this hypothesis to be supported, my newly derived crater count ages on single flows would need to yield the same age for each channel within statistical uncertainty. This result would strongly support rapid emplacement of the channelized lavas, as previously hypothesized (Jaeger et al., 2010; Hamilton, 2013), prohibiting any significant changes in rheology, and thus the crater retention characteristics, within a single flow.

Based on my initial crater count results, I develop additional explanatory mechanisms for the lava emplacement, described in the *Possible Mechanisms to Explain Intra-Channel Age Discrepancies* section.

Methods and Data

Testing of these hypotheses was accomplished using multiple sequential approaches: **(1)** geomorphological mapping to define the full extent of the lavas and determine locations for crater counts on the lava surfaces; **(2)** crater counting on high resolution images to refine the emplacement ages of the lavas; and **(3)** crater scaling techniques to determine a single, robust emplacement age for each channelized lava. From these data, I infer the effect of various target properties on the final CSFDs.

Data Sets

High-resolution images were used for geomorphologic mapping of the lava flows (as in Vaucher et al., 2009; Jaeger et al., 2010; Hamilton, 2013; Tanaka et al., 2014), and to count craters for age-dating. These tasks utilized Thermal Emission Imaging System (THEMIS) 100 meters per pixel (mpp) infrared day- and nighttime mosaics (Christensen et al., 2004), Mars Orbiter Laser Altimeter (MOLA) 463 mpp gridded topography (Smith et al., 2001), High Resolution Stereo Camera (HRSC) ~15 mpp images (Neukum et al., 2004), Context Camera (CTX) 6 mpp images (Malin et al., 2007), and High Resolution Imaging Science Experiment (HiRISE) ~0.25 mpp images (McEwen et al., 2007). Gravity and crustal thickness maps (Genova et al., 2016) were used to interpret subsurface anomalies.

Channelized Lava Flow Mapping

I mapped the lavas in the ESRI ArcGIS environment, using a CTX basemap at a scale of 1:100K, enabling the discrimination of flow contacts in previously identified flows. THEMIS,

HRSC, and HiRISE images were used to supplement the CTX basemap where gaps exist in data coverage. Mapping the maximum extent of the lavas was important to identify locations for crater counting, so I focused my mapping efforts on the identification of the margins of the lava flows. Previous mapping by Vaucher et al. (2009), Jaeger et al. (2010), and Hamilton (2013) of lava flows within Athabasca, Grjótá, and Marte Valles, respectively, served as the foundation and check on this mapping. I determined the extent of the lava flows within the channels based on superposition, embayment, onlapping, cross-cutting and local topographic relationships. Changes in the surface texture of the lava flows, examined in CTX image data, were used to distinguish flow margins. The lava units were traced back to their apparent sources along the fissure network, potentially pinpointing previously unidentified source locations. I also used these refined boundaries of the lavas to determine locations for subsequent crater counting.

Crater Counting

To derive model ages and thus test the competing hypotheses, crater counting was performed in several locations within a single lava flow unit in the channels (Fig. 1C-E). I chose locations that were proximal-, medial-, and distal-to-source, approximating count locations in Athabasca and Marte Valles from previous work (e.g., Vaucher et al., 2009), and extending this method into Grjótá Valles. In the case of Marte Vallis, for which the latest flow originated within the Cerberus plains, I added an additional location upstream of the buried fossae segment (directly south of Hibes Montes; Fig. 1B, E). For each location, craters were counted over an ~1000 km^2 or greater area coverage, a minimum area recommended to provide a statistically representative sampling of crater sizes (Warner et al., 2015). I used the CraterTools plug-in within ArcGIS to perform crater counts (Kneissl et al., 2011), whereas final crater count model ages were computed in Craterstats2 (Michael and Neukum, 2010; Michael, 2013) from fits of measured crater

distributions to model isochrons, crater production functions, and chronology functions (e.g., Ivanov, 2001; Hartmann and Neukum, 2001; Hartmann, 2005; Michael, 2013; Hartmann and Daubar, 2017). The best-fits for the isochrons for these data were determined using the Michael (2013) chronology function and the Hartmann (2005) production function. I also checked the derived ages with the Hartmann and Daubar (2017) production function and found the same results. Craters <40 m in diameter were excluded when fitting the observed crater populations to the isochrons, to account for observation loss due to resolution limits and/or resurfacing processes (Michael and Neukum, 2010).

All craters that are circular, have a raised rim, or retain an ejecta blanket within the chosen sites were counted. Craters that exhibit lava embayment predate the lava surface being age-dated and so were excluded. I also excluded craters with non-circular rims, which are typically secondaries, as well as obvious secondary crater clusters which were identified in THEMIS and CTX images. For this work, locations for crater counting (Fig. 1C-E) were chosen to avoid the mapped Zunil and Corinto secondaries (McEwen et al., 2005; Golombek et al., 2014; Williams et al., 2014), along with any previously unidentified secondary clusters.

Results

Channelized Lava Flow Mapping

The extent of the Athabasca and Marte lavas (Fig. 1C, E) were readily identified due to their well-defined flow margins, which were texturally distinct from their surroundings. The western flow margins near the Grjótá Valles source are also clear, but the margins to the north, south, and east are episodically obscured (Fig. 1D). In particular, the contact between the lava in the main Valles reach and the northward extension is obscured by the Kotka impact crater (Fig. 1 B). Thus, the mapped extent of the lava within this valley was restricted to readily identifiable

contacts or to regions where inferred contacts could be determined with relatively high confidence. I also mapped the lava flow from the Cerberus plains that fed into Marte Vallis (Fig. 1B), representing the youngest observed flow in the channel. The lava flows within the Cerberus plains and additional geomorphologic units were not mapped at the same resolution as those within the channels.

Although the channelized lavas are primarily confined within the aqueous flood channels, effusions into the surrounding terrain (e.g., Cerberus plains) are discernable. Beyond the limits of the topographic confinement, the lava in Athabasca extends westward into Elysium Planitia, the lava in Grjótá extends northward into Arcadia Planitia, and the lava in Marte extends northward into Amazonis Planitia (Fig. 1A). Small outbreaks are found along the margins on each channelized flow, whereas relatively larger outbreaks are located along the eastern lateral margins of the Marte Vallis (Fig. 2). Platy-ridged textures (Fig. 2; e.g., Keszthelyi et al., 2000; 2004) are found across nearly the entirety of Athabasca and Marte, but conversely are extremely limited within Grjótá. Pitted cones, interpreted as rootless cones, are observed in Athabasca, as well as in segments of Grjótá (Burr and Parker, 2006; Hamilton et al., 2010) and in Marte, and are typically found in chains (Fig. 2; Lanagan et al., 2001; Burr et al., 2005). Large craters that predate the lavas are embayed and filled by the lava filling the three channels.

Crater Counts: Intra-Channel Age Discrepancies

The model ages I derived for the channelized lavas (Fig. 3) reflect the latest lava flow that filled each channel and fall within the ranges of previously published data (Table 1). In a downstream direction, the derived model ages for the Athabasca Valles lava at the proximal-to-medial-to-distal locations decrease slightly from 3.3 ± 0.2 Ma, to 3.2 ± 0.2 Ma, to 2.9 ± 0.1, respectively. For the Grjótá Valles lava, the ages in a downstream direction decrease moderately

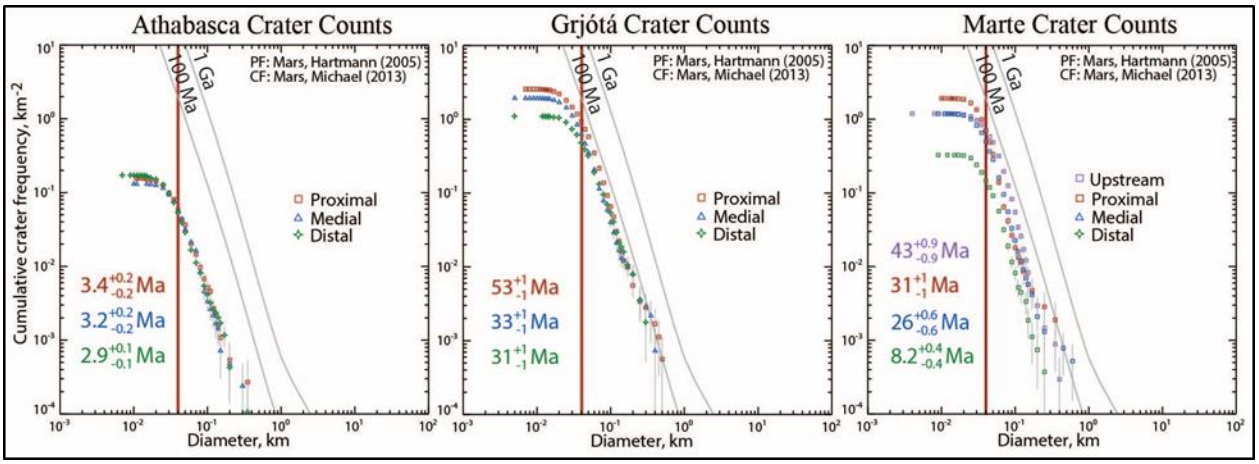

Figure 3. Model ages for the channelized lavas at locations relative to the inferred source at the Cerberus Fossae (see Figure 1C, D, and E for count locations). The lavas in each channel exhibit a downstream decreasing age trend. Craters below the 40 m threshold were not used when determining the isochron fits to calculate the surface ages (red line) due to the inferred loss of data at these small sizes.

from 53 ± 1 Ma, to 33 ± 1 Ma, to 31 ± 1 Ma, and in Marte Vallis the lava ages decrease significantly from 43 ± 0.9 Ma, to 31 ± 1 Ma, to 26 ± 0.6 Ma, to 8.4 ± 0.4 Ma. The observed rollover at small crater diameters, also seen in previous crater counts in this area (Burr et al. 2002b), is interpreted to be a result of observation loss due to resolution limits and/or resurfacing processes (Fig. 3; Michael and Neukum, 2010). Thus, the data reveal a proximal-to-distal trend of decreasing age outside of the uncertainty in the data for each of the channels.

Possible Mechanisms to Explain Intra-Channel Age Discrepancies

Downstream decreasing age trends, identified in all three channelized lavas investigated here, require explanation. Mechanisms that might explain the observed age trend, explained in detail below, include: (1) sub-carapace flows; (2) preferential erosion of craters; (3) additional lava sources; (4) slow emplacement; and (5) rheological property changes.

(1) Younger sub-carapace lava flows intruding beneath an insulating preexisting crust, or utilizing a preexisting lava tube, and breaking out distally after emplacement of the original flow could have resulted in younger crater count ages at downstream locations. The occurrence of this mechanism would be supported by evidence of a breakout, such as a texturally distinct lobe of lava emanating from beneath the platy-ridged crust downstream between the crater count locations. For my age dates for Grjótá and Marte Valles, sub-carapace flow would require the reactivation of a preexisting flow structure tens of millions of years after it was initially emplaced. Assuming similar thermal and mechanical properties of martian and terrestrial lavas (e.g., Keszthelyi and Self, 1998; Keszthelyi et al., 2004; Jaeger et al., 2010), this long lag time between reactivation events seems unlikely. For comparison, one of the largest igneous provinces on Earth, the Deccan Traps, were emplaced within ~3 Ma (e.g., Self et al., 1998), an order of magnitude longer than the span of derived ages for the Marte Vallis lavas.

(2) Preferential erosion of craters in the downstream portion of the lava flow might have removed the smallest craters within the diameter range of this study, thereby biasing the model ages to a younger result. Evidence to support this mechanism would include small degraded or muted craters or erosional landforms (e.g., channels) within the distal reaches of the flows, suggesting that material was removed preferentially from these distal reaches.

(3) Previously unidentified lava sources located downstream from the identified lava flow sources might have contributed younger lavas to these downstream reaches. Support for this possibility could include the presence of fissure- or vent-sourced flows and related flow fronts that overtop or intermingle with the lava surfaces in the channels. The presence of muted fissure segments within the lava channels could also suggest previously active points of eruption.

(4) Gradual emplacement over the course of months, years, or decades as compound sheet lavas, with slow inflation of individual lobes (Self et al., 1996), is a potential explanation for the development of the channelized flows in the Cerberus region. This alternative might also be relevant if there were no rheological changes between potential eruption pulses, and each lobe represented the emplacement of lava with the same characteristics at different times. However, this option may not directly account for age discrepancies, as the timeframe of emplacement would be relatively short. If these later pulses of volcanic activity utilized the preexisting channel structure and larger time intervals, downstream portions of the lava flow may exhibit younger ages. Support for this possibility would include investigating the surfaces at HiRISE scale resolution to identify any overlapping flow fronts, tumuli, and inflation features such as marginal fracturing (e.g., Bleacher et al., 2018; Hamilton et al., 2018).

(5) As discussed earlier, the rheology of the emplaced lavas might have changed during their emplacement (e.g., Keszthelyi et al., 1998; Polacci et al., 1999; Dundas and Keszthelyi,

2014), thereby altering the crater retention properties of different portions of the lava flows. Changes in the size and total population of craters between the proximal and distal locations of a known single lava flow would suggest different retention properties within that flow, supporting the occurrence of rheological changes during emplacement. Consistent crater dimensions and populations between the proximal and distal count locations would argue against rheological property changes during flow emplacement.

To evaluate which of these mechanisms might best explain the decreasing ages within the Cerberus channels, I examined the interior of my mapped lava flows. Whereas my initial mapping of the lavas focused on the flow margins, I now focused on the lava surfaces in order to identify whether there are (1) textural changes indicating sub-carapace flow extension; (2) muted craters or fluvial features that may indicate sediment deposition, erosion, or a combination of both processes; (3) muted fissure segments or vents that suggest downstream lava sources contributing younger lavas to the channels; and (4) evidence of overlapping flow fronts, tumuli, and inflation features suggesting an extended period of emplacement or multiple emplacement events.

Results of Examination of Channelized Lava Flow Surfaces

Surface textures in the three channels are generally consistent along their entire lengths. As inferred by previous works (e.g., Jaeger et al., 2010; Hamilton, 2013), flow fronts within my mapped boundaries are absent, implying that the channelized lavas were not emplaced by multiple eruptive events. This result weighs against sub-carapace flow as the mechanism that produced the observed age trends. No clear evidence is present for extensive erosion on the surface of these lava flows (e.g., few channels are present, and little evidence of significant dust cover), so craters have not been preferentially removed from, or mantled, along the downstream segments of these lava flows.

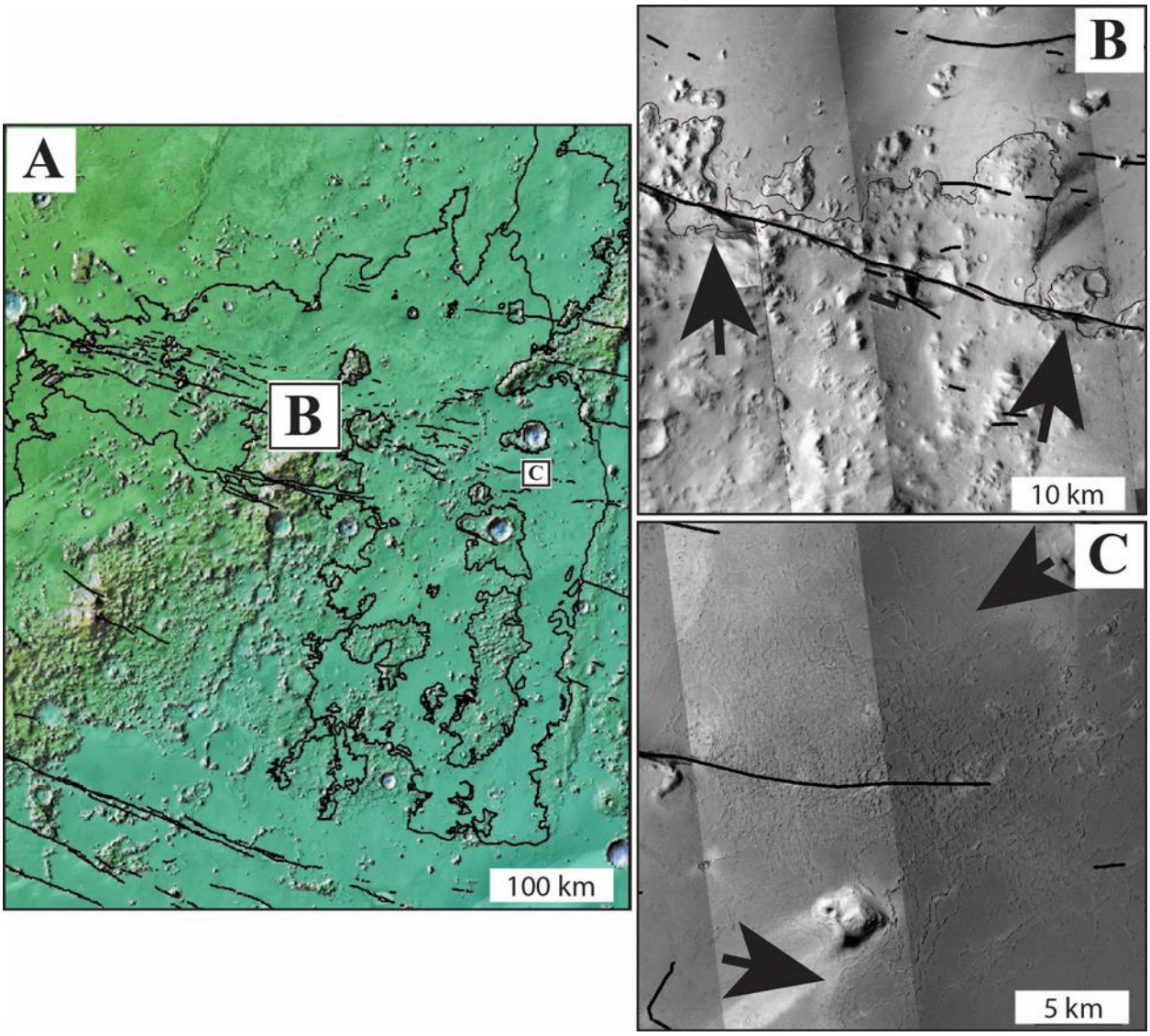

Figure 4. A: Context image of the main reach of Grjótá Valles. B: A northern fissure segment which contributed flow to Grjótá Valles. Located to the southeast of the medial count location. Black arrows indicate locations where fluid flow originated along this portion of the fissure segment. C: Muted fissure segment that appears to have been the site of minor eruptions. Located directly adjacent to the distal count location. Black arrows indicate the approximate maximum lateral extent of this small flow, to the north and south, respectively.

My examination of the flows revealed multiple locations within Grjótá and Marte that may have acted as additional lava sources. Fissure segments in the medial and distal reaches of Grjótá might have contributed some material directly to the channel (Fig. 4), though whether this possible contribution was contemporaneous with the initial emplacement of the channelized lava, or occurred later, is unclear. Also, the type of material that was contributed is not certain. Although material in the southern segment (Fig. 4C) was likely lava, based on surface morphologies, the material in the northern segment may have been either water or lava (Fig. 4B), as typical lava textures and erosional features are both apparent. The potential contributing locations identified within the medial and distal reaches of Marte appear to be older than the youngest lava flow, as they are superposed by the channelized lava (Fig. 5), and so were unlikely to have directly added young lavas to the distal flow surface.

A qualitative assessment of the lava surfaces along the lengths of the channels using scattered high-resolution HiRISE images revealed little significant morphology changes downstream from the source, further supporting the emplacement of the channelized lavas as a single, geologically rapid unit. There are limited examples of apparent smaller, overlapping flows within the channelized lavas in Athabasca, but these individual flows are not the dominant surface morphology in the region. This absence of overlapping flow fronts, multiple lava flows within the channel, tumuli, or inflation features further supports the emplacement of the channelized lavas as a single unit. There is clear evidence of overlapping flows on the Cerberus plains at CTX resolutions (e.g., Vaucher et al., 2009), unlike within the channelized lavas, suggesting that overlapping flows in the channelized lavas would be detectable. Some limited evidence of marginal fracture systems exists in the northern reaches of Grjótá Valles, supporting local inflation

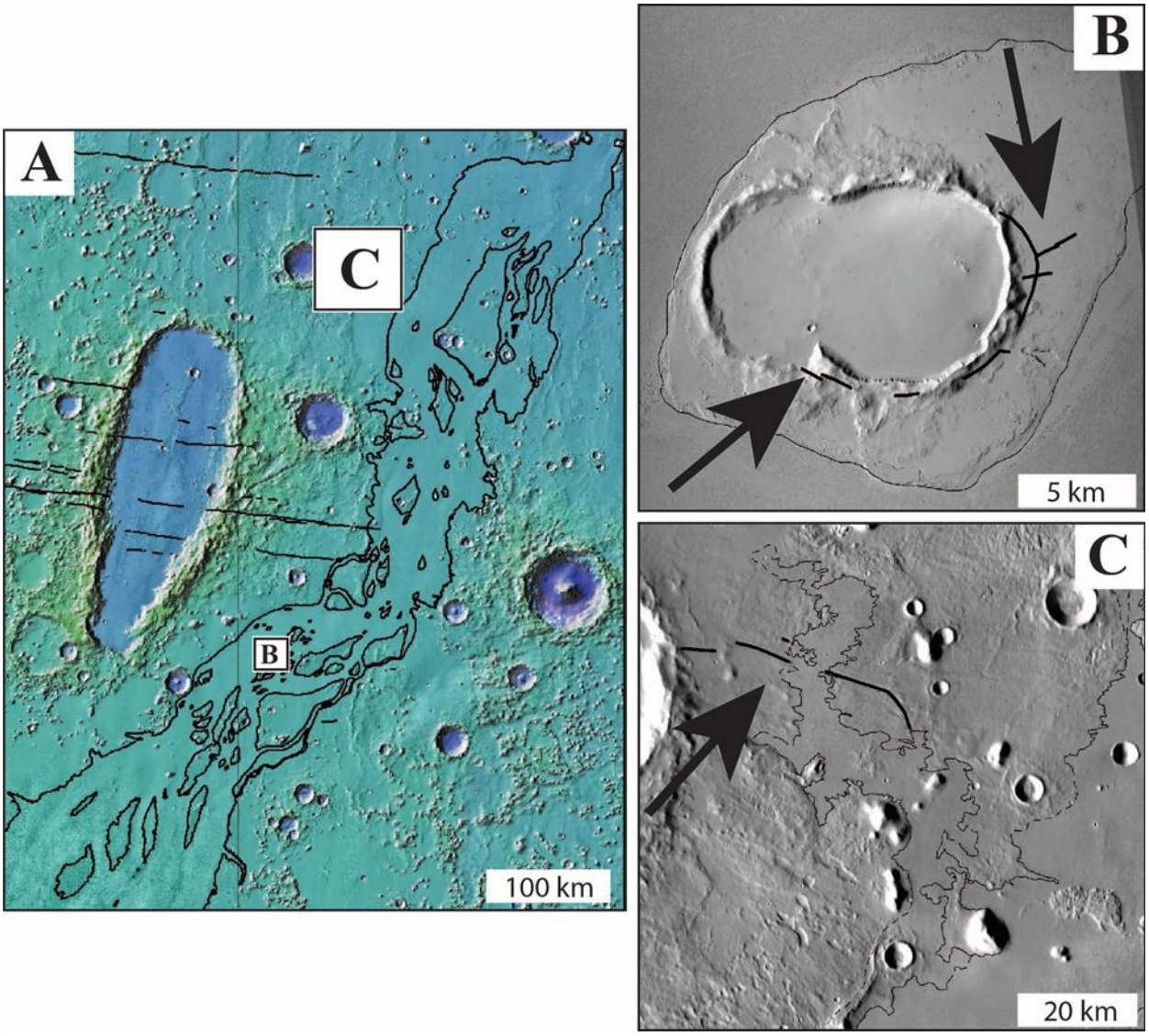

Figure 5. A: Context image of the main reach of Marte Vallis. B: Muted circumferential and radial fissure segments around a crater and streamlined landform, located southwest of the medial crater count location, that has been embayed by the latest lava flow in Marte Vallis (black arrows). C: A fissure-fed lava flow, the margins of which are superposed by the latest lava flow in Marte Vallis. Black arrow indicates likely source fissure. Located due west of the distal count location. Neither of these potential fissure sources could have contributed younger flows to the channel, as they are both overprinted by the youngest lava filling Marte.

of the lava flow (Bleacher et al., 2018; Hamilton et al., 2018), but is not found within the main channelized lavas.

My investigations of the first four scenarios to explain the intra-channel age discrepancies did not provide convincing evidence that any of those possibilities could account for the large age differences in each channel. Therefore, I determined that further in-depth investigation of target property effects on crater counts was required.

Crater Scaling

Without significant evidence for sub-carapace flow, preferential erosion, additional lava sources, or slowly emplaced overlapping flows, I consider a change in material properties to be the most likely mechanism for producing decreasing ages with distance. Thus, I investigated how possible changes in the material properties during emplacement may have altered the crater populations along the lengths of these lava flows. For this investigation, I incorporated scaling methods to reduce the model ages to a single age and to quantify the effect of the scaling parameters.

Size-scaling of Channelized Lava Crater Counts to Derive a Single Model Age

Previous identification of crater size differences between adjacent geologic units on Mars (e.g., Page et al., 2009; Dundas et al., 2010) and the Moon (van der Bogert et al., 2010, 2017; Zanetti et al., 2015) discussed or implemented a simple size scaling relationship to account for the observed differences, which they interpreted to be related to target property effects. Likewise, my initial investigation into the effects of target properties on final crater diameters involved a similar size scaling correction to account for the observed differences in crater diameters observed between the proximal and distal count locations. In size-scaling of my CSFD data, I

iteratively altered the crater diameters until the model ages from the proximal and distal count locations aligned. To scale the craters, I multiplied the crater diameter data from CraterTools by a range of percentages in 5% increments, e.g., 1.05, 1.10, etc. to increase the diameters, or 0.95, 0.90, etc. to decrease the diameters. Each of these arithmetically scaled crater diameter datasets was input back into CraterStats2 to determine the best qualitative fit of the modified CSFD curve to the original CSFD. This process was repeated to find the best approximate match between original unmodified and modified CSFDs (Fig. 6). This match could be accomplished either by reducing the crater sizes of the proximal sites so as to give a younger age, or increasing the crater sizes of the distal sites so as to give an older age. The changes in scaled crater sizes alter the number of craters in each bin, which in turn alters the best fit to the isochrons.

Because of the disparity of proximal-to-distal age differences in the three different channels, the results of this diameter scaling yield a range of size reductions/increases to align the proximal and distal model ages (Table 2). The percentage size-scaling increment of 5% precludes exact matches of the proximal and distal ages, but gives approximate values for the observed size differences. A 5% reduction in crater diameters for the proximal site in Athabasca Valles produces a single age for that channel of ~3 Ma, whereas a 5% increase in the distal crater diameters produces a single age for that channel of 3.3 Ma. For Grjótá Valles, a 25% crater size decrease reduces the model age from the proximal site to 33 Ma, similar to the age of 31 Ma for the distal site, whereas a 25% increase in the distal crater diameters brings the model age up to 51 Ma consistent with the age of 53 Ma for the proximal site. For Marte Vallis, a 45% size reduction for the crater population in the proximal location adjusts the age to 7.6 Ma to approximate the 8.4 Ma age of the distal location, whereas a 215% increase in the distal crater diameters yields an age of 42 Ma to approximate the 43 Ma age of the proximal location.

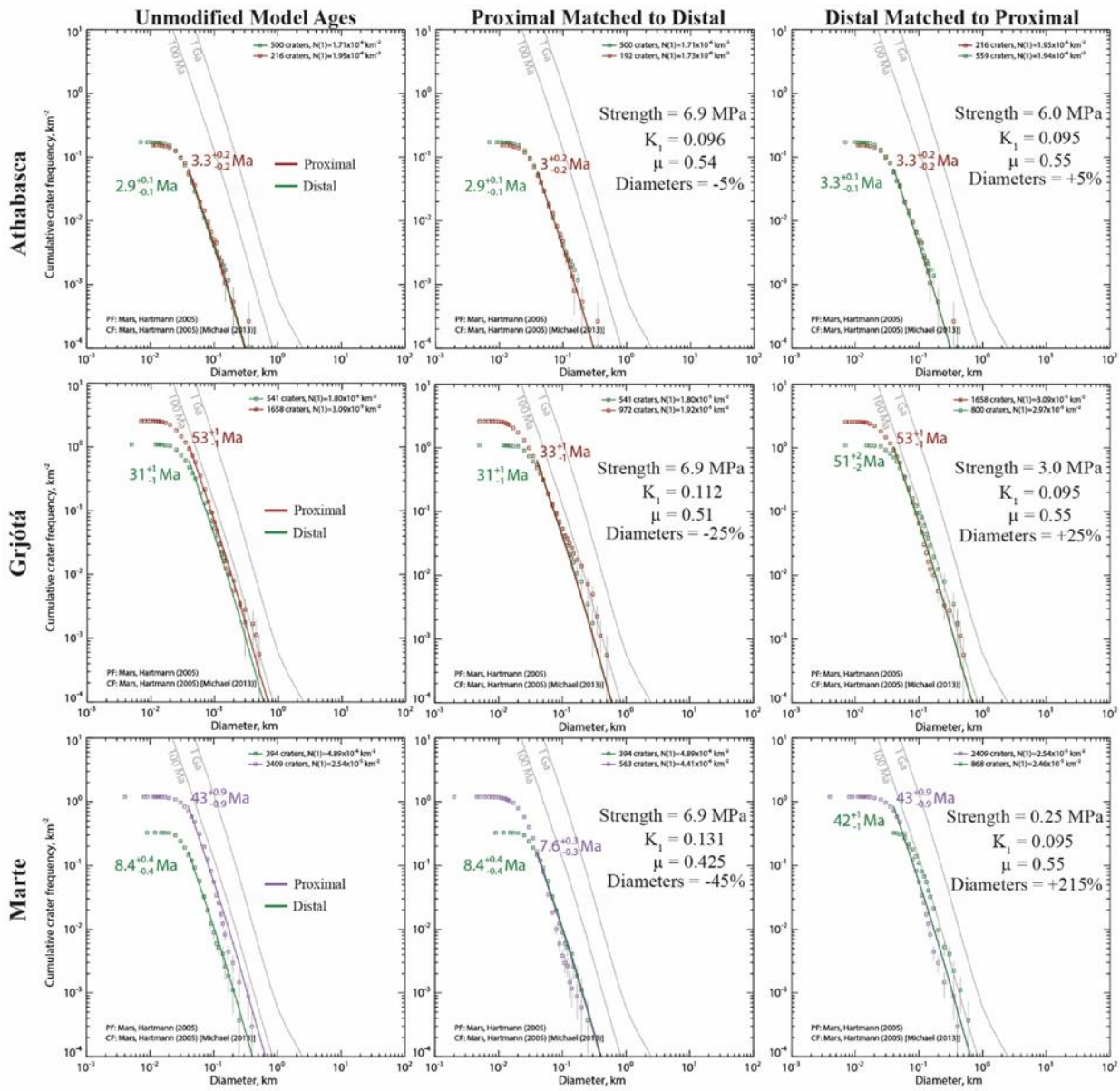

Figure 6. Left column: Original model ages for the proximal and distal count locations in Athabasca Valles, Grjótá Valles, and Marte Vallis. Center column: Aligned model ages based on proximal site crater diameter size reductions and corresponding K_1 and μ adjustments. Right column: Aligned model ages based on distal site crater diameter size increases and corresponding strength (Y) adjustments. Y, K_1, and μ values, and corresponding percentage of size decreases or increases are shown in Table 2. Density (ρ) was not included in these calculations due to its negligible modifying effect on the CSFDs.

Table 2. Values of the *Y*, K_1, μ parameters and diameter increase (+) or decrease (-) required to align the proximal and distal model ages, respectively.

Y (MPa)	K_1 / μ	Δ crater dia. (%)	Athabasca age (Ma)	Grjótá age (Ma)	Marte age (Ma)
6.9	0.096/0.54	-5	2.9 (distal)		
6.0	0.095/0.55	+5	3.3 (proximal)		
6.9	0.112/0.51	-25		31 (distal)	
3	0.095/0.55	+25		53 (proximal)	
6.9	0.131/0.425	-45			8.4 (distal)
0.25	0.095/0.55	+215			43 (proximal)

This scaling approach only considers the change in size of the craters between the proximal and distal count locations and does not consider target property effects on these size changes. To quantify the effect of target properties on crater diameters and the resultant model ages, I performed pi-group scaling calculations.

Pi-group Scaling to Determine Target Property Effects on Final Model Ages

An impactor of a given size and velocity generates different crater diameters based on the gravity of the target planetary body and the properties of the impacted material(s). Estimations of these final crater sizes can be made using pi-group scaling calculations, which include the characteristics of both the impactor and target body (Eq. 1, 2; e.g., Melosh, 1989; Holsapple, 1993; Ivanov, 2001; Holsapple and Housen, 2007; Richardson et al., 2007; Dundas et al., 2010; van der Bogert et al., 2017). The following equations, initially derived through pi-group scaling by Holsapple (1993), adopt the Richardson et al. (2007) formulation:

(1) $$V = K_1 \left(\frac{m_i}{\rho_{tar}}\right)\left[\left(\frac{ga}{v_i^2}\right)\left(\frac{\rho_{tar}}{\rho_i}\right)^{-\frac{1}{3}} + \left(\frac{Y}{\rho_{tar} v_i^2}\right)^{\frac{2+\mu}{\mu}}\right]^{-\frac{3\mu}{2+\mu}}$$

(2) $$V = \frac{1}{24}\pi D_t^3$$

where V is the transient crater volume, m_i is the mass of the impactor, ρ_i and ρ_{tar} are the bulk densities of the impactor and target, respectively, g is the gravitational acceleration of the target body, a is the radius of the impactor, v_i is the velocity of the impactor, and Y is the effective strength of the target material. K_1 and μ are dimensionless constants for porous and non-porous target materials (Richardson et al., 2007; van der Bogert et al., 2017). The values for the K_1 and μ constants were derived from lab and field experiments of explosions and their resultant craters, formed in various types of geologic materials, such as rock and soil (Schmidt and Housen, 1987; Holsapple, 1993). For porous, weak material, the values of these constants have been set as K_1 =

0.132 and μ = 0.41, whereas for non-porous, strong rock, the values have been set as K_1 = 0.095 and μ = 0.55 (Holsapple, 1993; corrected values available online at http://keith.aa.washington.edu/craterdata/scaling/theory.pdf). D_t is the transient crater diameter, and final crater diameter for simple craters only is 1.3 times D_t. Using the relationships derived from pi-group scaling above and the conversion from transient to final diameter, I calculated the expected final diameters of craters on Mars formed in various target materials, based on the initial impactor diameters. These results illustrate that a stronger target and/or a more porous target will yield smaller craters (Fig. 7; Dundas et al., 2010; van der Bogert et al., 2017).

I calculated CSFDs for impacts into various target materials expected on the surface of Mars, ranging from strong non-porous rock to relatively weak and porous rocks (e.g., Dundas et al., 2010; Kiefer et al., 2012; van der Bogert et al., 2017). I used the Neukum time dependence equation for varying crater diameters (e.g., $N_{D>1\ km} = 5.44(10^{-14})\ [(e^{6.93T}) -1] + 8.38(10^{-4})T$; cf. Hartmann, 2005) , where N is the total number of crater at a given diameter (D), that have accumulated on a surface over a specific time (T) in gigayears. This equation was used to calculate the total accumulated craters per km^2 for my derived model ages (Fig. 3; Neukum et al., 2001; Hartmann, 2005). Impacts were assumed to occur at 10 km/s at 45° (e.g., Ivanov and Hartmann, 2007; Dundas et al., 2010), with a bulk density of 2700 kg/m^3, the average density inferred for S-type asteroids (Britt et al., 2002). Due to the relative youth and nearly pristine nature of the observed surface features, and based on previous interpretations of surface composition, I restricted the test range of materials to those consistent with basaltic characteristics, excluding regolith or soil-like properties. The standard material properties (ρ = 3460 kg/m^3, Y = 6.9 MPa) were chosen to recreate a crater population generated in a surface of coherent rock (low porosity and high strength, respectively). These calculated CSFDs are consistent with martian isochrons,

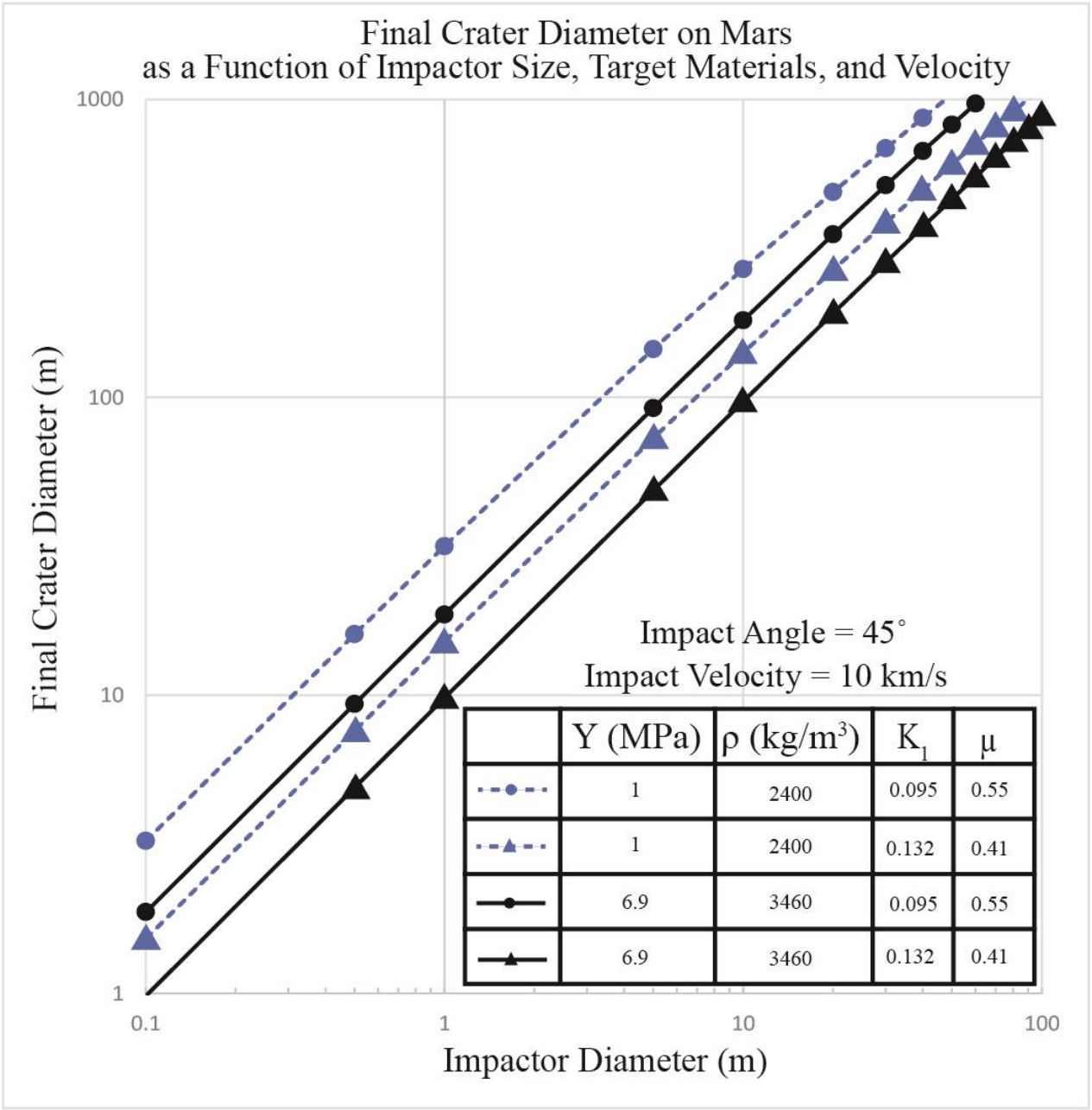

Figure 7. The final crater diameter for the same initial impactor diameter and impact velocity varies based on the target properties of the impact site. The offset between the two solid lines and the two dashed lines of the same color, respectively connoting the same strength and density of material, shows that porous material yields smaller craters. The offset between the pair of dashed blue lines, connoting lower density material, from the pair of solid black lines, connoting higher density material, shows that the denser material will yield smaller craters. Y=effective strength, ρ=density, K_1 and μ=dimensionless constants for porous and non-porous target materials.

which correspond to the production functions derived for the "average lunar mare" (Ivanov, 2001), and so should reflect similar material properties to the mare (e.g., basaltic compositions). With density, strength, and porosity values from previous work (e.g., Dundas et al., 2010; Kiefer et al., 2012; van der Bogert et al., 2017), I used a combination of two different target densities (ρ = 2400 - 3460 kg/m^3) and two different target strengths (Y = 1 - 6.9 MPa) and dimensionless constants representing porosity (K_1 = 0.132 - 0.095 and μ = 0.55 - 0.41) to give four model rock types.

Using my calculated CSFDs, for the proximal and distal sites of each channelized lava, I then incrementally adjusted the Y, K_1, and μ values in the pi-group scaling Eq. 1. These adjustments altered the diameters of the craters, until the CSFDs representing the "older" proximal sites matched the "younger" distal sites, similar to the crater size-scaling process (Fig. 6). Adjustments to the strength or porosity parameters have an inverse effect on the behavior of the calculated CSFDs. Any adjustment to Y, within the range of 1 - 6.9 MPa., caused a rightward shift of the CSFD (Fig. 6), and was used to fit the distal model ages to the proximal model ages. I increased the range of values for Y, spanning 0 - 1 MPa, for Marte Vallis only, due to the anomalously high size-scaling value needed to align the distal to proximal sites. Any adjustment of the K_1 and μ values, within the ranges of K_1 = 0.132 - 0.095 and μ = 0.55 - 0.41, caused a leftward shift of the idealized CSFD (Fig. 6), and was used to fit the proximal model ages to the distal model ages. When adjusting within the density parameter range, the maximum effect was negligible compared to changes associated with adjustments to the Y, K_1 and μ parameters, and I therefore did not include it in my final analysis of target properties. Though I tested changes to one parameter at a time, it is highly likely changes to these parameters in a real-world environment would not happen in isolation from each other but would occur as some combination of varying values.

I infer that the target properties of the proximal sites, having more and larger craters that yield older model ages, are represented by weaker, more porous rock, in comparison to the target properties of the distal sites that, having smaller craters in CSFDs that yield younger model ages, are represented by stronger, non-porous rock. I scaled the model ages to both the proximal and distal model ages, to ensure that all model ages and reasonable target property combinations were covered. Percentage changes in K_1, μ, and Y are generally comparable to changes in diameter used to align the proximal and distal CSFDs (Table 2). My results are consistent with previously observed terrestrial lava flows, where changes in vesicularity, porosity, density, and crystallinity have been identified with increased distance from the eruption source (e.g., Swanson, 1973; Wilmoth and Walker, 1993; Flóvenz and Sæmundsson, 1993; Polacci et al., 1999; Keszthelyi et al., 2004). My parameter ranges (Y = 1 - 6.9 MPa, K_1 = 0.132 - 0.095, μ = 0.55 - 0.41) are realistic for basaltic compositions derived from terrestrial experiments (Schmidt and Housen, 1987; Holsapple, 1993) and previously applied on extraterrestrial bodies (e.g., Housen and Holsapple, 2007; Dundas et al., 2010, van der Bogert et al., 2017). I excluded parameter ranges from these previous studies for non-volcanic rocks, soils, and regolith.

Discussion and Implications

My detailed mapping and analysis of morphological evidence at available image scales strongly supports the interpretations from previous work that the channelized lavas were emplaced as single units. Whereas the length of time for that emplacement has been inferred to have been days to weeks (e.g., Jaeger et al., 2010), or months to years (e.g., Self et al., 1996), crater-based model age data presented show millions to tens of millions of years between distal and proximal locations (Fig. 3). The decreasing model ages with distance support previous hypotheses that an increase in the cohesive strength of the lava with increasing distance from the source would result

in smaller craters and a lower total population relative to the weaker, near-source material (e.g., Dundas et al., 2010; Wünnemann et al., 2011), as also inferred for decreasing ages observed in Kasei Valles (Chapman et al., 2010; Dundas and Keszthelyi, 2014). Thus, changes in the strength of the lava during the eruption can explain the age discrepancies observed in each of the Cerberus region channelized lavas. My results also suggest that the greater the age discrepancy, the greater the change to either the strength and/or porosity that must have occurred with increasing distance from the source.

The percentage change required to reduce the size-scaled data to a single model age is indicative of the difference in the target properties that influence crater retention, and is reflected in the comparable percent changes in the K_1, μ, and Y parameters. The slight size differences (5%) in Athabasca Valles, and moderate (25%) size differences Grjótá Valles, indicate relatively slight and moderate changes to the material properties of the lavas occurred, respectively, in these two channels. For Marte Vallis, a 45% size reduction for the proximal crater population, or a 215% increase in the distal crater diameters, is needed to derive a single age for this longest channel. The larger values required to align the proximal and distal model ages for Marte Vallis indicate that larger rheological changes occurred during the emplacement of the lava flow. These rheological changes may result from the longer channel, which provided greater distance and time for greater rheological evolution of the lava to occur. Unlike the identical percentages for the scaled decrease or increase in crater diameters for Athabasca and Grjótá, the values used for Marte do not match. I do not have an explanation for this size-scaling discrepancy in Marte Vallis, but it may be directly related to the significant changes in rheological properties I inferred.

Implications for Crater Count Derived Ages in the Solar System

Differences in the material properties of two distinct units have also been identified on the Moon, based on a particularly striking example of a single crater exhibiting different sizes when overprinted across two units formed contemporaneously (van der Bogert et al., 2010), as well as different CSFDs on additional coeval lunar geologic units (van der Bogert et al., 2017). My results for the Cerberus region on Mars, strongly suggesting that material property changes within a single geologic unit caused model age discrepancies, are consistent with the material property effect on crater populations previously inferred on the Moon (van der Bogert et al., 2010, 2017). The derivation of isochrons for age dating surfaces throughout the Solar System is based on the lunar chronology, which is derived from radiometrically age-dated samples returned from the surface correlated to the crater density in the corresponding regions (e.g., Neukum and Ivanov, 1994; Hiesinger et al., 2000; Hartmann and Neukum, 2001; Ivanov, 2001; Neukum et al., 2001; Hartmann, 2005). Model ages for the individual lunar basalts found in the mare have been determined from performing counts on spectrally distinct units defined by Galileo and Clementine imaging data (Hiesinger et al., 2000; Hiesinger et al., 2011). These counts rarely cover the entire unit, and were generally derived from either a single, or multiple subset areas within the target region (e.g., Hiesinger, et al., 2011). When multiple count locations were chosen for a target unit, these locations were often separated by 100s of km, but combined into a single crater population for the unit (e.g., Hiesinger et al., 2011). If differences in crater retention exist in these units, particularly when the count areas are separated by 100s of km, the overall model age that has been calculated may incorporate increased (but unknown) uncertainty. My results may have some bearing and provide insight on age determinations of young planetary surfaces, particularly those that are volcanic in origin, and are not old enough to have been homogenized by impact processes (van der Bogert et al., 2017).

Potential Magma Source(s) for the Cerberus Region Lavas

This investigation into target properties was part of a larger study into the magma source(s) for these young lava flows on Mars. Below I discuss implications of the single model ages that I derived for each channelized lava on the question of Cerberus lava source(s).

Recent Magma Generation on Mars

Emplacement of these long lava flows is hypothesized to have occurred on the order of days to several weeks for Athabasca Valles (Jaeger et al., 2010), though emplacement for large-scale terrestrial lava flows can occur on timescales that range from months to decades (Self et al., 1996). This emplacement over a great distance (>1000 km) might require very hot, low viscosity, high effusion rate eruptions (Keszthelyi et al., 2004; Jaeger et al., 2010). The eruption conditions in Athabasca Valles can reasonably be inferred to have been the same for Grjótá and Marte Valles due to the similar lava extents and surface morphologies. Comparison with terrestrial magma chamber behavior suggests that magma capable of feeding these young and voluminous lava flows was generated shortly before their emplacement, geologically speaking, to avoid magma crystallization before eruption. Terrestrial magma chambers, with thicknesses on the order of 1 km and depths ≥ 10 km, have been modeled to crystallize in under 1 million years (e.g., Marsh, 1989; Larsen and Tegner, 2006). Martian magma chambers are expected to be deeper than those found on Earth by a factor of ~4 (Wilson and Head, 1994). These terrestrial magma chamber crystallization timescales, coupled with the young ages of the Cerberus region volcanism, strongly suggest recent magma generation on Mars. Thus, although rapid interior cooling is expected for Mars (e.g., Montesi and Zuber, 2003; McGovern et al., 2002, 2004), the young Cerberus volcanism suggests recent magma formation. A thick insulating crust, inefficient convection in the mantle, inefficient heat loss from the interior, and heterogeneous heat flows are all hypothesized to have led to a warmer planetary interior for Mars (e.g., McGovern et al., 2002,

2004; Schumacher and Breuer, 2007; Ruiz et al., 2010; Baratoux et al., 2011; Ruiz et al., 2011). Locations of increased crustal thickness and the localized concentration of radioactive heat producing elements in the crust would be more conducive to melt formation (McGovern et al., 2002, 2004; Schumacher and Breuer, 2007; Ruiz et al., 2010). A thick insulating crust is present around the major volcanic provinces of the planet (e.g., McGovern et al., 2002, 2004) and is attributed to ancient plume-fed mantle upwelling (e.g., Kiefer, 2003; Steinberger et al., 2010). However, the Cerberus plains is a region with relatively thin crust (Lemoine et al., 2001; Genova et al., 2016), which would limit the insulating effect of the surrounding crust and possibly decrease the concentration of heat producing elements. A thicker crust and greater concentration of heat producing elements are factors more consistent with the OTVP and EVP as potential magma sources responsible for the geologically recent generation of magma that fed the Cerberus eruptions, though the sub-Cerberus region cannot be precluded based on these conditions.

Dike Propagation and Magma Pathways

Pathways for magma to the surface include magmatic dikes, which have been inferred on the Moon and Mars from the surface morphology of graben networks (Wilson and Head, 2002; Head et al., 2003; Schultz et al., 2004; Klimczak, 2014). In general, overpressure from the magma chamber forces a fracture to open and permits lateral and vertical propagation of dikes away from the magma source (e.g., Rubin, 1993; Wilson and Head, 2002; Buck et al., 2006). As the dikes propagate laterally, fissures might develop that allow the dikes to intersect with the surface (Ernst, 2014). The stresses involved in the development of these fissure systems can favor localized magma pooling (McGovern and Solomon, 1993), forming elongated reservoirs that extend away from the magmatic center along which lava can subsequently erupt (Mège et al., 2003). Dikes that are both deep (~11 km) and wide (≥100 m) can radiate laterally away from their magma sources

for 1000s of km (e.g., Parfitt and Head, 1993; Wilson and Head, 1994; Rubin, 1995; Ernst et al., 2001), and may be sourced by large, single magma chambers (Mège and Masson, 1996b). The inferred widths of ≥100 m for some martian dikes (Wilson and Head, 2002) and the increased depths of magma chambers within the crust, relative to Earth, due to a deeper level of neutral buoyancy in the lower gravity of Mars (Wilson and Head, 1994), suggest that martian dikes could propagate to great distances from the initial magma source. Some of the inferred dike systems on Mars extend radially for 100s or 1000s of km from the OTVP (e.g., Wilson and Head, 2002).

Fissure networks have been used on terrestrial planets to infer the presence of massive dike swarms (Wilson and Head, 2002; Schultz et al., 2004; Klimczak, 2014), which were then traced to their apparent magma sources (e.g., Parfitt and Head, 1993; Ernst et al., 2001; Ernst, 2014; Patterson et al., 2016). A terrestrial example of a large-scale dike system is the Mackenzie dike swarm in Canada, which extends for ~2500 km from its magma source (e.g., Parfitt and Head, 1993; Ernst et al., 2001; Ernst, 2014). The Cerberus Fossae fissures have been modeled as radial to the OTVP (Hall et al., 1986), although they also exhibit an apparent radial relationship to the EVP (e.g., Burr et al., 2002b; Plescia, 2003; Platz and Michael, 2011). These fissures have been interpreted as the result of loading stresses related to the development of the OTVP (Hall et al., 1986) and/or the EVP (Mège and Masson, 1996a; Mège et al., 2003), or the expression of underlying intrusive dikes that generated surface collapse (Wilson and Head, 2002; Head et al., 2003; Schultz et al., 2004; Vetterlein and Roberts, 2010; Kattenhorn and Meyer 2010; Klimczak, 2014; Pendleton, 2015; Nahm et al., 2015). Whether the result of surface loading or dike intrusion, the Cerberus Fossae evidently provided conduits for the channel-infilling lavas from the magma source(s).

Possible Source Regions for the Channelized Cerberus Lavas

The orientations of the Cerberus Fossae, which provide ready subsurface flow pathways, suggest three potential magma source regions (Fig. 8). Potential magma sources could be associated with the adjacent large volcanic provinces, namely, the OTVP and EVP (e.g., Schumacher and Breuer, 2007; Ruiz et al., 2010; Steinberger et al., 2010; Baratoux et al., 2011), or a localized melt zone beneath the Cerberus region (Vaucher et al., 2009). The bulk of constructional volcanic activity at both the OTVP and EVP is also old, but limited volcanism at both sites continued into the latest- Amazonian (e.g., Anderson et al., 2001; Neukum et al., 2004; Hiesinger et al., 2007; Vaucher et al., 2009; Werner, 2009; Platz and Michael, 2011; Isherwood et al., 2013). The youngest flows associated with either OTVP or EVP coincide with the previously derived oldest emplacement ages of the lavas within the Cerberus plains and channels, consistent with these volcanic provinces as the magma source region(s) that fed these effusive plains eruptions. Thermal evolution models suggest that melt could have been produced at the base of either volcanic province into the late- Amazonian (Fig. 8, scenarios S1 and S2; e.g., Schumacher and Breuer, 2007; Ruiz et al., 2010; Steinberger et al., 2010; Baratoux et al., 2011). As an additional or alternative possibility, magma could have formed below the Cerberus plains region, Fig. 8, scenario S3), potentially the result of a combination of concentrated radioactive elements within an insulating crust and mantle convection processes (Schumacher and Breuer, 2007; Vaucher et al., 2009), which intruded through the relatively thin crust in the region (Lemoine et al., 2001; Genova et al., 2016). Though I developed three mutually exclusive scenarios to investigate, a fourth alternative scenario is possible in which contributions from multiple sources, consisting of a combination of the three identified possibilities, fed the eruptions in the Cerberus region.

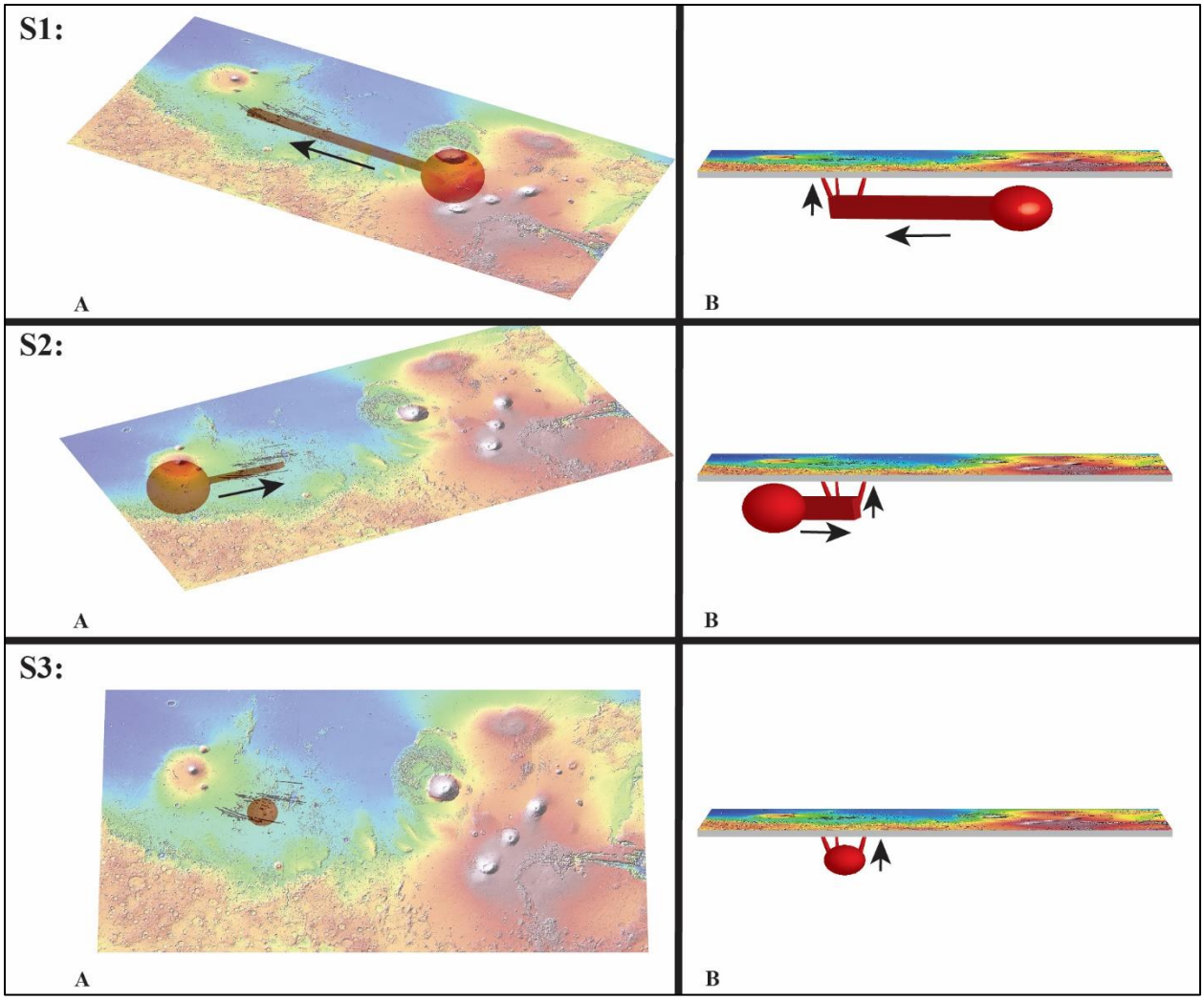

Figure 8. Magma migration models representing three potential magma source regions. Scenario 1 (S1) represents the westward migration of a dike from a magma source found beneath the OTVP. Scenario 2 (S2) represents the eastward migration of a dike from a magma source found beneath the EVP. Scenario 3 (S3) represents a magma source directly beneath the Cerberus plains volcanic units. S1(B) and S2(B) represent a subsurface perspective of the primary dike radiating from the hypothesized magma source, with vertical feeder 'pipes' connecting to the surface fissures that sourced the lava flows. S3(B) represents a subsurface perspective of the primary magma source, with vertical feeder 'pipes' connecting to the surface fissures that sourced the lava flows. The magma source, dike, and feeder pipe sizes are not to scale, nor is the depth of the magma source, but provide schematic illustrations of the directional components of the proposed migration pathways. The size of the magma source in S3 was decreased to highlight the potential vertical feeder pipes, rather than indicating a difference in size of the source from S1 and S2.

Inferred High Density Regions and Crustal Thickness

Mass concentrations (mascons) are typically associated with regions of high density (Turcotte and Schubert, 2002; Genova et al., 2016), and can be used to identify potential magmatic centers on planetary bodies. Recent examples include the identification of positive gravity anomalies, interpreted to represent magmatic intrusions, in Gravity Recovery and Interior Laboratory (GRAIL) data of the Moon (Thorey et al., 2015). A strong candidate for a magma chamber was identified below Syrtis Major on Mars using gravity data derived from the Mars Global Surveyor (Kiefer, 2004). These previously identified high-density regions may represent the extinct magma chambers for these volcanic regions, and may represent the fully crystallized remnants, post-eruption, that is composed of denser igneous cumulates (Kiefer, 2004), or simple magmatic intrusions (Thorey et al., 2015).

Regionally, the crust in the Cerberus plains is relatively thin, particularly when compared to the bordering volcanic provinces and hemispheric dichotomy boundary (Fig. 9B; e.g., Lemoine et al., 2001; Genova et al., 2016). The crustal thickness map suggests areas of thinner crust (Fig. 9B), correspond to the positive gravity anomalies (Fig. 9A), which are located subjacent and adjacent to the observed or inferred surface sources for the lava flows. These mascons could be the result of magma injected through a dike system related to one of the bordering volcanic provinces, or from a magma source located directly below the region. In that case, the magma may be pooling near the surface in regions of local extension, perhaps related to the development of the Cerberus Fossae fissure network (e.g., McGovern and Solomon, 1993; Mège et al., 2003). Alternatively, the positive gravity anomalies could represent cooled magma chambers residing within a constant-thickness crust, as a result of mantle material undergoing decompression melting as it neared the surface (Turcotte and Schubert, 2002). Each of these gravity data

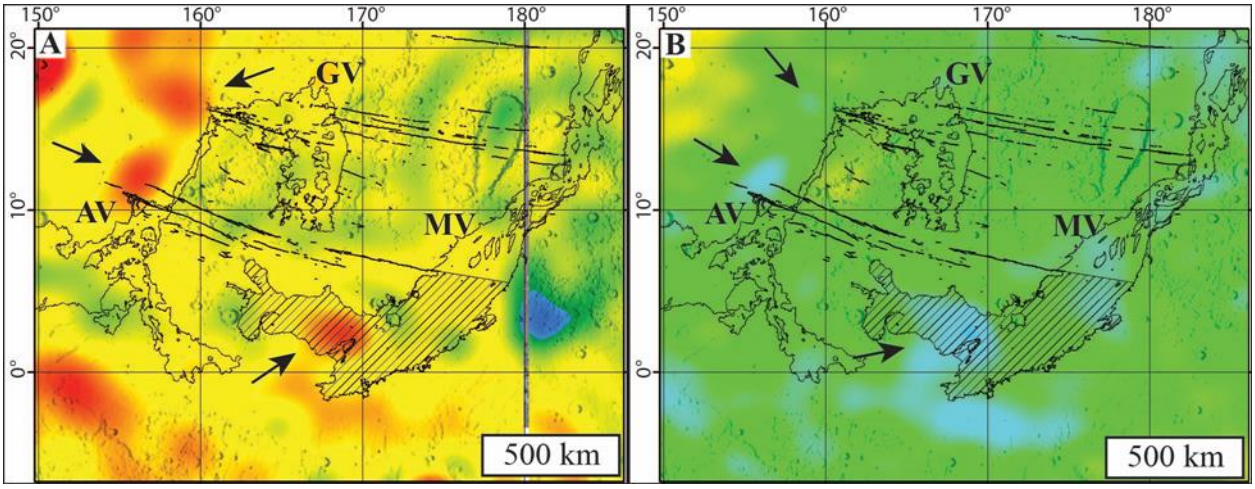

Figure 9. The mapped extent of the three main channels and their associated lavas in the study area, Athabasca (AV), Grjótá (GV), and Marte Valles (MV). A: Free-air gravity anomaly map (data from Genova et al, 2016), where warm colors denote positive anomalies and cool colors denote negative anomalies. Three anomalies (black arrows) are found in proximity to the source regions for the channelized lavas. The lack of topographic variability (Fig. 1) indicates that the regions of high density associated with the positive gravity anomalies are due to subsurface variation. B: Crustal thickness map (data from Genova et al., 2016), where warm colors denote thicker regions and cool colors denote thinner regions. Relatively low crustal thicknesses (black arrows) are found in proximity to the source regions for the channelized lavas. An apparent spatial correlation exists between the positive gravity anomalies and regions of relatively thin crust.

interpretations entails magma upwelling near the Cerberus Fossae, likely having formed shallow, near-surface magma chambers that fed each of the channelized lava flows.

Inferred Sub-Cerberus Region Magma Source

The derived ages of the channelized lavas help to address the question of Cerberus lava source(s). Whether I used the youngest (distal) age or the oldest (proximal) model ages as my fixed data points, my results yield an emplacement sequence starting at Grjótá, proceeding south-southeast to the Cerberus plains for Marte, and finally westward for Athabasca. Thus, I find no clear directional eruption sequence for these lavas (Table 3). Eruptions may occur along many points of a rift system, as demonstrated within the Cerberus region itself (e.g., Burr et al., 2002a, 2002b; Plescia, 2003; Keszthelyi, et al., 2004; McEwen et al., 2005; Vaucher et al., 2009; Jaeger et al., 2010) or terrestrial examples such as the Laki and Eldgá fissures (e.g., Thordarson and Self, 1993; Keszthelyi et al., 2000; Thordarson et al., 2001). Thus, this finding is not definitive regarding an emplacement sequence but represents an observed lack of a trend.

The emplacement of the channelized lavas is likely the result of a combination of volcanic and tectonic activity in the Cerberus region, based on the clear relationship between the fissures as the eruption sources (Plescia, 1990; Burr et al., 2002a, 2002b; Berman and Hartmann, 2002; Plescia, 2003; Keszthelyi, et al., 2004; McEwen et al., 2005; Burr et al., 2009; Vaucher et al., 2009; Jaeger et al., 2010), and the magma source comprised of a long-lived melt zone. Crater count model ages of the Cerberus plains and channels indicate that this melt zone was active for ~250 Ma, as recorded in the episodic eruptions during the late Amazonian (Vaucher et al., 2009). Terrestrial large igneous provinces (LIPs) go through pulses of activity that typically last up to 15 Ma (Ernst, 2014 and references therein) with some periodically active over the course of >30 Ma (Ernst 2014 and references therein). This timescale is comparable to the duration of volcanic activity associated with the channelized lavas in the Cerberus region. However, these LIPs

Table 3. Size-scaled model ages and emplacement order for the channelized lavas. Regardless of the size-scaling approach, the emplacement order of these lavas does not change.

	GV	MV	AV
Ages reduced to distal (youngest) age	31 Ma	8 Ma	3 Ma
Ages reduced to proximal (oldest) age	53 Ma	43 Ma	3 Ma
Emplacement order for *both approaches*	1st	2nd	3rd

typically consist of stacked inflated lava flows, rather than a single channelized flow (e.g., Self et al., 1996). Smaller, shorter duration terrestrial lava flows may be more accurate analogies for emplacement style and morphology comparable to the Cerberus channelized lavas, such as the Laki basalt flows (e.g., Thordarson and Self, 1993; Keszthelyi et al., 2000; Thordarson et al., 2001), the McCartys basalt flow within the Zuni-Bandera volcanic field (e.g., Ander et al., 1981; Bleacher et al., 2018). The inferred duration of regional volcanic activity of ~250 Ma is more difficult to account for. The bordering volcanic provinces, the OTVP and EVP, have been active over billions of years in a single location (e.g., Anderson et al., 2001; Werner, 2009; Platz and Michael, 2011), so a smaller volcanic region potentially sourced by a regionally underlying melt zone may be able to remain active for a few percent of the age of these volcanic provinces. The development of such voluminous eruptions in the Cerberus region might be analogous to the early plume-fed edifice building events that gave rise to the OTVP and EVP, and over the course of time could give rise to a new large-scale edifice.

The channelized lava flows are localized examples of region-wide volcanism, and along with those found in the Cerberus plains, may represent a monogenetic lava flow field, where each observed volcanic landform represents a single eruption event (Vaucher et al., 2009). Similarities in morphology and inferred lava characteristics (e.g., low-viscosity, high volume) between the channelized and plains lavas suggest similar rheologies. Numerical modeling results of the emplacement of small shield volcanoes in the Cerberus plains point to very low viscosity, fluid lavas, which are interpreted to suggest that their source magma chambers were both deep and had low volatile contents (Baratoux et al., 2009). Thus, the Cerberus channelized lavas and low shield volcanoes may have originated from a single deep magma source (Mège and Masson, 1996b; Mège et al., 2003; Vaucher et al., 2009). Under this scenario, the positive gravity anomalies identified in

proximity to the surface sources for the channelized lavas (Fig. 9) would represent the crystallized remnants of shallow magma chambers (Kiefer, 2004) that were sourced from a deeper underlying chamber, or magmatic intrusions (Thorey et al. 2015). The presence of crystallized shallow magma chamber remnants or conduits beneath the respective source areas of Athabasca, Grjótá, and Marte Valles may be the result of the compressional stress in the crust squeezing a dike shut after an eruption (Rubin, 1995) This cutting off of the magma pathway would require the propagation of a new dike from the deep source magma chamber, corresponding to each successive eruption.

The inferred presence of young, high volume and low viscosity lavas in Athabasca (Jaeger et al, 2010), within the Cerberus plains (Baratoux et al., 2009), and possibly for Grjótá and Marte, strongly implies the recent generation of very fluid, low viscosity magma (Baratoux et al., 2009) and/or the requirement of large volumes of magma and its corresponding high pressures required to overcome the deeper neutral buoyancy level of Mars (Wilson and Head, 1994). The smaller flows and shields in the Cerberus plains are also likely composed of this same low viscosity lava, but are significantly smaller in volume than those flows which filled the channels (Vaucher et al., 2009). This decrease in volume could be representative of smaller packets of magma ascending from the source, during relatively quiescent periods between major pulses of activity represented by the channelized eruptions. These lavas were interpreted as low viscosity based on morphological and modeling investigations (e.g., Keszthelyi et al., 2004; Baratoux et al., 2009; Jaeger et al., 2010). A low viscosity lava is more likely to have been emplaced along the entire length of the flow while retaining a consistent surface morphology. Furthermore, the presence of a thin veneer in the proximal regions of Athabasca Valles with thickening towards the distal Cerberus Palus suggest draining of lava during the waning stages of the eruption, which is more likely at lower viscosities (Jaeger et al., 2007, 2010).

Conclusions

From my analyses of the ages of the circum-Cerberus channelized lavas, I find that changes in the material properties during emplacement are most likely to be responsible for the observed crater-based age trends, which can be accounted for using size- and pi-group-scaling of the data. The age discrepancies are most pronounced in Marte Vallis, the channel with the greatest lava flow distance from its approximate source to termination, suggesting that the greatest rheological changes occurred within this lava flow. Based on the available evidence from crater counting, scaling to reduce the counts to a single model age, and gravity data, I conclude that the possible magma source region that fed the channelized lavas in the Cerberus region is an underlying regional melt zone. My interpretation of the results best supports a sub-Cerberus magma source as the most parsimonious explanation, but contributions from multiple sources may also have occurred. The inference that the sub-Cerberus region is the apparent source region implies that the formation of magma is not confined to the large volcanic provinces but may occur in regions less obviously suitable for melt formation. The ideal sites to search for such volcanic landforms are along the lengths of fissure networks on Mars.

The possibility for recent or future volcanic activity also has implications for future NASA missions, specifically with regards to environmental conditions that may be considered habitable, in the past or presently. The Cerberus region contains significant volcanic landforms comingled with extensive fluvial and periglacial features. Locations where water may be available, as evidenced by previous water-lava interactions in Athabasca and Grjótá Valles (e.g., Burr et al., 2005; Hamilton et al., 2010), and a ready energy source derived from increased thermal flux in the near-surface may be ideal locations to investigate for evidence of biological activity, past or present. The salts precipitated from near-surface brines heated by surface lava

flows can protect microbiota, as demonstrated by the isolation and growth of a 250-Ma halotolerant bacterium from a salt crystal (Vreeland et al., 2010). These conditions fall within the scope of NASA's Decadal Survey, and suggest that the Cerberus region would be a reasonable target for future robust lander missions that can survive and operate in rough terrain. The results from the ongoing InSight mission to Elysium Planitia (e.g., Banerdt et al., 2013) may yield clues from its seismometer and thermal probe as to whether local magmatic processes are continuing in the region. Finally, crater count derived model ages for the lunar mare basalts may need to be reexamined due to a potentially increased, but unknown, level of uncertainty, along with the calibration of lunar and non-lunar isochrons.

References

Alberti, G., Castaldo, L., Orosei, R., Frigeri, A., & Cirillo, G. (2012). Permittivity estimation over Mars by using SHARAD data: the Cerberus Palus area. Journal of Geophysical Research: Planets, 117(E9).

Ander, M. E., Heiken, G., Eichelberger, J., Laughlin, A. W., & Huestis, S. (1981). Geologic and geophysical investigations of the Zuni-Bandera volcanic field, New Mexico (No. LA-8827-MS). Los Alamos National Lab., NM (USA); Sandia National Labs., Albuquerque, NM (USA); New Mexico Univ., Albuquerque (USA). Dept. of Geology.

Anderson, R. C., et al., (2001). Primary centers and secondary concentrations of tectonic activity through time in the western hemisphere of Mars. Journal of Geophysical Research: Planets, 106(E9), 20563-20585.

Banerdt, W. B., Smrekar, S., Lognonné, P., et al. (2013, March). InSight: a discovery mission to explore the interior of Mars. In Lunar and Planetary Science Conference (Vol. 44, p. 1915).

Baratoux, D., Pinet, P., Toplis, M. J., Mangold, N., Greeley, R., & Baptista, A. R. (2009). Shape, rheology and emplacement times of small Martian shield volcanoes. Journal of Volcanology and Geothermal Research, 185(1-2), 47-68.

Baratoux, D., Toplis, M. J., Monnereau, M., & Gasnault, O. (2011). Thermal history of Mars inferred from orbital geochemistry of volcanic provinces. Nature, 472(7343), 338-341.

Berman, D. C., & Hartmann, W. K. (2002). Recent fluvial, volcanic, and tectonic activity on the Cerberus plains of Mars. Icarus, 159(1), 1-17.

Bleacher, J. E., Crumpler, L. S., Hamilton, C. W., Zimbelman, J. R., Garry, W. B., de Wet, A. P., ... & Scheidt, S. P. (2018, March). Implications of Inflated Sheet-Like Flow Emplacement on Planetary Surfaces. In Lunar and Planetary Science Conference (Vol. 49).

Boisson, J., Heggy, E., Clifford, S. M., Frigeri, A., Plaut, J. J., Farrell, W. M., Putzig, N.E., Picardi, G., Orosei, R., Lognonné, P., and Gurnett, D. A. (2009). Sounding the subsurface of Athabasca Valles using MARSIS radar data: Exploring the volcanic and fluvial hypotheses for the origin of the rafted plate terrain. Journal of Geophysical Research: Planets (1991–2012), 114(E8).

Britt, D.T. , Yeomans, D. , Housen, K. , Consolmagno, G. , 2002. Asteroid density, porosity, and structure. In: Bottke, W.F., Cellino, A., Paolicchi, P., Binzel, R.P. (Eds.), Asteroids III. University of Arizona Press, pp. 485–500.

Buck, W. R., Einarsson, P., & Brandsdóttir, B. (2006). Tectonic stress and magma chamber size as controls on dike propagation: Constraints from the 1975–1984 Krafla rifting episode. J. Geophys. Res.: Solid Earth, 111(B12).

Burr, D. M., McEwen, A. S., et al. (2002a). Recent aqueous floods from the Cerberus Fossae, Mars. Geophys. Res. Letters, 29(1), 13-1.

Burr, D. M., Grier, J. A., et al. (2002b). Repeated aqueous flooding from the Cerberus Fossae: Evidence for very recently extant, deep groundwater on Mars. Icarus, 159(1), 53-73.

Burr, D. (2005). Clustered streamlined forms in Athabasca Valles, Mars: Evidence for sediment deposition during floodwater ponding. Geomorphology, 69(1), 242-252.

Burr, D. M., & Parker, A. H. (2006). Grjótá Vallis and implications for flood sediment deposition on Mars. Geophys. Res. Letters, 33(22).

Burr, D.M., L. Wilson, and A.S. Bargery (2009) Floods from Fossae: a review of Amazonian-aged extensional tectonic megaflood channels on Mars. In Megaflooding on Earth and Mars,

D.M. Burr, V.R. Baker and P.A. Carling (eds), Cambridge University Press, Cambridge, UK. pp. 194-208.

Chapman, M. G., Neukum, G., Dumke, A., Michael, G., Van Gasselt, S., Kneissl, T., Zuschneid, W., Hauber, E., Mangold, N. (2010). Amazonian geologic history of the Echus Chasma and Kasei Valles system on Mars: New data and interpretations. Earth and Planetary Science Letters, 294(3), 238-255.

Christensen, P.R., Jakosky, B.M., et al. (2004), The Therman Emission Imaging System (THEMIS) for the Mars 2001 Odyssey Mission. Space Science Reviews, 110, 85-130.

Dundas, C. M., Keszthelyi, L. P., Bray, V. J., & McEwen, A. S. (2010). Role of material properties in the cratering record of young platy-ridged lava on Mars. Geophysical Research Letters, 37(12).

Dundas, C. M., & Keszthelyi, L. P. (2014). Emplacement and erosive effects of lava in south Kasei Valles, Mars. Journal of Volcanology and Geothermal Research, 282, 92-102.

Ernst, R. E., Head, J. W., Parfitt, E., Grosfils, E., & Wilson, L. (1995). Giant radiating dyke swarms on Earth and Venus. Earth-Science Reviews, 39(1-2), 1-58.

Ernst, R. E., Grosfils, E. B., & Mege, D. (2001). Giant dike swarms: Earth, Venus, and Mars. Annual Review of Earth and Planetary Sciences, 29(1), 489-534.

Ernst, R. E. (2014). Large igneous provinces. Cambridge University Press.

Feldman, W. C., et al., (2004). Global distribution of near-surface hydrogen on Mars. Journal of Geophysical Research: Planets, 109(E9).

Ferrill, D. A., Wyrick, D. Y., Morris, A. P., Sims, D. W., & Franklin, N. M. (2004). Dilational fault slip and pit chain formation on Mars. GsA Today, 14(10), 4-12.

Flóvenz, Ó. G., & Saemundsson, K. (1993). Heat flow and geothermal processes in Iceland. Tectonophysics, 225(1-2), 123-138.

Genova, A., Goossens, S., Lemoine, F. G., Mazarico, E., Neumann, G. A., Smith, D. E., & Zuber, M. T. (2016). Seasonal and static gravity field of Mars from MGS, Mars Odyssey and MRO radio science. Icarus, 272, 228-245.

Golombek, M., Bloom, C., Wigton, N., & Warner, N. (2014). Constraints on the Age of Corinto Crater from Mapping Secondaries in Elysium Planitia on Mars. In Lunar and Planetary Science Conference (Vol. 45, p. 1470).

Grott, M., Baratoux, D., Hauber, E., Sautter, V., Mustard, J., Gasnault, O., Ruff, S.W., Karato, S.-I., Debaille, V., Knapmeyer, M., Sohl, F., Van Hoolst, T., Breuer, D., Morchhauser, A., Toplis, M.J., (2013). Long-term evolution of the Martian crust-mantle system. Space Science Reviews, 174(1-4), 49-111.

Hall, J. L., Solomon, S. C., & Head, J. W. (1986). Elysium region, Mars: Tests of lithospheric loading models for the formation of tectonic features. J. Geophys. Res.: Solid Earth, 91(B11), 11377-11392.

Hamilton, C. W., and Fagents, S. A. (2009), The Tartarus-Colles Cone Group and Its Implications for Explosive Lava-Water Interactions in the Grjota Valles Region of Mars. In Lunar and Planetary Science Conference (Vol. 40, p. 1924).

Hamilton, C. W., Fagents, S. A., & Wilson, L. (2010). Explosive lava-water interactions in Elysium Planitia, Mars: Geologic and thermodynamic constraints on the formation of the Tartarus Colles cone groups. Journal of Geophysical Research: Planets, 115(E9).

Hamilton, C. W. (2013), Flood Lavas Associated with the Cerberus Fossae 2 unit in Elysium Planitia, Mars. In Lunar and Planetary Institute Science Conference Abstracts (Vol. 44, p. 3070).

Hamilton, C. W., Mouginis-Mark, P. J., Sori, M. M., Scheidt, S. P., & Bramson, A. M. (2018, March). Evidence of Lava Flow Inflation Near Hrad Vallis, Mars. In Lunar and Planetary Science Conference (Vol. 49).

Hartmann, W. K., and G. Neukum (2001), Cratering Chronology and the Evolution of Mars, Space Science Reviews, 96(1/4), 165-194.

Hartmann, W. K. (2005). Martian cratering 8: Isochron refinement and the chronology of Mars. Icarus, 174(2), 294-320.

Hartmann, W. K., & Daubar, I. J. (2017). Martian cratering 11. Utilizing decameter scale crater populations to study Martian history. Meteoritics & Planetary Science, 52(3), 493-510.

Head, J. W., and Coffin, M. F. (1997). Large igneous provinces: a planetary perspective. Geophysical Monograph-American Geophysical Union, 100, 411-438.

Head, J. W., Wilson, L., & Mitchell, K. L. (2003). Generation of recent massive water floods at Cerberus Fossae, Mars by dike emplacement, cryospheric cracking, and confined aquifer groundwater release. Geophysical research letters, 30(11).

Head, J. W., Murchie, S. L., Prockter, L. M., Solomon, S. C., Chapman, C. R., Strom, R. G., Watters, T.R., Blewett, D.T., Gillis-Davis, J.J., Fassett, C.I., Dickson, J.L., Morgan, G.A., Kerber, L. (2009). Volcanism on Mercury: Evidence from the first MESSENGER flyby for extrusive and explosive activity and the volcanic origin of plains. Earth and Planetary Science Letters, 285(3), 227-242.

Hiesinger, H., Jaumann, R., Neukum, G., & Head, J. W. (2000). Ages of mare basalts on the lunar nearside. Journal of Geophysical Research: Planets, 105(E12), 29239-29275.

Hiesinger, H., Head, J. W., & Neukum, G. (2007). Young lava flows on the eastern flank of Ascraeus Mons: Rheological properties derived from High Resolution Stereo Camera (HRSC) images and Mars Orbiter Laser Altimeter (MOLA) data. Journal of Geophysical Research: Planets, 112(E5).

Hiesinger, H., Head, J. W., Wolf, U., Jaumann, R., & Neukum, G. (2011). Ages and stratigraphy of lunar mare basalts: A synthesis. Geological Society of America Special Papers, 477(1), 1-51.

Holsapple, K. A. (1993). The scaling of impact processes in planetary sciences. Annual review of earth and planetary sciences, 21(1), 333-373.

Holsapple, K. A., & Housen, K. R. (2007). A crater and its ejecta: An interpretation of Deep Impact. Icarus, 191(2), 586-597.

Housen, K. R., & Holsapple, K. A. (2011). Ejecta from impact craters. Icarus, 211(1), 856-875.

Isherwood, R. J., Jozwiak, L. M., Jansen, J. C., & Andrews-Hanna, J. C. (2013). The volcanic history of Olympus Mons from paleo-topography and flexural modeling. Earth and Planetary Science Letters, 363, 88-96.

Ivanov, B.A., 2001. Mars/Moon cratering rate ratio estimates. Space Sci. Rev. 96, 87–104.

Ivanov, B. A., & Hartmann, W. K. (2007). Exogenic dynamics, cratering and surface ages. 207-242.

Jaeger, W. L., Keszthelyi, L. P., et al. (2007). Athabasca Vallis, Mars: A lava-draped channel system. Science, 317(5845), 1709-1711.

Jaeger, W. L., Keszthelyi, L. P., Skinner, J. A., Milazzo, M. P., McEwen, A. S., Titus, T. N., Rosiek, M.R., Galuszka, D.M., Howington-Kraus, E., Kirk, R. L., the HiRISE Team (2010). Emplacement of the youngest flood lava on Mars: A short, turbulent story. Icarus, 205(1), 230-243.

Kattenhorn, S. A., & Meyer, J. A. (2010, March). Magmatic dikes and megafloods: a protracted

history of interactions between magma and subsurface ice, Cerberus Fossae, Mars. In Lunar and Planetary Science Conference (Vol. 41, p. 1271).
Keszthelyi, L., and Self, S. (1998). Some physical requirements for the emplacement of long basaltic lava flows. Journal of Geophysical Research: Solid Earth (1978–2012), 103(B11), 27447-27464.
Keszthelyi, L., McEwen, A. S., Thordarson, T. (2000). Terrestrial analogs and thermal models for Martian flood lavas. Journal of Geophysical Research: Planets (1991–2012), 105(E6), 15027-15049.
Keszthelyi, L., Thordarson, T., McEwen, A., Haack, H., Guilbaud, M. N., Self, S., Rossi, M. J. (2004). Icelandic analogs to Martian flood lavas. Geochemistry, Geophysics, Geosystems, 5(11).
Keszthelyi, L. P., Jaeger, W. L., et al. (2010). Hydrovolcanic features on Mars: Preliminary observations from the first Mars year of HiRISE imaging. Icarus, 205(1), 211-229.
Kiefer, W. S. (2003). Melting in the martian mantle: Shergottite formation and implications for present-day mantle convection on Mars. Meteoritics & Planetary Science, 38(12), 1815-1832.
Kiefer, W. S. (2004). Gravity evidence for an extinct magma chamber beneath Syrtis Major, Mars: A look at the magmatic plumbing system. Earth and Planetary Science Letters, 222(2), 349-361.
Kiefer, W. S., Macke, R. J., Britt, D. T., Irving, A. J., & Consolmagno, G. J. (2012). The density and porosity of lunar rocks. Geophysical Research Letters, 39(7).
Klimczak, C. (2014). Geomorphology of lunar grabens requires igneous dikes at depth. Geology, 42(11), 963-966.
Kneissl, T., van Gasselt, S., & Neukum, G. (2011). Map-projection-independent crater size-frequency determination in GIS environments—New software tool for ArcGIS. Planetary and Space Science, 59(11), 1243-1254.
Lanagan, P. D., McEwen, A. S., Keszthelyi, L. P., & Thordarson, T. (2001). Rootless cones on Mars indicating the presence of shallow equatorial ground ice in recent times. Geophysical Research Letters, 28(12), 2365-2367.
Larsen, R. B., & Tegner, C. (2006). Pressure conditions for the solidification of the Skaergaard intrusion: eruption of East Greenland flood basalts in less than 300,000 years. Lithos, 92(1-2), 181-197.
Le Feuvre, M., and Wieczorek, M. A. (2011). Nonuniform cratering of the Moon and a revised crater chronology of the inner Solar System. Icarus, 214(1), 1-20.
Lemoine, F. G., Smith, D. E., Rowlands, D. D., Zuber, M. T., Neumann, G., Chinn, D. S., & Pavlis, D. E. (2001). An improved solution of the gravity field of Mars (GMM-2 B) from Mars Global Surveyor. Journal of Geophysical Research, 106(E10), 23-359.
Malin, M.C., et al. (2007), Context Camera Investigation on board the Mars Reconnaissance Orbiter. J. Geophys. Res., 112, E05S04, doi:10.1029/2006E002808.
Marsh, B. D. (1989). Magma chambers. Annual Review of Earth and Planetary Sciences, 17(1), 439-472.
McEwen, A. S., Preblich, B. S., et al. (2005). The rayed crater Zunil and interpretations of small impact craters on Mars. Icarus, 176(2), 351-381.
McEwen, A. S., and Bierhaus, E. B. (2006). The importance of secondary cratering to age constraints on planetary surfaces. Annu. Rev. Earth Planet. Sci., 34, 535-567.
McEwen, A.S., et al. (2007), Mars Reconnaissance Orbiter's High Resolution Imaging Science

Experiment (HiRISE). J. Geophys. Res., 112, E05S02.
McGovern, P. J., & Solomon, S. C. (1993). State of stress, faulting, and eruption characteristics of large volcanoes on Mars. J. Geophys. Res.: Planets, 98(E12), 23553-23579.
McGovern, P. J., Solomon, S. C., Smith, D. E., Zuber, M. T., Simons, M., Wieczorek, M. A., Phillips, R.J., Neumann, G.A., Aharonson, O., Head, J. W. (2002). Localized gravity/topography admittance and correlation spectra on Mars: Implications for regional and global evolution. Journal of Geophysical Research: Planets, 107(E12).
McGovern, P.J. et al., (2004). Correction to localized gravity/topography admittance and correlation spectra on Mars: Implications for regional and global evolution. Journal of Geophysical Research: Planets, 109, E07007.
Mège, D., & Masson, P. (1996a). Stress models for Tharsis formation, Mars.Planetary and Space Science, 44(12), 1471-1497.
Mège, D., and Masson, P. (1996b). A plume tectonics model for the Tharsis province, Mars. Planetary and Space Science, 44(12), 1499-1546.
Mège, D., Cook, A. C., et al. (2003). Volcanic rifting at Martian grabens. J. Geophys. Res.: Planets (1991–2012), 108(E5).
Melosh, H. J. (1989). Impact cratering: A geologic process. Research supported by NASA. New York, Oxford University Press (Oxford Monographs on Geology and Geophysics, No. 11), 1989, 253 p., 1.
Melosh, H. J. (2011). Planetary surface processes (Vol. 13). Cambridge University Press.
Michael, G. G., & Neukum, G. (2010). Planetary surface dating from crater size–frequency distribution measurements: Partial resurfacing events and statistical age uncertainty. Earth and Planetary Science Letters, 294(3), 223-229.
Michael, G. G. (2013). Planetary surface dating from crater size–frequency distribution measurements: Multiple resurfacing episodes and differential isochron fitting. Icarus, 226(1), 885-890.
Montési, L. G., & Zuber, M. T. (2003). Clues to the lithospheric structure of Mars from wrinkle ridge sets and localization instability. Journal of Geophysical Research: Planets, 108(E6).
Morgan, G. A., Campbell, B. A., et al. (2013). 3D Reconstruction of the Source and Scale of Buried Young Flood Channels on Mars. Science, 340(6132), 607-610.
Murray, J. B., Muller, J. P., Neukum, G., Werner, S. C., van Gasselt, S., Hauber, E., Markiewicz, W.J., Head, J.W., Foing, B.H., Page, D., Mithcell, K.L., Portyankina, G., & HRSC Co-Investigator Team. (2005). Evidence from the Mars Express High Resolution Stereo Camera for a frozen sea close to Mars' equator. Nature, 434(7031), 352-356.
Nahm, A. L., Kattenhorn, S. A., & Pendleton, M. W. (2015). Unraveling the Formation Mechanism (s) of the Cerberus Fossae, Mars: Evacuated Dikes, Graben, or Both?. In Lunar and Planetary Science Conference (Vol. 46, p. 2367).
Neukum, G., and B. A. Ivanov, Crater size distributions and impact probabilities on Earth from lunar, terrestrial-planet and asteroid cratering data, in Hazard Due to Comets and Asteroids , edited by T. Gehrels, pp. 359-416, Univ. of Ariz. Press Tucson, 1994.
Neukum, G., Ivanov, B.A., Hartmann, W.K., (2001). Cratering records in the inner solar system in relation to the lunar reference system. Space Sci. Rev. 96, 55–86.
Neukum, G., and Jaumann, R., (2004), HRSC: The High Resolution Stereo Camera of Mars Express. ESA Special Publication, ESA-SP 1240, 17-35.
Page, D. P., and Murray, J. B. (2006). Stratigraphical and morphological evidence for pingo genesis in the Cerberus plains. Icarus, 183(1), 46-54.

Page, D. P. (2007). Recent low-latitude freeze–thaw on Mars. Icarus, 189(1), 83-117.
Page, D. P. (2008). Comment on" Athabasca Valles, Mars: A Lava-Draped Channel System". Science, 320(5883), 1588-1588.
Page, D. P., Balme, M. R., & Grady, M. M. (2009). Dating Martian climate change. Icarus, 203(2), 376-389.
Parfitt, E. A., & Head III, J. W. (1993). Buffered and unbuffered dike emplacement on Earth and Venus: Implications for magma reservoir size, depth, and rate of magma replenishment. Earth, Moon, and Planets, 61(3), 249-281.
Patterson, C. W., Ernst, R. E., & Samson, C. (2016). Pit Chains Associated with Radiating Graben-Fissure Systems on Venus: Formation During Lateral Dyke Injection?. Lunar and Planetary Science Conference. Vol. 47, 2097.
Pendleton, MW, 2015, Geomorphic evidence for geologically recent groundwater flow associated with the Cerberus Fossae magmatic and volcanic system, Mars, MSc. thesis, University of Idaho, 157 pp.
Platz, T., and Michael, G. (2011). Eruption history of the Elysium volcanic province, Mars. Earth and Planetary Science Letters, 312(1), 140-151.
Plescia, J. B. (1990). Recent flood lavas in the Elysium region of Mars. Icarus, 88(2), 465-490.
Plescia, J. B. (1993). Wrinkle ridges of Arcadia Planitia, Mars. Journal of Geophysical Research: Planets, 98(E8), 15049-15059.
Plescia, J. B. (2003). Cerberus Fossae, Elysium, Mars: A source for lava and water. Icarus, 164(1), 79-95.
Polacci, M., Cashman, K. V., & Kauahikaua, J. P. (1999). Textural characterization of the pāhoehoe–'a 'a transition in Hawai'ian basalt. Bulletin of Volcanology, 60(8), 595-609.
Rice Jr, J. W., Parker, T. J., Russell, A. J., & Knudsen, O. (2002), Morphology of fresh outflow channel deposits on Mars. In Lunar and Planetary Science Conference (Vol. 33, p. 2026).
Richardson, J. E., Melosh, H. J., Lisse, C. M., & Carcich, B. (2007). A ballistics analysis of the Deep Impact ejecta plume: Determining Comet Tempel 1's gravity, mass, and density. Icarus, 190(2), 357-390.
Rubin, A. M. (1993). Tensile fracture of rock at high confining pressure: implications for dike propagation. J. Geophys. Res.: Solid Earth, 98(B9), 15919-15935.
Rubin, A. M. (1995). Propagation of magma-filled cracks. Annual Review of Earth and Planetary Sciences, 23, 287-336.
Ruiz, J., López, V., & Dohm, J. M. (2010). The present-day thermal state of Mars. Icarus, 207(2), 631-637.
Ruiz, J., McGovern, P. J., Jiménez-Díaz, A., López, V., Williams, J. P., Hahn, B. C., & Tejero, R. (2011). The thermal evolution of Mars as constrained by paleo-heat flows. Icarus, 215(2), 508-517.
Schmidt, R. M., & Housen, K. R. (1987). Some recent advances in the scaling of impact and explosion cratering. International Journal of Impact Engineering, 5(1-4), 543-560.
Schultz, R. A., Okubo, C. H., Goudy, C. L., & Wilkins, S. J. (2004). Igneous dikes on Mars revealed by Mars Orbiter Laser Altimeter topography. Geology, 32(10), 889-892.
Schumacher, S., & Breuer, D. (2007). An alternative mechanism for recent volcanism on Mars. Geophysical Research Letters, 34(14).
Self, S., Keszthelyi, L., Thordarson, T. (1998). The importance of pahoehoe. Annual Review of Earth and Planetary Sciences, 26(1), 81-110.
Smith, D.E., et al., (2001), Mars Orbiter Laser Altimeter: Experiment summary after the first year

of global mapping of Mars. J. Geophys. Res., 106, E10, 23,689-23,722.
Steinberger, B., Werner, S. C., & Torsvik, T. H. (2010). Deep versus shallow origin of gravity anomalies, topography and volcanism on Earth, Venus and Mars. Icarus, 207(2), 564-577.
Swanson, D. A. (1973). Pahoehoe flows from the 1969–1971 Mauna Ulu eruption, Kilauea volcano, Hawai'i. Geological Society of America Bulletin, 84(2), 615-626.
Tanaka, K. L., Scott, D. H., & Greeley, R. (1992). Global stratigraphy. Mars, 1, 345-382.
Tanaka, K.L., Skinner, J.A., et al. (2014). Geologic map of Mars: U.S. Geological Survey Scientific Investigations Map 3292, scale 1:20,000,000, pamphlet 43 p.
Thomas, R. J. (2013). Identification of possible recent water/lava source vents in the Cerberus plains: stratigraphic and crater count age constraints. Journal of Geophysical Research: Planets, 118(4), 789-802.
Thordarson, T., and Self, S. (1993). The Laki (Skaftár Fires) and Grímsvötn eruptions in 1783-1785. Bulletin of Volcanology, 55, 233-263.
Thordarson, T., Miller, D.J., Larsen, G., Self, S., Sigurdsson, H. (2001). New estimates of sulfur and atmospheric mass-loading by the 934 AD Eldgjá eruption, Iceland. Journal of Volcanology and Geothermal Research, 108, 33-54.
Thorey, C., Michaut, C., & Wieczorek, M. (2015). Gravitational signatures of lunar floor-fractured craters. Earth and Planetary Science Letters, 424, 269-279.
Turcotte, D. L., & Schubert, G. (2002). Geodynamics, 456 pp.
van der Bogert, C. H., Hiesinger, H., McEwen, A. S., Dundas, C., Bray, V., Robinson, M. S., Plescia, J.B., Reiss, D., Klemm, K., & Team, L. (2010). Discrepancies between crater size-frequency distributions on ejecta and impact melt pools at lunar craters: An effect of differing target properties?. In Lunar and Planetary Science Conference (Vol. 41, p. 2165).
van der Bogert, C. H., Hiesinger, H., Dundas, C. M., Krüger, T., McEwen, A. S., Zanetti, M., & Robinson, M. S. (2017). Origin of discrepancies between crater size-frequency distributions of coeval lunar geologic units via target property contrasts. Icarus, 298, 49-63.
Vaucher, J., Baratoux, D., et al. (2009). The volcanic history of central Elysium Planitia: Implications for martian magmatism. Icarus, 204(2), 418-442.
Vetterlein, J., & Roberts, G. P. (2010). Structural evolution of the northern Cerberus Fossae graben system, Elysium Planitia, Mars. Journal of Structural Geology, 32(4), 394-406.
Vreeland, R. H., Rosenzweig, W. D., & Powers, D. W. (2000). Isolation of a 250 million-year-old halotolerant bacterium from a primary salt crystal. Nature, 407(6806), 897.
Warner, N. H., Gupta, S., Calef, F., Grindrod, P., Boll, N., & Goddard, K. (2015). Minimum effective area for high resolution crater counting of martian terrains. Icarus, 245, 198-240.
Werner, S. C. (2009). The global martian volcanic evolutionary history. Icarus, 201(1), 44-68.
Werner, S. C., & Tanaka, K. L. (2011). Redefinition of the crater-density and absolute-age boundaries for the chronostratigraphic system of Mars. Icarus, 215(2), 603-607.
Williams, J. P., Pathare, A. V., & Aharonson, O. (2014). The production of small primary craters on Mars and the Moon. Icarus, 235, 23-36.
Wilmoth, R. A., & Walker, G. P. (1993). P-type and S-type pahoehoe: a study of vesicle distribution patterns in Hawai'ian lava flows. Journal of Volcanology and Geothermal Research, 55(1-2), 129-142.
Wilson, L., and Head, J. W. (1994). Mars: Review and analysis of volcanic eruption theory and relationships to observed landforms. Reviews of Geophysics, 32(3), 221-263.
Wilson, L., and Head, J. W. (2002). Tharsis-radial graben systems as the surface manifestation of

plume-related dike intrusion complexes: Models and implications. Journal of Geophysical Research: Planets (1991–2012), 107(E8), 1-1.

Wilson, L., and Mouginis-Mark, P. J. (2014). Dynamics of a fluid flow on Mars: Lava or mud?. Icarus, 233, 268-280.

Wünnemann, K., Nowka, D., Collins, G. S., Elbeshausen, D., & Bierhaus, M. (2011). Scaling of impact crater formation on planetary surfaces: Insights from numerical modeling. In Proceedings of the 11th Hypervelocity Impact Symposium (pp. 1-16).

Wyrick, D., Ferrill, D. A., Morris, A. P., Colton, S. L., & Sims, D. W. (2004). Distribution, morphology, and origins of Martian pit crater chains. Journal of Geophysical Research: Planets, 109(E6).

Zanetti, M., Stadermann, A., Jolliff, B., van der Bogert, C.H., Hiesinger, H., Plescia, J.B., (2015). Auto-secondary cratering vs. target property effects on ejecta blankets of Copernican craters: What are the implications for age dating using small-diameter crater statistics? Lunar Planet. Sci. Conf. 46 #1209.

Zimbelman, J. R. (1998). Emplacement of long lava flows on planetary surfaces. Journal of Geophysical Research: Solid Earth (1978–2012), 103(B11), 27503-27516.

CHAPTER 2
EMPLACEMENT OF WIDESPREAD LAVA FLOWS ON MARS: INVESTIGATING THE EFFECT OF BULK VISCOSITIES ON FLOW EMPLACEMENT THROUGH MODELING

Abstract

Volcanism has shaped the surfaces of the terrestrial planets. Lava plains and flood basalts range in length from 10s of km to greater than 1000 km, respectively, and represent some of the most common, large-scale emplacements of lava. Terrestrial examples within this range of sizes include both the McCartys and Laki flows, as well as the far larger Columbia River Basalt and Deccan Basalt Groups. Mars also hosts volcanic features within this size range, with some of the largest flows concentrated in and around the Cerberus region. Although extrinsic factors, such as the total erupted volume, effusion rate, regional slope, and planetary gravity are critical elements in determining the length and areal extent of lava flows, a full understanding of flow emplacement must also consider the intrinsic factors, such as the composition, density, crystallinity, gas content, and the overall effect of these parameters on flow viscosity. The results of previous morphological analyses, flow rate modeling, and spectral evidence suggest the composition of large-scale flows on Mars' surface is generally basaltic, which would correspond to lavas with initial bulk viscosity values ranging from 1-1000 Pa·s. Based on the observed constraints for the extrinsic factors, the extent and inferred emplacement mode for the lava flows of interest, I hypothesize that low viscosity lava (~10 Pa·s) is required to account for the channelized lava flows in the Cerberus region on Mars.

To test the effect of viscosity on the areal extent and length of martian lava flows, and to constrain the bulk viscosity of these lava flows during their emplacement, here I use multi-step sequential procedures during this investigation. Mapping the areal extent and length of terrestrial (McCartys and Laki) and martian (Athabasca and Grjótá Valles) sites permits the comparison between example of real-world lava flow lengths and those derived using an empirical relationship between effusion rate and final flow length. This comparison demonstrates the

variable effect of changes to bulk viscosity on flows with constant volumes and slopes. To benchmark the model and set a standard for comparison to illustrate the viscosity effects in the results, I use empirically derived lengths, which show that low viscosity flows are thinner and have greater lengths than high viscosity flows of the same volume. A Python-based cellular automata model is then used to simulate lava flows on topography representing both the terrestrial and martian lava flow sites. The model is calibrated and validated using comparisons between mapped and simulated terrestrial lava flows, which then permit simulations to be performed on the martian investigation sites. During the calibration and validation of the model, changes to the bulk viscosity (1-1000 Pa·s), yield strength (1-1000 Pa), and density (1000-3000 kg/m^3) parameter, demonstrated a clear effect on the length and extent of the simulated lava flows. I then applied this calibrated and validated model to the martian lava flows using a constant volume and density, and varied the bulk viscosity and yield strength, to investigate the overall effect of viscosity on flow area and length. The results of these model outputs were compared to the observed extents of the lava flows in Athabasca and Grjótá Valles, Mars, to gauge the effect of viscosity on the final flow length. This work suggests the simulations using the lowest bulk viscosities and yield strengths (1 Pa·s, and 1 Pa) result in the best fit for length and areal extent of the martian examples, confirming the hypothesis of this chapter. Coupled with the results from Chapter 1, inferences can be made regarding the recent interior conditions on Mars that have led to the eruption of very low viscosity lavas that can flow over greater distances, inundating large areas.

Introduction

Volcanism has played a primary role in shaping the surfaces of the terrestrial planets, specifically the emplacement of widespread and voluminous lava flows. Large-scale flood basalts

are characterized by sheet-like flows that inundate large areas, resulting in relatively smooth, low-relief plains that lack a large, obvious edifice (e.g., Geikie, 1880; Washington, 1922; Tyrrell, 1937). Flood basalts originate from fissures and are typically larger in scale than plains-style volcanic flows, which originate from discrete vents, although if the erupted volume for these smaller flows increased and the vents coalesced into fissures, these flows would become more similar to flood basalts (e.g., Greeley, 1976; Greeley and King, 1977; Greeley, 1982; Sakimoto et al., 2003; Vaucher et al., 2009). A variety of factors influence the final areal extent of lava flows; these can be categorized as either intrinsic or extrinsic to the volcanic system (e.g., Walker, 1967; 1971; 1973; Hulme, 1974; Wilson and Head, 1994; Keszthelyi, 1995; Miyamoto and Sasaki, 1998; Griffiths, 2000; Wilson and Head, 2002; Jaeger et al., 2010; Harris, 2013; Cordonnier et al., 2015). Extrinsic factors can be generally well-constrained through orbital observations. For instance, the local slope can be estimated from the post-emplacement slope and the total erupted volume can be approximated based on the observed dimensions and approximate thickness of the flow. The effusion rate can be approximated using empirical relationships derived from terrestrial observations and modeling (e.g., Thordarson and Self, 1993; Keszthelyi and Self,). Although extrinsic factors play a role the final length and extent of lava flows, this investigation focuses on the effect of the intrinsic bulk viscosity on the final extent of lava flows. To explore these effects, I use a numerical model to (1) reproduce the areal extent and thickness of observed terrestrial and martian lava flows, and (2) to determine the magnitude of the effect of viscosity changes on the final extent of the lava flows.

Understanding the emplacement of these widespread lava flows can shed light on the similarities and dissimilarities in their development on the terrestrial planets and constrain the effect of viscosity. Knowing the bulk viscosity can be used to infer the overall composition and

temperature of the lavas during their emplacement. This work can also shed light on the internal conditions of Mars present in the recent geological past, which led to the formation of these extensive lava flows. Terrestrial analogues provide a method for the calibration and validation of this approach, as well as providing a reasonable input range for the parameter values to be applied to the martian flows. These terrestrial values constrain the parameter space and can lead to reasonable reproductions of observed lava flows, from which inferences on the effect of viscosity can be made. I focused my initial investigations on Earth and Mars, though this work can be expanded to include the study of any planetary body that hosts widespread lava flows and has topographic data that covers the full extent of those flows.

Background

Large Lava Flows on Earth and Mars

Evidence of volcanism has been found on all the terrestrial planets (e.g., BSVP, 1981; Head and Coffin, 1997; Zimbelman, 1998; Bandfield et al., 2000; Keszthelyi et al., 2006; Head et al., 2009). Many of the lava flows identified on these bodies are categorized as flood basalts, which inundate large areas and result in relatively low relief (<100 m relief) smooth plains (e.g., Geikie 1880; Washington 1922; Tyrrell 1937; Keszthelyi et al., 2000). Smaller-scale lava flows are typically categorized as plains-style volcanism, and are recognized as part of a continuum of eruption style (Greeley, 1976; Greeley and King, 1977; Greeley, 1982; Sakimoto et al., 2003; Vaucher et al., 2009). On Earth and Mars, such flood basalts are commonly associated with multiple lava flows that form thick successions. Flood basalts are common components of large igneous provinces (LIPs), which represent voluminous lava emplacement, typically of basaltic composition (e.g., Coffin and Eldholm, 1994; Keszthelyi et al., 2006). Investigations of these large-scale planetary flood basalts often rely on the study of terrestrial lava flows (e.g.,

Keszthelyi et al., 2000, 2004), which are used to inform our understanding of extraterrestrial volcanic sites.

Despite the difference in planetary gravity, terrestrial examples of lava flows (Fig. 10 A,B) are excellent comparative locations from which to infer emplacement conditions for martian lava flows. For this study, several terrestrial analogue sites were used. First, the McCartys basalt flow within the Zuni-Bandera volcanic field (Fig. 10A; Nichols, 1946; Ander et al., 1981; Crumpler and Aubele, 2001; Zimbelman and Johnston, 2002) and the Icelandic Eldgá and Laki basalt flows (Fig. 10B; e.g., Thordarson and Self, 1993; Keszthelyi et al., 2000; Thordarson et al., 2001), are used as examples of smaller-scale effusive flows, and the Deccan Basalt Group (DBG; e.g., Self et al., 2008) and the Columbia River Basalt Group (CRBG; e.g., Self et al., 1996) are used as examples of large-scale flood basalts.

The McCartys basalt flow is one of the youngest and longest lava flows within the continental United States. At ~3000 years old, the McCartys flow is ~10 m thick and ~50 km in length, and consists of rubbly, fractured plates of pahoehoe that were sourced from a single vent (e.g., Nichols, 1946; Ander et al., 1981; Crumpler and Aubele, 2001; Zimbelman and Johnston, 2002). The Eldgá and Laki lava flows in Iceland were emplaced in 934 C.E. and 1783-85 C.E., respectively. These flows are ~15 m thick and extend for nearly 50 km, and represent fissure-fed eruptions (Thordarson and Self, 1993; Thordarson et al., 2001). Terrestrial LIPs are typified by the Deccan Basalt Group (DBG; e.g., Keszthelyi et al., 2006; Self et al., 2008) and the Columbia River Basalt Group (CRBG; e.g., Self et al., 1996; Keszthelyi et al., 2006). These voluminous deposits are comprised of stacks of inflated pahoehoe, where magma continued to flow underneath a lifted and chilled crust, producing a distinct surface morphology containing tumuli, inflation plateaus, and inflation pits (Keszthelyi et al., 2006). The majority of these stacked sheet

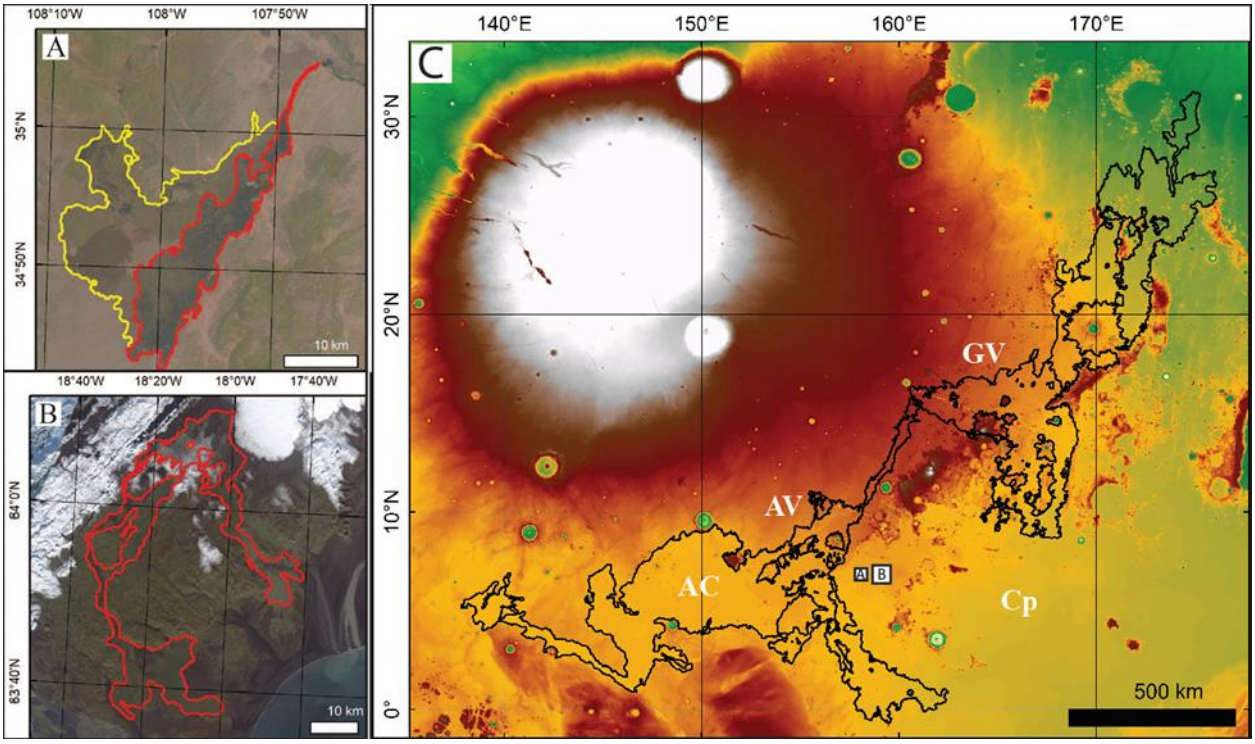

Figure 10. Comparative extents of the terrestrial McCartys (A), Laki (B), and martian Athabasca and Grjótá (C) lava flows. The extent of the McCartys flow (A, red outline) was mapped using Landsat 7 data, whereas the extent of the Laki lava flow (B, red outline) was mapped using Landsat 8 data. The extents of Athabasca (AV) and Grjótá Valles (GV) were mapped using a CTX basemap and are displayed (black outlines) on MOLA topography basemap. The small white boxes (A and B) located east of AV and Athabasca Colles (AC) in the Cerberus plains (Cp) are the extent of the McCartys and Laki flows displayed-to-scale for comparison with AV.

flows were emplaced over a period of ~3 Ma, with individual flows forming rapidly during a single pulse, or during more prolonged eruptions that involved multiple pulses of activity (e.g., Walker et al., 1971; Self et al., 1996, 2008; Keszthelyi et al., 2006; Ernst, 2014).

On Mars, a variety of voluminous lava flows have been observed, particularly near volcanic provinces (e.g., Tharsis Montes). In the Cerberus region, these voluminous lavas include channelized flows that have been the subject of prior analyses (e.g., Plescia, 1990; Burr et al. 2002a; Keszthelyi et al., 2004; Vaucher et al., 2009). These channelized flows are relatively young, have well constrained flow margins, and have distinct and pristine-looking surfaces that extend for >1000 km within the three circum-Cerberus aqueously-carved flood channels, Athabasca, Grjótá, and Marte Valles (Fig 1B, 10C; Plescia, 1990; Burr et al., 2002a, 2002b; Berman and Hartmann, 2002; Plescia, 2003; Keszthelyi, et al., 2004; McEwen et al., 2005; Burr et al., 2009; Vaucher et al., 2009; Jaeger et al., 2010), and in Kasei Valles located to the east of the Tharsis Montes (Chapman et al., 2010; Dundas and Keszthelyi, 2014; Dundas et al., 2019). Each of these flows is inferred to have formed during a single eruptive event, based on the contiguous surface texture of the lava flows, lack of flow fronts within the channels, and absence of obvious downstream vents or fissures that may have provided a secondary source for lava (e.g., Vaucher et al., 2009; Jaeger et al., 2010; Hamilton, 2013; Dundas and Keszthelyi, 2014; Golder et al., 2020). Typical thicknesses, measured from topographic data of lava flow fronts, are ~20 m within Athabasca Valles (Vaucher et al., 2009; Jaeger et al., 2010), and up to ~30 m in Grjótá Valles (Burr and Parker, 2006). A rapid, turbulent emplacement has been suggested for the lava in Athabasca Valles, based on mapping of the disrupted lava surface and modeling of its emplacement rate (Jaeger et al., 2010), although longer emplacement times are possible. If this rapid emplacement inference is correct for Athabasca, as well as for the similar lavas found in

Kasei Valles (Dundas and Keszthelyi, 2014), then the similarity in surface texture in Grjótá Valles would suggest that lava flow was also emplaced geologically rapidly. Based on modeling, this emplacement might have spanned days or weeks (Jaeger et al., 2010) or have been more gradual over the course of months, years, or decades, as observed in analogous terrestrial systems, such as the CRBG (Self et al., 1996).

Utility of Terrestrial Analogues

Terrestrial analogues are sites that represent varying geological processes and can be used to better understand the origin and evolution of similar terrains identified on other planetary bodies (e.g., Osinski et al., 2006). This study uses modeling to simulate lava flows to better understand the effects of viscosity on flow length and areal extent. Terrestrial analogues are used to calibrate and validate the model, to make inferences about the bulk viscosity of martian lava flows during their emplacement. Identification of appropriate analogues is necessary for comparative analyses between planets, as well as between observed lava flows and model outputs. Terrestrial analogue sites include the McCartys lava flow, because it is similar in scale, displays surface eruption source (vents), and has compositions and morphology similar to plains-style lava flows, particularly the smaller flows found in the Cerberus plains (Vaucher et al., 2009; Bleacher et al., 2010, 2012, 2017). Another terrestrial analogue site in the Laki flow, Iceland, which has previously been used as a terrestrial analogue site, based on its surface texture, flow morphology, composition, and eruption style (fissure), that is similar to the channelized flood basalts bounding the Cerberus region (e.g., Keszthelyi et al., 2004). The CRBG and DBG are areally extensive, and analogous in areal extent to the martian channelized lavas, whereas the Laki and McCartys, though much smaller (Fig. 10), are similar in surface morphology and eruption source type (Table 4).

Table 4. Characteristics of long terrestrial and martian lava flows. Previously derived crater-count age estimates for the lava-infilled channel systems and Cerberus plains. *Vaucher et al. (2009) only performed crater counts in one location within their ACo unit, of which they determined Grjótá Valles was a part. Multiple overlapping flows are termed complex, while single flows are termed simple.

Volcanic Field	Age	Lava Source	Max. Length	Type	Reference(s)
EARTH					
Deccan Basalt Group, India	~65 Ma	Dike swarms, surface fissures	~1000 km	Complex	Self et al., 2008
Columbia River Basalt Group, USA	17-6 Ma	Dike swarms, surface fissures	~600 km	Complex	Self et al., 1996
McCartys, USA	3 Ka	Vent	~50 km	Simple	Ander et al., 1981
Eldgjá & Laki, Iceland	934 CE & 1783-85 CE	Surface fissure	~50 km	Simple	Thordarson et al., 2001
MARS					
Athabasca Valles	2-8 Ma 1.5-200 Ma 2.5-2.81 Ma ~3 Ma	Cerberus Fossae fissures	~1400 km	Simple	Burr et al., 2002b McEwen et al., 2005 Vaucher et al., 2009 Golder et al., 2020
Grjótá Valles	10-40 Ma 62-250 Ma 500 Ma* 31-53 Ma	Cerberus Fossae fissures	~1400 km	Simple	Burr et al., 2002b; Hamilton et al., 2010; Vaucher et al., 2009 Golder et al., 2020
Marte Vallis	35-140 Ma 10-200 Ma 8-24 Ma 8-43 Ma	Cerberus plains/ Cerberus Fossae	~1800 km (from fissure) ~2500 km (total length)	Simple	Burr et al., 2002b Berman & Hartmann, 2002 Vaucher et al., 2009 Golder et al., 2020
Cerberus Plains	2.5-234 Ma	Vents/Fissures	Highly Variable	Complex	Vaucher et al., 2009

Though not exact analogues for the channelized lava found in the Cerberus region, the McCartys and Laki flows are well-constrained terrestrial lava flows with similarities in composition, eruption source and style to the martian flows under investigation that they can be used as a basis to develop the model. Far smaller than the channelized lavas on Mars (Fig. 10; e.g., Ander et al., 1981), the McCartys flow is similar in size to the lava flows and small shield volcanoes in the Cerberus plains (e.g., Vaucher et al., 2009; Bleacher et al., 2012), but emanates from a point-source vent rather than a fissure (e.g., Ander et al., 1981). McCartys is a basaltic lava (Ander et al., 1981), compositionally similar to the Cerberus plains features and the bounding channelized lavas (e.g., Vaucher et al., 2009; Jaeger et al., 2010), which had been previously characterized as basaltic using observations of surface textures, modeling, and spectral data (e.g., Keszthelyi et al., 2004; Vaucher et al., 2009; Jaeger et al., 2010). The surface of the McCartys flow hosts a thicker measured crust than that of the Laki flow, suggesting a potentially slower emplacement. The bulk of the McCartys was emplaced during a single effusive event from a distinct vent (Nichols, 1946), and is analogous to the volcanic features found in the Cerberus plains (Table 4; Bleacher et al., 2017). Some segments of the McCartys flow behaved as an inflated pahoehoe (Nichols, 1946; Ander et al., 2010; Bleacher et al., 2010, 2012; 2017). Based on the volume and inferred effusion rate, the McCartys flow was likely emplaced within a single month (Zimbelman and Johnston, 2002). Though not an exact analogue for the channelized lava, the McCartys and Laki flows are well-constrained lava flows with similarities in composition, eruption source, and style to the martian flows under investigation that it can be used as a basis to develop the model.

The Laki lava flow is also significantly smaller than the martian lava flows (Fig. 10, Table 4; e.g., Thordarson et al., 2001; Keszthelyi et al., 2004), and is more similar in size to the

lava flows found in the Cerberus plains (e.g., Vaucher et al., 2009; Bleacher et al., 2012). This flow emanates from a fissure (e.g., Thordarson et al., 2001; Keszthelyi et al., 2000, 2004), similar to Athabasca and Grjótá Valles flows. Laki is also basaltic in composition (Keszthelyi et al., 2000, 2004), comparable to the Cerberus lavas (e.g., Vaucher et al., 2009; Jaeger et al., 2010). The Laki crust has a platy-ridged texture (e.g., Keszthelyi et al.,2004), similar to the surfaces observed in Athabasca and Grjótá Valles (e.g., Keszthelyi et al., 2000, 2004, 2010; Burr et al., 2002b; Plescia, 2003; Vaucher et al., 2009; Jaeger et al., 2010). This crust likely formed once the flow stagnated, stabilizing the surface once the flow velocity had decreased to the point that the crust would not autobrecciate, or fracture under the stress of its own flow (Macdonald, 1953; Keszthelyi et al., 2000; Jaeger et al., 2010). By contrast, the presence of an auto-brecciated crust suggests the bulk of the flow was emplaced prior to formation of the crust, the flow then stagnated leading to the formation of the crust, and a late surge of lava disrupted the crust prior to the flow finally ceasing (Jaeger et al., 2010). The bulk of the Laki flow was emplaced during a single effusive event from a distinct fissure (Keszthelyi et al., 2004), analogous to the Cerberus channelized lavas (Table 1; Keszthelyi et al., 2000, 2004). As the Laki and martian lava flows host the same surface texture, flow morphology, source and eruption style (Keszthelyi et al., 2004), the disrupted crusts observed within the Cerberus lavas likely formed late in the emplacement of the lavas, and did not have a significant constraining effect on the initial lateral extent of the flows. Portions of the longer and more extensive Laki flow reached nearly their maximum length within days while the bulk of the flow was emplaced within months, although the eruption continued sporadically through the following year (Thordarson and Self, 1993; Keszthelyi et al., 2000, 2004).

The CRBG and DBG are similar in areal extent and are comprised of complex overlapping basaltic lava flows (Self et al., 1996; Self et al., 2008, respectively). A major difference between these terrestrial LIPs and the martian flood basalts is that the terrestrial flows are comprised of multiple overlapping lava flows (e.g., Self et al., 1996; Self et al., 2008), whereas the martian flows are suggested to have been emplaced during single eruption events, generally based on their surface textures (Vaucher et al., 2009; Jaeger et al., 2010; Hamilton, 2013; Golder et al., 2020). Thus, the CRBG and DBG are primarily analogous to the martian channelized lavas due to their basaltic composition, widespread nature, and sourcing from dikes that feed surface fissures (e.g., Self et al., 1996; Self et al., 2008), not due to a rapid emplacement from a single source.

Despite a lack of precise equivalence in every factor between these terrestrial and martian lava flows, modeling of terrestrial lava flows can inform our understanding of the parameters that result in the formation of long and areally extensive lava flows (Keszthelyi et al., 1998; Harris and Rowland 2001; Ratto and Saltelli, 2001; Howard, 2007; Bilotta et al., 2012). This terrestrial analogue work in turn better constrains the martian modeling work. These terrestrial analogues provide a range of eruption types, sources, and areal extents from which a robust numerical model can be developed. Such models can then simulate how varying bulk viscosities affect the development of both terrestrial and martian flood basalts, providing key insight into the intrinsic properties of martian lava.

Controls on Emplacement of Long Lava Flows

Intrinsic and Extrinsic Factors

Factors that influence the areal extent of silicate lavas are categorized as either intrinsic or extrinsic to the lava. Intrinsic factors include the yield strength (internal resistance to flow),

density, composition (especially silica content), crystallinity, volatile content, exsolved gas (bubble) content, pressure, and temperature (Fig. 11; e.g., Walker 1967, 1973; Hulme 1974; Ishihara et al., 1990; Griffiths, 2000; Herault et al., 2009; Harris, 2013; Cordonnier et al., 2015). Each of these factors can affect the overall bulk viscosity of the lava and can therefore be considered a subset of the viscosity (Fig. 11; e.g., Harris, 2013; Cordonnier et al., 2015). By contrast, extrinsic factors include the effusion rate, total erupted volume, regional slope, and planetary gravity (Fig. 11; Walker, 1971, 1973; Hulme, 1974; Wilson and Head, 1994; Keszthelyi, 1995; Miyamoto and Sasaki, 1998; Wilson and Head, 2002; Jaeger et al., 2010), each of which plays a direct role in the length and extent of a lava flow.

Modes of Emplacement

Factors that play a significant role in the final extent of the lava flow can also be dependent on the mode of lava emplacement, specifically whether the lava system is cooling-limited or volume-limited. In a cooling-limited system, the flow initiates at a high temperature and ceases once the temperature has decreased to the point at which the increase in the temperature-dependent viscosity impedes further propagation (e.g., Pinkerton and Wilson, 1994). This change in viscosity occurs with heat loss to the surroundings (surface and atmosphere), producing a decreasing lava temperature with increasing distance from the source, and this temperature dependence leads to an exponential increase in viscosity, that ultimately restricts the flow extent of the lava (Fig. 12, Scenario 1; e.g., Dragoni et al., 1997; Blatt et al., 2006; Diniega et al., 2013; Cordonnier et al., 2015). In a volume-limited scenario, the lava flow is controlled by the total erupted volume, where the lava will continue to flow until the erupted volume has been exhausted (Fig. 12, Scenario 2; e.g., Walker, 1973; Wilson and Head, 1983; Pinkerton and Wilson, 1988). This study focuses solely on volume-limited systems, because the terrestrial and martian lava flows being investigated have been interpreted to have been emplaced very rapidly

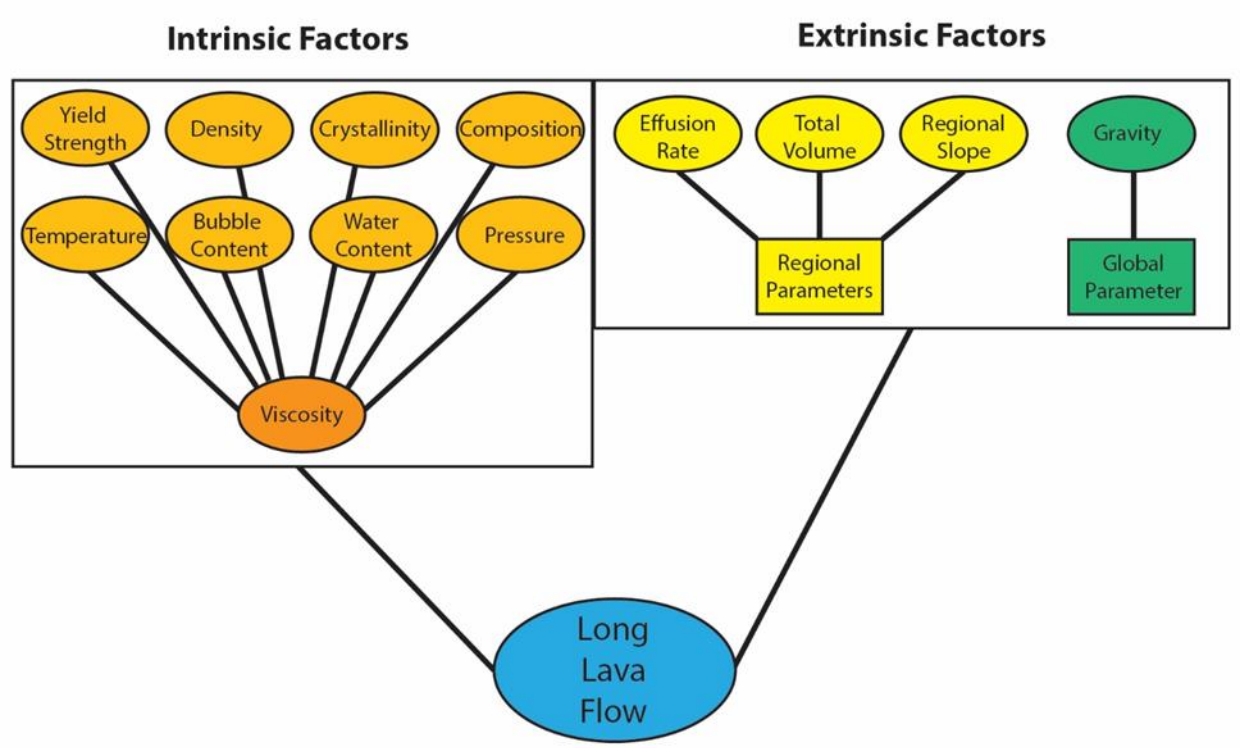

Figure 11. Intrinsic and extrinsic factors that influence the development of long and areally extensive lava flows. The sub-factors that affect the overall viscosity of the lava are not included in this model. In the case of the yield strength and density parameters, they were included as they are integral components of the governing equations, but their values were made constant.

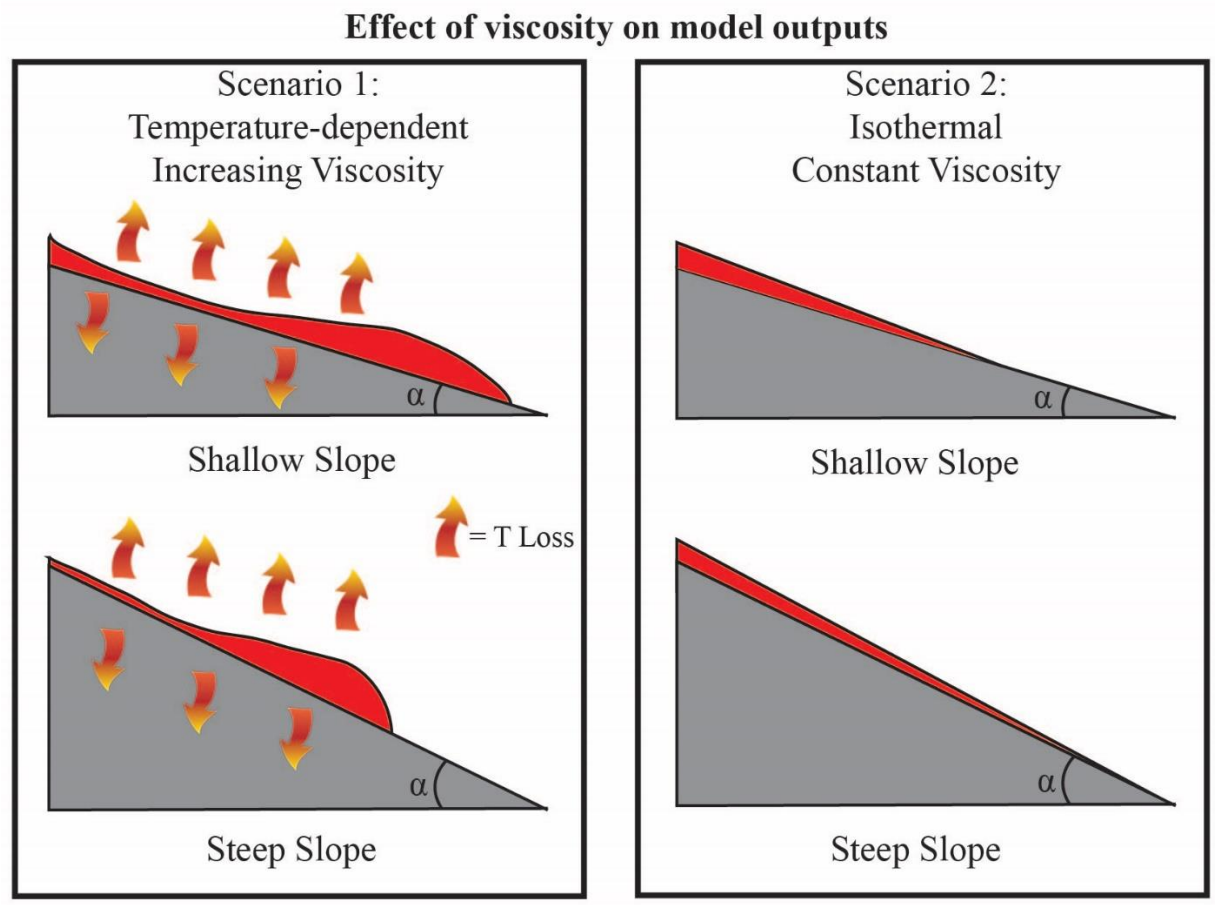

Figure 12. Influences on lava flow length and thickness under cooling- and volume-limited emplacement modes, with a fixed erupted volume. Changes to the bulk viscosity parameter in Scenario 1, caused by heat loss to the atmosphere and substrate, will lead to changes in thickness and length of the flow, by either generating thicker and shorter flows (high viscosity), or thinner and longer flows (low viscosity). In Scenario 2, the flows behave isothermally so no change in the bulk viscosity occurs during emplacement. In this case, a shallow slope affects the extent of the flow, so its final form is shorter and thicker, while a steep slope results in a longer and thinner flow.

and would have ceased once the erupted supply was exhausted (e.g., Ander et al., 1981; Thordarson and Self, 1993; Keszthelyi et al., 2000, 2004; Zimbelman and Johnston, 2002; Jaeger, et al., 2010).

The total erupted volume plays a critical role in the maximum lateral extent of the lava (e.g., Walker, 1973; Wilson and Head, 1983; Pinkerton and Wilson, 1988). For an idealized volume-limited system with a fixed volume, variable slope, and lava which is isothermal and assumed to have a constant viscosity, I briefly explore two slope-based endmembers (Fig. 12, Scenario 2). For a low slope angle, and neglecting heat loss, the lava has a higher critical thickness and the flow will propagate until the volume is exhausted. An expected trend in decreasing thickness of the emplaced lava will occur downslope. The flow would be relatively short because volume is exhausted faster as the lava increases in thickness as a result of its internal resistance to flow. For a high slope angle, the lava has a lower critical thickness, no heat loss, and the flow will propagate until volume is exhausted. The same decreasing thickness trend downslope would occur. This high-slope flow would result in a relatively longer length as volume is exhausted due to lower storage capacity of cells.

Effect of Bulk Viscosity on Lava Flow Length

The relationship between bulk viscosity and final lava flow length can be demonstrated using the empirical relationship between effusion rate and final flow length (Eq. 3). This equation can show the effect of changing bulk viscosity on final flow length (Wilson and Head, 1983;

(3) $$L_{fin} = (\alpha^{\frac{2}{3}} E^{\frac{2}{3}} t (\tau\eta)^{\frac{1}{3}})/(24^{\frac{1}{3}} d)$$

Pinkerton and Wilson, 1988). The final length (L_{fin}) of the theoretical lava flows were calculated with the mean gradient (α), mean effusion rate (E), length of time of eruption (t), yield strength (τ), viscosity (η), and mean flow depth (d). Here I set constant values for the slope, volume,

duration, yield strength, and varied the bulk viscosity of the flow. The results indicate that rapidly emplaced lavas on a shallow slope with a lower bulk viscosity will be longer than those flows with a higher bulk viscosity (Fig. 13). This relationship holds true for lower effusion rates and flows on higher slopes. These data the volume-limited mode of emplacement given in Scenario 2 (Fig. 12), and lead to the expectation of a strong coupling between lava flow length and viscosity. I used this demonstration of the viscosity effect on flow length in a volume-limited system as a benchmark for the model outputs, as this relationship clearly demonstrated that lava flows that form on a shallow slope, with different bulk viscosities, will have different final lengths. The low viscosity lava will flow the greatest distance, and the high viscosity lava will flow the least distance.

Constant Viscosity in Volume-Limited Flows

As the effect of the bulk viscosity parameter is the primary focus of this work, a model was developed that can be used to measure the effect of viscosity on the emplacement of these flows. This model isolates the differences in the lava flow length and extent associated with changes to the bulk viscosity. The different emplacement modes for lavas (i.e., volume- or cooling-limited) will also have significant effects on the behavior of the lava. In a volume-limited system, temperature changes will not affect the overall viscosity of the lava because the rapid emplacement causes the lava to behave isothermally. By contrast, emplacement of a cooling-limited system has viscosity changes that correspond to temperature changes within the flow. Once the temperatures of a flow decrease by ~100°C from its initial estimated eruption temperatures, based on laboratory and field measurements (e.g., Diniega et al., 2013), changes in viscosity cause the flow to slow its propagation, until it ceases. With cooling rates of 0.05 – 0.5°C/km (Keszthelyi and Self, 1998; Keszthelyi, et al., 2000), this temperature decrease would have occurred over ~1000 - 1500+ km flow distance, or nearly the full length of the longest

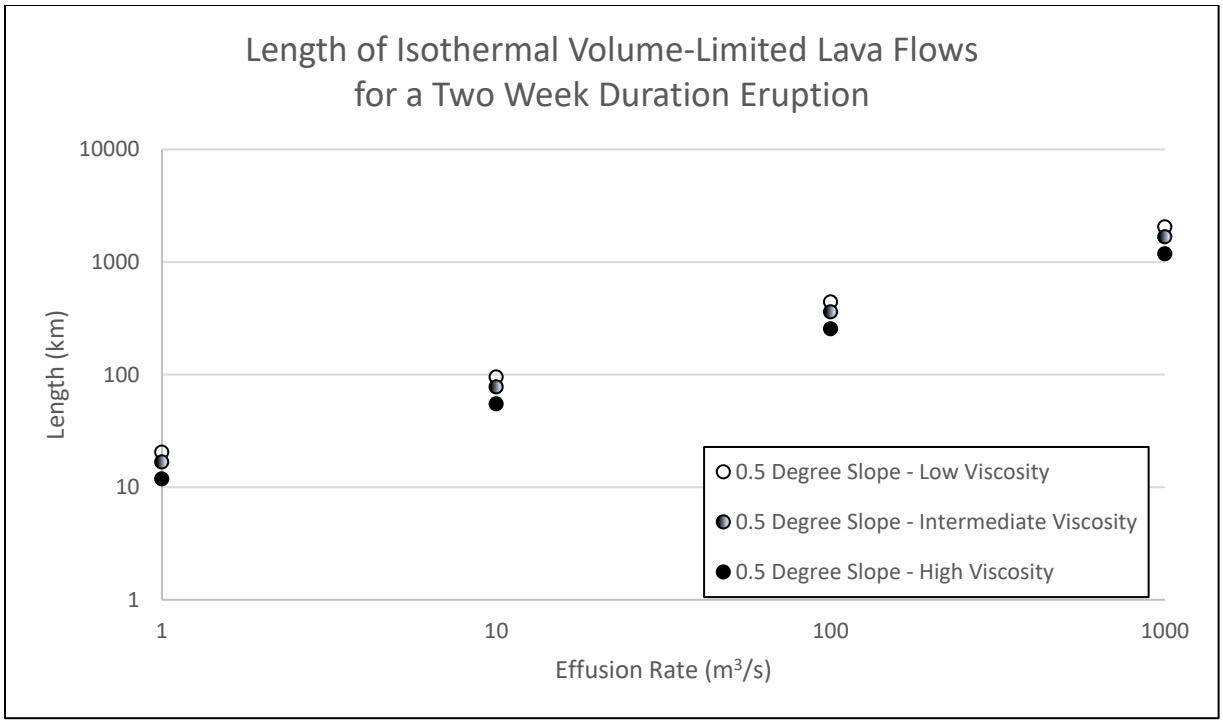

Figure 13. The relationship between effusion rate and final length of a lava flow is affected by the viscosity of the lava. This plot represents the results of Eq. 3, which indicate lava flows with lower overall bulk viscosities will have a greater length than those with higher bulk viscosities.

martian flows being investigated. Therefore, I focused my investigations on the orders-of-magnitude differences in bulk viscosity (e.g., Keszthelyi et al., 2000; Jaeger et al., 2010) in the model explored below.

Spectral Constraints of Bulk Viscosity

Previous investigations of the bulk composition of Mars have suggested that the surface is composed primarily of basalt and andesite (e.g., Bandfield et al., 2000; Wyatt et al., 2001; Hamilton et al., 2001), and range from ultramafic-to-intermediate compositions. The lavas in the Cerberus region have also been previously interpreted as basaltic in composition, based on observations of surface textures, modeling, and spectral data (e.g., Keszthelyi et al., 2004; Vaucher et al., 2009; Jaeger et al., 2010). Few examples of evolved lavas have been identified on Mars, though felsic high-silica compositions have been found, these exposures are both old (pre-Amazonian) and volumetrically rare (e.g., McSween, 2015). Examples of these evolved lavas include dacite, identified in Syrtis Major (Christensen et al., 2005), and volcanic edifices in the Eridania basin which are suggestive of highly viscous lavas (Golder, 2013; Brož et al., 2015). In situ evidence, from browse products for the Compact Reconnaissance Imaging Spectrometer for Mars (CRISM; Murchie et al., 2007; Pelkey et al., 2007), provide a mechanism to interpret the surface composition in the Cerberus region. CRISM is a 15 – 19 m/pixel hyperspectral imager that can be used to investigate surface compositions. Previous investigations over the region using the Dust Cover Index (DCI) derived from the Thermal Emission Spectrometer (TES) 3.5 km/pixel thermal images (Christensen et al., 1992) suggest that the Cerberus region was blanketed in extensive silicate dust (Ruff and Christensen, 2002), which can obscure the underlying rock, preventing spectral analyses of the surface composition.

Several CRISM browse products (Fig. 14) provide full-resolution targeted (FRT) and half-resolution long targeted (HRL) footprints (Murchie et al., 2007) that are not completely

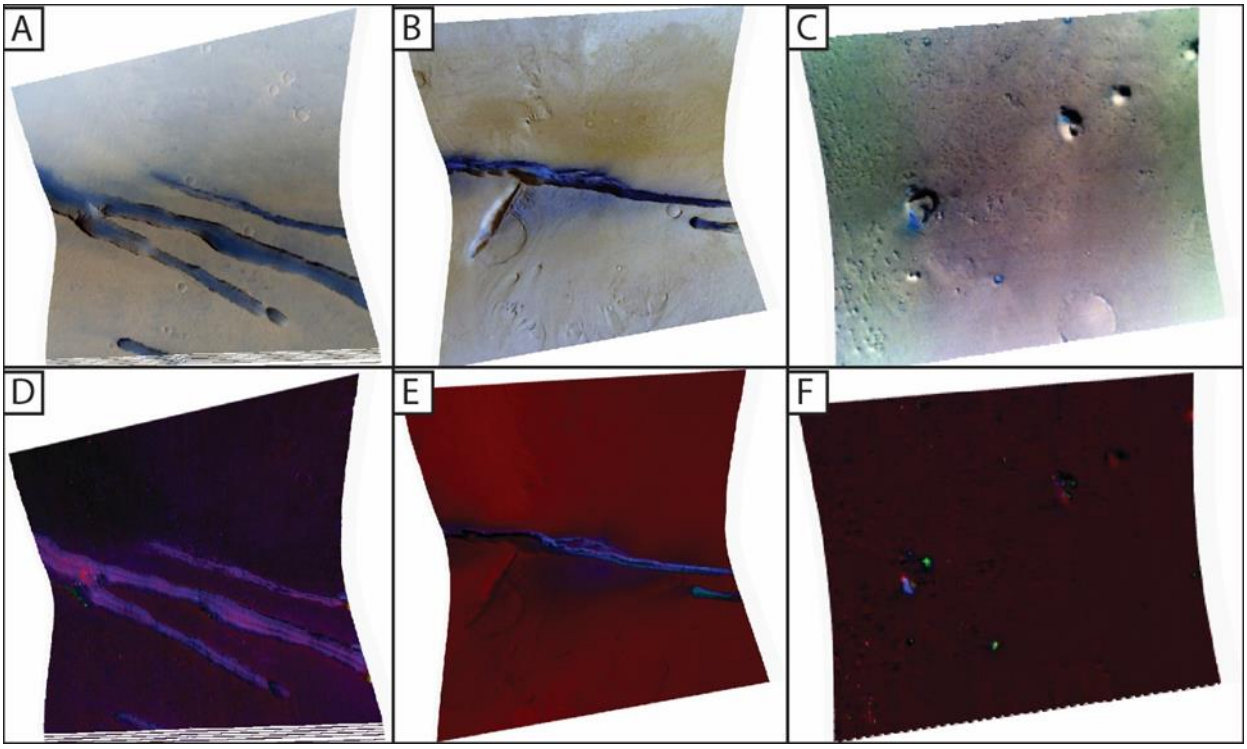

Figure 14. Spectral evidence of volcanic origins identified in CRISM browse products which highlight local mineralogy. A-C: These images are VNIR enhanced color, stretched to highlight the dynamic range of the sites. D-F: These images comprise the RGB combinations that highlight mafic compositions, where red denotes the presence of olivine and Fe-bearing phyllosilicates, blue denotes the presence of low-Ca pyroxene, and green denotes the presence of high-Ca pyroxene. (A,D) CRISM image FRT000251B5. (B,E) CRISM image FRT000091F3. (C,F) CRISM image HRS00013683.

dust covered and display interpretable spectral signatures. One enhanced color image (Fig. 14A) covers a portion of the Athabasca fissure, and the spectral data (Fig. 14D) indicate the presence of olivine and Fe-bearing phyllosilicates as well as low-Ca pyroxene. These minerals suggest a mafic composition for the material that filled Athabasca Valles. A portion of the Grjótá fissure was also imaged (Fig. 14B), and its spectral data (Fig. 14E) indicates the presence of both low and high Ca pyroxenes, which suggest a mafic composition comprising the material that filled Grjótá Valles. The final image (Fig. 14C) covers a medial distance portion of Grjótá Valles, where small craters have excavated through the overlying dust cover and exposed the underlying material (Fig. 14F). Spectral data indicate the presence of high-Ca pyroxene, further suggesting mafic compositions in the region. These inferred compositions are consistent with low viscosity lavas having filled both Athabasca and Grjótá Valles.

Methodology

Investigating the effect of viscosity on terrestrial and martian lava flow length and extent was completed using a three sequential step procedure: (1) mapping the extent of terrestrial analogue sites and using previously mapped extents of martian sites (Golder et al., 2020); (2) modification of a Python ArcGIS CA-based lava flow model to incorporate governing equations (e.g., Navier-Stokes equation of flow) and parameters that affect lava flow length and extent, with an emphasis on viscosity; and (3) application of the model to martian fissure-fed lava flows. Model outputs were analyzed after steps 2 and 3, to calibrate and validate the model, and to determine the effects of the viscosity parameter on the development of extensive lava flows on Mars, respectively (Fig. 15). During the testing of these parameters, identification of non-unique solutions must be considered when evaluating the magnitude of the effect of viscosity in the model.

Figure 15. This flow chart illustrates the progression through all stages of the model development, calibration, validation, application, and evaluation. The preparation of the model included the mapping of all four lava sites, and preconditioning the individual DEMs to remove the average thickness of the lavas. I derived the initial parameter values from literature sources or from the DEMs. These parameters fed into the governing equations of the model. During the calibration stage (red box), I varied the density, viscosity, and yield strength, while keeping all other values constant. These outputs were evaluated using the PLR and fitness function (see Measurement of Model Accuracy section), and the density value that yielded the best fit was used as constant input value in the validation (yellow box) and application (green box) phases. During the validation stage, I held all parameter values constant, except the bulk viscosity and yield strength. The outputs from this stage were evaluated using the PLR and fitness function and the results validated the model. Once validated, I then applied the model to the martian sites, and we varied the bulk viscosity and yield strength values for the simulations that covered both channelized lavas. These results were evaluated using the PLR and fitness function, and the results with the best overall fit for both Athabasca and Grjótá Valles were used to determine the viscosity value(s) that resulted in these long lava flows on Mars. The input parameters related to the viscosity and yield strength were modified for the current version of the model, to reflect the 1-2 orders of magnitude difference in their values, rather than the 1:1 value change that was used in previous versions of the model.

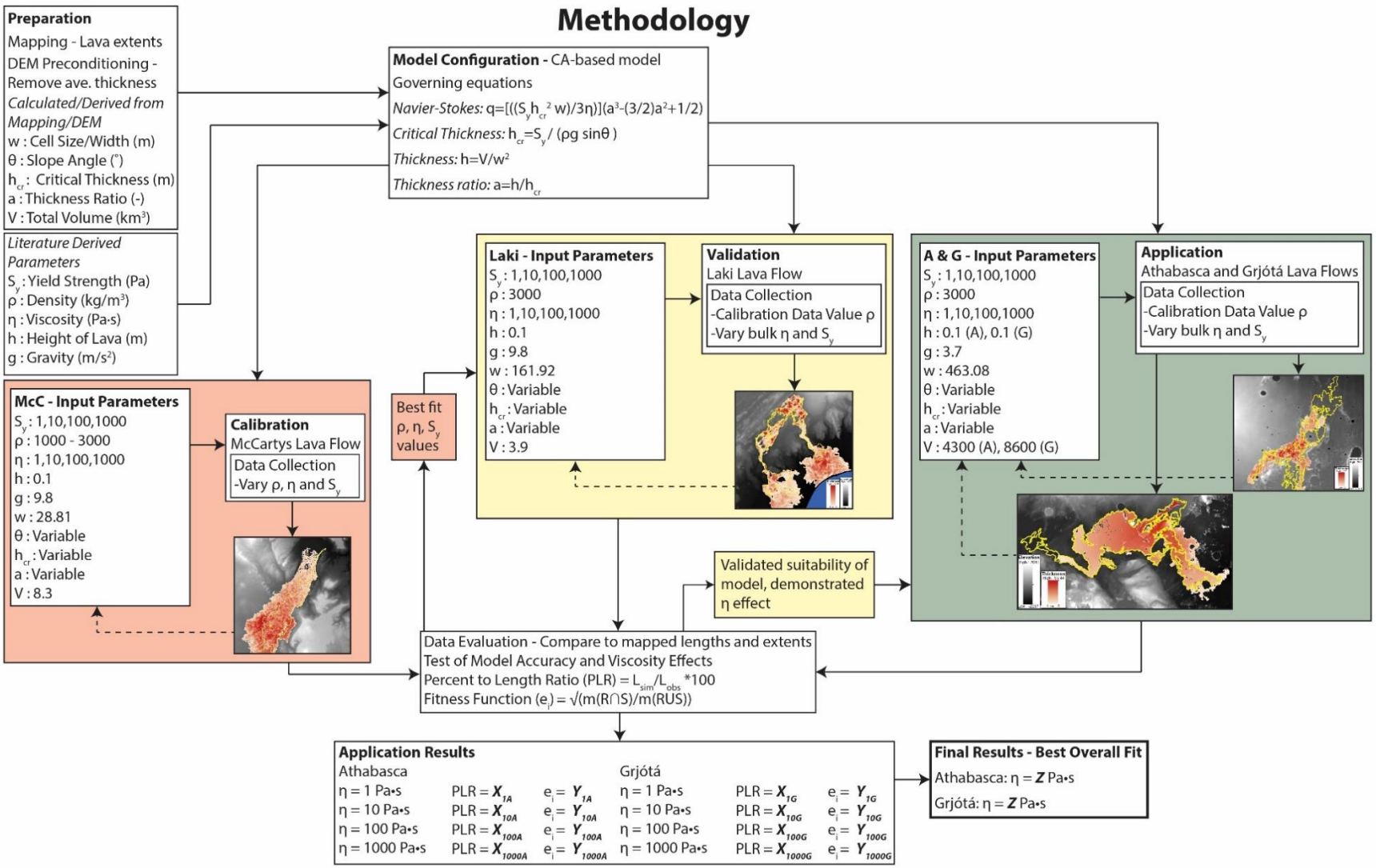
Methodology
Preparation
Mapping - Lava extents
DEM Preconditioning - Remove ave. thickness
Calculated/Derived from Mapping/DEM
w : Cell Size/Width (m)
θ : Slope Angle (°)
h_cr : Critical Thickness (m)
a : Thickness Ratio (-)
V : Total Volume (km³)
Literature Derived Parameters
S_y : Yield Strength (Pa)
ρ : Density (kg/m³)
η : Viscosity (Pa·s)
h : Height of Lava (m)
g : Gravity (m/s²)
Model Configuration - CA-based model
Governing equations
Navier-Stokes: q=[((S_y h_cr² w)/3η)](a³-(3/2)a²+1/2)
Critical Thickness: h_cr=S_y / (ρg sinθ)
Thickness: h=V/w²
Thickness ratio: a=h/h_cr
McC - Input Parameters
S_y : 1,10,100,1000
ρ : 1000 - 3000
η : 1,10,100,1000
h : 0.1
g : 9.8
w : 28.81
θ : Variable
h_cr : Variable
a : Variable
V : 8.3
Calibration
McCartys Lava Flow
Data Collection
-Vary ρ, η and S_y
Best fit ρ, η, S_y values
Laki - Input Parameters
S_y : 1,10,100,1000
ρ : 3000
η : 1,10,100,1000
h : 0.1
g : 9.8
w : 161.92
θ : Variable
h_cr : Variable
a : Variable
V : 3.9
Validation
Laki Lava Flow
Data Collection
-Calibration Data Value ρ
-Vary bulk η and S_y
A & G - Input Parameters
S_y : 1,10,100,1000
ρ : 3000
η : 1,10,100,1000
h : 0.1 (A), 0.1 (G)
g : 3.7
w : 463.08
θ : Variable
h_cr : Variable
a : Variable
V : 4300 (A), 8600 (G)
Application
Athabasca and Grjótá Lava Flows
Data Collection
-Calibration Data Value ρ
-Vary bulk η and S_y
Validated suitability of model, demonstrated η effect
Data Evaluation - Compare to mapped lengths and extents
Test of Model Accuracy and Viscosity Effects
Percent to Length Ratio (PLR) = L_sim/L_obs *100
Fitness Function (e_i) = √(m(R∩S)/m(RUS))
Application Results
Athabasca
η = 1 Pa•s PLR = X_1A e_i = Y_1A
η = 10 Pa•s PLR = X_10A e_i = Y_10A
η = 100 Pa•s PLR = X_100A e_i = Y_100A
η = 1000 Pa•s PLR = X_1000A e_i = Y_1000A
Grjótá
η = 1 Pa•s PLR = X_1G e_i = Y_1G
η = 10 Pa•s PLR = X_10G e_i = Y_10G
η = 100 Pa•s PLR = X_100G e_i = Y_100G
η = 1000 Pa•s PLR = X_1000G e_i = Y_1000G
Final Results - Best Overall Fit
Athabasca: η = Z Pa•s
Grjótá: η = Z Pa•s

As all models are abstractions of reality, the development of this work required multiple evolutions which incorporated successively more accurate lava distribution modes to improve the final outputs. Multiple versions of this lava flow model were developed, initially building upon preexisting models and then significantly modifying them in both ArcGIS ModelBuilder and Python scripts (see Chapter 2 Appendix 1). ModelBuilder was initially used to develop the general model architecture, while Python scripting was used because of its robust nature that could be easily modified to include the governing equations and incorporate loops within the lava distribution modes. Each of the models successfully generates lava flows that distributed lava from their eruption sites and propagated the flow to the point at which the erupted volume was exhausted. These versions are capable of recreating the approximate length and areal extent of the target lava flows. Despite significant simplifications of real-world phenomena, these initial models are useful tools to tease out details concerning the development of lava flows with different emplacement characteristics.

Once these initial simple models for lava distribution were developed, additional model versions could be developed which are more physically realistic and that are able to produce potentially more accurate simulation results. Each model revision led to an increase in both functionality and accuracy of the derived outputs. The development steps outlined above were followed during the development of each iterative version of the model.

There have been six primary evolutions of this model during its development, with multiple modifications made to these primary versions. The results displayed in the following sections of this chapter were derived from Version 5 of the model. The current model, Version 6, is the result of redeveloping Version 5 to better handle flow propagation and issues distributing

excess lava within looped code segments (see Chapter 2 Appendices 2 and 3). All model results in this chapter were derived using Version 5, using DEMs for topographic representation.

Data Sets for Lava Flow Mapping and Lava Modeling

Geological maps of the McCartys and Laki flows (e.g., Ander et al., 1981; Thordarson et al., 2001, respectively) were used as context to map these terrestrial flows. Similarly, mapping by Vaucher et al. (2009), Jaeger et al. (2010), and Hamilton (2013) of lava flows within Athabasca and Grjótá Valles served as the context within which Golder et al. (2020) was done. For the terrestrial analogue flows, visible-wavelength data from Landsat 7 at 30 meters per pixel (mpp; Irish, 2000) were used to map the extent of the McCartys lava flow, and (to avoid excessive cloud cover in the appropriate Landsat 7 data) visible-wavelength data from Landsat 8 at 30 mpp (Roy et al., 2014) to map the Laki lava flow. For martian flows, the previously derived extents of the martian lava flows were used, as mapped by Golder et al. (2020), using visible-wavelength data from a Context Camera (CTX) basemap (cf. Malin et al., 2007). The maximum extent of the lavas was used to define the observed extent of the lava flow and place boundaries for comparison to the simulation outputs. Mapping of the terrestrial lava flows was performed in the ESRI ArcGIS environment at a scale of 1:100K, the same scale previously used for the martian lava flows (Golder et al., 2020). Lava flows were differentiated from surrounding terrain and bordering lava flows based on changes in the surface texture of the flows, as well as superposition, embayment, onlapping, cross-cutting and local topographic relationships, which distinguished the flow margins (see Golder et al., 2020, Fig. 2). Within the Cerberus region, Marte Vallis flows were excluded from this study because its surface source is obscured (Burr et al., 2002b; Plescia, 2003; Vaucher et al., 2009: Golder et al., 2020), which prohibited mapping the accurate extent of the lava flows

in the context of their eruption site, thereby not providing critical data required for modeling lava distribution into this channel.

Topographic data were used as the base on which simulations were performed. For the McCartys flow, topographic data was from the Advanced Spaceborne Thermal Emission and Reflection Radiometer (ASTER) digital elevation model (DEM) with 30 mpp horizontal resolution (Yamaguchi et al., 1998; Tighe and Chamberlain, 2009). For the Laki flow, topographic data was extracted from a 161 mpp GMTED2010 image mosaic (Danielson and Gesch, 2011). Topographic data for the martian lava flows were extracted from the Mars Orbiter Laser Altimeter (MOLA) 463 mpp horizontal resolution gridded mosaic (Smith et al., 2001).

Lava Flow Modeling using Cellular Automata

Numerical modeling has been widely used to study pathways and extents of lava flows during emplacement and the effect of various parameters on the flow dimensions (e.g., Ratto et al., 2001; Bilotta et al., 2012), to provide hazard assessments (e.g., Felpeto et al., 2001, 2007; Vicari et al., 2007; Gislason, 2013), and to infer surface modification processes and emplacement conditions of ancient lava flows on planetary bodies (e.g., Keszthelyi et al., 1998; Harris and Rowland 2001; Howard, 2007). With knowledge of the fundamental physical properties of terrestrial lavas (cf., Griffiths, 2000; Harris, 2013), the known flow margins of terrestrial (e.g., Ander et al., 1981; Thordarson et al., 2001) and martian environments (Vaucher et al., 2009; Jaeger et al., 2010; Hamilton, 2013; Golder et al., 2020), and the governing equations for flowing lava (e.g., Dragoni, 1986; Ishihara et al., 1990; Keszthelyi and Self, 1998; Griffiths, 2000; Harris, 2013), this work developed a model to investigate the magnitude of the effect of various parameters (i.e., viscosity) on the emplacement of areally extensive lava flows on both Earth and Mars.

Inverse modeling is the primary route taken where the goal is the reproduction of observed data. With inverse modeling, a calibrated model is used in the determination of the initial input parameters (e.g., Parker, 1977; Connor and Connor, 2006). An inverse-modeling approach is also helpful to determine the effect of these parameters on the lava flow emplacement. This approach allows for simulation of lava flows to constrain emplacement conditions, which is particularly useful when only observational evidence (e.g., remotely sensed planetary data) of the lava flow is available. In particular, I seek to determine the bulk viscosity value of the martian lava flows during their initial emplacement, to infer how Mars was capable of generating geologically young magmas that sourced voluminous eruptions at the surface.

Cellular automata (CA)-based models can be used to define a system and simulate lava flow propagation that includes governing equations, such as the Navier-Stokes equation of flow (e.g., Ishihara et al., 1990; Vicari et al., 2007; Harris, 2013), which control the behavior of the flow during the simulation. CA-based models allow for the simplification of differential equations, resulting in less computationally intensive simulations while still producing outputs comparable to differential-equation based models (e.g., Schiff, 2001). The use of simplified equations in this type of parametric model allows the input of user-defined parameter values within the governing equations (Eq. 4–6), which are then used to investigate various bulk viscosities and test their effect on lava flow emplacement. This type of model can be further simplified, beyond the differential equations, by making use of constant values for parameters that would naturally vary in a complex, evolving system (e.g., composition, density, thermal properties). A CA-based model that incorporates each of these components can be used to reproduce the extent of observed lava flows by calculating the volume of lava that can be distributed to surrounding cells, based on the topography and the lava conditions (Fig. 16).

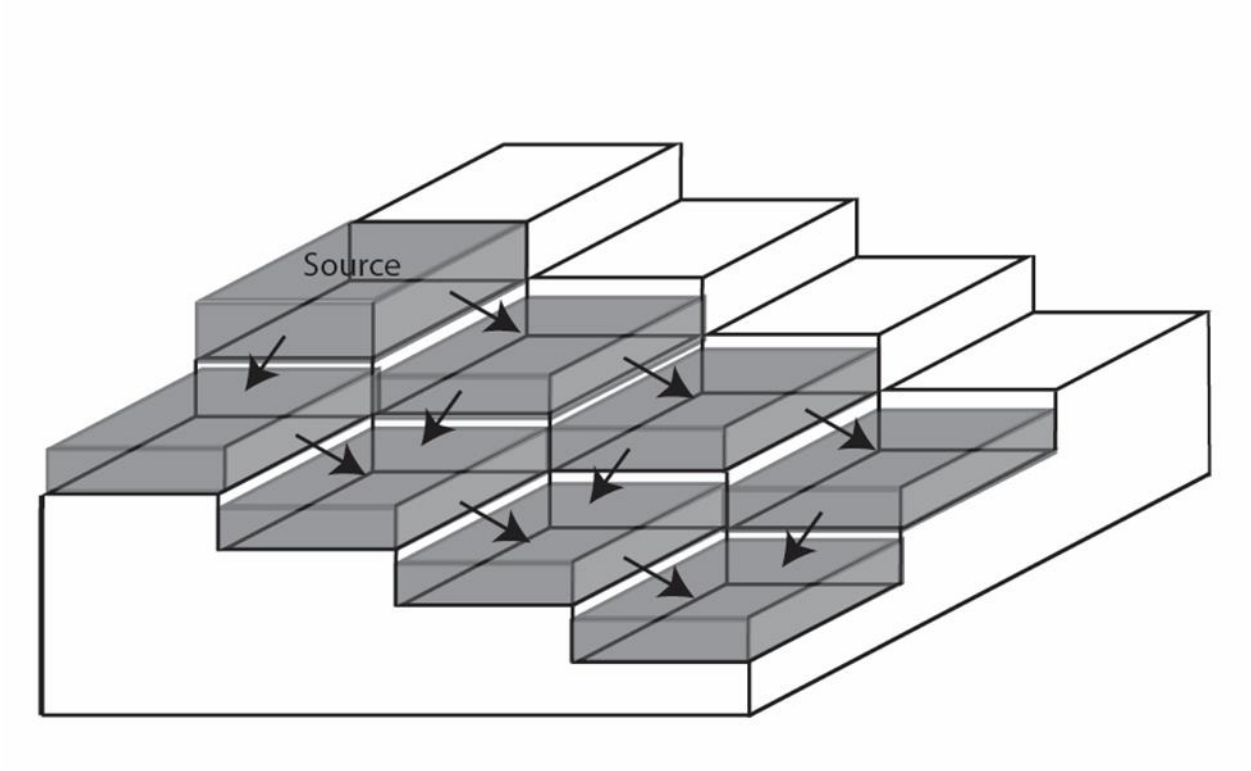

Figure 16. Schematic of a CA-model, illustrating the spread of lava from a source vent/fissure to the surrounding terrain (after Ishihara et al., 1990; Harris, 2013).

Governing Equations

The following equations (e.g., Ishihara et al., 1990; Vicari et al., 2007; Harris, 2013) were incorporated into the model to allow lava to propagate from the source into the surrounding cells. The Navier-Stokes equation for steady state flow (Eq. 4) describes the flux (q) of lava from the processing cell into neighboring cells. The flux is governed by the yield strength (S_y), critical thickness (h_{cr}) and viscosity (η) of the lava, the area of the processing cell (w), and the ratio between h and h_{cr} (a).

(4) $$q = \left[\left(\frac{S_y h_{cr}^2 w}{3\eta}\right)\right]\left(a^3 - \left(\frac{3}{2}\right)a^2 + \frac{1}{2}\right)$$

The critical thickness (h_{cr}) of the lava within the processing cell (Eq. 5) is a value that must be exceeded to allow flow to propagate into neighboring cells. The h_{cr} is governed by the yield strength (S_y) and density (ρ) of the lava, the planetary gravity (g), and regional slope (Θ). The lava flow thickness at the processing cell, released as a pulse of new lava volume at the beginning of each iteration, was set at a constant value, typically 1 m, and governs the total available volume of lava that can be propagated into the neighboring cells.

(5) $$h_{cr} = \frac{S_y}{\rho g \sin\theta}$$

The ratio (Eq. 6) of the thickness of the lava within the processing cell (h) and the critical thickness (h_{cr}) is a component of solving the Navier-Stokes equation.

(6) $$a = \frac{h}{h_{cr}}$$

Model Architecture

A variety of CA models were investigated to determine whether they could be used as either a framework upon which to build a new lava flow model or could be modified to incorporate the appropriate governing equations. These models included the Volcanic Risk

Information System (VORIS; Felpeto et al., 2001, 2007), MARSSIM (Howard, 2007), MAGFLOW (Vicari et al., 2007), and Growing Volcano (Mehta, 2008). VORIS and MARSSIM are heuristic models that use a probability of flow function based on topography (Felpeto et al., 2001; Howard et al., 2007), but lack the numerous physical parameters that can affect the flow of lava and its final extent. MAGFLOW is proprietary and access to the code is restricted, and therefore cannot be used as a basis from which to build a new model to investigate terrestrial and martian lava flows. The Growing Volcano is a parametric model that uses topography as a base for simulating the growth of volcanic edifices (Mehta, 2008). This model contains a filament-like distribution system that is a single processing cell wide, and exhausts the volume of lava during each iteration by flowing to its maximum lateral extent (100-1000+ km). This distribution method could not realistically reproduce lava flows, as the accumulation of the filaments into a cohesive lava flow does not adequately reproduce how a lava flow spreads across a surface.

The model developed during this investigation, the LArge-scale Volcanic Area Simulator (LAVAS), is a CA-based model that governs the spread of lava from cell-to-cell from a source vent or fissure (Fig. 16). For this simplified CA model, an inverse-modeling approach was used to determine the parameter values that result in a reasonable reproduction of the observed lava flows. This model is based on a CA model programed in Python that generates lava flows that spread over a surface in a relatively realistic manner (Gislason, 2013). The Gislason (2013) model served as the framework in the initial development of this model, which was then modified to incorporate governing equations of flow propagation (Eq. 4–6) and to accept both point and linear features as eruption sources (see Chapter 2 Appendices 1 and 3, for complete model scripts of Version 5 and Version 6, respectively). Modifications also resulted in differences of how the lava is distributed from cell-to-cell and how much lava accumulates in the

cells, based on the critical thickness (Eq. 5) of the lava and the maximum storage capacity of each cell. Lava is added to the source at the beginning of each iteration, and any given cell is filled to its specific critical thickness. That critical thickness of lava must be reached prior to the distribution of lava to any adjacent cells. Once the lava has exceeded the critical thickness of the source location, the local neighborhood is determined. Excess lava from the source is then distributed to the neighboring cells. The lava fills the neighboring cells to their individual critical thickness values, and any lava volume that remains is then distributed to additional neighboring cells prior to any further lava being added at the source location. All lava eruptions are treated as volume-limited, isothermal fluids. A total model volume for the eruption is set for the simulation, based on the average thickness of observed lava flows and their areal extents. The model progresses sequentially through each step, then loops through the sequence until the total erupted volume has been reached (Fig. 17).

Model Inputs and Preconditioning

Input for the model (Version 5) include DEMs of the regional topography for the terrestrial and martian flows of interest. Regional DEMs also include surrounding terrain to permit model outputs that exceed the boundaries of the actual lava flows. Point and line feature files were converted to rasters with the corresponding elevation data and were used as the input for the location of the vent or fissure source for the lava flows. The original DEMs of each surface retains the full areal extent and the approximate thicknesses (10-30 m) of the lava flows (Table 2; e.g., Ander et al., 1981; Thordarson et al., 2001; Keszthelyi et al., 2004; Burr and Parker, 2006; Vaucher et al., 2009; Jaeger et al., 2010; Bleacher et al., 2010).

The regional DEMs required preconditioning to remove the lava from the preexisting surface to recreate an approximation of the pre-flow topography. Preconditioning of the terrestrial

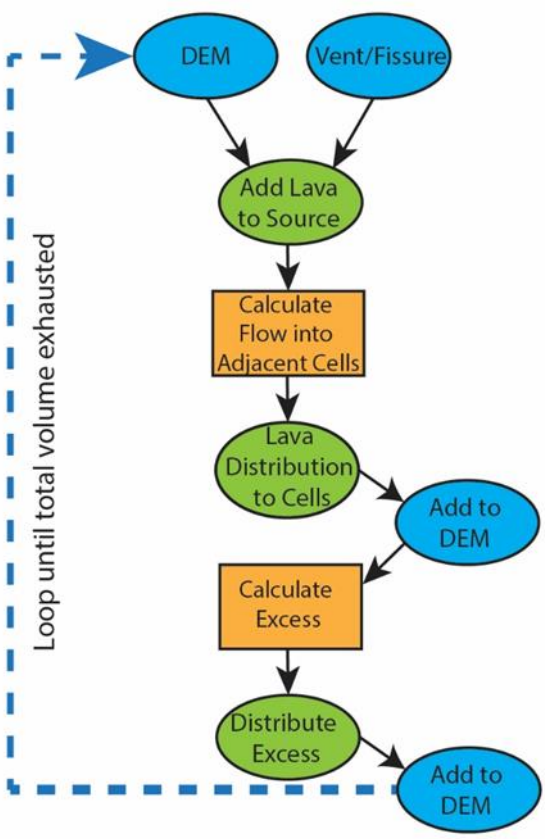

Figure 17. Simplified schematic of model architecture. Lava is erupted from the vent or fissure and added at the source. The flow into adjacent cells is calculated and then distributed to these cells. Once the initial distribution is completed, if any volume from that iteration remains, the amount of excess lava is calculated and then distributed to the next adjacent cells. Once the full volume of each iteration has been distributed, the model loops back to the beginning, to distribute the next pulse of lava along the flow pathway. (Blue ovals denote model inputs, green ovals denote a process, and orange rectangles denote a calculation).

and martian DEMs involved the subtraction of a slab of material from the mapped flow region that corresponds to the average thickness for each preexisting lava flow from the DEM (Table 5). None of the observed flows are completely flat, or of a constant thickness, nor is the underlying topography. Removal of a constant thickness slab of material from any of these four flows, which corresponds to previously measured average flow thicknesses (e.g., Nichols, 1946; Thordarson and Self., 1993; Ander et al., 1981; Crumpler and Aubele, 2001; Zimbelman and Johnston, 2002; Burr and Parker, 2006; Vaucher et al., 2009; Jaeger et al., 2010), can be considered to reasonably approximate the pre-flow surfaces.

Model Parameter Values

The initial values for the density, yield strength, viscosity, height of the lava, and planetary gravity were derived from the literature, whereas the values for the cell size, slope angle, critical thickness, thickness ratio, and total volume were either extracted from the DEM, derived from the mapped extents, or calculated using these data (Fig. 15, Table 5). A constant value of 1 m for the thickness of the lava was used for each eruption pulse, representing the volume erupted from the source site at the beginning of each iteration. Values for lava thickness ranged from 0.1-10 m during testing, which allowed modification of the erupted volume as each model loop commenced. The values for the cell size and total volume differ between the terrestrial and martian flows but are constant within the framework of the modeling of each individual flow. The total erupted volume of each lava flow was approximated based on their areal extent and the average thickness of each flow (Fig. 15, Table 5). The total number of iterations for each simulation was determined by the total volume and the number of pulses that would be required to erupt specific volumes.

The initial literature-derived density values encompass varied lava compositions and span a range from 850-2820 kg/m^3 (Harris, 2000; Greeley et al., 2005; Vicari et al., 2007; Del Negro

Table 5. Parameters used in the model calculations during the calibration, validation, and application stages. The initial calibration values used constant values for the McCartys cell size, viscosity that corresponded to an ultramafic composition, Earth's gravity, and volume. I used different density and yield strength values in each simulation run during calibration until I identified the model output with the best fit to the observed extent and length of the McCartys lava flow. I narrowed down the final values for density and yield strength during that calibration process and identified a final density of 3000 kg/m3 and yield strength of 1 Pa, that combined with the constant values of the other parameters, resulted in the best fit. These density and yield strength values were used in the validation and application processes along with the flow specific values inserted for thickness, cell size, planetary gravity, and total volume. M denotes the McCartys flow, L denotes Laki, A and G represent Athabasca and Grjótá, respectively.

Parameter	Symbol	Units	Initial Calibration Values	Calibration References	Final Values	Validation/Application References
Density	ρ	kg/m^3	2600 2820 2700 2600 850-2300 1000-3000	Harris, 2000 Greeley et al., 2005 Vicari et al., 2007 Del Negro et al., 2008 Jaeger et al., 2010	1000 1500 2000 2500 3000	Calibration Result
Yield Strength	S_y	Pa	10^3-10^6 10^{-3}-10^4	Ishihara et al., 1990 Harris, 2000	0.01 0.1 1 10 100	Ishihara et al., 1990 Harris, 2000
Ave. Thickness		m	10 - M	Nichols, 1946; Ander et al., 1981; Crumpler and Aubele, 2001; Zimbelman and Johnston, 2002	15 - L 20 - A 30 - G	Thordarson and Self, 1993; Thordarson et al., 2001 Vaucher et al., 2009; Jaeger et al., 2010 Burr and Parker, 2006
Height of Lava	h	m	0.1-10	Pulse thickness during eruption	1	Calibration Results
Critical Thickness	h_{cr}	m	Variable	Calculated	Variable	Calculated
Thickness Ratio	a	-	Variable	Calculated	Variable	Calculated
Cell Size/Width	w	m	1 (standard) 28.81 - M	Horizontal Plain Yamaguchi et al., 1998; Tighe and Chamberlain, 2009	161.92-L 463.08-A,G	Danielson and Gesch, 2011 Smith et al., 2001
Viscosity	η	Pa·s	1 10 100 1000		1 10 100 1000	e.g., Keszthelyi et al., 2000
Gravity	g	m/s^2	9.8 - Earth		9.8 - Earth 3.7 - Mars	
Slope Angle	θ		0.05 at 0º Variable		0.05 at 0º Variable	
Volume	V	km^3	2 - M	Calculated from ave. thickness and mapped area.	9 - L 4300 - A 8600 - G	Calculated from ave. thickness and mapped area.

et al., 2008; Jaeger et al., 2010). The model permits density values of 1000, 1500, 2000, 2500, and 3000 kg/m^3 to approximate the wide range of possible densities. Initial testing used a density value of 2700 kg/m^3, a typical density of terrestrial basaltic lavas (e.g., Vicari et al., 2007). During the calibration stage, I identified a final value of 3000 kg/m^3 for the density parameter coupled with varying yield strength and viscosity values led to the best model fits.

The yield strength in the critical thickness equation was modified with each change to the viscosity parameter. The initial yield strength values span a range from 10^{-3} – 10^6 Pa (Ishihara et al., 1990; Harris, 2000). During development, testing, and implementation of the model (through Version 5) the yield strength in the critical thickness equation was changed 1:1 with the viscosity parameter (e.g., η = 10 and *Sy* =10), because of the dependent nature of their change in behavior in a natural system. Another aspect of the yield strength modification that arose between simulations was the fact that any viscosity and yield strength parameter combination that had the same bulk density value would result in the same critical thickness values. This would ultimately be problematic when considering similar parameter combinations, as the output results wound up being nearly identical, but is emblematic of the potential for non-unique solutions to different parameter combinations.

An issue that arose in the ArcGIS environment resulted from the moving window average method of slope calculation, using a 3 x 3 window size. This issue resulted in the overall suppression of the derived slope values for every cell, which typically returned slope values approximately 50% lower than the slope values that would be derived from individually calculating them on a cell-by-cell basis. Calculating the slope relationship between each cell on an individual basis was not feasible, because the slope relationship would differ from multiple adjacent cells. Therefore, any critical thickness values calculated using these derived slope

values are not representative of the true critical thickness values for the actual surface. These lower slope values led to a corresponding increase in the critical thickness values for each cell and a subsequent increase in the thickness of the simulated lava flow. The average method provides a reasonable approximation of the slope between cells across the entire surface, but its ultimate effect on the overall thickness of the simulated flows must be taken into consideration when judging the overall accuracy of the model.

The cell-to-cell slope relationship was then used to calculate the critical thickness of each cell utilizing the variable slope values for the surface. One critical aspect of the horizontal plain model version was the need to set a constant value for the cells that neighbor the central processing vent, and then continuing this trend for all subsequent calculations of the focal neighborhood. This action was taken to ensure that all cells were properly filled to the lowest critical thickness value of each focal neighborhood, which would then allow lava to flow into neighboring cells that would be downslope of the vent. Changes in the distributed thickness of lava and varying slope relationship, particularly the development of very low slope angles once lava had been distributed into the cells bordering the vent location, which resulted in some subsequent neighborhoods with higher critical thickness values than the previous, inner neighborhood. These higher critical thickness values necessitated back-filling of the cells that had previously had lava distributed into them. This step was necessary to allow further propagation of flow. This method of critical thickness calculation and distribution has been modified in Version 6 of the model to remove this artificial critical thickness restriction, and allows for the cells to more naturally fill to their maximum critical thickness, depending on the erupted volume and the actual underlying topography. Once each of those cells has been filled to

their maximum critical thickness values, then flow can propagate to surrounding cells that can accept additional flow volume.

The cell size for each simulation was varied to reflect the resolution of the underlying DEM, with the basic horizontal plain having a cell size equal to 1 m, the McCartys DEM cell size equal to 28.81 m, the Laki cell size equal to 161.92 m, and the Athabasca and Grjótá cell size equal to 463.08 m. I adjusted the planetary gravity within the model based on whether the flow was terrestrial (9.8 m/s^2) or martian (3.7 m/s^2).

Model Calibration and Validation

Calibration of the model consisted of adjusting the model parameters until the accuracy of the model outputs reasonably approximated the extent and length of the McCartys flow, my terrestrial test lava flow. Once the initial calibration of the model was completed, the next step was validation of the functionality of the model. Validating the model involved applying the model to the Laki lava flow, which demonstrated that the model could reproduce lava flows sourced from either a fissure or a single vent, and demonstrated that the model produced differences in areal extent and length as the bulk viscosity changed.

Measurement of Model Accuracy

In the model calibration, two methods were used to quantify the agreement between the observed lava flows and the model outputs, the Percent-to-Length ratio (PLR) and the fitness function (e_i). The PLR (Eq. 7) quantifies the accuracy of the final model length compared to the observed length, where L_{sim} is the length of the model output and L_{obs} is the length of the observed flow (Proietti et al., 2009).

(7) $$PLR = \frac{L_{sim}}{L_{obs}} * 100 ,$$

A perfect PLR fit value would equal 100, an underestimate of length would be any value below 100, and an overestimate of length would be any value above 100. For the length measurement inputs for Eq. 7, the lengths of the observed and modeled lava flows were measured from the origin point of the lava, either at the vent or a set point along the fissure, to the farthest edge of the flow lobe(s). This measurement was performed five times for each flow then averaged those values, using the average length of the observed and modeled lava flow to determine the PLR.

The fitness function (Eq. 8) measures the accuracy of the area of the model output compared to the observed flow, as the m(R∩S) is the measure of the intersection, or overlap between R and S, which are the areas affected by the observed and simulated events, respectively, and m(R∪S) is the union, or total combined area of the simulated and observed flow (Spataro et al., 2004; Proietti et al., 2009).

(8) $$e_i = \sqrt{\left(\frac{m(R \cap S)}{m(R \cup S)}\right)}.$$

A perfect fitness function fit value would equal 1.0, and any value below 1 would denote some combination of under- and over-estimation of the total area of the flow. The areal extent of the lavas was extracted using the mapped extent of each flow and simulation to determine the best fit derived from this model. First, I used the mapped flows as a mask to extract the total number of pixels from the original DEM, for a baseline flow area from which to compare the simulation results. I then added to the ArcGIS project the simulation output layer that contained the total number of pixels that represented the simulated flow area. Using the mapped extent as a mask, I extracted the overlap between the simulation and mapped extents. Performing this function provided the total number of non-zero value pixels that either intersected or fell outside the boundaries of the mapped region. These values were used in Eq. 8 to calculate the fitness function.

Calibration and Validation using Terrestrial Analogues Sites

In testing the accuracy of the model, for both the calibration and validation stages, the mapped extent of the lava flows was used to define the geospatial boundaries that the lava flow simulations must approximate. Both the fitness function (e_i) and Percent-to-Length Ratio (PLR) were used to evaluate how well the areal extent and length of the model outputs agreed with that of the observed lava flows during the calibration and validation processes (Eq. 7–8; Spataro et al., 2004; Proietti et al., 2009). The fitness function and PLR values are a quantification of the accuracy of the model outputs, but these values change based on the viscosity values. Therefore, the fitness function and PLR values are only used to compare the results of each simulation of a single site. Fitness function values from previous modeling of terrestrial lava flows ranged from ~0.5–0.8, with the majority of the values sitting between 0.6–0.7 (Spataro et al., 2004; Proietti et al., 2009). PLR values from previous modeling of terrestrial lava flows ranged from ~70–210, with the majority of the values sitting between 80–120 (Proietti et al., 2009). The fitness function values were compared from each simulation of a target site to determine which produced the best result. A minimum or maximum PLR value was not set, as that relationship highlights the comparative length of the simulation outputs to the observed lava flows.

The model was calibrated by adjusting the initial variable parameter values for density, yield strength, and viscosity (ρ, Sy, η) and running successive simulations to identify a parameter combination that was capable of reasonably reproducing the McCartys lava flow (Fig. 18). A simplified range of 1000, 2000, 2700, and 3000 kg/m^3 was used to approximate the range of density values, without requiring an investigation of each individual value. 2700 kg/m^3 was also chosen for investigation, as it represents an approximately average value of a terrestrial basaltic lava (Vicari et al., 2007). 3000 kg/m^3 is outside of the general density range of viscosity, and was used to the sake of simplifying the parameter space during the development of this model. A

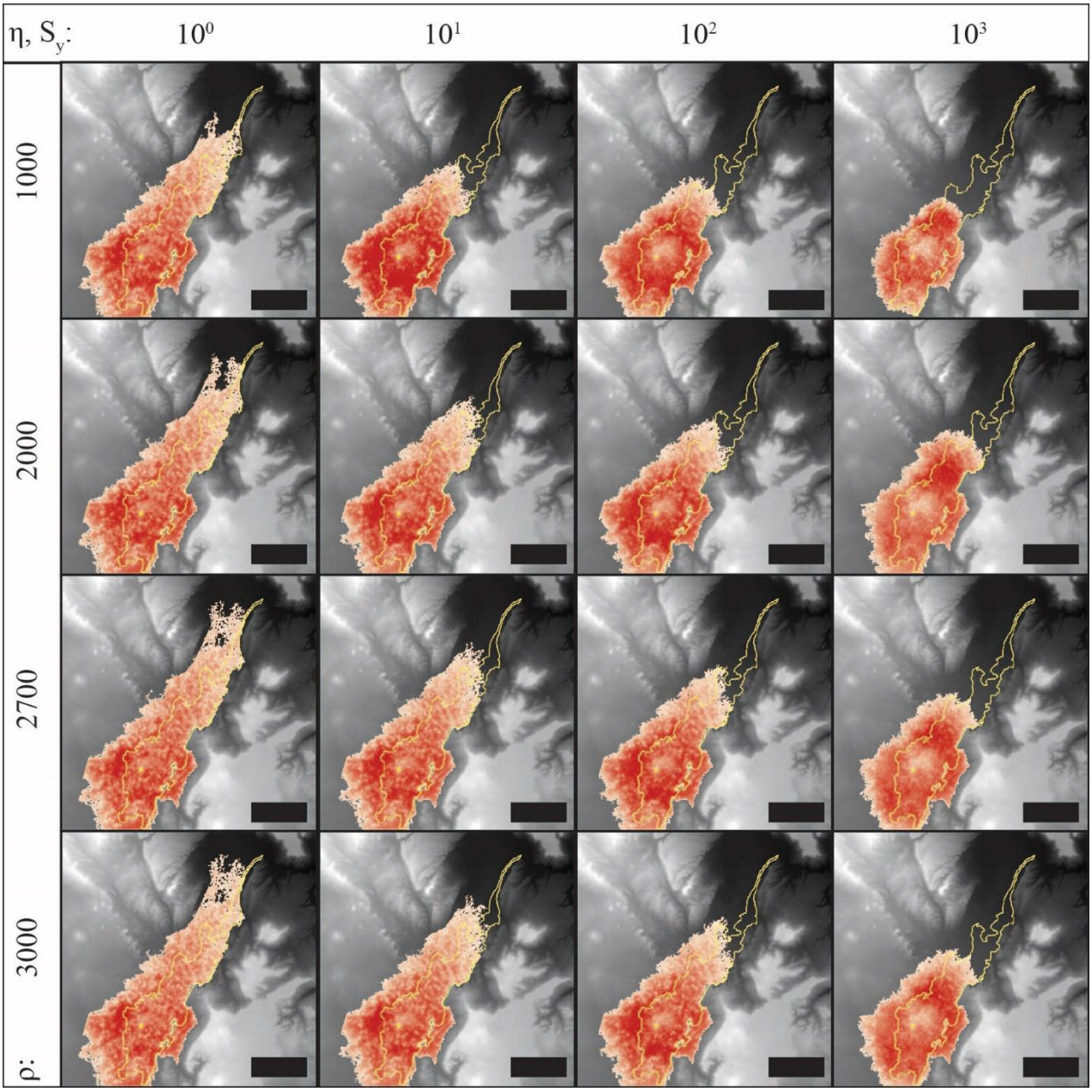

Figure 18. Model outputs from the calibration of the model. The full extent of the McCartys lava flow is given with the yellow outline, and the source vent location is denoted by the yellow star. Each image stamp represents the individual model outputs for the parameter combinations of different densities (ρ, kg/m^3) viscosities (η, Pa) and yield strengths (Sy, Pa·s). Black scale bars represent 10 km.

corresponding range of yield strength to viscosity (Table 5), from 1–1000 Pa·s/Pa, was used during this stage. Simulations were run at a constant density (e.g., 1000, 2000, 2700, 3000) and the yield strength and viscosity were varied together (e.g., 1, 10, 100, 1000). At each of these stages the fit of the model was checked to see the extent to which toe model variables were affecting the replication of known flow morphologies. Values of ρ equal to 3000 kg/m^3, η equal to 1 Pa·s, and *Sy* equal to 1 Pa (Fig. 18, Table 6) resulted in the best approximation of the McCarty lava flow (Fig. 19), based on the PLR and fitness function fits. These parameter values resulted in the best fitness function value (= 0.677), and the best PLR value (= 93.46) (Table 6). This density value was then chosen to represent the bulk density of a basaltic lava based on these calibration results, and was subsequently used during the validation stage of the model for both terrestrial and martian lava flows. Overall, the fitness function values varied by only ~1– 2% between the various parameter combinations for the McCartys flow. These minor fluctuations resulted from the lateral spread of the lava when using low viscosity values; the lava had a more restricted lateral extent and greater vertical thickness with higher viscosity values.

During the validation of the model on the Laki flow, a constant value of 3000 kg/m^3 was used for ρ while varying the η and *Sy* parameters from 1–1000, respectively. The best fitness function value was 0.71 (Fig. 19), corresponding to the 10 Pa/Pa·s parameter values. The best PLR value for Lobe 1 (= 95.56) of the Laki flow came from the 10 Pa/Pa·s run of the model, while the best PLR value for Lobe2 (= 106.71) came from the 1 Pa/Pa·s run of the model (Fig. 20). The fitness function and PLR values derived from the calibration and validation portions of this work suggests the model is capable of producing representations of the observed lava flows to an acceptable degree for the purposes of comparing the effect of bulk viscosity. The thickness of the lava flow increased with increasing viscosity for both terrestrial lava flows, as anticipated.

Table 6. Derived fitness function (e_i) and Percent to Length (PLR) values for the calibration performed on the McCartys lava flow. Each parameter combination resulted in varying fitness function and PLR values. Ultimately, the best fitness function value was achieved using a density of 3000 kg/m^3, yield strength of 1 Pa and, viscosity of 1 Pa·s (bolded values). The fitness function values fall within the range of those values previously derived from the modeling of lava flows with a similar CA-based model (e.g., Spataro et al., 2004; Proietti et al., 2009) The PLR value was a close match to the observed lava flow length, with the best results achieved in the 1 Pa yield strength and 1 Pa·s viscosity simulation regime.

η (Pa·s) & Sy (Pa) →	**1**	**10**	**100**	**1000**
ρ (kg/m^3) ↓				
3000				
PLR:	**93.46**	71.46	61.50	43.75
e_i:	**0.677**	0.651	0.644	0.648
h_{max}:	**45.15**	48.75	52.14	61.76
2700				
PLR:	91.96	70.31	59.50	43.71
e_i:	0.659	0.647	0.650	0.648
h_{max}:	44.11	48.24	50.40	59.59
2000				
PLR:	90.99	66.61	53.61	46.70
e_i:	0.644	0.649	0.642	0.650
h_{max}:	45.29	48.01	53.43	61.25
1000				
PLR:	82.69	53.70	44.83	33.32
e_i:	0.642	0.647	0.651	0.648
h_{max}:	46.14	53.43	55.96	61.77

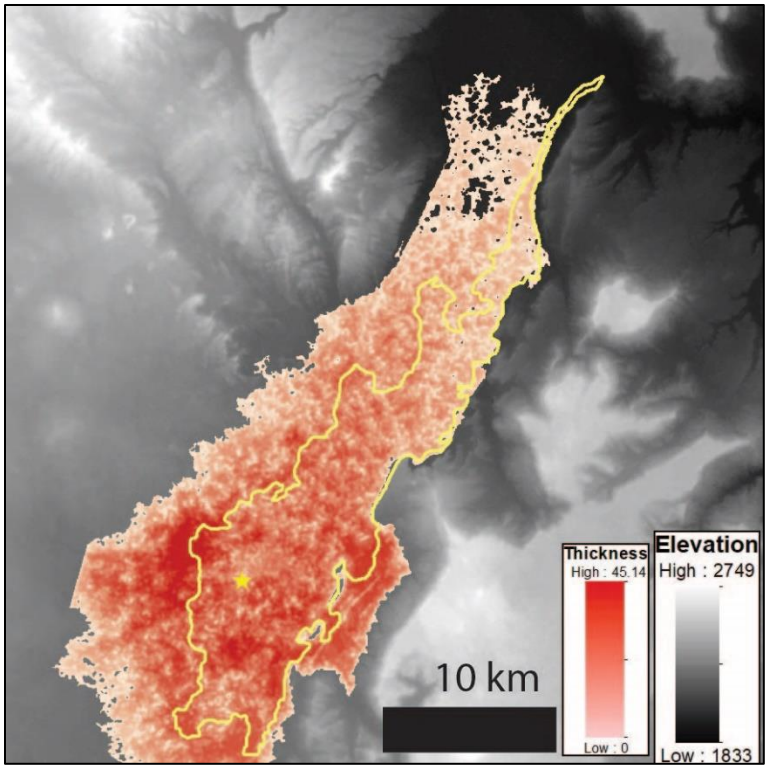

Figure 19. Model output from the calibration stage on the McCartys flow, with the parameter combination (ρ = 3000, Sy = 1, η = 1) that resulted in the best fit (PLR = 93.46, e_i = 0.677) with red-gradient-scale overlay representing the modeled lava flow on the topographic map of the region.

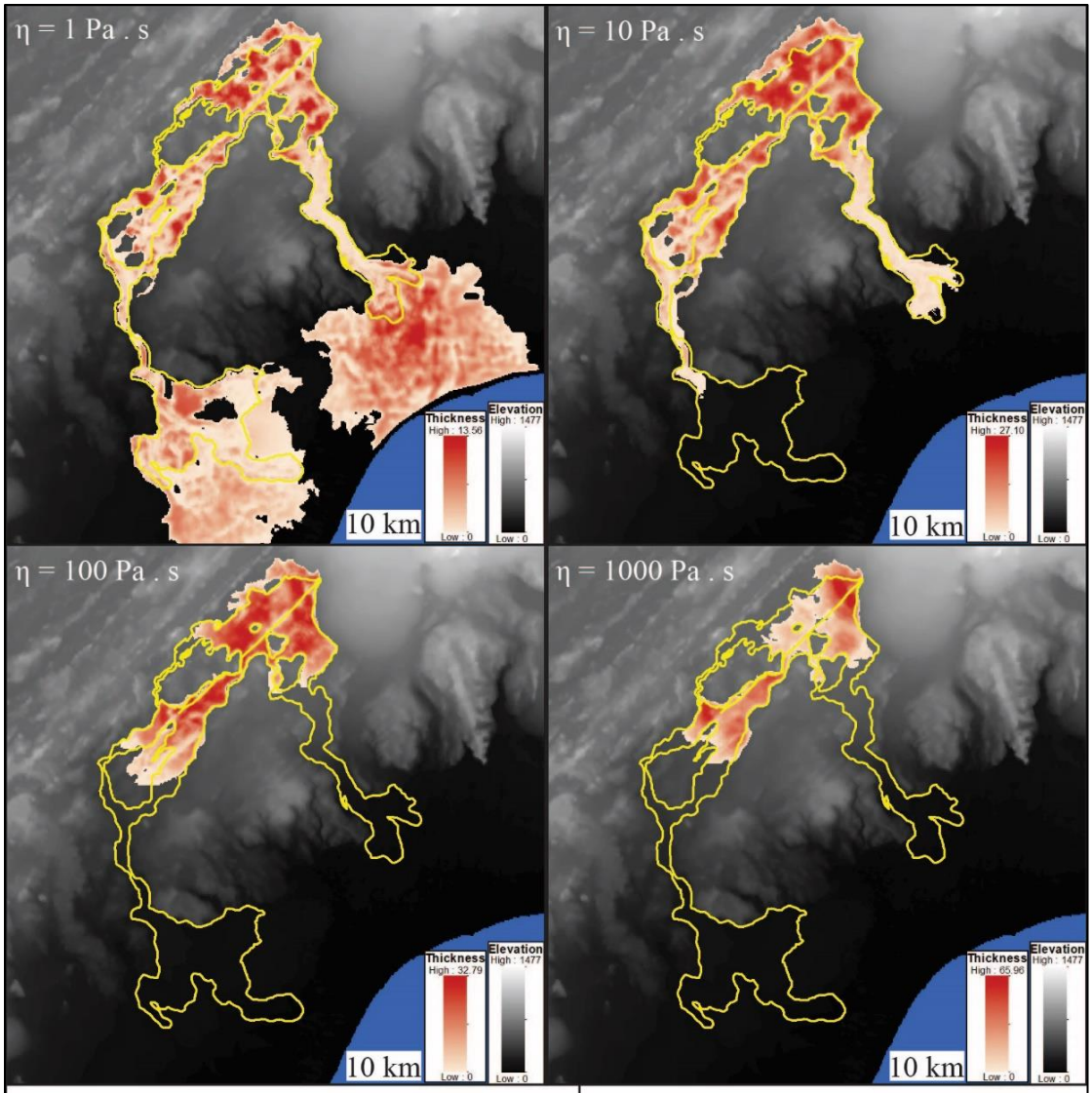

Fitness function and PLR values

η, S_y	e_i	PLR Lobe 1	PLR Lobe 2	h_{max}
1 Pa · s	0.61	137.02	106.71	13.56
10 Pa · s	0.71	95.56	61.96	27.10
100 Pa · s	0.58	30.90	19.17	32.79
1000 Pa · s	0.52	21.69	13.20	65.96

Figure 20. Results from the model validation on the Laki lava flow. The flow lengths and extents for each viscosity value (1–1000 Pa·s) are shown as the red-gradient-scale overlay on the topographic map of the region. The fitness function and PLR values for these simulations (table on left) indicate the fit of the model improved with increasing viscosity values, while the length decreased.

Model Application and Evaluation

Once the calibration and validation of the model were successful in replicating the terrestrial lava flows, the model was applied to the martian flows. Model simulations focused on the two circum-Cerberus channelized lava flows, Athabasca and Grjótá Valles (Fig. 10). Lava flow simulations initiated at the source fissures and propagated across the surface until the total erupted volume of lava had been exhausted. The fitness function (e_i) of each model output was generated and compared to the observed lava flows to determine the accuracy of the simulations and to gauge the effect of viscosity on the final areal extent of each simulation. The PLR of each model output was compared to the observed flows to gauge the effect of viscosity on the final length.

Preliminary Results

Mars Modeling

The model outputs generally fill the mapped boundaries of the martian lava flows (Figs. 21, 22), though the simulated flows could cross these boundaries. After performing a parameter sweep, the fitness function values suggest the model adequately reproduced the Athabasca and Grjótá lava flows, with the best fitness function fit for Athabasca at 0.85 and the best fit for Grjótá at 0.64. The PLR values show variable approximations of the lengths for each of the primary lobes of the martian lava flows (Figs. 21, 22). In Athabasca Valles, the PLR of the 1Pa/Pa·s simulations indicate the closest approximation of the Lobe 1 and 2 lengths, decreasing significantly at higher viscosity values. In Grjótá Valles, the PLR values from the 1Pa/Pa·s for Lobes 1 and 2 are the closest matches. The 1000 Pa/Pa·s simulations produced the shortest and thickest outputs for both Athabasca and Grjota, and the 1Pa/Pa·s simulations produced the closest approximation of the observed flows.

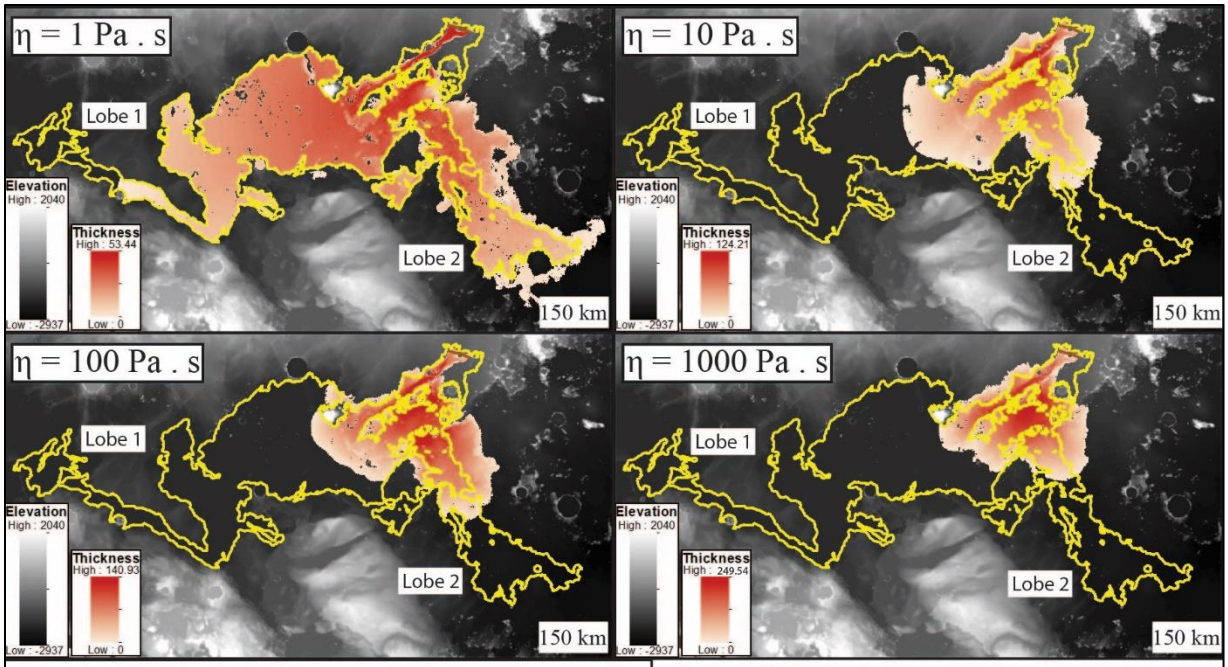

Fitness function and PLR values

η, S_y	e_i	PLR Lobe 1	PLR Lobe 2	h_{max}
1 Pa · s	0.85	75.46	111.70	53.44
10 Pa · s	0.55	32.71	56.59	125.21
100 Pa · s	0.49	28.19	56.36	140.93
1000 Pa · s	0.42	25.99	48.09	249.54

Figure 21. Results from the model application on the Athabasca lava flow. The flow lengths and extents for each viscosity value (1-1000 Pa·s) are shown as the red-gradient-scale overlay on the topographic map of the region. The fitness function and PLR values for these simulations (table on left) indicate the fit of the model improved with increasing viscosity values, while the length of the overall flow decreased in Lobe 1 and the excess simulated lava decreased around Lobe 2.

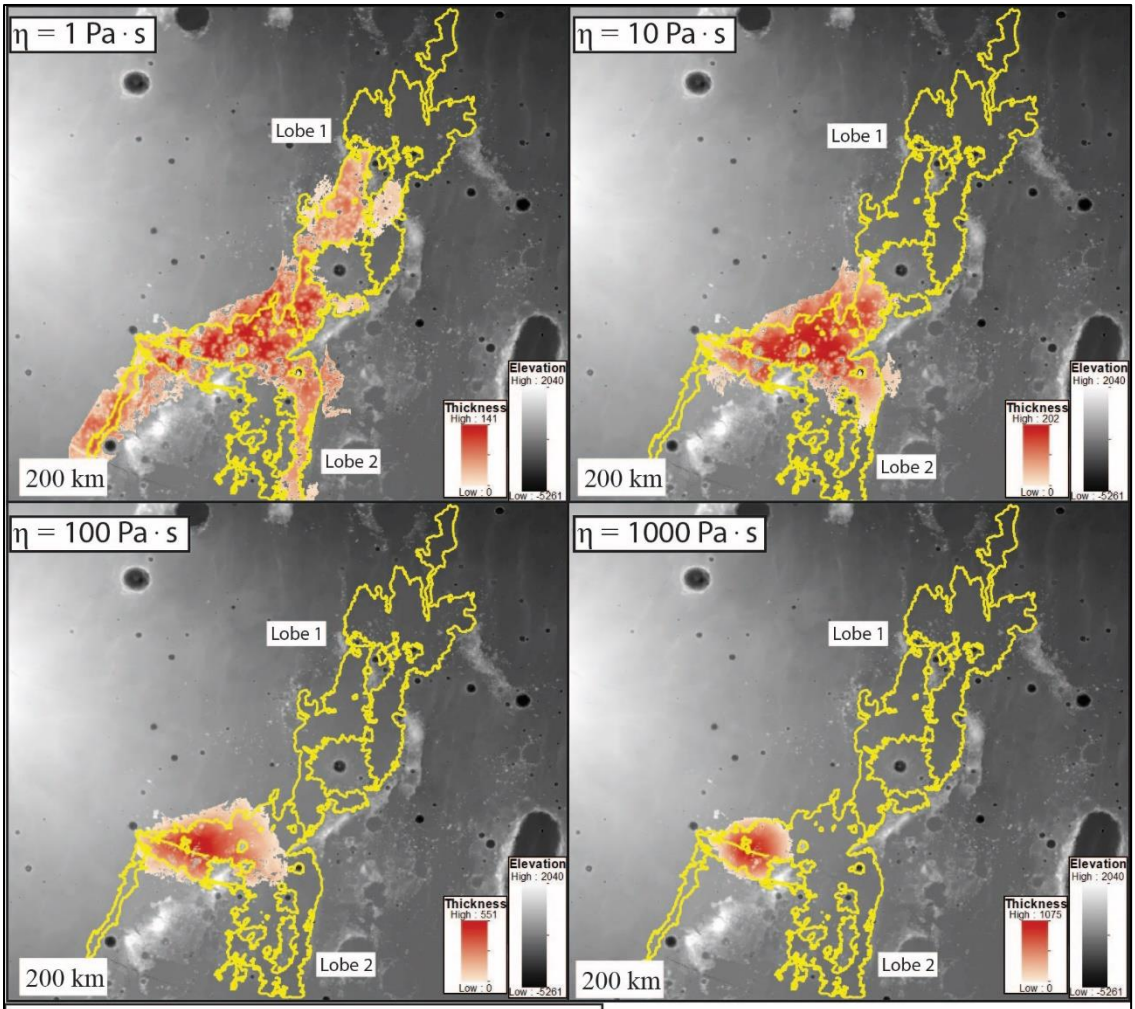

Fitness function and PLR values

η, S_y	e_i	PLR Lobe 1	PLR Lobe 2	h_{max}
1 Pa · s	0.64	60.13	116.85	141.1
10 Pa · s	0.53	33.16	69.73	202.1
100 Pa · s	0.42	18.10	45.88	551.4
1000 Pa · s	0.30	9.44	NA	1074.9

Figure 22. Results from the model application on the Grjótá lava flow. The flow lengths and extents for each viscosity value (1-1000 Pa·s) are shown as the red-gradient-scale overlay on the topographic map of the region. The fitness function and PLR values for these simulations (table on left) indicate the fit of the model improved with increasing viscosity values, with the best overall fit occurring during the 100 Pa·s simulation. The overall length in Lobe 1 decreased and the length in Lobe 2 was more variable.

Discussion

Discussion of Model Results

The results derived from the model for both the McCartys (Figs. 18, 19, Table 6) and Laki (Fig. 20) lava flows have shown the probable validity of the model. The simulations were capable of reproducing both lava flows to a reasonable approximation of the observed flows. Once results showed high PLR and e_i values for the terrestrial target sites, the model was applied to the martian lava flows. Results from those simulations demonstrate reasonable approximations of the martian target sites, and yielded results that can be interpreted with regards to the lava conditions present during their emplacement.

Implications for the Emplacement of Long Martian Lava Flows

Results derived from this model (Version 5) suggests that martian lava flows (Figs. 21, 22), require the lowest bulk viscosities (~1 Pa·s) and correspondingly low yield strengths (~1 Pa). Viscosity and yield strength values greater than these resulted in flows that were neither sufficiently long nor areally extensive enough to reproduce the observed flows. These results strongly support my hypothesis that both low viscosity and a correspondingly low yield strength, are necessary to produce long lava flows, particularly those found in the Cerberus region of Mars, which can exceed 1500 km in length. These results suggest that extremely low viscosity lavas (i.e., komatiites) may have been recently formed on Mars. Previous interpretations (e.g., Keszthelyi et al., 2000; Vaucher et al., 2009; Jaeger et al., 2010) and spectral data (Fig. 14), suggest basaltic compositions and their corresponding low viscosities are supported, but these results suggest a wider parameter space than those associated with a basic basalt.

The 1Pa/ Pa·s simulation of the Athabasca flow resulted in a high degree of accuracy (e_i = 0.85, PLR1 = 75.46, PLR2 = 111.70), though the Lobe 1 lateral extent was not capable of reaching the most distal lengths of the flow. This lack of flow distance could be corrected by

increasing the overall volume of erupted lava, but would likely be offset by greater intrusion of Lobe 2 into the Cerberus plains. The 1Pa/ Pa·s simulation of the Grjótá Valles did not produce the same high level of accuracy as the Athabasca simulations (e_i = 0.64, PLR1 = 60.13, PLR2 = 116.85), but suitably reproduced the observed flow. This simulation also did not reach the full lateral extent of Lobe 1, which could be rectified by increasing the overall erupted volume. Increasing the total erupted volume would also likely result in a corresponding over-estimation of the Lobe 2 length and areal extent, similar to what would occur in the Athabasca Valles simulation. The initial erupted volumes for each of these lava flow simulations were approximations based on the overall areal extent of the mapped lava flows, multiplied by their average thickness (Fig. 15, Table 5). This apparent volume shortage may be indicative of the lava in the model building thickness in a manner that is not directly comparable to the observed flows, or an underestimation of the actual erupted volume of lava in these sites.

These results supporting low viscosities are also consistent with previous interpretations of the basaltic lava composition in the Cerberus region (e.g., Keszthelyi et al., 2000; Vaucher et al., 2009; Jaeger et al., 2010). The young ages of these lavas (e.g., Golder et al., 2020), their composition (e.g., Keszthelyi et al., 2000; Vaucher et al., 2009; Jaeger et al., 2010), and the results of this work support the hypotheses that Mars has been capable of generating hot, low-viscosity lava in the relatively recent past, which would have fed the eruptions resulting in the Cerberus region lava flows. This inference would imply that Mars may still support geologic activity driven by internal heat flow processes, and that further volcanic eruptions may occur in the future.

Emplacement over a great distance (~1500 km) likely required very hot, low viscosity, high effusion rate eruptions (Keszthelyi et al., 2004; Jaeger et al., 2010) in the relatively recent

past (e.g., Golder et al., 2020). Comparison with terrestrial magma storage region behavior suggests that magma capable of feeding these young and voluminous lava flows was generated shortly before their emplacement, geologically speaking, to avoid magma crystallization before eruption. Terrestrial magma chambers, with thicknesses on the order of 1 km and depths ≥ 10 km, have been modeled to crystallize in under 1 million years (e.g., Marsh, 1989; Larsen and Tegner, 2006). Martian magma chambers are expected to be deeper than those found on Earth by a factor of ~4 (Wilson and Head, 1994). These terrestrial magma chamber crystallization timescales, coupled with the young ages of the Cerberus region volcanism, strongly suggest recent magma generation on Mars. Thus, although rapid interior cooling is expected for Mars (e.g., Montesi and Zuber, 2003; McGovern et al., 2002, 2004), the young Cerberus volcanism suggests recent magma generation. A thick insulating crust, inefficient convection in the mantle, inefficient heat loss from the interior, and heterogeneous heat flows are all hypothesized to have led to a warmer planetary interior for Mars (e.g., McGovern et al., 2002, 2004; Schumacher and Breuer, 2007; Ruiz et al., 2010; Baratoux et al., 2011; Ruiz et al., 2011). Locations of increased crustal thickness and the localized concentration of radioactive heat-producing elements in the crust would be more conducive to melt formation (McGovern et al., 2002, 2004; Schumacher and Breuer, 2007; Ruiz et al., 2010). Additionally, numerical modeling results for the emplacement of small shield volcanoes in the Cerberus plains point to very low viscosity, fluid lavas, which are interpreted to suggest that their source magma chambers were both deep and had low volatile contents (Baratoux et al., 2009). Each of these point leads to the implication of the recent generation of very fluid, low viscosity magma (Baratoux et al., 2009) that would have been capable of feeding the eruptions that filled Athabasca and Grjótá Valles.

Intrinsic Parameter Effects on Viscosity

As previously discussed, there are numerous factors that influence the final length and areal extent of lava flows which are either intrinsic or extrinsic to the lava (Fig. 11; e.g., Walker 1967, 1971, 1973; Hulme 1974; Ishihara et al., 1990; Wilson and Head, 1994; Keszthelyi, 1995; Miyamoto and Sasaki, 1998; Griffiths, 2000; Wilson and Head, 2002; Herault et al., 2009; Jaeger et al., 2010; Harris, 2013; Cordonnier et al., 2015). This work is focused specifically on the effect of viscosity, and did not delve into the extrinsic factors beyond their necessary input values for this model.

As the viscosity parameter clearly has a strong effect of the final length and areal extent of a lava flow, ultimately the factors that affect viscosity itself must contribute to the evolution of each flow. Here, I briefly discuss the effect of each of the other intrinsic parameters, their effect on lava flow development, and their effect on viscosity. The changes to many of these sub-parameters that affect viscosity are time dependent and result from cooling, crystallization, and vesiculation within the lava (e.g., Griffiths, 2000). The composition of the lava, in particular the silica content, has a strong effect on the bulk viscosity. Highly silicic lavas on Earth tend to be lower temperature and typically have a higher crystal content. Highly silicic magma has greater melt viscosity by virtue of its composition and generally cooler temperature (e.g., Griffiths, 2000). Lava flows have varying crystal content that changes along their lengths. Near the vent, basalts may have <5% crystal content, which can increase to 45%–50% with increasing distance (Cashman et al., 1999). This increase in crystal content may also directly relate an increase in the strength of the lava with increasing downstream distance (Golder et al., 2020). This increase in crystal content also works to inhibit flow propagation, due to crystals overlapping and interlocking within the lava (Kerr and Lister, 1991). Water content can also influence

crystallinity, by inhibiting crystal growth (Bilotta et al., 2012). The crystal fraction, their size and shape, all work to affect viscosity, and potentially inhibit flow.

Volatiles, including gas and water can affect the viscosity of lava, through the generation of bubbles during exsolution. Bubbles range from a few percent by volume up to 90% in highly vesiculated portions of a flow (Griffiths, 2000). Very small bubbles in a flow do not deform and are effectively rigid and can increase the viscosity within a flow, whereas larger bubbles deform under shear stress, which can decrease viscosity by providing slippage within the flow (Manga and Stone 1994; Cashman and Scheu, 2015). Bubbles are thought to affect lava viscosity to a lesser extent than crystals (Manga et al., 1998). Another component to consider is the pressure within the flow itself, which can be related to volatile content, in part. It is assumed that the lava does not deform anywhere but at its base, where the pressure is greatest and equal to the yield stress (Griffiths, 2000). This deformation is a due to the pressure gradient being too low elsewhere in the flow to cause deformation except at the base, where sufficient pressures are generated due to flow thickness and by exsolution of volatiles (Griffiths, 2000). Finally, the temperature of the lava is critical to the overall viscosity of the flow. The hottest lava, komatiite, with both low silica and high magnesium content, are inferred to have erupted at temperatures of ~1400–1600°C, and basaltic lavas range from 1100-1200°C (Griffiths, 2000). However, more silicic and viscous lavas, such as andesite and dacite erupt and lower temperatures, ~900°C, and have a far higher proportion of crystals from cooling (Griffiths, 2000). Each of these sub-parameters is a key component of lava flow evolution, and their investigation in further modeling would be useful, particularly to understand their relative effect on viscosity changes with relation to flow area and length.

Cooling-Limited Systems

Cooling-limited eruptions were not addressed in this model, but are expected to evolve differently than those that are restricted by the total erupted volume. Cooling of the lava during its eruption would lead to a corresponding modification of the parameter values discussed in the previous section, particularly associated with the lava temperature having decreased to the point at which the increase in the temperature-dependent viscosity impedes further propagation (e.g., Pinkerton and Wilson, 1994). Heat loss to the surroundings (surface and/or atmosphere), would lead to an exponential rise in viscosity as distance from the source increased, which ultimately restricts the final extent to which the lava can flow (e.g., Dragoni et al., 1997; Blatt et al., 2006; Diniega et al., 2013; Cordonnier et al., 2015).

Based on temperature driven changes, viscosity plays a critical role in the maximum extent of the lava (e.g., Cordonnier et al., 2015). To explore an idealized cooling-limited system with a fixed volume, variable slope, and decreasing temperature that leads to increasing viscosity, two endmembers are briefly explored here (Fig. 12, Scenario 1). For a low slope angle, the lava has a higher critical thickness, where more lava can be stored in each cell, leading to a correspondingly shorter propagation of the flow. The flow will continue until the temperature drops, leading to increased viscosity near the toe, increasing lava thickness and preventing further propagation. For a high slope angle, the lava has a lower critical thickness, wherein less lava can be stored in each cell, than the shallow slope scenario and will have a correspondingly greater volume of lava that can spread further, leading to a thinner and longer flow. These differences between volume-limited and cooling-limited emplacement modes, particularly regarding the changes in behavior of the sub-parameters of viscosity affected by temperature changes, strongly support additional updates to the model to include thermal evolution for future investigations.

Future Work

Model Modifications

Beyond the implementation of the current model version on the terrestrial and martian sites that have been discussed in the preceding sections, further modifications of the model are in order. As this model is currently configured to investigate volume-limited systems, it would need to be modified to incorporate the parameters involved in cooling-limited systems. Specifically, this model is also not configured to simulate thermally evolving lava flows and the corresponding changes to viscosity within those flows. Future work would add this thermal evolution into the model, to investigate the effect of the other intrinsic factors that affect the overall viscosity. The equations related to thermal variation within the flow should be added to the model (e.g., Ishihara et al., 1990 [see their Fig. 4, Eq. 22–38]; Vicari et al., 2007; Harris, 2013), to better simulate changes within the flow itself. These changes to the model would produce a more robust method for the investigation of a far broader range of volcanic systems across the solar system. Refinement of surface preconditioning processes for the DEM inputs should also be priority, in order to more accurately represent the pre-flow surface. One method for refined surface preconditioning should seek to remove surface material that better reflects the tapering of the lava thickness towards the distal portions of the flow, rather than removing a single slab of material at a constant thickness.

Though the results presented here were generated from Version 5 of the model and cannot be considered as the most accurate outputs, I ultimately expect the same general trends of the model outputs to be found when the target flows are reexamined using Version 6 of the model. One caveat to consider is that the outputs generated from the horizontal plain with the current version of the model suggest a wider possible range of parameter combinations that could result in long and areally extensive lava flows (see Chapter 2 Appendix 2). However, this

inference cannot yet be extrapolated to either the terrestrial or martian sites with full confidence, as Version 6 of the model still requires additional modification for it to incorporate DEMs that represent actual topography as basis for simulations.

Additional Investigation Sites

The results derived from the theoretical lava flow lengths, investigation of terrestrial analogues, and comparison of a limited number of martian lava flows strongly support low viscosity basaltic lava in the Cerberus region. Expansion of this investigation would include additional lava flows within the Cerberus plains region (Vaucher et al., 2009), Kasei Valles (Dundas and Kesthelyi, 2014), along with additional flows within the Tharsis Montes region (e.g., Bleacher et al., 2017). The expansion to additional sites would offer the opportunity to investigate potentially different compositions, or at least a wider range of relatively low viscosity basalts. These sites may also provide insight into similarities, or dissimilarities, between the two largest volcanic provinces on Mars, Tharsis and Elysium. The inclusion of lava flows that have been roofed over and insulated, as well as those that have undergone significant thermal evolution during their emplacement would be useful in the comparison of parameter effects on a wide range of emplacement mechanisms.

Conclusions

The analyses of the results derived from the Version 5 model outputs concerning the bulk viscosities of the lavas of the terrestrial sites and the simulations performed on Athabasca and Grjótá Valles, indicate that the lowest bulk viscosities and yield strengths that were investigated (1 Pa·s/1 Pa) resulted in the best overall model fits to the observed lava flows. The highest-viscosity and yield strength configurations (1000 Pa·s/1000 Pa) resulted in shorter and thicker flows compared to the low-viscosity variants. The viscosity values that resulted in the best model output fits are most consistent with high temperature basaltic compositions, though komatiite-

style volcanism cannot be discounted. This result supports previous interpretations of martian lavas being primarily composed of basalt. These simulations also suggest that Mars has been capable of generating significant volumes of magma that then fed large-scale eruptions hot, low-viscosity lava in the relatively recent past (~3 Ma), and may be capable of doing so again.

References

Ander, M. E., Heiken, G., Eichelberger, J., Laughlin, A. W., & Huestis, S. (1981). Geologic and geophysical investigations of the Zuni-Bandera volcanic field, New Mexico (No. LA-8827-MS). Los Alamos National Lab., NM (USA); Sandia National Labs., Albuquerque, NM (USA); New Mexico Univ., Albuquerque (USA). Dept. of Geology.

Baker, V. R., & Bunker, R. C. (1985). Cataclysmic late Pleistocene flooding from glacial Lake Missoula: A review. Quaternary Science Reviews, 4(1), 1-41.

Bandfield, J. L., Hamilton, V. E., & Christensen, P. R. (2000). A global view of Martian surface compositions from MGS-TES. Science, 287(5458), 1626-1630.

Baratoux, D., Pinet, P., Toplis, M. J., Mangold, N., Greeley, R., & Baptista, A. R. (2009). Shape, rheology and emplacement times of small Martian shield volcanoes. Journal of Volcanology and Geothermal Research, 185(1-2), 47-68.

Baratoux, D., Toplis, M. J., Monnereau, M., & Gasnault, O. (2011). Thermal history of Mars inferred from orbital geochemistry of volcanic provinces. Nature, 472(7343), 338-341.

Basaltic Volcanism Study Project (1981) Basaltic Volcanism on the Terrestrial Planets. Pergamon Press, Inc., New York.

Berman, D. C., & Hartmann, W. K. (2002). Recent fluvial, volcanic, and tectonic activity on the Cerberus plains of Mars. Icarus, 159(1), 1-17.

Bilotta, G., Cappello, A., Hérault, A., Vicari, A., Russo, G., and Del Negro, C. (2012). Sensitivity analysis of the MAGFLOW Cellular Automaton model for lava flow simulation. Environmental Modelling & Software, 35, 122-131.

Blatt, H., R. Tracy, and B. Owens (2006), Petrology: Igneous, Sedimentary and Metamorphic, 3rd ed., Freeman, New York.

Bleacher, J. E., Garry, W. B., Zimbelman, J. R., Crumpler, L. S., & Aubele, J. C. (2010). The Zuni-Bandera Volcanic Field, NM: An Analog for Exploring Planetary Volcanic Terrains. In AGU Fall Meeting Abstracts (Vol. 1, p. 1387).

Bleacher, J. E., Crumpler, L. S., Garry, W. B., Zimbelman, J. R., Self, S., & Aubele, J. C. (2012). Surface Textures and Features Indicative of Endogenous Growth at the McCartys Flow Field, NM, as an Analog to Martian Volcanic Plains.

Bleacher, J. E., Orr, T. R., Andrew, P., Zimbelman, J. R., Hamilton, C. W., Garry, W. B., et al. (2017). Plateaus and sinuous ridges as the fingerprints of lava flow inflation in the Eastern Tharsis Plains of Mars. Journal of Volcanology and Geothermal Research, 342, 29-46.

Brož, P., Hauber, E., Platz, T., & Balme, M. (2015). Evidence for Amazonian highly viscous lavas in the southern highlands on Mars. Earth and Planetary Science Letters, 415, 200-212.

Burr, D. M., McEwen, A. S., et al. (2002a). Recent aqueous floods from the Cerberus Fossae, Mars. Geophys. Res. Letters, 29(1), 13-1.

Burr, D. M., Grier, J. A., et al. (2002b). Repeated aqueous flooding from the Cerberus Fossae: Evidence for very recently extant, deep groundwater on Mars. Icarus, 159(1), 53-73.

Burr, D. M., & Parker, A. H. (2006). Grjótá Vallis and implications for flood sediment deposition on Mars. Geophys. Res. Letters, 33(22).

Burr, D.M., L. Wilson, and A.S. Bargery (2009) Floods from Fossae: a review of Amazonian-aged extensional tectonic megaflood channels on Mars. In Megaflooding on Earth and Mars, D.M. Burr, V.R. Baker and P.A. Carling (eds), Cambridge University Press, Cambridge, UK. pp. 194-208.

Cashman, K., Pinkerton, H., Stephenson, J. (1998). Introduction to special section: Long lava

flows. Journal of Geophysical Research: Solid Earth (1978–2012), 103(B11), 27281-27289.
Cashman, K. V., Thornber, C., & Kauahikaua, J. P. (1999). Cooling and crystallization of lava in open channels, and the transition of Pāhoehoe Lava to'A'ā. Bulletin of Volcanology, 61(5), 306-323.
Cashman, K. V., & Scheu, B. (2015). Magmatic fragmentation. In The Encyclopedia of Volcanoes, pp. 459-471. Academic Press.
Chapman, M. G., Neukum, G., et al. (2010). Amazonian geologic history of the Echus Chasma and Kasei Valles system on Mars: New data and interpretations. Earth and Planetary Science Letters, 294, 238-255.
Christensen, P. R., Anderson, D. L., Chase, S. C., Clark, R. N., Kieffer, H. H., Malin, M. C., Pearl, J.C., Carpenter, J., Bandiera, N., Brown, F.G., Silverman, S. (1992). Thermal emission spectrometer experiment: Mars Observer mission. Journal of Geophysical Research: Planets, 97(E5), 7719-7734.
Christensen, P. R., McSween, H. Y., Bandfield, J. L., Ruff, S. W., Rogers, A. D., Hamilton, V. E., Gorelick, N., Wyatt, M.B., Jakosky, B.M., Kieffer, H.H., Malin, M.C., & Moersch, J. E. (2005). Evidence for magmatic evolution and diversity on Mars from infrared observations. Nature, 436(7050), 504-509.
Coffin, M.F. & Eldholm, O. (1994). Large igneous provinces: Crustal structure, dimensions, and external consequences. Reviews of Geophysics, 32, 1–36.
Connor, L. J., & Connor, C. B. (2006). Inversion is the key to dispersion: understanding eruption dynamics by inverting tephra fallout. Statistics in volcanology. Geological Society, London, 231-242.
Crumpler, L. S., & Aubele, J. C. (2001). Volcanoes of New Mexico: an abbreviated guide for non-specialists. Volcanology in New Mexico. New Mexico Museum of Natural History and Science Bulletin, 18, 5-15.
Cordonnier, B., Lev, E., & Garel, F. (2015). Benchmarking lava-flow models. Geological Society, London, Special Publications, 426, SP426-7.
Danielson, J. J., & Gesch, D. B. (2011). Global multi-resolution terrain elevation data 2010 (GMTED2010) (No. 2011-1073). US Geological Survey.
Del Negro, C., Fortuna, L., Herault, A., & Vicari, A. (2008). Simulations of the 2004 lava flow at Etna volcano using the magflow cellular automata model. Bulletin of Volcanology, 70(7), 805-812.
Diniega, S., Smrekar, S. E., Anderson, S., & Stofan, E. R. (2013). The influence of temperature-dependent viscosity on lava flow dynamics. Journal of Geophysical Research: Earth Surface, 118(3), 1516-1532.
Dragoni, M., Bonafede, M., & Boschi, E. (1986). Downslope flow models of a Bingham liquid: implications for lava flows. Journal of Volcanology and Geothermal Research, 30(3-4), 305-325.
Dragoni, M. (1997). Physical modelling of lava flows. Annals of Geophysics, 40(5).
Dundas, C. M., & Keszthelyi, L. P. (2014). Emplacement and erosive effects of lava in south Kasei Valles, Mars. Journal of Volcanology and Geothermal Research, 282, 92-102.
Dundas, C. M., Cushing, G. E., & Keszthelyi, L. P. (2019). The flood lavas of Kasei Valles, mars. Icarus, 321, 346-357.
Ernst, R. E. (2014). Large igneous provinces. Cambridge University Press.
Felpeto, A., Arana, V., Ortiz, R., Astiz, M., & Garcia, A. (2001). Assessment and modelling of

lava flow hazard on Lanzarote (Canary Islands). Natural hazards, 23(2-3), 247-257.
Felpeto, A., Martí, J., & Ortiz, R. (2007). Automatic GIS-based system for volcanic hazard assessment. Journal of Volcanology and Geothermal Research, 166(2), 106-116.
Geikie, A. 1880. The lava-fields of North-western Europe. Nature, 23, 3–5.
Gíslason, G. L. (2013). Lava Flow Modelling In Iceland.
Golder, K. B. (2013). Geomorphology of Eridania Basin, Mars: A Study of the Evolution of Chaotic Terrain and a Paleolake. Masters Thesis.
Golder, K. B., Burr, D. M., & Kattenhorn, S. A. (2020). Investigation of target property effects on crater populations in long lava flows: A study in the Cerberus region, Mars, with implications for magma source identification. Icarus, 113388.
Greeley, R. (1976). Modes of emplacement of basalt terrains and an analysis of mare volcanism in the Orientale Basin. In Lunar and Planetary Science Conference Proceedings (Vol. 7, pp. 2747-2759).
Greeley, R., & King, J. S. (1977). Volcanism of the Eastern Snake River Plain, Idaho: A comparative planetary geology-guidebook. http://www. sti. nasa. gov/RECONselect. html.
Greeley, R. (1982). The Snake River Plain, Idaho: representative of a new category of volcanism. Journal of Geophysical Research: Solid Earth, 87(B4), 2705-2712.
Griffiths, R. W. (2000). The dynamics of lava flows. Annual Review of Fluid Mechanics, 32(1), 477-518.
Hamilton, V. E., Wyatt, M. B., McSween Jr, H. Y., & Christensen, P. R. (2001). Analysis of terrestrial and Martian volcanic compositions using thermal emission spectroscopy: 2. Application to Martian surface spectra from the Mars Global Surveyor Thermal Emission Spectrometer. Journal of Geophysical Research: Planets, 106(E7), 14733-14746.
Hamilton, C. W. (2013), Flood Lavas Associated with the Cerberus Fossae 2 unit in Elysium Planitia, Mars. In Lunar and Planetary Institute Science Conference Abstracts (Vol. 44, p. 3070).
Harris, A. J., & Rowland, S. (2001). FLOWGO: A kinematic thermo-rheological model for lava flowing in a channel. Bulletin of Volcanology, 63(1), 20-44.
Harris, A. J. L. (2013). Lava flows. Modeling volcanic processes: The physics and mathematics of volcanism. Cambridge University Press, New York, 85-106.
Head, J. W., and Coffin, M. F. (1997). Large igneous provinces: A planetary perspective. Geophysical Monograph-American Geophysical Union, 100, 411-438.
Head, J. W., Murchie, S. L., Prockter, L. M., Solomon, S. C., Chapman, C. R., Strom, R. G., Watters, T.R., Blewett, D.T., Gillis-Davis, J.J., Fassett, C.I., Dickson, J.L., Morgan, G.A., Kerber, L. (2009). Volcanism on Mercury: Evidence from the first MESSENGER flyby for extrusive and explosive activity and the volcanic origin of plains. Earth and Planetary Science Letters, 285(3), 227-242.
Herault, A., Vicari, A., Ciraudo, A., & Del Negro, C. (2009). Forecasting lava flow hazards during the 2006 Etna eruption: Using the MAGFLOW cellular automata model. Computers & Geosciences, 35(5), 1050-1060.
Howard, A. D. (2007). Simulating the development of Martian highland landscapes through the interaction of impact cratering, fluvial erosion, and variable hydrologic forcing. Geomorphology, 91(3), 332-363.
Hulme, G. (1974). The interpretation of lava flow morphology. Geophysical Journal International, 39(2), 361-383.
Irish, R. R. (2000). Landsat 7 science data users handbook. National Aeronautics and Space

Administration, Report, 2000, 415-430.
Ishihara, K., Iguchi, M., & Kamo, K. (1990). Numerical simulation of lava flows on some volcanoes in Japan. In Lava Flows and Domes, pp. 174-207. Springer Berlin Heidelberg.
Jaeger, W. L., Keszthelyi, L. P., Skinner, J. A., Milazzo, M. P., McEwen, A. S., Titus, T. N., Rosiek, M.R., Galuszka, D.M., Howington-Kraus, E., Kirk, R. L., the HiRISE Team (2010). Emplacement of the youngest flood lava on Mars: A short, turbulent story. Icarus, 205(1), 230-243.
Kerr, R.C., & Lister, J.R. (1991). The effects of shape on crystal settling and on the rheology of magmas. The Journal of Geology, 99(3), 457-467.
Keszthelyi, L. (1995). A preliminary thermal budget for lava tubes on the Earth and planets. Journal of Geophysical Research: Solid Earth (1978–2012), 100(B10), 20411-20420.
Keszthelyi, L., and Self, S. (1998). Some physical requirements for the emplacement of long basaltic lava flows. Journal of Geophysical Research: Solid Earth (1978–2012), 103(B11), 27447-27464.
Keszthelyi, L., McEwen, A. S., Thordarson, T. (2000). Terrestrial analogs and thermal models for Martian flood lavas. Journal of Geophysical Research: Planets (1991–2012), 105(E6), 15027-15049.
Keszthelyi, L., Thordarson, T., McEwen, A., Haack, H., Guilbaud, M. N., Self, S., Rossi, M. J. (2004). Icelandic analogs to Martian flood lavas. Geochemistry, Geophysics, Geosystems, 5(11).
Keszthelyi, L., Self, S., & Thordarson, T. (2006). Flood lavas on Earth, Io and Mars. Journal of the Geological Society, 163(2), 253-264.
Larsen, R. B., & Tegner, C. (2006). Pressure conditions for the solidification of the Skaergaard intrusion: Eruption of East Greenland flood basalts in less than 300,000 years. Lithos, 92(1-2), 181-197.
Macdonald, G. A. (1953). Pahoehoe, aa, and block lava. American Journal of Science, 251(3), 169-191.
Malin, M.C., et al. (2007), Context Camera Investigation on board the Mars Reconnaissance Orbiter. Journal of Geophysical Research, 112, E05S04, doi:10.1029/2006E002808.
Manga, M., & Stone, H. A. (1994). Interactions between bubbles in magmas and lavas: effects of bubble deformation. Journal of Volcanology and Geothermal Research, 63(3-4), 267-279.
Manga, M., Castro, J., Cashman, K. V., & Loewenberg, M. (1998). Rheology of bubble-bearing magmas. Journal of Volcanology and Geothermal Research, 87(1-4), 15-28.
Marsh, B. D. (1989). Magma chambers. Annual Review of Earth and Planetary Sciences, 17(1), 439-472.
McEwen, A. S., Keszthelyi, L., Spencer, J. R., Schubert, G., Matson, D. L., Lopes-Gautier, R., Klassen, K.P., Johnson, T.V., Head, J.W., Geissler, P., Fagents, S., Davies, A.G., Carr, M.H., Breneman, H.H., Belton, M. J. S. (1998). High-temperature silicate volcanism on Jupiter's moon Io. Science, 281(5373), 87-90.
McEwen, A. S., Preblich, B. S., et al. (2005). The rayed crater Zunil and interpretations of small impact craters on Mars. Icarus, 176(2), 351-381.
McGovern, P. J., Solomon, S. C., Smith, D. E., Zuber, M. T., Simons, M., Wieczorek, M. A., Phillips, R.J., Neumann, G.A., Aharonson, O., Head, J. W. (2002). Localized gravity/topography admittance and correlation spectra on Mars: Implications for regional and global evolution. Journal of Geophysical Research: Planets, 107(E12).
McGovern, P.J. et al., (2004). Correction to localized gravity/topography admittance and

correlation spectra on Mars: Implications for regional and global evolution. Journal of Geophysical Research: Planets, 109, E07007.
McSween Jr, H. Y. (2015). Petrology on Mars. American Mineralogist, 100(11-12), 2380-2395.
Mehta, S., (2008). Growing Volcano. Computer software. Volcano Feedback Loop Example - Case Study. ESRI, 2008. Web. <http://arcscripts.esri.com/details.asp?dbid=15727>.
Miyamoto, H., and Sasaki, S. (1998). Numerical simulations of flood basalt lava flows: Roles of parameters on lava flow morphologies. Journal of Geophysical Research: Solid Earth (1978–2012), 103(B11), 27489-27502.
Miyamoto, H., Komatsu, G., Baker, V. R., Dohm, J. M., Ito, K., & Tosaka, H. (2007). Cataclysmic scabland flooding: Insights from a simple depth-averaged numerical model. Environmental Modelling & Software, 22(10), 1400-1408.
Montési, L. G., & Zuber, M. T. (2003). Clues to the lithospheric structure of Mars from wrinkle ridge sets and localization instability. Journal of Geophysical Research: Planets, 108(E6).
Morgan, G. A., Campbell, B. A., et al. (2013). 3D Reconstruction of the Source and Scale of Buried Young Flood Channels on Mars. Science, 340(6132), 607-610.
Murchie, S., Arvidson, R., et al. (2007). Compact reconnaissance imaging spectrometer for Mars (CRISM) on Mars reconnaissance orbiter (MRO). Journal of Geophysical Research: Planets, 112(E5).
Nichols, R. L. (1946). McCartys basalt flow, Valencia County, New Mexico. Geological Society of America Bulletin, 57(11), 1049-1086.
Osinski, G. R., Léveillé, R., Berinstain, A., Lebeuf, M., & Bamsey, M. (2006). Terrestrial analogues to Mars and the Moon: Canada's role. Geoscience Canada, 33(4).
Parker, R. L. (1977). Understanding inverse theory. Annual Review of Earth and Planetary Sciences, 5, 35.
Pelkey, S. M., Mustard, J. F., Murchie, S., Clancy, R. T., Wolff, M., Smith, M., et al. & (2007). CRISM multispectral summary products: Parameterizing mineral diversity on Mars from reflectance. Journal of Geophysical Research: Planets, 112(E8).
Pinkerton, H., & Wilson, L. (1988). The Lengths of Lava Flows. In Lunar and Planetary Science Conference (Vol. 19). 937-938.
Pinkerton, H., and Wilson, L. (1994). Factors controlling the lengths of channel-fed lava flows. Bulletin of Volcanology, 56(2), 108-120.
Plescia, J. B. (1990). Recent flood lavas in the Elysium region of Mars. Icarus, 88(2), 465-490.
Plescia, J. B. (2003). Cerberus Fossae, Elysium, Mars: A source for lava and water. Icarus, 164(1), 79-95.
Proietti, C., Coltelli, M., Marsella, M., & Fujita, E. (2009). A quantitative approach for evaluating lava flow simulation reliability: LavaSIM code applied to the 2001 Etna eruption. Geochemistry, Geophysics, Geosystems, 10(9).
Ratto, M., Tarantola, S., & Saltelli, A. (2001). Sensitivity analysis in model calibration: GSA-GLUE approach. Computer Physics Communications, 136(3), 212-224.
Roy, D. P., Wulder, M. A., Loveland, T. R., Woodcock, C. E., Allen, R. G., Anderson, M. C., ... & Scambos, T. A. (2014). Landsat-8: Science and product vision for terrestrial global change research. Remote sensing of Environment, 145, 154-172.
Ruff, S. W., & Christensen, P. R. (2002). Bright and dark regions on Mars: Particle size and mineralogical characteristics based on Thermal Emission Spectrometer data. Journal of Geophysical Research: Planets (1991–2012), 107(E12), 2-1.
Ruiz, J., López, V., & Dohm, J. M. (2010). The present-day thermal state of Mars. Icarus, 207(2),

631-637.
Ruiz, J., McGovern, P. J., Jiménez-Díaz, A., López, V., Williams, J. P., Hahn, B. C., & Tejero, R. (2011). The thermal evolution of Mars as constrained by paleo-heat flows. Icarus, 215(2), 508-517.
Sakimoto, S. E. H., Gregg, T. K. P., Hughes, S. S., & Chadwick, J. (2003). Re-assessing plains-style volcanism on Mars. In Sixth International Conference on Mars.
Schiff, J. L. (2011). Cellular automata: A discrete view of the world. John Wiley & Sons.
Schumacher, S., & Breuer, D. (2007). An alternative mechanism for recent volcanism on Mars. Geophysical Research Letters, 34(14).
Self, S., Thordarson, T., Keszthelyi, L., Walker, G. P. L., Hon, K., Murphy, M. T., Long, P., Finnemore, S. (1996). A new model for the emplacement of Columbia River basalts as large, inflated pahoehoe lava flow fields. Geophysical Research Letters, 23(19), 2689-2692.
Self, S., Jay, A. E., Widdowson, M., Keszthelyi, L. P. (2008). Correlation of the Deccan and Rajahmundry Trap lavas: Are these the longest and largest lava flows on Earth? Journal of Volcanology and Geothermal Research, 172(1), 3-19.
Shaw, J., Munro-Stasiuk, M., Sawyer, B., Beaney, C., Lesemann, J., Musacchio, L., Rains, B., Young, R.R., 1999. The Channeled Scabland:back to Bretz? Geology 27, 605-608.
Smith, D.E., et al., (2001), Mars Orbiter Laser Altimeter: Experiment summary after the first year of global mapping of Mars. Journal of Geophysical Research, 106, E10, 23,689-23,722.
Spataro, W., D'Ambrosio, D., Rongo, R., and Trunfio, G. A. (2004). An evolutionary approach for modelling lava flows through cellular automata. In Cellular Automata (pp. 725-734). Springer Berlin Heidelberg.
Thordarson, T., and Self, S. (1993). The Laki (Skaftár Fires) and Grímsvötn eruptions in 1783-1785. Bulletin of Volcanology, 55, 233-263.
Thordarson, T., Miller, D.J., Larsen, G., Self, S., Sigurdsson, H. (2001). New estimates of sulfur and atmospheric mass-loading by the 934 AD Eldgjá eruption, Iceland. Journal of Volcanology and Geothermal Research, 108, 33-54.
Tighe, M. L., and Chamberlain, D. (2009). Accuracy Comparison of the SRTM, ASTER, NED, NEXTMAP® USA Digital Terrain Model over Several USA Study Sites. In Proceedings of the ASPRS/MAPPS 2009 Fall Conference, San Antonio, TX.
Tyrrell, G.W. 1937. Flood basalts and fissure eruption. Bulletin of Volcanology, 1, 87–111.
Vaucher, J., Baratoux, D., et al. (2009). The volcanic history of central Elysium Planitia: Implications for martian magmatism. Icarus, 204(2), 418-442.
Vicari, A., Alexis, H., Del Negro, C., Coltelli, M., Marsella, M., & Proietti, C. (2007). Modeling of the 2001 lava flow at Etna volcano by a cellular automata approach. Environmental Modelling & Software, 22(10), 1465-1471.
Walker, G. P. L. (1967). Thickness and viscosity of Etnean lavas. Nature, 213, 484-485.
Walker, G. P. L. (1971). Compound and simple lava flows and flood basalts. Bulletin Volcanologique, 35(3), 579-590.
Walker, G. P. L., (1973). Lengths of lava flows. Philosophical Transactions of the Royal Society of London A: Mathematical, Physical and Engineering Sciences, 274(1238), 107-118.
Washington, H.S. (1922). Deccan Traps and the other plateau basalts. Geological Society of America Bulletin, 33, 765–804.
Wilson, L., & Head III, J. W. (1983). A comparison of volcanic eruption processes on Earth, Moon, Mars, Io and Venus. Nature, 302(5910), 663.

Wilson, L., and Head, J. W. (1994). Mars: Review and analysis of volcanic eruption theory and relationships to observed landforms. Reviews of Geophysics, 32(3), 221-263.

Wilson, L., and Head, J. W. (2002). Tharsis-radial graben systems as the surface manifestation of plume-related dike intrusion complexes: Models and implications. Journal of Geophysical Research: Planets, 107(E8), 1-1.

Wyatt, M. B., Hamilton, V. E., McSween Jr, H. Y., Christensen, P. R., & Taylor, L. A. (2001). Analysis of terrestrial and Martian volcanic compositions using thermal emission spectroscopy: 1. Determination of mineralogy, chemistry, and classification strategies. Journal of Geophysical Research: Planets, 106(E7), 14711-14732.

Yamaguchi, Y., Kahle, A. B., Tsu, H., Kawakami, T., & Pniel, M. (1998). Overview of advanced spaceborne thermal emission and reflection radiometer (ASTER). Geoscience and Remote Sensing, IEEE Transactions on geoscience and remote sensing, 36(4), 1062-1071.

Zimbelman, J. R. (1998). Emplacement of long lava flows on planetary surfaces. Journal of Geophysical Research: Solid Earth, 103(B11), 27503-27516.

Zimbelman, J. R., & Johnston, A. K. (2002). New precision topographic measurements of Carrizozo and McCartys basalt flows, New Mexico. Geology of white sands.

Appendix

Appendix 1: Model Script (Version 5)

The following code is the model version built upon the framework of the Gislason (2013) model,

from which the results of this chapter were derived.

#Import arcpy and extensions: Import arcpy and all necessary extensions that will be used by the script for running this model.

```
import arcpy
from arcpy.sa import *
from arcpy import env
import datetime
import os
import math
```

#return current date and time: Display start time for the model run.

```
now = datetime.datetime.now()
print now.strftime("%Y-%m-%d %H:%M")
```

#Allow overwriting of previous outputs: Set environment conditions that allows for overwriting of outputs during iterations.

```
arcpy.gp.overwriteOutput = 1
```

#Check licenses: Check license state of spatial analyst, an extension that is required for many of the processes included in the script.

```
arcpy.CheckOutExtension("spatial")
```

#Define file pathways and variables (model inputs)

```
path = "D:\..."  #Basic pathway where processing occurs, and new folders and geodatabases are created.
volcanoes = "D:\..." #Feature class of either vents or fissure representing source area.
DEM = "D:\..." #Raster of regional topography.
lava = int("20") #Maximum thickness of lava.
total_lava = int(20 * 249)
maxit = int("3000") #Maximum number of iterations for the model.
rastersize = float("463.0836") #Cell size of the DEM.
```

These geodatabases and folders are where the outputs from each step in the iteration are stored. *Could be condensed into a single geodatabase and single folder.

#make geodatabases and folders

```
arcpy.CreateFileGDB_management(path, "trash.gdb")
arcpy.CreateFileGDB_management(path, "inputpoints.gdb")
arcpy.CreateFileGDB_management(path, "lavaraster.gdb")
arcpy.CreateFileGDB_management(path, "lavas.gdb")
arcpy.CreateFileGDB_management(path, "finaloutput.gdb")
os.makedirs(path + "\\lavapoints")
 #removed lavaraster directory
```
This constant raster is used to create another raster, with a value of 1 for each cell, that represents the source location, be it a point or line.
```
#Create constant raster
CreateConsta1 = path + "\\trash.gdb\\lava_sum"
arcpy.gp.CreateConstantRaster_sa(CreateConsta1, (20 * 249), "INTEGER", rastersize, DEM)
CreateConsta2 = path + "\\trash.gdb\\raster"
arcpy.gp.CreateConstantRaster_sa(CreateConsta2, 1, "INTEGER", rastersize, DEM) #extent changed to that of the DEM rather than the shapefile
print "Raster created"
```

#Convert raster to point: If the source is a point, rather than a line, the following lines must be included in the script:
```
#Create a copy of the original feature, so as to not overwrite.
points = path + "\\inputpoints.gdb"
arcpy.FeatureClassToShapefile_conversion(volcanoes, points)
```

The following lines in the script are necessary when the input feature is a line rather than a point. A new field must be added, in order to make the split, and subsequent addition of the processes rasters possible.

```
#The following add field is for when using a polyline rather than points
inFeature = path + "\\inputpoints.gdb\\Fissure_COPY.shp"
arcpy.AddField_management(inFeature, "pointid", "LONG")
arcpy.CalculateField_management(inFeature, "pointid", "[OBJECTID] + 10000", "VB", "")
arcpy.AddField_management(inFeature, "grid_code", "LONG")
arcpy.CalculateField_management(inFeature, "grid_code", "1", "VB", "")

#Local Variables
lavapoints = path + "\\lavapoints"
arcpy.env.workspace = lavapoints
pointscut = path + "\\inputpoints.gdb\\Fissure_COPY"
```

Split the feature class into individual components, to run the focal statistics on each component, which will then be added together at the end.
```
#Split Layer by Attributes
arcpy.SplitByAttributes_analysis(pointscut, lavapoints, ['pointid']) #Had to update as old too didn’t work any longer
print "points made"
```

```
#Set extent of the raster layers
arcpy.env.extent = DEM
#Set the workspace
arcpy.env.workspace = path + "\\lavapoints"
num = 10000
DEM1 = Raster(DEM)
sum = 0
shp_List = arcpy.ListFiles("*.shp")
#This field contains the lava thickness
valField = "grid_code"
for layer in shp_List:
   num = num + 1
   s = str(num) #Number has to be a string in the next step
   inFeatures = path + "\\lavapoints\\" + s + ".shp"
   outRaster = path + "\\trash.gdb\\lava" + s #newly created raster layer
   cellSize = 463.0836
   #Execute FeatureToRaster
   arcpy.FeatureToRaster_conversion(inFeatures, valField, outRaster, cellSize)
   #arcpy.PolylineToRaster_conversion(inFeatures, valField, outRaster, "", "", cellSize)
   #add DEM to Lava Flow layers
   lavadem = DEM1 + Raster(outRaster)
   lavadem.save(path + "\\lavaraster.gdb\\lavas" + s)
   #lavadem.save(path + "\\lavaraster.gdb\\lavasbackup" + s)
   print layer + "is being calculated"
   now = datetime.datetime.now()
   print now.strftime("%Y-%m-%d %H:%M")
   numit = 0
   while numit < maxit:
      print numit
      sum = 0
      while sum < total_lava:
         rastercalc = Raster(path + "\\lavaraster.gdb\\lavas" + s)
         rastercalc2 = Con(IsNull(rastercalc), 0, rastercalc)
         rastercalc2.save(path + "\\lavacal" + s)
         #rastercalc2.save(path + "\\lavacalbackup" + s)
         #del rastercalc
         focal1 = path + "\\focal1"
         focal2 = path + "\\focal2"
         #Process Focal Statistics
         arcpy.gp.FocalStatistics_sa(rastercalc2, focal1, "Rectangle 3 3 CELL", "MAXIMUM",
"DATA")
         arcpy.gp.FocalStatistics_sa(rastercalc2, focal2, "Circle 1 CELL", "MAXIMUM",
"DATA")
         focal1 = Raster(path + "\\focal1")
         focal2 = Raster(path + "\\focal2")
```

```
        #The same slope calculation but in a new location within the loop itself, as the slope
needs to be calculated repeatedly.
        #slope = path + "\\trash.gdb\\slope"
        outSlope = Slope(DEM1, "DEGREE", 1)
        outSlope.save(path + "\\trash.gdb\\slope")
        slope = path + "\\trash.gdb\\slope"
        #slope1 = Raster(slope)
        #slope2 = slope1*(3.14159/180)
        #slope2.save(path + "\\trash.gdb\\slope2")
        #for 0 degree slope, convert to very low slope value, will not run otherwise
        slope1 = Con(slope, slope, 0.01, "Value > 0")
        slope1.save(path + "\\trash.gdb\\slope1")

        slope2 = slope1*(3.14159/180)
        slope2.save(path + "\\trash.gdb\\slope2")
        #Critical Thickness
        #Calculate the critical thickness value, which is the equivalent of the yield strength of the
        #lava. Above a certain thickness, any excess lava will flow into adjacent cells, and
        #continue until either the volume is exhausted, or the critical thickness cannot be
        #exceeded.

        #The critical thickness, or alpha value, winds up being the amount of lava that can be left
        #in a cell, per iteration, and adds up to the maximum thickness that's defined in the first
        #lines of this code.
        #New alpha represents the critical thickness, rather than the lowering factor
        alpha = (10/(2700*3.7*Sin(slope2)))
        alpha.save(path + "\\trash.gdb\\alpha")
        #Set Flux
        lava1 = ((10*(Power(alpha,2))*463.0836)/(3*10))*((Power(lava/alpha,3))-
((3/2)*(Power(lava/alpha,2)))+(1/2))
        lava1.save(path + "\\trash.gdb\\lava1")
        #available thickess for cells
        lava2 = lava1/ (Power(cellSize,2))
        lava2.save(path + "\\trash.gdb\\lava2")

        #lowering = path + "\\trash.gdb\\lowering"
        low = alpha
        outcon = Con((((rastercalc2 > focal1 - low*1.414) | (rastercalc2 > focal2 - low)) &\
        (rastercalc2 > 0)), rastercalc2, Con(focal1 - low*1.414 > focal2 - low,\
        (Con(DEM1 + (low*1.414)>= focal1, 0, Con(focal1 - DEM1 >= lava + (low*1.414),\
        DEM1 + low, focal1 - (lava2*1.414)))),\
        (Con(DEM1 + lava2 >= focal2, 0,Con(focal2 - DEM1 >= lava + low, DEM1 +
lava2,focal2 – lava2)))))
        outcon.save(path + "\\lavaraster.gdb\\lavas" +s)
        extent = Raster(path + "\\lavaraster.gdb\\lavas" +s)
        outRas = SetNull(extent == 0, extent)
```

```
        outRas.save(path + "\\trash.gdb\\mask" +s)
        mask1 = Raster(path + "\\trash.gdb\\mask" +s)
        #Convert mask raster to integer
        outRas = Int(mask1)
        outRas.save(path + "\\trash.gdb\\intmask" +s)
        intmask = Raster(path + "\\trash.gdb\\intmask" +s)
        #Convert mask raster to polygon
        arcpy.RasterToPolygon_conversion(intmask,(path + "\\trash.gdb\\polymask"
+s),"NO_SIMPLIFY")
        mask = (path + "\\trash.gdb\\polymask" +s)
        outRas = ExtractByMask(DEM, mask)
        outRas.save(path + "\\trash.gdb\\extract" + s)
        extract = Raster(path + "\\trash.gdb\\extract" + s)
        outRas = Minus(mask1,extract)
        outRas.save(path + "\\trash.gdb\\add" + s)
        add = Raster(path + "\\trash.gdb\\add" + s)
        #Convert null to zero
        outRas = Con(IsNull(add),0,add)
        outRas.save(path + "\\lavas.gdb\\rastertoadd" + s)
        rastertoadd = Raster(path + "\\lavas.gdb\\rastertoadd" + s)
        rastersum = (path + "\\trash.gdb\\zonestats")
        field = "SUM"
        sum1 = ZonalStatisticsAsTable(CreateConsta2, "VALUE", rastertoadd, rastersum,
"NODATA", "SUM")
        cursor = arcpy.SearchCursor(rastersum)
        row = cursor.next()
        print(row.getValue(field))
        sum = sum + (row.getValue(field))

      numit = numit + 1
      #print numit
   print "Lava flow from eruption vent #" + s + "is complete"
   now = datetime.datetime.now()
   print now.strftime("%Y-%m-%d %H:%M")
arcpy.env.workspace = path + "\\lavas.gdb"
#creater a list of rasters in the workspace
rasters = arcpy.ListRasters("*", "ALL")
i = 0
iname = str(i)
#Create raster with the value 0 as the base from which to calculate the number of flows
conras = path + "\\finaloutput.gdb\\sumras0"
arcpy.gp.CreateConstantRaster_sa(conras, "0", "FLOAT", "28.8112458", DEM)
#Loop through raster in this List
for raster in rasters:
   print raster + "is processing"
```

```
    i = i + 1
    iname = str(i)
    outSum.save(path + "\\finaloutput.gdb\\sumras" + iname)
print "model run complete"
now = datetime.datetime.now()
```

Appendix 2: Horizontal Plain Model Version (Version 6)

Version 5 of the model was used to create the simulations that the results from this chapter were derived from. While simulating terrestrial and martian lava flows, an issue within the code of Version 5 was identified for the parameter combinations at the highest viscosity and yield strength values. The entire volume of lava that was erupted was not being fully distributed, and some of this volume was being lost during subsequent loops. This issue occurred because the calculated critical thickness values for each cell were not updated accurately during successive iterations through the model and introduced an artificial maximum storage capacity for some cells. If that maximum storage capacity was reached for too many cells in relatively close proximity to the eruption site, then that excess volume could not be properly distributed into adjacent cells that were outside of the initially calculated neighborhood derived at the beginning of the iteration, and would be lost at the beginning of the next iteration. That extra volume Therefore, it was concluded that the model was missing a nested loop that could account for any excess lava could not be distributed to cells that had reached their maximum critical thickness.

The newest model version (Version 6) was reworked to simulate lava flows on an initial horizontal plain, rather than on a surface representing the actual topography of both the terrestrial and martian sites. Version 6 can more accurately handle overall flow propagation while rectifying issues of excess lava distribution within looped code segments. Version 6 is undergoing additional modification that will allow for flow to be modeled using DEMs representative of actual surfaces.

Model Adjustments

A new DEM representing a horizontal plain was generated in the ArcGIS environment. A constant raster representing the horizontal plain had no initial elevation component where all

cells were set to a 0 m elevation, leaving the resultant surface without an intrinsic slope. This surface was used as the most basic DEM for development of this model version.

Some additional parameter modifications were necessary for Version 6. For the horizontal plain DEM there was no inherent slope, and I did not adjust the slope of the underlying regional topography, other than in special circumstances where a cell had a 0º slope and I changed the cell value to 0.05º. Otherwise, without this slope angle adjustment, the subsequent critical thickness calculation using the derived 0º slope value for that cell would return a null value and generate a point where propagation would fail. This issue was of primary concern when performing simulations on the horizontal plain, as the central processing cell that corresponded to the erupting vent location only returned a 0º slope value and led to an issue where no lava could be properly added to the source. This issue was the result of the moving window average method of slope calculation performed by ArcGIS. By replacing the 0º slope value with a value of 0.05º, a plug of lava was added with a sufficient thickness that allowed flow to propagate into surrounding cells.

Additionally, it was identified that the treatment of both viscosity and yield strength, in which the parameter values were adjusted on a 1:1 basis (e.g., η = 10 and *Sy* =10), was not accurate to reality. The viscosity of the lava is typically 1 to 2 orders of magnitude higher than the yield strength (e.g., η = 1000 and *Sy* =100; Harris, 2000), and each constant viscosity and yield strength parameter needed to be set accordingly before each simulation. This change to the yield strength was necessary, as the critical thickness (Eq. 5) would not change between model runs with different viscosities while using a constant *Sy* value, which would have resulted in outputs with the same overall extent. This change in yield strength is in line with the expectation of an increasing yield strength with increased viscosity of a lava, where a higher viscosity lava

would have a greater internal resistance to flow (e.g., Ishihara et al., 1990; Harris, 2000). This increased strength and resultant increased critical thickness would need to be reached prior to flow propagation into neighboring cells.

Version 5 of the model used a range of viscosity values, from 1 - 1000 Pa·s, representing a generally basaltic composition (e.g., Keszthelyi et al., 2000; Diniega et al., 2013), and Version 6 of the model uses the same range of viscosity values. Version 5 used a range of corresponding yield strength values (1 – 1000 Pa) which were matched to the viscosity values. Version 6 of the model was modified to use a wider range of yield strength values, from 0.01 – 1000 Pa, which more accurately represented the yield strengths associated with the range of viscosity values used in this model.

Horizontal Plain Model

The basic horizontal plain model was developed to ensure that flow propagation was occurring as intended, and that the total volume of lava was correctly being distributed to those cells that could accept any volume, based on their intrinsic critical thickness values. A pulse of lava was added to the central processing cell, representing the location of the source vent. This volume was then distributed to the closest neighboring cells, up to their intrinsic critical thickness values. Any excess volume beyond what these cells could accept would then be distributed to a newly derived group of neighboring cells that were further downslope. Once the full volume of the lava pulse was exhausted, the model would conclude the loop, and return to the beginning of the model to add another pulse of lava at the vent and repeat the process of distributing this volume to any cells that could accept a packet of lava.

The following examples of the model outputs from Version 6 (Figs. 23, 24), demonstrate the maximum areal extent for a simulated lava flow using this model would be achieved with

relatively low viscosity and yield strengths, and a wide range of densities. In these cases, there was little distinction between the model outputs, suggesting numerous parameter combinations representative of various basaltic compositions could results in long and widespread lava flows. The highest viscosity and yield strength parameter combinations resulted in less laterally extensive flow, as well as an increase in the overall thickness, particularly with regards to the volcanic plug that would develop at the site of the eruption.

Several parameter combinations were not simulated because of an issue where some critical thickness values were calculated using different yield strengths but would return the same critical thickness value. This issue resulted from the relevant equation (Eq. 5), where the yield strength had a direct bearing on the final critical thickness value. This issue meant that for certain parameter combinations, if the yield strength was the same (e.g., η:100/Sy:1 and η:10/Sy:1) the resulting critical thickness would be the same. Therefore, any results derived from these parameter combinations would ultimately be identical and could be skipped to avoid repetition.

Preliminary Results

The development of this version of the model was to determine the functionality of the lava distribution method and confirm complete distribution of the erupted lava. There was no calculation for the fitness of these outputs, as no observed flow was available for comparison to these results. The effectiveness for the distribution of the erupted volume was calculated based on the constant value for the total erupted volume, compared to the sum of the full thickness of

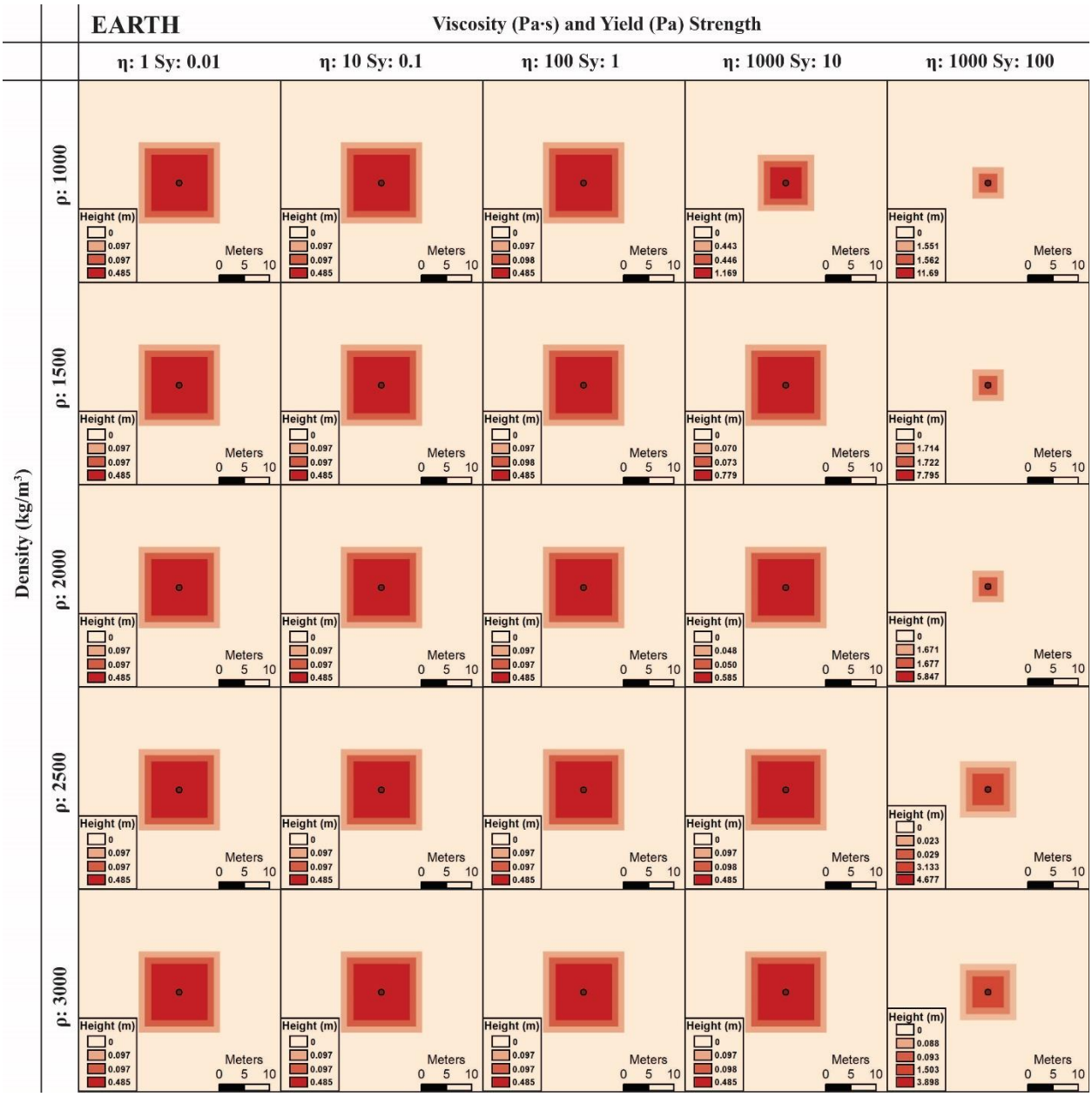

Figure 23. Terrestrial (g: 9.8 m/s^2) examples of flat-plain model outputs using various parameter combinations. All simulations were set with 1 m cell width and run through 50 complete iterations. Each iteration added 1 m of lava thickness to the central processing cell (red dot), which was then distributed to the neighboring cells until the erupted volume was exhausted. Variation in simulated thickness became apparent when reaching the highest viscosity and yield strength values, with a corresponding increase in the critical thickness value derived from those values in combination with decreasing density. All combinations of low viscosity and yield strengths (η:1/Sy:0.01, η:10/Sy:0.1/, η:100/Sy:1) generated outputs where the maximum thickness of the flow did not exceed the apparent flow minimum of 0.485 m, as well as two simulations of the η:1000/Sy:10 combination, with the highest density values at 2500 and 3000 kg/m^3. These results indicate that the maximum areal extent for a simulated lava flow using this model would be achieved with relatively low viscosity and yield strengths, and for simulations performed on a horizontal plain little-to-no distinction can be found for a wide range of representative basaltic characteristics.

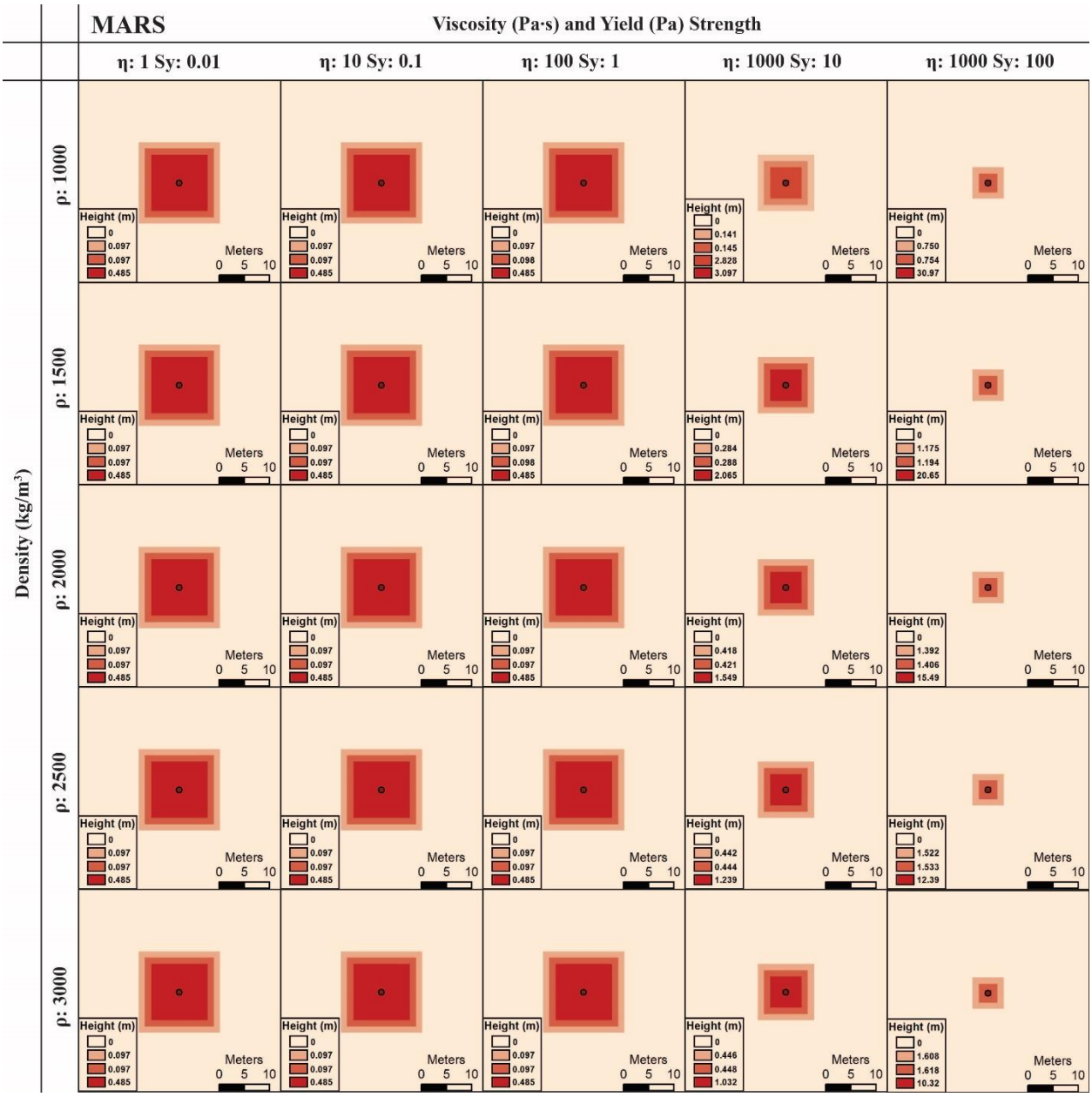

Figure 24. Martian (g: 3.7m/s^2) examples of flat-plain model outputs using various parameter combinations. All simulations were set with 1 m cell width and run through 50 complete iterations. Each iteration added 1 m of lava thickness to the central processing cell (red dot), which was then distributed to the neighboring cells until the erupted volume was exhausted. Variation in simulated thickness became apparent when reaching the highest viscosity and yield strength values, with a corresponding increase in the critical thickness value derived from those values in combination with decreasing density. All combinations of low viscosity and yield strengths (η:1/Sy:0.01, η:10/Sy:0.1/, η:100/Sy:1) generated outputs where the maximum thickness of the flow did not exceed the apparent flow minimum of 0.485 m. These results indicate that the maximum areal extent for a simulated lava flow using this model would be achieved with relatively low viscosity and yield strengths, and for simulations performed on a horizontal plain little-to-no distinction can be found for a wide range of representative basaltic characteristics.

lava present in each 1 m^2 cell that accepted lava. Version 6 was capable of fully distributing the total erupted volume, which was a constant value for each tested parameter combination, generating volcanic constructs that were taller and more areally restricted for high η and *Sy* parameter values, while shorter and more areally extensive volcanic constructs formed for low η and *Sy* parameter values (Fig. 23, 24).

An unexpected result identified during the development of the Version 6 was the observation of an apparent minimum thickness for the simulated lava flows on a horizontal plain. This minimum thickness of distributed lava was consistently found to be 0.485 m (Fig. 23, 24), regardless of the different parameter combinations and planetary gravities. No simulated lava flow ultimately supported a final flow thickness below this threshold. The various raster outputs for the relevant vent location, neighboring cells, slope, and critical thickness values were all individually inspected and manually calculated to ensure that this value was not an anomaly, but representative of a valid result. This apparent minimum thickness also leads to results for various parameter combinations that are nearly indistinguishable from each other, besides some minor variations in the distributed lava thickness near the edges of the derived flows. The parameter combinations with the lowest viscosities and yield strengths resulted in areal extents and thicknesses that were indistinguishable (Figs. 23, 24).

Discussion of Preliminary Results

Though the results for this chapter were generated from Version 5 of the model and cannot be considered as the most accurate outputs, I expect the same general trends of the model outputs to be found when the target flows are reexamined using the current version of the model. One caveat to consider is that the outputs generated from the horizontal plain using Version 6 of the model suggest a wider possible range of parameter combinations that could result in long and

areally extensive lava flows. However, this inference cannot be extrapolated to either the terrestrial or martian sites with confidence, as the model cannot yet be applied using DEMs that represent actual topography. Therefore, further modification of Version 6 is required, particularly the incorporation of topographic data representing real surfaces, with the understanding that new data may indicate several viscosity and yield strength parameter combinations could ultimately suffice for the development of long and areally extensive lava flows.

Appendix 3: Model Script (Version 6)

The following code is the heavily modified model version initially built upon the framework of the Gislason (2013) model.

```
import arcpy
from arcpy.sa import *
from arcpy import env
import datetime
import os
import math
#Return current date and time - repeated usage throughout model to identify timing of code segments
now = datetime.datetime.now()
print now.strftime("%m-%d-%Y %H:%M")
#Allow overwriting of previous outputs
arcpy.env.overwriteOutput = 1
#Check licenses to ensure usability on the python/Arc code segments
arcpy.CheckOutExtension("spatial")
#Define file pathways
path = "C:\Users\kgold\Desktop\NewModel" #Used to save space when saving raster outputs
volcanoes = "C:\Users\kgold\Desktop\NewModel\NewTest2.gdb\CenterPoint_cs1_1089cells" #Location of the vent/fissure
BaseDEM = "C:\Users\kgold\Desktop\NewModel\NewTest2.gdb\ConstantRaster_cs1_1089cells" #Base DEM that sets the extent and cell size
#Define variables (model inputs)
lava = float("1") #thickness of lava being extruded per iteration
Visc = 1000  #Viscosity at 1 to 2 orders of magnitude higher than the yield strength. Per Harris 2000
Yield = 100
Angle = 0.05 #Angle to be used for the source vent/fissure on a horizontal surface.
Density = 3000
Gravity = 9.8
maxit = int("50") #maximum number of iterations for the model - total number of top level loops to be performed
cellsize = int("1") #Cell size. Can also be defined by the extent of a raster
#make geodatabases and folders, where the raster/feature outputs will be saved
arcpy.CreateFileGDB_management(path, "workspace.gdb") #save all rasters to one place

os.makedirs(path + "\\lavapoints") #points and lines are saved here, issues arise when saved in the raster geodatabase
#Create constant rasters   #MAKE SURE CALLING TO CORRECT RASTERS
CreateConsta1 = path + "\\workspace.gdb\\lava_source" #USE THIS RASTER FOR THE ERUPTION SITE
arcpy.gp.CreateConstantRaster_sa(CreateConsta1, (0.00000001), "FLOAT", cellsize, BaseDEM) #Needed for point conversion. Also needs to have a non-zero value.
```

```
CreateConsta2 = path + "\\workspace.gdb\\raster" #USE THIS RASTER FOR SUMS AND
EXTENTS
arcpy.gp.CreateConstantRaster_sa(CreateConsta2, 0, "INTEGER", cellsize, BaseDEM) #extent
changed to that of the DEM rather than the shapefile
#print "Raster created"
#Convert raster to point - these steps will define the location of the source vent/fissure
inRaster = path + "\\workspace.gdb\\lava_source"
outPoint = path + "\\workspace.gdb\\pointsuncut"
field = "Value"
arcpy.RasterToPoint_conversion(inRaster, outPoint, field)
#clip the points to the polygons assigned to source locations
pointscut = path + "\\workspace.gdb\\pointscut"
arcpy.Clip_analysis(outPoint,volcanoes,pointscut, "")
#Calculate new field
arcpy.CalculateField_management(pointscut, "pointid", "[OBJECTID] + 1", "VB", "")
#The additional numbers are added in case there are additional vents/fissures.
#Most eruptions can be simulatsed with single point/line features

lavapoints = path + "\\lavapoints"
pointscut = path + "\\workspace.gdb\\pointscut"
#Split Layer by Attributes

arcpy.SplitByAttributes_analysis(pointscut, lavapoints, ['pointid'])
#print "points made"

#Set extent of the raster layers
arcpy.env.extent = BaseDEM
#Set the workspace
arcpy.env.workspace = path + "\\lavapoints"
shp_List = arcpy.ListFiles("*.shp")
valField = "grid_code"
inFeatures = pointscut
outRaster = path + "\\workspace.gdb\\lava" #newly created raster layer - the vent where lava is
added
cellSize = 1
#Execute FeatureToRaster - converts the vent point to a raster, for processing
arcpy.FeatureToRaster_conversion(inFeatures, valField, outRaster, cellSize)
print "Vent location processed"
arcpy.CopyRaster_management(outRaster, path + "\\workspace.gdb\\DEM")
#copy of rasters that will be updated and replaced within loops
DEM = path + "\\workspace.gdb\\DEM"
arcpy.CopyRaster_management(outRaster, path + "\\workspace.gdb\\updateHCR")

arcpy.CopyRaster_management(CreateConsta2, path + "\\workspace.gdb\\DEM_COPY")

now = datetime.datetime.now()
```

```
print now.strftime("%m-%d-%Y %H:%M")
#Zero values for various rasters that are copied, update, deleted, and replaced throughout the
model
numit = 1
num = 0
num1 = 0
num2 = 0
Value1 = 0
Value2 = 0
Value2update = 0
Value6 = 0
Value7 = 0
Value8 = 0
HCR1 = 0
HCR2 = 0
DEMupdate_newVal2a = 0
rasterDEM = (path + "\\NewTest2.gdb\\raster")
DEM = Raster(path + "\\workspace.gdb\\DEM")
updateHCR = Raster(path + "\\workspace.gdb\\updateHCR")
vent = Raster(path + "\\workspace.gdb\\lava")

while numit < maxit:
    print"ITERATION #"
    print numit
    now = datetime.datetime.now()
    print now.strftime("%m-%d-%Y %H:%M")

    #add pulse of lava to the vent
    vent_add1 = (lava + vent)
    vent_add1.save(path + "\\workspace.gdb\\vent_add1")
    #replace original vent with updated vent thickness
    arcpy.Delete_management(vent)
    arcpy.CopyRaster_management(vent_add1, vent)
    #Setting the vent as the DEM that focal statistics can be performed on.
    #By changing the name here, can be replaced with updated DEM values
    #later in the model that take into account the updated topography as
    #lava is added.
    vent_add2 = Con(IsNull(vent_add1), 0, vent_add1)
    vent_add2.save(path + "\\workspace.gdb\\vent_add2")
    vent_add2_b = Con(IsNull(DEM), 0, DEM)
    vent_add2_b.save(path + "\\workspace.gdb\\vent_add2_b")
    vent_add3 = Con(vent_add2_b > vent_add2, vent_add2_b, vent_add2)
    vent_add3.save(path + "\\workspace.gdb\\vent_add3")
    #replace DEM with updated value
    arcpy.Delete_management(DEM)
    arcpy.CopyRaster_management(vent_add3, DEM)
```

```
    rastercalc = Con(IsNull(DEM), 0, DEM)
    rastercalc.save(path + "\\workspace.gdb\\rastercalc")
    #Initial slope calculation performed on just the initial processing cell and
    #doesn't include any neighbors. The area of the slope calculation increases as
    #the neighborhood expands.
    slope = Slope(rastercalc, "DEGREE", 1)
    slope.save(path + "\\workspace.gdb\\slope")

    focal_DEM = path + "\\workspace.gdb\\focal_DEM"
    arcpy.gp.FocalStatistics_sa(rastercalc, focal_DEM, "Rectangle 3 3 CELL", "MAXIMUM",
"NODATA")
    focal_DEM = Raster(path + "\\workspace.gdb\\focal_DEM")

    slope_extent = SetNull(focal_DEM == 0, focal_DEM)
    slope_extent.save(path + "\\workspace.gdb\\slope_extent")

    mask_slope1 = ExtractByMask(slope, slope_extent)  #changed raster for extraction from
DEM to rastercalc, issue with values when using DEM
    mask_slope1.save(path + "\\workspace.gdb\\mask_slope1")

    #For 0 degree slope, convert to low slope value. A horizontal plain has no slope,
    #but the surface needs a slope value to overcome the internal resistance to flow.
    #The higher the slope angle, the lower the hcr value.

    slope1 = Con(mask_slope1 == 0, Angle, mask_slope1)
    slope1.save(path + "\\workspace.gdb\\slope1")

    #Critical Thickness - Set desired density and planetary gravity
    #Slope value multiplication in this stage is due to the SIN function being set in
    #radians by default, and the slope calculation outputs being set in degrees, and
    #the resultant conversion that is required.
    #This value will change as more lava is added to the source vent,
    #as the slope angle will change with the neighboring cells.

    #separated the Sin calculation to ensure it was being performed correctly.
    #Can be reconsolidated into the hcr calculation
    Sin1 = Sin(slope1*(3.14159/180))
    Sin1.save(path + "\\workspace.gdb\\Sin1")

    hcr = (Yield/(Density*Gravity*(Sin1)))
    hcr.save(path + "\\workspace.gdb\\hcr")
    hcr = Raster(path + "\\workspace.gdb\\hcr")

    num1 = num1 + 1
    n = str(num1) #Number has to be a string in the next step
```

```
    HCR_COPY = path + "\\workspace.gdb\\HCR_COPY" + n #extraneous and can be removed
    arcpy.CopyRaster_management(hcr, HCR_COPY) #extraneous and can be removed

    #Extract the value of the lava that has been added to the source vent/fissure.
    lava_sum = Con(IsNull(vent),0,vent)
    lava_sum.save(path + "\\workspace.gdb\\lava_sum")
    rastersum_lava = (path + "\\workspace.gdb\\zonestats1")
    field = "SUM"
    sum1 = ZonalStatisticsAsTable(CreateConsta2, "VALUE", vent, rastersum_lava, "DATA",
"SUM")
    cursor = arcpy.SearchCursor(rastersum_lava)
    row = cursor.next()
    print "Value1 - Lava being added to the source vent"
    print (row.getValue(field))
    Value1 = (row.getValue(field))

    #Extract the HCR value of just the vent.
    vent_hcr = SetNull(vent == 0, hcr)
    vent_hcr.save(path + "\\workspace.gdb\\vent_hcr")

    #need to have a conditional statement here regarding the replacement value for the vent,
    #after it was filled to the new HCR2 value
    new_vent_hcr = Con(vent_hcr > DEMupdate_newVal2a, vent_hcr, DEMupdate_newVal2a)
    new_vent_hcr.save(path + "\\workspace.gdb\\new_vent_hcr")

    vent_sum = Con(IsNull(new_vent_hcr),0,new_vent_hcr)
    vent_sum.save(path + "\\workspace.gdb\\vent_sum")
    rastersum_vent = (path + "\\workspace.gdb\\zonestats2")
    field = "SUM"
    sum2 = ZonalStatisticsAsTable(CreateConsta2, "VALUE", new_vent_hcr, rastersum_vent,
"DATA", "SUM")
    cursor = arcpy.SearchCursor(rastersum_vent)
    row = cursor.next()
    print "Value2 - Vent critical thickness"
    print(row.getValue(field))
    Value2 = (row.getValue(field))
    #Extract the extent of each new neighboring ring, for the extraction of new HCR values.
    ring_extent = SetNull(rastercalc == 0, rastercalc) #changed from DEM to rastercalc
    ring_extent.save(path + "\\workspace.gdb\\ring_extent")

    mask_ring_a = ExtractByMask(hcr, ring_extent)
    mask_ring_a.save(path + "\\workspace.gdb\\mask_ring_a")

    mask_ring_b = Con(IsNull(mask_ring_a),0,mask_ring_a)
    mask_ring_b.save(path + "\\workspace.gdb\\mask_ring_b")
```

```
    ring_minus = Minus(hcr, mask_ring_b)
    ring_minus.save(path + "\\workspace.gdb\\ring_minus")

    ring_null = SetNull(ring_minus == 0, ring_minus)
    ring_null.save(path + "\\workspace.gdb\\ring_null")
    #Extract new minimum HCR values from each successive ring. Sets the value at which
    #each cell will fill to.
    rastersum_hcr = (path + "\\workspace.gdb\\zonestats_hcr")
    field = "MIN"
    sum_hcr = ZonalStatisticsAsTable(CreateConsta2, "VALUE", ring_null, rastersum_hcr,
"DATA", "MINIMUM")
    cursor = arcpy.SearchCursor(rastersum_hcr)
    row = cursor.next()
    print "HCR1 - HCR zonestats acquired - Initial Minimum Neighbor HCR Value"
    print(row.getValue(field))
    HCR1 = (row.getValue(field))

    ring_hcr = Con(ring_null > HCR1, HCR1, ring_null)
    ring_hcr.save(path + "\\workspace.gdb\\ring_hcr")

    numit = numit + 1

    while Value1 > Value2:

        print "Lava distribution happening"
        now = datetime.datetime.now()
        print now.strftime("%m-%d-%Y %H:%M")

        #Determine the excess lava beyond the critical thickness - to be distributed to surrounding
cells
        lavas2 = lava_sum - vent_sum
        lavas2.save(path + "\\workspace.gdb\\lavas2")
        #This is the amount of lava that can actually be distributed
        rastersum_excess = (path + "\\workspace.gdb\\zonestats3")
        sum_excess = ZonalStatisticsAsTable(CreateConsta2, "VALUE", lavas2, rastersum_excess,
"NODATA", "SUM")
        cursor = arcpy.SearchCursor(rastersum_excess)
        row = cursor.next()
        field = "SUM"
        print "Excess lava to be distributed"
        print(row.getValue(field))
        Value_excess = (row.getValue(field))
        #Set the extent to that of only the focal stats.
        #This is to change the value of the cells surrounding the processing cell
        #to null.
```

```
        focal_extent1a = SetNull(focal_DEM == 0, focal_DEM)
        focal_extent1a.save(path + "\\workspace.gdb\\focal_extent1a")

        mask_neighborhood = ExtractByMask(rastercalc, focal_extent1a)  #changed raster for
extraction from DEM to rastercalc, issue with values when using DEM
        mask_neighborhood.save(path + "\\workspace.gdb\\mask_neighborhood")

        #Flux calculations broken down into separate components to ensure accuracy of
calculations.
        #Can be consolidated
        flux1 = ((Yield*cellSize*(Power(new_vent_hcr,2)))/(3*Visc))
        flux1.save(path + "\\workspace.gdb\\flux1")
        flux2 = (Power((lavas2/new_vent_hcr),3))
        flux2.save(path + "\\workspace.gdb\\flux2")
        flux3 = ((1.5)*(Power((lavas2/new_vent_hcr),2)))
        flux3.save(path + "\\workspace.gdb\\flux3")

        #Set Total Flux Volume
        flux4 = flux1*(flux2 - flux3 + 0.5)
        flux4.save(path + "\\workspace.gdb\\flux4")
        #Extract value for the total available flux that can flow into any neighboring cells.
        flux_sum = Con(IsNull(flux4),0,flux4)
        flux_sum.save(path + "\\workspace.gdb\\flux_sum")
        rastersum_flux = (path + "\\workspace.gdb\\zonestats4")
        field = "SUM"
        sum3 = ZonalStatisticsAsTable(CreateConsta2, "VALUE", flux_sum, rastersum_flux,
"NODATA", "SUM")
        cursor = arcpy.SearchCursor(rastersum_flux)
        row = cursor.next()
        print "Value3"
        print "Total available flux for flow into neighboring cells per time step"
        print(row.getValue(field))
        Value3 = (row.getValue(field))

        CreateConsta3 = path + "\\workspace.gdb\\dist_raster"
        arcpy.gp.CreateConstantRaster_sa(CreateConsta3, Value2, "FLOAT", cellsize, BaseDEM)

        CreateConsta4 = path + "\\workspace.gdb\\dist_raster2"
        arcpy.gp.CreateConstantRaster_sa(CreateConsta4, Value3, "FLOAT", cellsize, BaseDEM)
        print "LOOK HERE"
        outcon3 = Con(mask_neighborhood < Value2, mask_neighborhood, Value2)
        outcon3.save(path + "\\workspace.gdb\\lava_dist")

        mask_neighborhood1 = ExtractByMask(CreateConsta2, focal_extent1a)
        mask_neighborhood1.save(path + "\\workspace.gdb\\mask_neighborhood1")
```

```
#adding the ring to the previous DEM, so there's a new HCR value for distribution.
#Need to replace the updateHCR raster in the last segment of the loop, before the
#model restarts at the beginning.
#add the ring_hcr to that raster on successive iterations

forMax0 = Con(IsNull(updateHCR), 0, updateHCR)
forMax0.save(path + "\\workspace.gdb\\forMax0")

forMax00 = Con(IsNull(new_vent_hcr), 0, new_vent_hcr)
forMax00.save(path + "\\workspace.gdb\\forMax00")

forMax000 = Plus(forMax0, forMax00)
forMax000.save(path + "\\workspace.gdb\\forMax000")

forMaxa = Con(forMax000 >= Value2, Value2, forMax000)
forMaxa.save(path + "\\workspace.gdb\\forMaxa")

forMaxb = Con(IsNull(ring_hcr), 0, ring_hcr)
forMaxb.save(path + "\\workspace.gdb\\forMaxb")

forMaxc = Con(forMaxa == 0, forMaxb, forMaxa)
forMaxc.save(path + "\\workspace.gdb\\forMaxc")

forMaxf = SetNull(forMaxc == 0, forMaxc)
forMaxf.save(path + "\\workspace.gdb\\forMaxf")

forMaxg = Con(forMaxf < HCR1, HCR1, forMaxf)
forMaxg.save(path + "\\workspace.gdb\\forMaxg")

forMaxgb = Con(IsNull(forMaxg), 0, forMaxg)
forMaxgb.save(path + "\\workspace.gdb\\forMaxgb")

arcpy.Delete_management(updateHCR)
arcpy.CopyRaster_management(forMaxg, updateHCR)

DistributedLava = 0

while DistributedLava < Value_excess and Value8 <= HCR1:
   print "Starting Distribution Loop"

   cell_count1a = Con(outcon3 < HCR1, HCR1, 0)
   cell_count1a.save(path + "\\workspace.gdb\\cell_count_lessthanhcr_sum")

   cell_count1b = SetNull(cell_count1a == 0, cell_count1a)
   cell_count1b.save(path + "\\workspace.gdb\\cell_count_null")
   #Extract the number of cells that the flux will be divided by
```

```
        rastersum_cells1 = (path + "\\workspace.gdb\\zonestats5")
        field = "COUNT"
        sum4 = ZonalStatisticsAsTable(mask_neighborhood1, "VALUE", cell_count1b,
rastersum_cells1, "DATA", "ALL")
        cursor = arcpy.SearchCursor(rastersum_cells1)
        row = cursor.next()
        print "Value4"
        print "Number of cells (below hcr)" #by which to divide flux value"
        print(row.getValue(field))
        Value4 = (row.getValue(field))
        #How much lava is going into each cell.
        Value5 = (Value3/Value4)
        print "Value5"
        print "Total Flux Value per time step Divided by the Number of Cells Available for flux"
        print(Value3/Value4)

        outconsub = Con(outcon3 >= HCR1, outcon3, 0)
        outconsub.save(path + "\\workspace.gdb\\outconsub")

        print "Total Lava That Can Be Distributed into each Cell"
        DistributedLavatoEachCell = (Value_excess / Value4)
        print DistributedLavatoEachCell

        outcon4 = Con(outconsub == 0, DistributedLavatoEachCell, outconsub)
        outcon4.save(path + "\\workspace.gdb\\lava_dist2")

        print "Excess lava"
        print Value_excess
        #This value change is to speed up the overall processing and distribute all of the lava in
        #this eruption pulse in one shot, rather than using a time step for each flux pulse that
        #is equal to Value 5. Retained calculations for the sake of transparency.
        DistributedLava = Value_excess
        print "Total Distributed Lava within this and the subsequent excess lava Loop"
        print Value_excess

        print "Current HCR"
        print HCR1

        outcon7 = Con(IsNull(outcon4), 0, outcon4)
        outcon7.save(path + "\\workspace.gdb\\sub_DEM2")

        NewDEM = Plus(rasterDEM, outcon7)
        NewDEM.save(path + "\\workspace.gdb\\NewDEM")

        DEMupdate_newVal2 = Con(new_vent_hcr < HCR1, HCR1, new_vent_hcr)
        DEMupdate_newVal2.save(path + "\\workspace.gdb\\DEMupdate_newVal2")
```

```
        vent_sum2 = Con(IsNull(DEMupdate_newVal2),0,DEMupdate_newVal2)
        vent_sum2.save(path + "\\workspace.gdb\\vent_sum2")
        rastersum_vent2 = (path + "\\workspace.gdb\\zonestats22")
        field = "SUM"
        sum2 = ZonalStatisticsAsTable(CreateConsta2, "VALUE", DEMupdate_newVal2,
rastersum_vent2, "DATA", "SUM")
        cursor = arcpy.SearchCursor(rastersum_vent2)
        row = cursor.next()
        print "Update of Value2 - Vent critical thickness"
        print(row.getValue(field))
        Value2update = (row.getValue(field))
        Value2 = Value2update

        outcon9 = Con(NewDEM >= Value2, Value2, NewDEM)
        outcon9.save(path + "\\workspace.gdb\\New_DEM2")

        arcpy.Delete_management(rasterDEM)

        arcpy.CopyRaster_management(outcon9, rasterDEM)

        CellThicknessa = Con(IsNull(rasterDEM),0,rasterDEM)
        CellThicknessa.save(path + "\\workspace.gdb\\CellThicknessa")

        CellThickness1a = Con(CellThicknessa == 0, Value2, CellThicknessa)
        CellThickness1a.save(path + "\\workspace.gdb\\CellThickness1a")

        CellThickness_suma = (path + "\\workspace.gdb\\zonestats_CellThicknessa")
        field = "MIN"
        sum_DEM = ZonalStatisticsAsTable(CreateConsta2, "VALUE", CellThickness1a,
CellThickness_suma, "NODATA", "MINIMUM")
        cursor = arcpy.SearchCursor(CellThickness_suma)
        row = cursor.next()
        print "Total Lava That Can Be Added to Each Raster Cell"
        print(row.getValue(field))
        Value8 = (row.getValue(field))

        DEMupdate_c = Con(CellThicknessa > forMaxg, forMaxg, CellThicknessa)
        DEMupdate_c.save(path + "\\workspace.gdb\\DEMupdate_c")

        DEMupdate_d = Con(IsNull(DEMupdate_c), 0, DEMupdate_c)
        DEMupdate_d.save(path + "\\workspace.gdb\\DEMupdate_d")

        DEMupdate_gb = Con(DEMupdate_d == 0, Value2, DEMupdate_d)
        DEMupdate_gb.save(path + "\\workspace.gdb\\DEMupdate_gb")
```

```
        arcpy.Delete_management(rasterDEM)
        arcpy.CopyRaster_management(DEMupdate_d, rasterDEM)

        #Actual Amount Distributed, if excess lava exists and the ring hcr was exceeded
        ActualDistribution = (path + "\\workspace.gdb\\zonestats_ActualDistribution")
        field = "MIN"
        sum_Dist = ZonalStatisticsAsTable(CreateConsta2, "VALUE", DEMupdate_gb,
ActualDistribution, "NODATA", "MINIMUM")
        cursor = arcpy.SearchCursor(ActualDistribution)
        row = cursor.next()
        print "Total ACTUAL Added Lava to Each Raster Cell"
        print(row.getValue(field))
        ActualDistributionValue = (row.getValue(field))
        print "Actual Distributed Amount"
        print "PER CELL"

        print "Lava distributed within loop"
        now = datetime.datetime.now()
        print now.strftime("%m-%d-%Y %H:%M")

      if DistributedLava >= Value_excess and DistributedLava <= HCR1:

        #print "Adding lava to raster and Determining if excess exists to expand neighborhood"
        print "Continue adding lava to the DEM until the HCR has been reached"
        print "Restarting Distribution Loop"

        new_vent = ExtractByMask(outcon9, vent)
        new_vent.save(path + "\\workspace.gdb\\new_vent")

        new_vent2 = Con(new_vent > forMaxg, forMaxg, new_vent)
        new_vent2.save(path + "\\workspace.gdb\\new_vent2")

        arcpy.Delete_management(vent)
        arcpy.CopyRaster_management(new_vent2, vent)

        Value1 = Value2
        print "update to Value1 - Distributed lava loop"
        print Value1

        print "HCR"
        print HCR1

        print "Added Lava to the primary DEM"
        print Value8

        now = datetime.datetime.now()
```

```
    print now.strftime("%m-%d-%Y %H:%M")

if DistributedLava > HCR1:

    #This loop only handles the excess lava from the previous segment.
    print "Distributing EXCESS lava"
    #This value needs to represent the excess of the lava that still
    #needs to be distributed after the HCR has been reached. This value
    #also needs to be the total excess across Value4 number of cells,
    #as the previous value was divided by Value 4.
    Value7 = (Value_excess - (ActualDistributionValue * 8))
    print "Value7 - New excess of excess lava for distribution"
    print Value7

    DistributedLava = 0
    print "Distributed lava reset #1"
    print DistributedLava

    Value_excess = Value7
    print "Excess lava reset"
    print Value_excess

    new_vent = ExtractByMask(outcon9, vent)
    new_vent.save(path + "\\workspace.gdb\\new_vent")

    new_vent2 = Con(new_vent > forMaxg, new_vent, forMaxg)
    new_vent2.save(path + "\\workspace.gdb\\new_vent2")

    arcpy.Delete_management(vent)

    arcpy.CopyRaster_management(new_vent2, vent)

    newest_surface = SetNull(rasterDEM == 0, rasterDEM)
    newest_surface.save(path + "\\workspace.gdb\\newest_surface")

    arcpy.Delete_management(DEM)
    arcpy.CopyRaster_management(newest_surface, DEM)

    print "DEM Replaced - New Neighborhood to be Calculated"
    Value1 = Value2

    print "update to Value1 - excess lava from this loop will add in Value7"
    print Value1

    add1a = (Value7 + vent)
    add1a.save(path + "\\workspace.gdb\\lava_NEW")
```

```
        arcpy.Delete_management(vent)
        arcpy.CopyRaster_management(add1a, vent)

        add1b = Con(IsNull(add1a), 0, add1a)
        add1b.save(path + "\\workspace.gdb\\add1b")

        add2 = Con(add1b == 0, DEM, add1b)
        add2.save(path + "\\workspace.gdb\\add2")

        arcpy.Delete_management(DEM)
        arcpy.CopyRaster_management(add2, DEM)

        rastercalc2 = Con(IsNull(DEM), 0, DEM)
        rastercalc2.save(path + "\\workspace.gdb\\rastercalc2")

        outSlope = Slope(rastercalc2, "DEGREE", 1)
        outSlope.save(path + "\\workspace.gdb\\slopeb")
        slopeb = path + "\\workspace.gdb\\slopeb"

        focal_DEM2 = path + "\\workspace.gdb\\focal_DEM2"
        arcpy.gp.FocalStatistics_sa(rastercalc2, focal_DEM2, "Rectangle 3 3 CELL",
"MAXIMUM", "DATA")
        focal_DEM2 = Raster(path + "\\workspace.gdb\\focal_DEM2")

        outRas = SetNull(focal_DEM2 == 0, focal_DEM2)
        outRas.save(path + "\\workspace.gdb\\slope_extent2")
        slope_extent2 = Raster(path + "\\workspace.gdb\\slope_extent2")

        mask_slope2 = ExtractByMask(slopeb, slope_extent2)
        mask_slope2.save(path + "\\workspace.gdb\\mask_slope2")

        slope2 = Con(mask_slope2 == 0, Angle, mask_slope2)
        slope2.save(path + "\\workspace.gdb\\slope2")

        Sin2 = Sin(slope2*(3.14159/180))
        Sin2.save(path + "\\workspace.gdb\\Sin2")
        rasterhcr2 = (Yield/(Density*Gravity*(Sin2)))
        rasterhcr2.save(path + "\\workspace.gdb\\rasterhcr2")
        rasterhcr2 = Raster(path + "\\workspace.gdb\\rasterhcr2")

        num2 = num2 + 1
        m = str(num2) #Number has to be a string in the next step

        ring_extent2 = SetNull(slope_extent == 0, slope_extent)
        ring_extent2.save(path + "\\workspace.gdb\\ring_extent2")
```

```
        mask_ring_2a = ExtractByMask(rasterhcr2, ring_extent2)
        mask_ring_2a.save(path + "\\workspace.gdb\\mask_ring_2a")

        mask_ring_2b = Con(IsNull(mask_ring_2a),0,mask_ring_2a)
        mask_ring_2b.save(path + "\\workspace.gdb\\mask_ring_2b")

        ring_minus2 = Minus(rasterhcr2, mask_ring_2b)
        ring_minus2.save(path + "\\workspace.gdb\\ring_minus2")

        ring_null2 = SetNull(ring_minus2 == 0, ring_minus2)
        ring_null2.save(path + "\\workspace.gdb\\ring_null2")

        rastersum_hcr2 = (path + "\\workspace.gdb\\zonestats_hcr2")
        field = "MIN"
        sum_hcr = ZonalStatisticsAsTable(CreateConsta2, "VALUE", ring_null2,
rastersum_hcr2, "DATA", "MINIMUM")
        cursor = arcpy.SearchCursor(rastersum_hcr2)
        row = cursor.next()
        print "HCR2 zonestats acquired - Minimum Neighbor HCR Value - NEW HCR AFTER
ADDED LAVA"
        print(row.getValue(field))
        HCR2 = (row.getValue(field))

        ring_hcr2 = Con(ring_null2 > HCR2, HCR2, ring_null2)
        ring_hcr2.save(path + "\\workspace.gdb\\ring_hcr2")

        while DistributedLava < Value_excess:

            print "Lava distribution happening"
            now = datetime.datetime.now()
            print now.strftime("%m-%d-%Y %H:%M")

            focal_extent2a = SetNull(focal_DEM2 == 0, focal_DEM2)
            focal_extent2a.save(path + "\\workspace.gdb\\focal_extent2a")

            mask_neighborhood2 = ExtractByMask(rastercalc2, focal_extent2a)
            mask_neighborhood2.save(path + "\\workspace.gdb\\mask_neighborhood2")

            flux1 = ((Yield*cellSize*(Power(new_vent_hcr,2)))/(3*Visc))
            flux1.save(path + "\\workspace.gdb\\flux1")
            flux2 = (Power((lavas2/new_vent_hcr),3))
            flux2.save(path + "\\workspace.gdb\\flux2")
            flux3 = ((1.5)*(Power((lavas2/new_vent_hcr),2)))
            flux3.save(path + "\\workspace.gdb\\flux3")
```

```
        flux4 = flux1*(flux2 - flux3 + 0.5)
        flux4.save(path + "\\workspace.gdb\\flux4")

        flux_sum2 = Con(IsNull(flux4),0,flux4)
        flux_sum2.save(path + "\\workspace.gdb\\flux_sum2")
        rastersum_flux2 = (path + "\\workspace.gdb\\zonestats4")
        field = "SUM"
        sum3 = ZonalStatisticsAsTable(CreateConsta2, "VALUE", flux_sum2,
rastersum_flux2, "NODATA", "SUM")
        cursor = arcpy.SearchCursor(rastersum_flux2)
        row = cursor.next()
        print "Value3a - Total available flux for flow into neighboring cells"
        print(row.getValue(field))
        Value3a = (row.getValue(field))

        CreateConsta3 = path + "\\workspace.gdb\\dist_rasterb"
        arcpy.gp.CreateConstantRaster_sa(CreateConsta3, Value2, "FLOAT", cellsize,
BaseDEM)

        CreateConsta4 = path + "\\workspace.gdb\\dist_raster2b"
        arcpy.gp.CreateConstantRaster_sa(CreateConsta4, Value3a, "FLOAT", cellsize,
BaseDEM)

        outcon3a = Con(mask_neighborhood2 < Value2, rasterDEM, Value2)
        outcon3a.save(path + "\\workspace.gdb\\lava_distb")

        mask_neighborhood2b = ExtractByMask(CreateConsta2, focal_extent2a)
        mask_neighborhood2b.save(path + "\\workspace.gdb\\mask_neighborhood2b")

        cell_count2a = Con(outcon3a < HCR2, HCR2, 0)
        cell_count2a.save(path + "\\workspace.gdb\\cell_count_lessthanhcr_sum2")

        cell_count2b = SetNull(cell_count2a == 0, cell_count2a)
        cell_count2b.save(path + "\\workspace.gdb\\cell_count_null2")

        rastersum_cells2 = (path + "\\workspace.gdb\\zonestats6")
        field = "COUNT"
        sum4 = ZonalStatisticsAsTable(mask_neighborhood2b, "VALUE", cell_count2b,
rastersum_cells2, "DATA", "ALL")
        cursor = arcpy.SearchCursor(rastersum_cells2)
        row = cursor.next()
        print "Number of cells (below hcr) by which to divide flux value"
        print(row.getValue(field))
        Value4a = (row.getValue(field))

        Value5 = (Value3a/Value4a)
```

```
        print "Value5 - Total Flux Value Divided by the Number of Cells Available for flux"
#how much is going into each cell
        print(Value3a/Value4a)

        outconsuba = Con(outcon3a >= HCR2, mask_neighborhood2b, 0) #changed the order
of the secondary traits
        outconsuba.save(path + "\\workspace.gdb\\outconsuba")

        DistributedLava = 0
        Value8 = 0

        while DistributedLava < Value_excess:
            print "Excess Distribution Loop"
            print "Value5"
            print Value5

            DistributedLavatoEachCell = (Value_excess / Value4a)

            outcon4b = Con(outconsuba == 0, DistributedLavatoEachCell, outconsuba)
            outcon4b.save(path + "\\workspace.gdb\\lava_dist2b")

            print "Excess lava"
            print Value_excess

            DistributedLava = Value_excess
            print "Distributed Lava"
            print Value_excess

            print "HCR"

            outcon7b = Con(IsNull(outcon4b), 0, outcon4b)
            outcon7b.save(path + "\\workspace.gdb\\sub_DEM2b")

            NewDEMb = Plus(rasterDEM, outcon7b)
            NewDEMb.save(path + "\\workspace.gdb\\NewDEMb")

            DEMupdate_newVal2a = Con(new_vent_hcr < HCR2, HCR2, new_vent_hcr)
            DEMupdate_newVal2a.save(path + "\\workspace.gdb\\DEMupdate_newVal2a")

            vent_sum2 = Con(IsNull(DEMupdate_newVal2a),0,DEMupdate_newVal2a)
            vent_sum2.save(path + "\\workspace.gdb\\vent_sum2")
            rastersum_vent2 = (path + "\\workspace.gdb\\zonestats22")
            field = "SUM"
            sum2 = ZonalStatisticsAsTable(CreateConsta2, "VALUE", DEMupdate_newVal2a,
rastersum_vent2, "DATA", "SUM")
            cursor = arcpy.SearchCursor(rastersum_vent2)
```

```
row = cursor.next()
print "Update of Value2 - Vent critical thickness"
print(row.getValue(field))
Value2update = (row.getValue(field))
Value2 = Value2update

forMax02 = Con(IsNull(updateHCR), 0, updateHCR)
forMax02.save(path + "\\workspace.gdb\\forMax02")

forMax002 = Con(IsNull(new_vent_hcr), 0, new_vent_hcr)
forMax002.save(path + "\\workspace.gdb\\forMax002")

forMax0002 = Plus(forMax02, forMax002)
forMax0002.save(path + "\\workspace.gdb\\forMax0002")

forMaxa2 = Con(forMax0002 >= Value2, Value2, forMax0002)
forMaxa2.save(path + "\\workspace.gdb\\forMaxa2")

forMaxb2 = Con(IsNull(ring_hcr2), 0, ring_hcr2)
forMaxb2.save(path + "\\workspace.gdb\\forMaxb2")

forMaxc2 = Con(forMaxa2 == 0, forMaxb2, forMaxa2)
forMaxc2.save(path + "\\workspace.gdb\\forMaxc2")

forMaxf2 = SetNull(forMaxc2 == 0, forMaxc2)
forMaxf2.save(path + "\\workspace.gdb\\forMaxf2")

forMaxg2 = Con(forMaxf2 < HCR2, HCR2, forMaxf2)
forMaxg2.save(path + "\\workspace.gdb\\forMaxg2")

forMaxgb2 = Con(IsNull(forMaxg2), 0, forMaxg2)
forMaxgb2.save(path + "\\workspace.gdb\\forMaxgb2")

arcpy.Delete_management(updateHCR)
arcpy.CopyRaster_management(forMaxg2, updateHCR)

outcon9b = Con(NewDEMb >= Value2, Value2, NewDEMb)
outcon9b.save(path + "\\workspace.gdb\\New_DEM2b")

arcpy.Delete_management(rasterDEM)
arcpy.CopyRaster_management(outcon9b, rasterDEM)

CellThicknessb = Con(IsNull(rasterDEM),0,rasterDEM) #this raster has the data
needed for adding to subsequent rasters
CellThicknessb.save(path + "\\workspace.gdb\\CellThicknessb")
```

```
            CellThickness1b = Con(CellThicknessb == 0, Value2, CellThicknessb)
            CellThickness1b.save(path + "\\workspace.gdb\\CellThickness1b")

            CellThickness_sumb = (path + "\\workspace.gdb\\zonestats_CellThicknessb")
            field = "MIN"
            sum_DEM = ZonalStatisticsAsTable(CreateConsta2, "VALUE", CellThickness1b,
CellThickness_sumb, "NODATA", "MINIMUM")
            cursor = arcpy.SearchCursor(CellThickness_sumb)
            row = cursor.next()
            print "Total Added Lava to Each Raster Cell"
            print "Value8"
            print(row.getValue(field))
            Value8 = (row.getValue(field))

            print "Excess lava distributed within loop"
            now = datetime.datetime.now()
            print now.strftime("%m-%d-%Y %H:%M")

        if DistributedLava >= Value_excess:

            new_vent = ExtractByMask(outcon9b, vent)
            new_vent.save(path + "\\workspace.gdb\\new_vent")

            new_vent2 = Con(new_vent > forMaxg, forMaxg, new_vent)
            new_vent2.save(path + "\\workspace.gdb\\new_vent2")

            arcpy.Delete_management(vent)
            arcpy.CopyRaster_management(new_vent2, vent)

            Value1 = Value2
            print "update to Value1 - Distributed lava loop"
            print Value1

            print "HCR1"
            print HCR1

            print "HCR2"
            print HCR2

            print "Added Lava to the primary DEM"
            print Value8

            Value7 = 0
            print "Zeroing out Value7"
            print Value7
```

```
now = datetime.datetime.now()
print now.strftime("%m-%d-%Y %H:%M")

print "Excess lava fully distributed"

#To close this loop and ensure that the correct amount of excess lava is distributed,
#before the loop restarts the model at the beginning. All the cells that are present
#should be filled to the HCR2 value before the next loop can commence.

while Value8 < HCR2 and numit < maxit:

    #This loop is used to fill up the rings and vent with lava to the new
    #HCR2 value derived from the previous segment. Backfilling if necessary

    #There is no excess lava that is being distributed here, only new lava
    #added at the vent. Therefore, the iteration counter needs to be increased
    #by a count of +1.

    #This segment should only be needed in cases where the outer ring has a higher
    #HCR than the inner ring, and any backfilling needs to occur.

    DistributedLava = 0
    print "Distributed lava reset #2"
    print DistributedLava
    print "Distributing lava up to the new HCR"

    print"ITERATION #"
    print numit
    now = datetime.datetime.now()
    print now.strftime("%m-%d-%Y %H:%M")

    DEM = rasterDEM
    #add new pulse of lava to the vent
    vent_add1b = (lava + vent)
    vent_add1b.save(path + "\\workspace.gdb\\vent_add1b")
    #replace original vent with updated vent thickness
    arcpy.Delete_management(vent)
    arcpy.CopyRaster_management(vent_add1b, vent)
    #Setting the vent as the DEM that focal statistics can be performed on.
    #By changing the name here, can be replaced with updated DEM values
    #later in the model that take into account the updated topography as
    #lava is added.
    vent_add2b = Con(IsNull(vent_add1b), 0, vent_add1b)
    vent_add2b.save(path + "\\workspace.gdb\\vent_add2b")
    vent_add3b = Con(vent_add2b == 0, DEM, vent_add2b)
    vent_add3b.save(path + "\\workspace.gdb\\vent_add3b")
```

```
                #replace DEM with updated value
                arcpy.Delete_management(DEM)
                arcpy.CopyRaster_management(vent_add3b, DEM)
                print "RASTERCALC3 MADE HERE"
                rastercalc3 = Con(IsNull(DEM), 0, DEM)
                rastercalc3.save(path + "\\workspace.gdb\\rastercalc3")

                #Extract the value of the lava that has been added to the source vent/fissure.
                lava_sum = Con(IsNull(vent),0,vent)
                lava_sum.save(path + "\\workspace.gdb\\lava_sum")
                rastersum_lava = (path + "\\workspace.gdb\\zonestats1")
                field = "SUM"
                sum1 = ZonalStatisticsAsTable(CreateConsta2, "VALUE", vent, rastersum_lava,
"DATA", "SUM")
                cursor = arcpy.SearchCursor(rastersum_lava)
                row = cursor.next()
                print "Value1 - Lava being added to the source vent"
                print (row.getValue(field))
                Value1 = (row.getValue(field))

                new_vent_hcr2 = DEMupdate_newVal2a
                lavas3 = lava_sum - vent_sum2
                lavas3.save(path + "\\workspace.gdb\\lavas3")
                #This is the amount of lava that can actually be distributed
                rastersum_excess = (path + "\\workspace.gdb\\zonestats3")
                sum_excess = ZonalStatisticsAsTable(CreateConsta2, "VALUE", lavas3,
rastersum_excess, "NODATA", "SUM")
                cursor = arcpy.SearchCursor(rastersum_excess)
                row = cursor.next()
                field = "SUM"
                print "Excess lava to be distributed up to the new HCR2 value"
                print(row.getValue(field))
                Value_excess = (row.getValue(field))

                numit = numit + 1
                print numit

                while DistributedLava < Value_excess:

                    print "Lava distribution happening"
                    now = datetime.datetime.now()
                    print now.strftime("%m-%d-%Y %H:%M")

                    flux1 = ((Yield*cellSize*(Power(new_vent_hcr,2)))/(3*Visc))
                    flux1.save(path + "\\workspace.gdb\\flux1")
                    flux2 = (Power((lavas3/new_vent_hcr),3))
```

```
                flux2.save(path + "\\workspace.gdb\\flux2")
                flux3 = ((1.5)*(Power((lavas3/new_vent_hcr),2)))
                flux3.save(path + "\\workspace.gdb\\flux3")

                flux4 = flux1*(flux2 - flux3 + 0.5)
                flux4.save(path + "\\workspace.gdb\\flux4")

                flux_sum2 = Con(IsNull(flux4),0,flux4)
                flux_sum2.save(path + "\\workspace.gdb\\flux_sum2")
                rastersum_flux2 = (path + "\\workspace.gdb\\zonestats4")
                field = "SUM"
                sum3 = ZonalStatisticsAsTable(CreateConsta2, "VALUE", flux_sum2,
rastersum_flux2, "NODATA", "SUM")
                cursor = arcpy.SearchCursor(rastersum_flux2)
                row = cursor.next()
                print "Value3a - Total available flux for flow into neighboring cells"
                print(row.getValue(field))
                Value3a = (row.getValue(field))

                CreateConsta3 = path + "\\workspace.gdb\\dist_rasterb"
                arcpy.gp.CreateConstantRaster_sa(CreateConsta3, Value2, "FLOAT", cellsize,
BaseDEM)

                CreateConsta4 = path + "\\workspace.gdb\\dist_raster2b"
                arcpy.gp.CreateConstantRaster_sa(CreateConsta4, Value3a, "FLOAT",
cellsize, BaseDEM)

                DEM_extent = SetNull(rastercalc3 == 0, rastercalc3)
                DEM_extent.save(path + "\\workspace.gdb\\DEM_extent")

                outcon3a = Con(DEM_extent < Value2, DEM_extent, Value2)
                outcon3a.save(path + "\\workspace.gdb\\lava_distc")

                cell_count3a = Con(outcon3a < HCR2, HCR2, 0)
                cell_count3a.save(path + "\\workspace.gdb\\cell_count_lessthanhcr_sum3")

                cell_count3b = SetNull(cell_count3a == 0, cell_count3a)
                cell_count3b.save(path + "\\workspace.gdb\\cell_count_null3")
                rastersum_cells3 = (path + "\\workspace.gdb\\zonestats7")
                field = "COUNT"
                sum7 = ZonalStatisticsAsTable(CreateConsta2, "VALUE", cell_count3b,
rastersum_cells3, "DATA", "ALL")
                cursor = arcpy.SearchCursor(rastersum_cells3)
                row = cursor.next()
                print "Number of cells (below hcr) by which to divide flux value"
                print(row.getValue(field))
```

```
                Value4a = (row.getValue(field))

                Value5 = (Value3a/Value4a)
                print "Value5 - Total Flux Value Divided by the Number of Cells Available for
flux" #how much is going into each cell
                print(Value3a/Value4a)

                outconsuba = Con(outcon3a >= HCR2, rastercalc3, 0)
                outconsuba.save(path + "\\workspace.gdb\\outconsub3a")

                DistributedLava = 0
                Value8 = 0

                while DistributedLava < Value_excess:
                   print "Excess Distribution Loop"
                   print "Value5"
                   print Value5

                   DistributedLavatoEachCell = (Value_excess / Value4a)

                   outcon4c = Con(outconsuba == 0, DistributedLavatoEachCell, outconsuba)
                   outcon4c.save(path + "\\workspace.gdb\\lava_dist2c")

                   print "Excess lava"
                   print Value_excess

                   DistributedLava = Value_excess
                   print "Distributed Lava"
                   print Value_excess

                   print "HCR"

                   outcon7c = Con(IsNull(outcon4c), 0, outcon4c)
                   outcon7c.save(path + "\\workspace.gdb\\sub_DEM3b")

                   NewDEMc = Plus(rasterDEM, outcon7c)
                   NewDEMc.save(path + "\\workspace.gdb\\NewDEMc")

                   NewDEMc_null = SetNull(NewDEMc == 0, NewDEMc)
                   NewDEMc_null.save(path + "\\workspace.gdb\\NewDEMc_null")

                   ForNewExcessValue = (path +
"\\workspace.gdb\\zonestats_ForNewExcess")
                   field = "MIN"
```

```
                sum_NewExcess = ZonalStatisticsAsTable(CreateConsta2, "VALUE",
NewDEMc_null, ForNewExcessValue, "DATA", "MINIMUM") #Needs to be "DATA" since
there are null values
                cursor = arcpy.SearchCursor(ForNewExcessValue)
                row = cursor.next()
                print "NEW EXCESS TO BE ADDED TO VENT"
                print "NEW EXCESS AFTER LAVA ADDED TO ALL CELLS UP TO
HCR2"
                print "Value for New Excess calculation"
                print(row.getValue(field))
                ForNewExcess = (row.getValue(field))

                outcon9c = Con(NewDEMc >= Value2, Value2, NewDEMc)
                outcon9c.save(path + "\\workspace.gdb\\New_DEM2c")

                arcpy.Delete_management(rasterDEM)
                arcpy.CopyRaster_management(outcon9c, rasterDEM)

                CellThicknessb = Con(IsNull(rasterDEM),0,rasterDEM) #this raster has the
data needed for adding to subsequent rasters
                CellThicknessb.save(path + "\\workspace.gdb\\CellThicknessb")

                CellThickness1b = Con(CellThicknessb == 0, Value2, CellThicknessb)
                CellThickness1b.save(path + "\\workspace.gdb\\CellThickness1b")

                CellThickness_sumb = (path +
"\\workspace.gdb\\zonestats_CellThicknessb")
                field = "MIN"
                sum_DEM = ZonalStatisticsAsTable(CreateConsta2, "VALUE",
CellThickness1b, CellThickness_sumb, "NODATA", "MINIMUM")
                cursor = arcpy.SearchCursor(CellThickness_sumb)
                row = cursor.next()
                print "LAVA ADDED TO ALL CELLS UP TO HCR2"
                print "Total Added Lava to Each Raster Cell"
                print "Value8"
                print(row.getValue(field))
                Value8 = (row.getValue(field))

                DEMupdate_2c = Con(CellThicknessb > HCR2, forMaxg2, CellThicknessb)
                DEMupdate_2c.save(path + "\\workspace.gdb\\DEMupdate_2c")

                DEMupdate_2d = Con(IsNull(DEMupdate_2c), 0, DEMupdate_2c)
                DEMupdate_2d.save(path + "\\workspace.gdb\\DEMupdate_2d")

                arcpy.Delete_management(DEM)
                arcpy.CopyRaster_management(DEMupdate_2d, DEM)
```

```
                num = num + 1
                s = str(num) #Number has to be a string in the next step

                new_vent = ExtractByMask(DEMupdate_2d, vent)
                new_vent.save(path + "\\workspace.gdb\\new_vent")

                new_vent2add = Con(new_vent < ForNewExcess, (new_vent +
(ForNewExcess - Value8)), 0)
                new_vent2add.save(path + "\\workspace.gdb\\new_vent2add")

                new_vent2 = Plus(new_vent, new_vent2add)
                new_vent2.save(path + "\\workspace.gdb\\new_vent2")

                arcpy.Delete_management(vent)
                arcpy.CopyRaster_management(new_vent2, vent)

                print "LAVA DISTRIBUTION UP TO HCR2"
                now = datetime.datetime.now()
                print now.strftime("%m-%d-%Y %H:%M")

                print "THIS SHOWS THAT THE LOOP WITH THE HIGHER HCR2
VALUE HAS BEEN REACHED"
                print numit

            #Extract the value from the NewDEMc raster, and subtract Value8 from it,
            #which would give the new excess value that needs to be distributed.
            #Could add that value directly to the lava value for when the entire
            #loop restarts, which would obviate the need to incorporate another loop.

            if Value8 >= HCR2:
                print "COMPLETING LOOP SEGMENT THAT BRINGS CELL VALUES
UP TO HCR2"

                new_vent = ExtractByMask(outcon9c, vent)
                new_vent.save(path + "\\workspace.gdb\\new_vent")

                new_vent2 = Con(new_vent < ForNewExcess, (new_vent + (ForNewExcess
- Value8)), 0)
                new_vent2.save(path + "\\workspace.gdb\\new_vent2")

                arcpy.Delete_management(vent)
                arcpy.CopyRaster_management(new_vent2, vent)
                print "VENT REPLACED"

                arcpy.Delete_management(DEM)
```

```
                arcpy.CopyRaster_management(outcon9c, DEM)
                print "DEM REPLACED"

                Value1 = Value2
                print "update to Value1 - Distributed lava loop"
                print Value1

                print "HCR1"
                print HCR1

                print "HCR2"
                print HCR2
                HCR2 = 0

                print "Added Lava to the primary DEM"
                print Value8

                Value7 = 0
                print "Zeroing out Value7"
                print Value7

                Value8 = 0
                print "Zeroing out Value8"
                print Value8

                now = datetime.datetime.now()
                print now.strftime("%m-%d-%Y %H:%M")

                print "Excess lava fully distributed"

            if numit >= maxit:
                print "COMPLETING LOOP SEGMENT"

                new_vent = ExtractByMask(outcon9c, vent)
                new_vent.save(path + "\\workspace.gdb\\new_vent")

                new_vent2 = Con(new_vent < ForNewExcess, (new_vent + (ForNewExcess
- Value8)), 0)
                new_vent2.save(path + "\\workspace.gdb\\new_vent2")

                arcpy.Delete_management(vent)
                arcpy.CopyRaster_management(new_vent2, vent)
                print "VENT REPLACED"

                arcpy.Delete_management(DEM)
                arcpy.CopyRaster_management(outcon9c, DEM)
```

```
                print "DEM REPLACED"

                Value1 = Value2
                print "update to Value1 - Distributed lava loop"
                print Value1

                print "HCR1"
                print HCR1

                print "HCR2"
                print HCR2
                HCR2 = 0

                print "Added Lava to the primary DEM"
                print Value8

                Value7 = 0
                print "Zeroing out Value7"
                print Value7

                Value8 = 0
                print "Zeroing out Value8"
                print Value8

                now = datetime.datetime.now()
                print now.strftime("%m-%d-%Y %H:%M")

                print "MODEL ITERATIONS COMPLETED"

elif Value8 > HCR1 and DistributedLava >= Value_excess:

    #This block of code is needed to reset the lava vent value for the
    #beginning of the next iteration.

    print "THIS IS THE VERY LAST LOOP SEGMENT OF THE MODEL"

    new_vent = ExtractByMask(outcon9, vent)
    new_vent.save(path + "\\workspace.gdb\\new_vent")

    new_vent2 = Con(new_vent > forMaxg, forMaxg, new_vent)
    new_vent2.save(path + "\\workspace.gdb\\new_vent2")

    arcpy.Delete_management(vent)
    arcpy.CopyRaster_management(new_vent2, vent)

    print "HCR"
```

```
print HCR1

print "Added Lava to the primary DEM"
print Value8

newest_surface = SetNull(rasterDEM == 0, rasterDEM)
newest_surface.save(path + "\\workspace.gdb\\newest_surface")

arcpy.Delete_management(DEM)
arcpy.CopyRaster_management(newest_surface, DEM)

print "DEM Replaced - New Neighborhood to be Calculated"
Value1 = Value2

Value8 = 0
print "Zeroing out Value8"
print Value8

now = datetime.datetime.now()
print now.strftime("%m-%d-%Y %H:%M")
```

CHAPTER 3
SOURCE(S) OF THE CIRCUM-CALORIS SMOOTH PLAINS ON MERCURY: MAPPING, REMOTE ANALYSES, AND SCENARIOS FOR FUTURE TESTING WITH BEPICOLOMBO DATA

Abstract

Mercury hosts widespread smooth plains that are concentrated in the Caloris impact basin, an annulus surrounding the Caloris basin, and the adjacent northern plains. These three plains localities have a narrow range of emplacement ages (~3.5–3.8 Ga), which post-date the Caloris impact event (~3.9 Ga), and exhibit varied spectra which suggests compositional differences. The portion of the annulus between Caloris and the northern smooth plains specifically contains intermingled high-reflectance red plains and low-reflectance blue plains, where “red” and “blue” refer to their spectral slope. The origins of these smooth plains are uncertain, although prior work suggests these plains in the northwestern Caloris annulus might reflect volcanic activity, impact ejecta, or a combination of the two. Deciphering the emplacement of these plains would provide a critical constraint on regional late-stage volcanism or impact effects. The region northwest of Caloris was investigated using geomorphological and color-based mapping, crater counting techniques, and spectral analyses with the goal of placing constraints on the source of the observed units and identifying the primary emplacement mechanism. Mapping and spectral analyses confirm previous findings of two distinct, yet intermingled, units within these plains, each with similar crater count model ages that post-date the formation of the Caloris impact basin. Mapping, spectra analysis, ages, and the interpretation of potential flow pathways, are more consistent with a predominantly volcanic origin for the smooth plains materials, although these data do not rule out contributions from impact ejecta or melt. Several hypothetical scenarios were developed, including post-emplacement modification by near-surface volatiles, to explain these observations and clarify the emplacement mechanism for these smooth plains. Further observations from the BepiColombo mission will provide data to potentially address the outstanding questions from this work.

Introduction

The Mariner 10 mission, as well as subsequent MErcury Surface, Space ENvironment, GEochemistry, and Ranging (MESSENGER) mission, provide evidence of a complex surface of Mercury that offers tantalizing hints about its evolution. The surface of Mercury is comprised of three primary terrain types: smooth plains, intermediate terrains, and low-reflectance material (LRM), which are characterized by a combination of differing spectral slopes, relative reflectances, and surface morphologies (e.g., Denevi et al., 2009). The intermediate terrain contains a subunit referred to as the intercrater plains (ICP), which are widespread and comprise approximately one-third of the exposed intermediate terrain. These materials have been interpreted as representing an effusive volcanic unit, perhaps not unlike the smooth plains unit, but which has experienced significant degradation and heavy cratering (Whitten et al., 2014). By contrast, the vast exposures of smooth plains, the Caloris interior plains (CIP), circum-Caloris exterior plains (CEP), and northern smooth plains (NSP), have been interpreted to have formed from impact ejecta, volcanism, or a mix between the two (Wilhelms, 1976; Kiefer and Murray, 1987; Spudis and Guest, 1988; Strom et al., 2008, 2011; Fassett et al., 2009; Head et al., 2009, 2011; Denevi et al., 2009, 2013; Whitten et al., 2014; Byrne et al., 2013, 2016; Ostrach et al., 2015; Klima et al., 2018). Smooth plain deposits in the CIP, CEP, and NSP share morphological characteristics that include sparse cratering, level terrain, distinct boundaries with adjacent terrain, embayment of older units, and lowland ponding (e.g., Trask and Guest, 1975; Denevi et al., 2009, 2013). After the recognition that post-emplacement deformation of the smooth plains had occurred, specifically related to the development of long-wavelength topographic undulations (Oberst et al., 2010; Zuber et al., 2012), the morphological description of these units was modified to include the presence of gently rolling topography (Denevi et al., 2013).

Background

Geological Background and Characteristics of Mercurian Smooth Plains

The CEP forms a nearly continuous annulus around the Caloris basin, the interior of which has been filled by smooth plains material (Fig 25A,B; e.g., Fassett et al., 2009; Head et al., 2009), and are intermingled in the northwest with the Caloris Montes, Nervo, Odin, and Van Eyck Formations (Fig 25C; e.g., Guest and Greeley, 1983). The origin of the CEP have attributed to emplacement of impact-related melt, direct deposition of impact ejecta, and surficial emplacement of volcanic melt. Such interpretations are based primarily on apparent stratigraphic relationships between the smooth plains and adjacent terrain, and geospatial proximity to Caloris (Wilhelms, 1976; Oberdeck et al., 1977; Schaber and McCauley, 1980; McCauley et al., 1981; Guest and Greeley, 1983). A volcanic origin for the smooth plains appears favored by most researchers, who suggest that the combinations of smooth morphology, wide distribution, relative youth compared to the largest impact basins, color characteristics, and embayment of the Caloris rim and other topographically highstanding terrain are more consistent with a volcanic origin (e.g., Trask and Guest, 1975; Kiefer and Murray, 1987; Strom et al., 2008, 2011; Fassett et al., 2009; Head et al., 2009, 2011; Prockter et al., 2010; Byrne et al., 2013; Hurwitz et al., 2013; Ostrach et al., 2015). Still, other investigators suggest that the smooth plains might result from mixing of impact and volcanic lithologies (e.g., Denevi et al., 2013; Ackiss et al., 2015). Potential lava flow paths (Fig. 25) have been identified leading from the NSP into the CEP (Byrne et al., 2013), and from the CIP into the CEP through the Caloris rim, utilizing the linear troughs of the Van Eyck formation (Fassett et al., 2009). Potential flow pathways of the CEP-bounding valleys that lead from the NSP also contain apparent flow structures, such as kipukas, that range in size up to ~20 km long (Byrne et al., 2013). The potential for limited pyroclastic activity has also been associated with coalesced depressions found within several smooth plains regions, though these features likely represent a

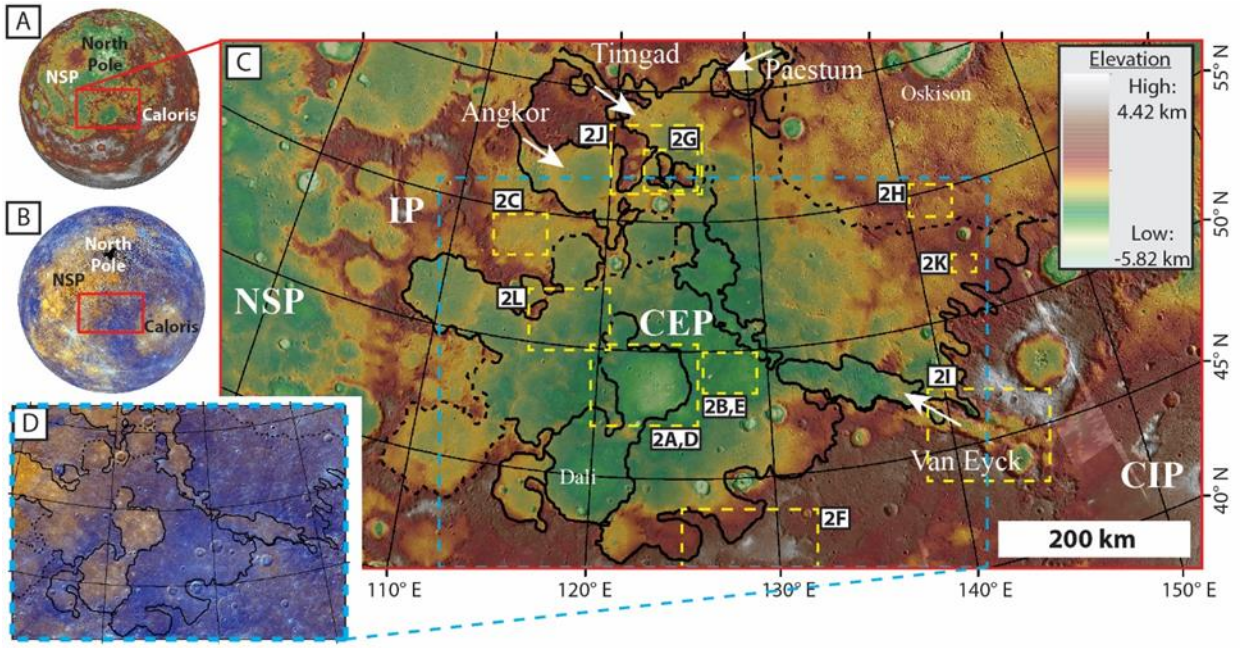

Figure 25. A: Global topography centered on the CEP (125°E, 60°N), with adjacent NSP to the northwest and the Caloris basin to the southeast. B: Global enhanced-color image (R: 430 nm, G: 750nm, B: 1000 nm) centered on the CEP, highlighting color differences between the LRP annulus containing the CEP and the HRP units in the NSP and CIP. C: Topographic overview of the study area with general unit outlines, solid black lines denoting certain contacts and dashed black lines denoting approximate contacts. The IP are adjacent to the CEP and NSP. Potential flow pathways from the NSP and CIP into the CEP are identified (white arrows). D: Subset of the enhanced-color mosaic covering the study area (shown by dashed blue box) in the CEP, highlighting the presence of both LRP in the south and east and HRP in the north and west in the region. Dashed yellow boxes denote the type locations shown in Figure 26 and described in Table 7. Image mosaics credit: NASA/Johns Hopkins University Applied Physics Laboratory/Carnegie Institution of Washington.

more effusive style of eruption (Byrne et al., 2013). Other features have been identified that suggest the potential for flow within, into, and out from the Caloris interior (Rothery et al., 2017).

Compositional variations of these smooth plains have been inferred from various spectral datasets covering a wide range of the electromagnetic spectrum, including 400–1000 nm (e.g., Robinson et al., 2008; Denevi et al., 2009; Watters et al., 2009), gamma-ray (Peplowski et al., 2015), and x-ray (Weider et al., 2015), and are consistent with observed color variations (Fig. 25B). Three spectrally distinct smooth plains units are present on Mercury: the high-reflectance red plains (HRP), intermediate-reflectance plains (IRP), and low-reflectance blue plains (LBP) (Denevi et al., 2009; Watters et al., 2009). The HRP have been interpreted as low-Fe, basalt-like mafic compositions, whereas the LBP has been similarly interpreted as low in Fe, has been identified as having higher Mg/Si and Ca/Si ratios, and lower Al/Si ratios, which is more consistent with ultramafic compositions (Nittler et al., 2011; Stockstill et al., 2012; Weider et al., 2012). The NSP and CIP have been spectrally classified as HRP, and the CEP have been classified as LBP (Fig. 25B, D; e.g., Denevi et al., 2009, 2013; Watters et al., 2009). Within the study area of the present work over in the northwestern portion of the CEP, comingled deposits of HRP and LBP are present (Fig. 25D; Fassett et al., 2009), and have an elemental composition intermediate between the plains units identified in the CEP and NSP (Peplowski et al., 2015; Weider et al., 2015).

Despite the spectral similarities between the HRP deposits in the NSP and CIP, elemental abundances show marked differences in composition among all three smooth plains regions, (e.g., Nittler et al., 2011; Stockstill et al., 2012; Peplowski et al., 2015; Weider et al., 2015). X-Ray Spectrometer (XRS) and Gamma-Ray Spectrometer (GRS) data measured during the MESSENGER mission were used to differentiate the surface of Mercury into different

geochemical terranes that represent distinct compositions (Peplowski et al., 2015; Weider et al., 2015). Compositional differences exist among the smooth plains units and present themselves as distinction between the CIP and NSP. Although both the CIP and NSP exhibit low-Mg abundances and the CIP exhibits a low- to intermediate-Mg abundance, a clear spatial trend exists for Al abundance; the CIP has high-Al abundances that decrease toward the NSP, which have low- to intermediate Al abundances (Peplowski et al., 2015, see their Fig. 9; Weider et al., 2015, see their Fig. 4; Nittler et al., 2018; Stockstill-Cahill et al., 2019). This Al-abundance trend has been interpreted as resulting from differing amounts of Na in source magmas of Mercury that affected the type of plagioclase produced and the final Al concentrations (Weider et al., 2015). The CEP are apparently intermediate in composition between the CIP and NSP regions, and may be gradational between the two adjacent smooth plains units.

Together, these geochemical signatures have been used to suggest the smooth plains in the CEP, CIP, and NSP are an indirect result from the Caloris impact event, which may have induced deep mantle melting and convection that tapped different portions of the mantle, leading to subsequent eruptions of varying compositions (Kiefer and Murray, 1987; Roberts and Barnouin, 2012; Peplowski et al., 2015; Weider et al., 2015). This timing of emplacement for surficial lava flows has been inferred to have occurred within < 0.5 Ma from the initial impact event, although remnant thermal anomalies in the mantle related to the impact might have been capable of generating limited melt after > 100 Ma (Roberts and Barnouin, 2012). Compositionally different portions of the mantle have been modeled to arise from sluggish mantle convection leading to lateral and vertical heterogeneities, which is consistent with the observed compositional heterogeneities between the CIP and NSP deposits (Charlier et al., 2013; Michel et al., 2013; Tosi et al., 2013; Peplowski et al., 2015; Weider et al., 2015). Coupling these

apparent geochemical signatures to newly mapped units in the CEP can provide a clearer understanding of the relationship between composition and surface materials.

The various smooth plains also have crater size frequency distributions (CSFDs) that suggest distinct timing of emplacement. Previous crater-count-derived model ages suggest that the ICP were emplaced during the late heavy bombardment (LHB; Whitten et al., 2014) whereas the NSP, CIP, and CEP were emplaced after the Caloris basin formed at ~3.9 Ga, either during the waning phases of the LHB or following its cessation (e.g., Strom et al., 2008, 2011; Fassett et al., 2009; Denevi et al., 2013). Previous results indicate the smooth plains deposits were emplaced in a relatively narrow ~200 Ma window of time, between ~3.7 and 3.9 Ga (Strom et al., 2008, 2011; Fassett et al., 2009; Denevi et al., 2013; Ostrach et al., 2015). Emplacement ages for the smooth plains units suggest they were emplaced prior to global contraction and the termination of large-scale volcanism on Mercury (Byrne et al., 2015).

The derived ages for the NSP and CIP are statistically indistinguishable (Strom et al., 2011; Denevi et al., 2013, Ostrach et al., 2015), whereas relative crater densities suggest the CEP are slightly younger (Strom et al., 2008, 2011; Fassett et al., 2009; Denevi et al., 2013), with the exception of a southern exposure (Denevi et al., 2013). Previous age estimates for the CEP have been based on crater counts performed across the entire unit (e.g., Strom et al., 2008, 2011), on a portion of the northwest CEP (Fassett et al., 2009), and on dispersed segments to the east, west, and south of Caloris (Denevi et al., 2013). The entire area of the CEP in the northwest was not fully counted, nor were targeted counts performed specifically within two contrasting spectral units in the area. A primary motivation for this study is adding targeted crater count-derived ages that include these specific CEP units.

Hypotheses

The northwestern CEP region, bounded by the NSP and CIP, provides a useful location to investigate the complex geologic history of smooth plains emplacement on Mercury, particularly related to the Caloris annulus. In this region, the CEP are spectrally distinct from both the NSP and the CIP, and contain both HRP and LBP material. This intermingling of units indicates multiple compositions are present in the CEP, and may have been sourced from more than a single location. The age of the CEP has been interpreted as younger than the NSP and CIP, though a southern segment of the CEP has been interpreted as older (Denevi et al., 2013). This age disparity demonstrates the potential for a non-uniform timing of emplacement for the CEP. An abundance of geologic units within the CEP has also resulted in various interpretations of origin, related to impact or volcanic processes, or a mixture of both. A detailed investigation of this complex region of the circum-Caloris smooth plains may help to place critical constraints on, and testable scenarios for, the evolution of the broader CEP of Mercury.

Hypothesis One

Based on the presence of HRP materials, compositions intermediate between the NSP and CIP, and potential flow pathways from the NSP or CIP (e.g., Robinson et al., 2008; Denevi et al., 2009; Fassett et al., 2009; Watters et al., 2009; Byrne et al., 2013; Weider et al., 2015; Peplowski et al., 2015), the Caloris annulus, and the northwest CEP in particular (Byrne et al., 2013), has been previously interpreted as consisting of predominantly volcanic units. Here, I hypothesize that *the CEP unit northwest of the Caloris impact basin consists of surficial volcanic flows.* This scenario does not distinguish whether the CEP might represent a single lava flow or, alternatively, multiple emplacement events, similar to those associated with the emplacement of the NSP. Identification of unambiguous flow structures within the CEP and spectral signatures that are comparable to either of the bordering volcanic regions would support a hypothesis that

the CEP consists of surficial lava flows. Crater count-derived ages that are clearly younger than the Caloris basin would lend implicit support to the hypothesis of volcanic emplacement and would be inconsistent with CEP emplacement as ejecta related to the Caloris impact event.

Hypothesis Two - Impact Ejecta

Based on previous interpretations of the circum-Caloris smooth plains units as impact material (e.g., Wilhelms, 1976; McCauley et al., 1981), and the interpretation that the annulus may consist of intermingled volcanic and impact materials (e.g., Denevi et al., 2013; Ackiss et al., 2015), a second origin hypothesis is that *the CEP unit northwest of the Caloris impact basin is primarily comprised of impact-related material, such as impact melt or ejecta, from a combination of local or regional impacts*. Crater count-derived ages within the study area that align with the age of the Caloris impact basin (Fassett et al., 2009), would support the potential emplacement of the CEP as impact melt or ejecta. Spectral signatures that do not closely match those of the purported volcanic provinces in the CIP and NSP would also suggest that the CEP is not volcanically derived. An interpretation of an impact origin would also require a conspicuous absence of flow structures in the CEP or clear connection to previously identified valleys would support ejecta debris or melt emplacement and argue against surficial lava flows.

Methodology

Hypotheses regarding the origin and emplacement of CEP materials, were examined via detailed geomorphological, color, and compositional based mapping of the study area (Fig. 25C), supplemented by crater counting, and interpretation of spectral analyses. Mapping within the study area was used to define the areal extent of the different plains units and their adjacent units, to identify potential structures that could be interpreted as tectonic structures and volcanic vents, to delineate locations for crater counting. Crater counts were performed in unit outcrops related to HRP and LBP materials within the study area to refine the emplacement age(s) for the smooth

plains in this northwestern segment of the CEP. Spectral analyses were then used to identify compositional similarities between units within the CEP and to identify similar spectral signatures in the adjacent NSP and CIP. Spectral analyses were supplemented by a qualitative assessment of previously derived principal component analyses, to further investigate differences between identified spectral units.

Geomorphological and Color/Compositional Mapping

Geomorphological units that had previously been identified within the circum-Caloris basin were discerned within the ArcGIS environment (cf., Head et al., 2009, 2011; Denevi et al., 2013) and mapped at a scale of 1:1M, enabling discrimination of morphological contacts, tectonic structures, and color differences. Surface morphology was characterized using the Mercury Dual Imaging System (MDIS) 250 meter per pixel (mpp) monochromatic basemap, supplemented by available higher-resolution MDIS Wide Angle Camera (WAC) and Narrow Angle Camera (NAC) images (Hawkins et al., 2007). The Mercury Laser Altimeter (MLA; Cavanaugh et al., 2007) 1 kmpp basemap supplemented data from visual images to identify the margins of the CEP and surrounding terrains and to further characterize units based on their topography. The MDIS WAC 8-band composite basemap at 665 mpp (Denevi et al., 2016) was used to identify the margins of any spectrally distinct units within and adjacent to the smooth plains basin. This basemap was also used to collect spectra from HRP and LBP units in the CEP, as well as spectra for the NSP and CIP for comparison with the CEP units. The mapping of color variations was supplemented by the 11-band enhanced color (PC2, PC1, 430/102 nm in RGB channels) 3.5 kmpp basemap (Denevi et al., 2016) that highlights spectral contrasts. Coarse resolution 20 kmpp X-Ray Spectrometer (XRS) and 100-1000 kmpp Gamma-Ray Spectrometer

(GRS) elemental abundances maps (Peplowski et al., 2015; Weider et al., 2015, respectively) were used to identify apparent spatial compositional trends.

Crater Counting

To derive model ages for the target LBP and HRP units, crater counts were performed in several distinct locations associated with each spectral unit within the CEP. Craters that are circular, have a raised rim, or retain an ejecta blanket within the chosen sites were counted. The size of my count areas was informed by the minimum ~1000 km^2 count area recommended for martian crater counts; for small areas with small crater populations, this area typically results in statistically robust crater counts (Warner et al., 2015). For each location, a minimum area of ~10,000 km^2 was used to provide a statistically representative sampling of larger craters (>1 km diameter). Such areas are one to two orders of magnitude smaller than previous regions defined for crater counting (e.g., Ostrach et al., 2015; Byrne et al., 2016), but are required to satisfy the more spatially focused nature of this investigation and the limited size of the exposures in the CEP. Such small areas, however, restricted counting to craters below 8–10 km in diameter. Craters below this size are typically dominated by populations of secondary craters on Mercury, rather than from primary impactors (e.g., Strom et al., 2011). It was therefore imperative that count locations were selected to avoid obvious secondary clusters and linear crater chains. Defining secondary clusters and linear chains were also instrumental in inferring the potential effect secondary craters might have had on excavating the surface in the study region. Craters that exhibit embayment relationships must predate the observed surface being age-dated and so were excluded, as were craters with non-circular rims and craters in clusters, interpreted as secondaries.

The CraterTools plug-in within ArcGIS was used to perform crater counts (Kneissl et al., 2011), and the final crater count model ages were computed in Craterstats2 (Michael and Neukum, 2010; Michael, 2013) from fits of measured crater distributions to model isochrons, crater production functions, and chronology functions for Mercury (Le Feuvre and Wieczorek, 2011). Craters <1 km in diameter were excluded when fitting the observed crater populations to the isochrons, to account for observation loss due to resolution limits, resurfacing processes, and contamination by secondary craters (e.g., Michael and Neukum, 2010).

Spectral Analyses

The MDIS 8-band enhanced color basemap was used to characterize the spectral properties of the HRP and LBP units in the study area, specifically their spectral slope, which is the measure of the relationship between the reflectance of a surface and the wavelength (λ) of the reflected light. In the ENVI image processing software suite, regions of interest (ROIs) were chosen to cover areas of the HRP and LBP units that exhibited distinct color differences within the CEP (Fig. 26), as well as similar regions in neighboring NSP and CIP terrains, for spectral comparison. Extraction of spectral data from the MDIS multispectral data relied on extracting the average reflectance values for each ROI within the ENVI environment. Although the spectral signatures from the surface of Mercury are typically muted (e.g., Denevi et al., 2018; McCoy et al., 2018; Murchie et al., 2018) due to space weathering (e.g., Dominique et al., 2014; Trang et al., 2017; Murchie et al., 2018), low iron content (e.g., Nittler et al., 2018), and high concentrations of carbon (e.g., Murchie et al., 2015, 2018), which all act to suppress spectral absorption features, these data are useful for basic first-order comparison of the spectral slopes between units. Results were then compared to previous interpretations of the smooth plains spectral characteristics (e.g., Robinson et al., 2008; Denevi et al., 2009; Watters et al., 2009) and

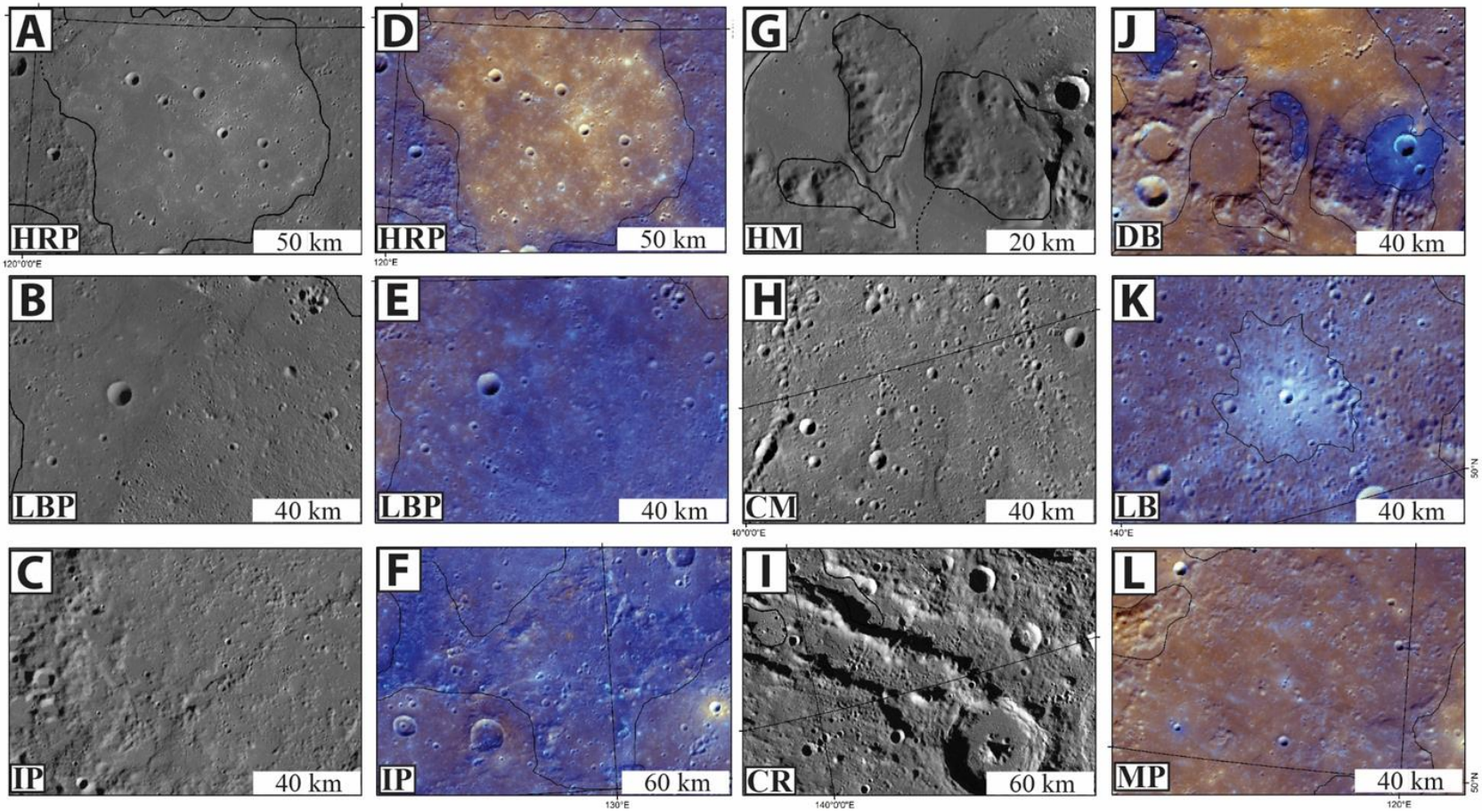

Figure 26. Geomorphological and color-based (R: 430 nm, G: 750nm, B: 1000 nm) units, from the MDIS WAC basemap and MDIS 8-color mosaic, respectively, used to map the CEP (see Table 7), with locations denoted in Figure 25. To highlight the differences in color between the units, they are displayed using the enhanced color RGB combination. Pairs A, D and B, E demonstrate the morphology and color characteristics of the HRP and LBP, respectively. Covering two different areas, C and F highlight the smaller-scale surface morphologies (C) and generally blue color (F). G and J, located in the same region, demonstrate the isolated nature of the mesas and their varied color characteristics. H shows a spread of secondary crater chains related to Oskison crater. K shows an example of the very bright, light blue material found scattered throughout the CEP in limited exposures, generally related to small and likely recent impact events. Image I highlights a segment of the crater rim material associated with the Caloris basin. L, an example of the intermediate plains, which exhibits a mix of red and blue material, with some small exposures of light blue interspersed throughout.

regional elemental abundances determined from XRS and GRS data (e.g., Peplowski et al., 2015; Weider et al., 2015, respectively), to both determine whether distinct spectral units existed within the CEP and to attempt to distinguish between different exposures of the same spectral class, i.e., the HRP or LBP.

Principal Component Analyses

A qualitative assessment of the previously derived principal component analyses (Denevi, et al, 2016), was used to supplement spectral interpretations of the units within the CEP, CIP, and NSP. These principal components highlighted differences between units derived from morphological and color-based mapping. The enhanced color mosaic for Mercury's surface includes Principal Component 1 (PC1) and Principal Compoent 2 (PC2) as part of the enhanced color mosaic RGB band combination (R: PC2, G: PC1; B: 430 nm/1000nm). These principal component transformations were derived from the 430 nm, 730 nm, and 1000 nm MDIS bands, to highlight subtle differences in reflectance (PC1) and specta (PC2) on the surface (e.g., Denevi et al., 2013; Ernst et al., 2015; Rothery et al., 2017; Klima et al., 2018). Using a spatial subset of the planetary PC2 dataset which highlights compositional differences represented by differences in surface brightness, spectral differences between the mapped spectral units, particularly the widely spaced HRP units, were able to be distinguised. A straightforward comparison of the digital number (DN) values of the pixels associated with the chosen ROIs using the PC2 data, further aided in distinguishing between mapped units. The PC1 data was not utilized, as it only highlighted the differences in relative reflectance between the units.

Results

Geomorphological and Color/Compositional Mapping

Unit delineation based on morphologies, textures, and color characteristics (Fig. 26, Table

7) yields a comprehensive map of the region at a higher-spatial resolution than that from different units in and around the northwestern CEP (Fig. 27). The mapped units in the region generally follow the morphological boundaries, although gradational units (e.g., IP) between the HRP and LRP units and impact related features diverge slightly from these boundaries (Fig. 27). The plains units are generally restricted to the interior of the CEP and also found within multiple nearly filled craters. The HRP are concentrated within two filled craters and within the arcuate corridor that extends from the distal margins of Timgad and Paestum Valles and extend through the CEP to the Van Eyck formation troughs that dissect the Caloris rim. The CEP lacks unambiguous flow structures. The LBP fill most of the CEP, and occur both north and south of the arcuate HRP unit that dissects the CEP. An intermediate plains unit is found in the western margins of the CEP, several filled craters, and south of the CEP, consisting of a reddish-blue hued plains unit that appears to be a mix between the HRP and LBP units.

In addition to the predominant HRP and LBP units, the geomorphologic and/or color-based units identified within and bordering the CEP include ICP, the CR, and HM along the outer margins of the plains. Crater-related outcrops include the large ejecta blanket of Oskison crater to the northeast, and various smaller craters and their associated rims and ejecta (Fig. 26, Table 7). The two least common units in the area (LB and DB), though distinct, are areally restricted within the CEP. In addition to the geological units in the CEP, mapping also identified the extent of wrinkle ridges in the region, and the location of several possible volcanic vents (Fig. 27). These potential vents correspond to previously identified structures in and around the CEP (e.g., Byrne et al., 2013; Denevi et al., 2013; Hurwitz et al. 2013), and are identified as probable volcanic vents based on their morphology, with broad flat floors, as well as scalloped margins evidencing coalescence (Byrne et al., 2013). A potential source vent for Dali (Fig. 25, 27) and the adjacent

Table 7. Units and their morphological- and/or color-based descriptions, derived from the MDIS monochrome basemap, MLA topography, and MDIS 8-band enhanced color basemap (R: 430 nm, G: 750nm, B: 1000 nm). These morphological and color characteristics define the units in the CEP (Fig. 26) and were used to map their contacts throughout the region, resulting in a comprehensive map (Fig. 27).

Unit	***Morphology / Texture***	***Color Characteristics***
High-Reflectance Red Plains (HRP)	Relatively smooth, few wrinkle ridges, extensional features present.	Red hue in color and enhanced-color images.
Low-Reflectance Blue Plains (LBP)	Relatively rough, knobs and wrinkle ridges present.	Blue hue in color and enhanced-color images.
Intermediate Plains (IP)	Generally located between expanses of HRP and LBP units.	Intermediate plains materials that exhibit a mixture of red and blue hues.
Intercrater Plains (ICP)	Relatively highstanding terrain that bounds the CEP. Knobs, wrinkle ridges, and craters are prevalent.	Generally blue with slight mixture of red.
Highstand Material (HM)	Isolated highstanding mesas, primarily located in valleys and bounded by HRP and LBP material.	Primarily red hued, but mixed with some dark and light blue exposures.
Crater Material (CM)	Significant ejecta blanket and secondary crater fields associated with Oskison crater. Craters with distinct ejecta blankets or rims.	Generally red hue surrounding portions of the crater
Caloris Rim (CR)	Continuous sections of the rim material bounding the Caloris basin, including the Van Eyck formation.	Generally mixed red and blue hues.
Light Blue (LB)	Associated with small impact craters.	Extremely light blue hue in enhanced color images.
Dark Blue (DB)	Isolated expanses, limited areal coverage.	Dark blue material generally surrounded by HRP material in enhanced color images.

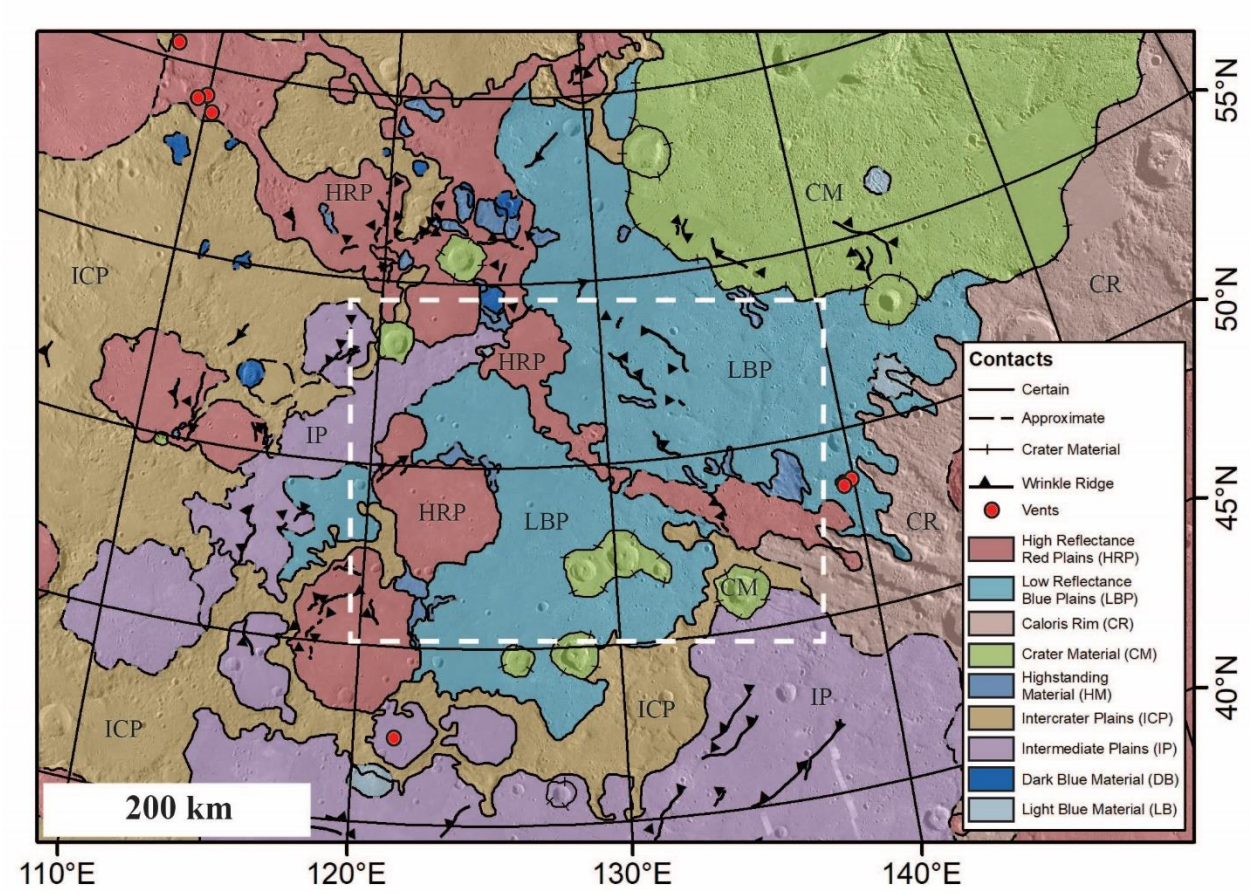

Figure 27. Geomorphological and color-based map of the CEP. The HRP and LRP units dominate the region of the basin (see Figure 25 for location context). Dashed white box denotes the extent of Fig. 28, the region where crater counts were performed.

unnamed crater, is located in a small bordering crater, which is categorized as a mixed plains unit.

Crater Size Frequency Distribution Analyses

Crater counting efforts were focused on areas that include distinct HRP and LBP regions (Fig. 28), that have previously been interpreted as volcanic or impact units, or a mixture of the two. While mapping the boundaries of the crater count locations no significant concentrations of secondaries were found. Though derived from smaller areas and including smaller crater diameters than in previous work, these data – specifically the CSFDs (Fig. 29), crater densities, and ages (Table 8) – align with the results of previous investigations (e.g., Strom et al., 2008, 2011; Fassett et al., 2009; Denevi et al., 2013; Ostrach et al., 2015; Byrne et al., 2016), suggesting primary-production crater populations, even in smaller regions, can provide an accurate assessment of surface ages. In comparison, previous workers avoided contamination from secondary craters by restricting the diameters of the counted craters to ≥4 km (Byrne et al., 2016) or ≥8-10 km (e.g., Fassett et al., 2009; Ostrach et al., 2015).

Crater counts were used to calculate both absolute and relative ages. Absolute age estimates for the HRP and LBP range from 3.58-3.73 Ga (Table 8), implying that the HRP and LBP units in the region were both emplaced within a span of ~150 My (Table 8); the cumulative and differential CSFDs also suggest overlapping ages for these units (Fig. 29). Errors for the model ages derived by CraterStats were determined using $1/\sqrt{n}$, where n is the number of counted craters, which is the conventional method for determining error in crater counting statistics (Arvidson et al., 1979; Michael et al., 2016). Although some of the ages might be separated based on these formal errors (Table 8), systemic uncertainties associated with crater counting on Mercury are 100-200 Ma, resulting from the unknown local effects of resurfacing and occurrence of secondary crater populations (e.g., Ostrach et al., 2015). Thus, although it appears certain that the CEP region is

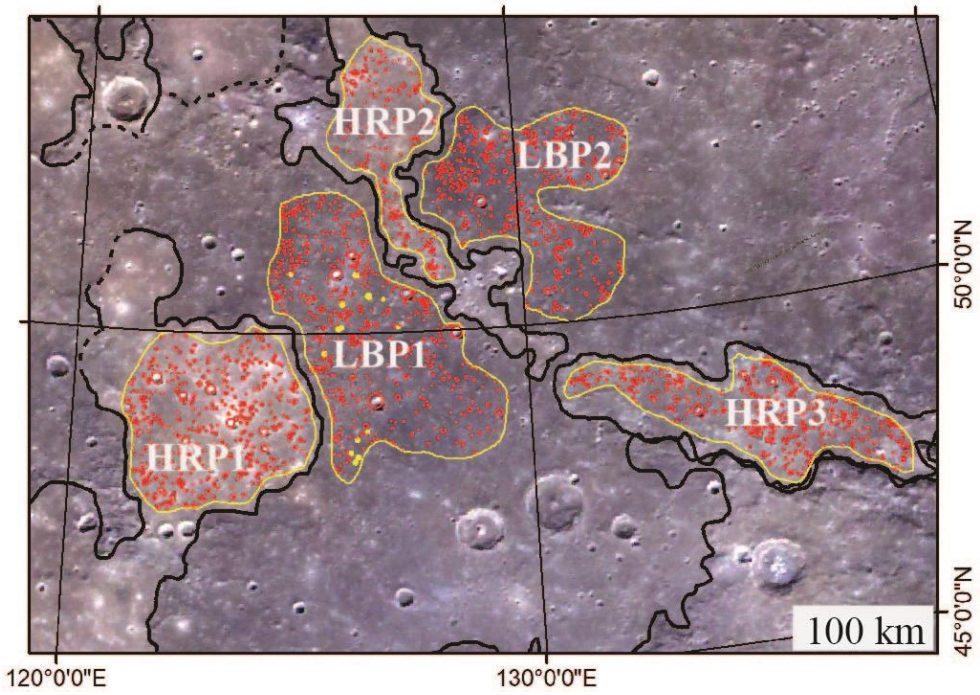

Figure 28. Crater count locations in the CEP covering the LBP and HRP units.

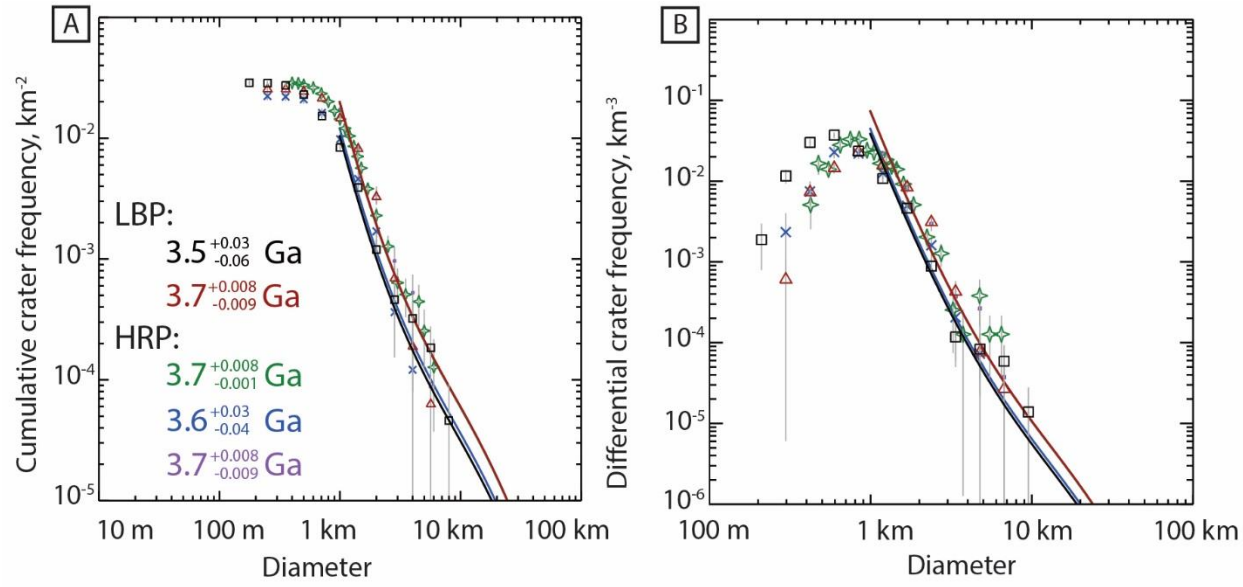

Figure 29. A: Cumulative CSFDs for the five count locations (Fig. 27), with their associated model ages. B: Differential CSFDs highlighting the same overlapping pattern as the cumulative CSFD display. The cumulative and differential CSFDs, and the derived model ages, overlap and are not separable from each other.

Table 8. Crater count derived absolute ages for the LBP and HRP units. These ages and N(4) crater densities correspond to previously derived ages and crater densities for similar, but larger, units.

Count Region	Age (Ga)	Area (km^2)	Craters (>1 km dia.)	N(4)
LBP 1	3.58 ± 0.03	21,700	182	322.58 ± 121
LBP 2	3.71 ± 0.01	15,900	233	188.68 ± 109
HRP1	3.70 ± 0.01	15,700	226	382.17 ± 156
HRP2	3.63 ± 0.02	8260	81	242.13 ± 171
HRP3	3.73 ± 0.01	11,400	197	526.32 ± 215

younger than the Caloris impact basin, the individual plains unit ages cannot be confidently separated from each other.

As a measure of relative age, crater densities for the HRP and LBP units were also calculated for craters > 4 km (N(4)) in diameter. This crater diameter enables direct comparison to previous relative age estimates for smooth plains. These N(4) data are similar to previous work in different smooth plains regions over larger areas (e.g., Ostrach et al., 2015; Byrne et al., 2016), and do not support distinctly different emplacement times for these two units. The fact that neither relative nor absolute age estimates are separable implies that HRP and LBP unit emplacement occurred either contemporaneously or within a geologically brief timeframe. These relative and absolute age estimates are consistent with previously derived relative and absolute age estimates, and further support the interpretation that these units were emplaced post-LHB and after the formation of the Caloris impact basin (e.g., Strom et al., 2008, 2011; Fassett et al., 2009; Denevi et al., 2013 Ostrach et al., 2015; Byrne et al., 2016).

Spectral Analyses

Though the LBP and HRP both have low Fe concentrations that can suppress their overall spectral variability, each have distinct characteristics owing to the differences in their Mg/Si, Ca/Si, and Al/Si ratios, which can be used to distinguish between mafic and ultramafic compositions (Nittler et al., 2011; Stockstill et al., 2012; Weider et al., 2012). The LBP spectra within the CEP are both similar to each other and similar to regional exposures of LBP within the CIP (Fig. 30). There were no LBP exposures in the NSP for comparisons. The LBP units in the CEP are nearly identical spectrally to the LBP unit in the CIP, The HRP spectra in the CEP, CIP, and NSP exhibit a wider range of reflectance values than those of the LBP spectral units, which show overlapping reflectance values. Spectral comparisons show a small amount of

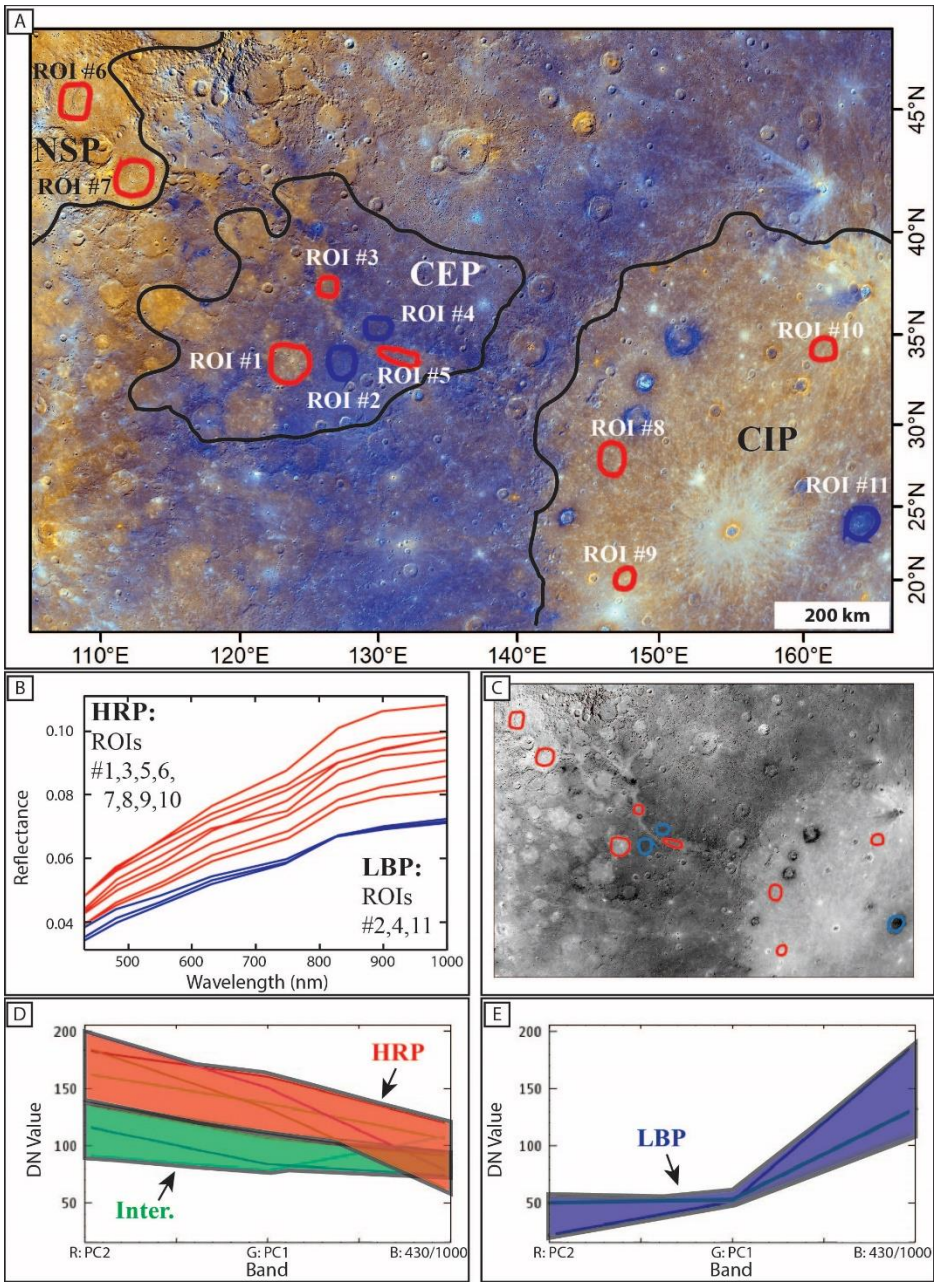

Figure 30. A: Color mosaic (R: 430 nm, G: 750nm, B: 1000 nm) with overlaid ROIs within the CEP, CIP, and NSP. These ROIs cover HRP (red) and LBP (blue) units in each of the CEP, CIP, and NSP, which are marked by black outlines. B: Spectra of the ROIs. The LBP spectra are tightly clustered while the HRP spectra exhibit a greater spread in spectral slopes. C: The extracted PC2 from the 8-band enhanced color mosaic, highlighting further differences between HRP and LBP units. The location of ROIs from A are represented by open circles, with red representing the HRP and blue representing the LBP. D: Enhanced color mosaic RGB combination (R: PC2, G: PC1, B: 430 nm/1000 nm) used for comparison from the enhanced color mosaic between HRP units in the CIP and NSP (red band) versus the red plains units in the CEP (green band), which I characterize as an "Intermediate" composition. E: Enhanced color mosaic RGB combination (R: PC2, G: PC1, B: 430 nm/1000 nm), where blue plains units cluster together (blue band), with clearly different slopes that the HRP and Intermediate units. The locations for these extracted data correspond to the ROIs in A. The PC2 DN values for the HRP are range from ~150-200, while the PC2 DN values for the LBP range from ~5-50.

variability in spectral slope of the HRP units in the map area and their similarity to those found in the NSP and CIP (Fig. 30B). The reflectance values of the CEP units are concentrated at the lower end of the HRP reflectance values, suggesting that the HRP units in the CEP are comprised of a more intermediate composition (cf. Weider et al., 2015; Peplowski et al., 2015).

Principal Component Analyses

Qualitative assessment of the brightness differences in the PC2 data indicate potential compositional differences between the HRP and LBP material. The observation of the PC2 data suggests the HRP materials in the CEP are generally darker than the HRP materials found in both the NSP and CIP (Fig. 30D, Intermediate). The HRP material in the CEP is more similar in brightness to those in the CIP, rather than the very bright HRP unit in the NSP (Fig. 30D). The PC2 brightness values of the LBP units in the CEP are nearly identical to the LBP unit identified in the CIP (Fig. 30E). These intermediate brightness values in the PC2 data that are attributed to the HRP material in the CEP lie between the LBP and HRP values identified from the CIP and NSP.

Discussion

Mapping identified distinct HRP units in the CEP, similar to those found in the CIP and NSP (Figs. 3,6). The LBP and HRP units identified in the CEP are concentrated in topographic lows, fill craters, and embay the margins of topographically higher terrain. The identification of these distinct HRP units is important, as they correlate to regions, the NSP and CIP, that have previously been interpreted as being volcanic in origin (e.g., Trask and Guest, 1975; Kiefer and Murray, 1987; Strom et al., 2008, 2011; Fassett et al., 2009; Head et al., 2009, 2011; Prockter et al., 2010; Byrne et al., 2013; Hurwitz et al., 2013; Ostrach et al., 2015). The identification of distinct HRP material in the CEP is suggestive of at least one lava flow in the region (Fig. 27).

Flow pathways from the NSP and CIP have also been previously identified (e.g., Byrne et al., 2013; Fassett et al., 2009, respectively), and suggest that lavas could have flowed from either of these potential source areas into the CEP (Fig. 25), particularly related to the arcuate HRP unit that dissects the CEP (Fig. 27). The small vent identified to the east of Dali might represent a potential source for the observed HRP materials in these filled craters, though the vent sits within a crater that is filled by material that is categorized as an IP unit, comprised of a potentially compositionally mixed plains unit (Fig. 27).

Crater count model ages (Table 8, Fig. 29) give a CEP age approximately equivalent to that of the CIP and NSP (~3.7-3.9 Ga; Strom et al., 2008, 2011; Fassett et al., 2009; Denevi et al., 2013; Ostrach et al., 2015), and younger than the formation of the Caloris basin (~3.9 Ga; Strom et al., 2008, 2011; Fassett et al., 2009; Denevi et al., 2013). Thus, the CEP are unlikely to be the result of impact ejecta from the formation of the basin.

The slopes of the reflectance values for both the LBP and HRP units identified in the CEP are consistent with the LBP and HRP units from the neighboring CIP and NSP (Fig. 30B). If the previous interpretations of the HRP materials in the CIP and NSP as extensive lava flows (e.g., Denevi et al., 2013; Ostrach et al., 2015) are correct, these data suggest spectral similarities among HRP exposures support the interpretation that the CEP contains lava flows. The spectra of LBP material in the CEP match those of LBP exposures in the CIP. These exposures correspond to a unit is found in and around craters within the CIP, that was likely excavated from depth beneath HRP material, (e.g., Denevi et al, 2009; Watters et al., 2009; Ernst et al., 2010, 2015; Murchie et al., 2015) and have been interpreted to be ancient volcanic materials (Nittler et al., 2011; Stockstill et al., 2012; Weider et al., 2012). These spectral similarities suggest the LBP in the CEP might be ancient volcanic material excavated from depth. In contrast to the LBP

identified in the CIP, the LBP materials in the CEP cover most of the region, are superposed on HRP material, and cannot be directly related to any specific impact structure that could have excavated the material. The distinct spectral signatures of the LBP and HRP are consistent with previous volcanic interpretations of the smooth plains, and may explain the observed intermediate composition of the CEP (Weider et al., 2015; Peplowski et al., 2015), resulting from a mixture of HRP and LBP units that were blended in the coarse data resolution of the XRS and GRS instruments.

Although my results support a predominantly volcanic emplacement of the CEP, and previous age dating is inconsistent with impact melt or ejecta, other lines of evidence add ambiguity and uncertainty into this interpretation. No unambiguous flow structures were identified within the CEP or within the valleys that fed into the CEP from the NSP or within the linear Van Eyck troughs, although the absence of observed flow features could also result from impact erosion or burial by late-stage flows or impact ejecta. The spectra for the HRP units found in the CEP, although similar to those found within the NSP and CIP, are not diagnostic of having originated in either of these regions. The spectra for the LBP units in the CEP are similar to the exposed LBP material in the CIP, and based on previous interpretation of LBP material (Watters et al., 2009; Denevi et al., 2009; Ernst et al., 2010, 2015; Murchie et al., 2015), these exposures could be representative of either older volcanically emplaced units or excavated material from impacts. The PC2 results suggest multiple compositions, ranging from HRP to LBP and including an intermediate unit between these two endmembers, and are not diagnostic of volcanic processes alone.

Results presented here favor a volcanic emplacement for the smooth plains units in the CEP, but do not lead to a conclusive result to definitively distinguish between the hypotheses of

lava or impact ejecta as comprising the CEP unit northwest of Caloris. Instead, they permit multiple explanatory scenarios for the origins of the plains units that form the basis of hypotheses that can be tested in subsequent work.

Scenario One

In this first scenario for the emplacement of CEP, topographic depressions may have formed first, including the Caloris impact basin, the northern lowlands, and portions of the annulus around Caloris. These depressions were infilled with older, volcanically emplaced LBP material (Fig. 31), possibly via now-buried vents or fissures, based on the inference of LBP/LRM deposits at depth (e.g., Denevi et al., 2009; Ernst et al., 2010, 2015; Murchie et al., 2015; Peplowski et al., 2016; Klima et al., 2018). These older volcanic LBP deposits were then covered by deposits of HRP as products of extensive extrusive volcanism (e.g., Denevi et al., 2013; Ostrach et al., 2015). The compositional differences between the NSP and CIP (e.g., Charlier et al., 2013; Michel et al., 2013; Tosi et al., 2013; Weider et al., 2015; Peplowski et al., 2015) suggest the HRP deposits within these two regions lavas may have been sourced from distinct magmas. Compositional differences between the NSP and CIP, particularly the Al-abundance trend, can be plausibly interpreted to result from varying Na concentrations in their source magmas that affected plagioclase production and the final Al concentrations (Weider et al., 2015). These HRP lavas were plausibly sourced from the NSP through valley networks into the CEP (Byrne et al., 2013; Hurwitz et al., 2013) and/or through the Van Eyck formation rimming the Caloris basin (Fassett et al., 2009). In this scenario, the separation of the HRP plains outcrops from each other by LBP plains, or intermingling of these units to form a mixed color unit, is explained as late-stage and possibly local eruptions of younger LBP material forming a partial veneer over the previously contiguous HRP units.

Figure 31. Various scenarios for the emplacement of the CEP, ranging from predominantly volcanic processes (Scenario 1), to primarily ejecta deposits (Scenario 2), and variations of both scenarios that have been modified by post-emplacement processes. The t1 and t2 steps represent common events for both scenarios. Prior to t1, the topographic depression that comprise the extent of the CEP, CIP, and NSP formed, either from impact or tectonic events. At t1, these depressions were filled with volcanically derived LBP material, likely fed by vertical conduits plumbing melt zones in the mantle. These initial conduits close or the magma sources were exhausted by t2, and were replaced by new conduits sampling different locations and compositions in the mantle, that resulted in HRP material filling the CIP and NSP. In **Scenario 1**, the HRP material then flowed into the CEP during t3, and was subsequently capped by a limited eruption of volcanically derived LBP material in t4. An alternative for Scenario 1 would involve complete fill of the CEP by the volcanically derived LBP material during t4, which was then dissected (dashed line) by the formation of hollows (yellow). In **Scenario 2**, several alternatives are presented. The first two options occur at t3, where the LBP was emplaced as diffuse ejecta deposits (dashed blue line) or emplaced as a continuous layer and partially covered by HRP material (dashed red line). If the LBP was once a continuous surface in the CEP, these ejecta-dominated scenarios **must** have been modified by post-emplacement processes. If the LBP material was originally continuous at t4, it might have been altered by hollow formation of partial HRP flows in the CEP during t5. Note: The depressions are not to scale and are mean to convey the general size difference between the adjacent terrains and areally limited CEP.

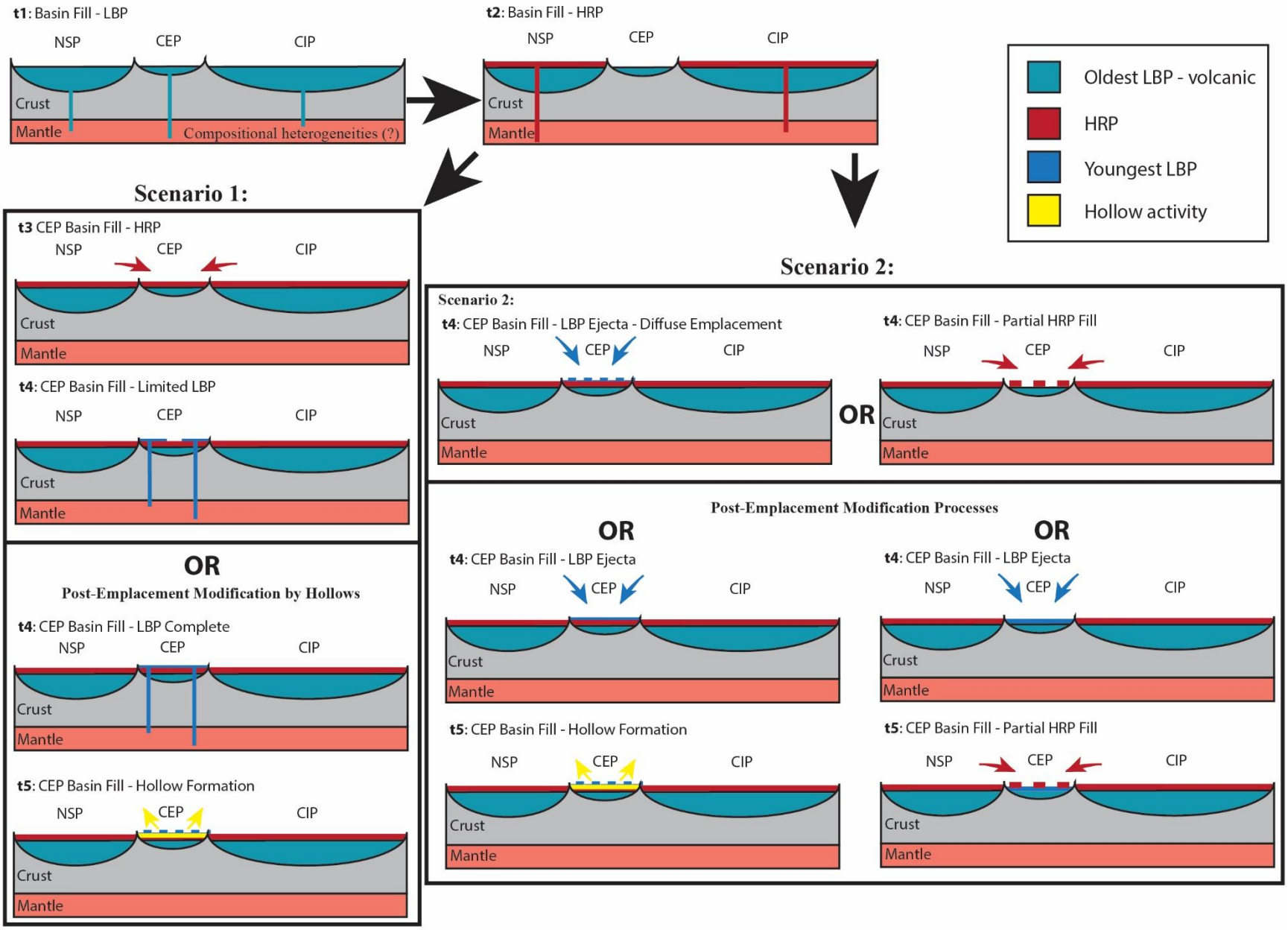
t1: Basin Fill - LBP
NSP
CEP
CIP
Crust
Mantle
Compositional heterogeneities (?)
t2: Basin Fill - HRP
NSP
CEP
CIP
Crust
Mantle
Oldest LBP - volcanic
HRP
Youngest LBP
Hollow activity
Scenario 1:
t3 CEP Basin Fill - HRP
NSP
CEP
CIP
Crust
Mantle
t4: CEP Basin Fill - Limited LBP
NSP
CEP
CIP
Crust
Mantle
OR
Post-Emplacement Modification by Hollows
t4: CEP Basin Fill - LBP Complete
NSP
CEP
CIP
Crust
Mantle
t5: CEP Basin Fill - Hollow Formation
NSP
CEP
CIP
Crust
Mantle
Scenario 2:
Scenario 2:
t4: CEP Basin Fill - LBP Ejecta - Diffuse Emplacement
NSP
CEP
CIP
Crust
Mantle
OR
t4: CEP Basin Fill - Partial HRP Fill
NSP
CEP
CIP
Crust
Mantle
Post-Emplacement Modification Processes
OR
t4: CEP Basin Fill - LBP Ejecta
NSP
CEP
CIP
Crust
Mantle
t5: CEP Basin Fill - Hollow Formation
NSP
CEP
CIP
Crust
Mantle
OR
t4: CEP Basin Fill - LBP Ejecta
NSP
CEP
CIP
Crust
Mantle
t5: CEP Basin Fill - Partial HRP Fill
NSP
CEP
CIP
Crust
Mantle

The development of the CEP might have occurred during the course of multiple pulses of volcanic activity in the region. This supposition is based on the presence of distinct HRP and LBP units in the CEP (e.g., Nittler et al., 2011; Stockstill et al., 2012; Weider et al., 2015; Peplowski et al., 2015). At least two phases of widespread effusive volcanism that occurred over an extended period of time are interpreted in the NSP, based on stratigraphic embayment relationships of ghost crater populations (Ostrach et al., 2015). The emplacement of the CEP plains might also have occurred over an extended period of time and, based on analogy to the proposed formation of the NSP (e.g., Ostrach et al., 2015), could have involved multiple eruptions. These volcanic pulses might have been triggered by the Caloris basin forming impact event, which could have induced melting in multiple regions within the mantle from remnant thermal anomalies, which later upwelled to the surface ~100 My after the Caloris impact event (Roberts and Barnouin, 2012), and continued to form for ~300 My. The different color characteristics of the mapped units and intermediate composition of the CEP (Weider et al., 2015; Peplowski et al., 2015) suggest packets of magma with differing compositions sourced the lavas, although a single fractionated magma chamber could have also produced lavas of different compositions on the surface.

If the covering by the potentially younger LBP material was complete over the HRP, a mechanism would be needed to expose the HRP unit. Local landforms that suggest a removal mechanism are hollows, found in the eastern HRP unit (Fig. 32). Hollows are small, shallow, irregularly-shaped, rimless depressions with flat floors, and inferred to have formed from the loss of volatiles (Fig. 32D; e.g., Blewett et al., 2011, 2013, 2018; Thomas et al., 2014). Although typically found in LBP/LRM deposits, hollows in the CEP have been identified within exposures of HRP material (Fig. 32; e.g., Denevi et al., 2009; Blewett et al., 2011, 2013, 2018; Thomas et

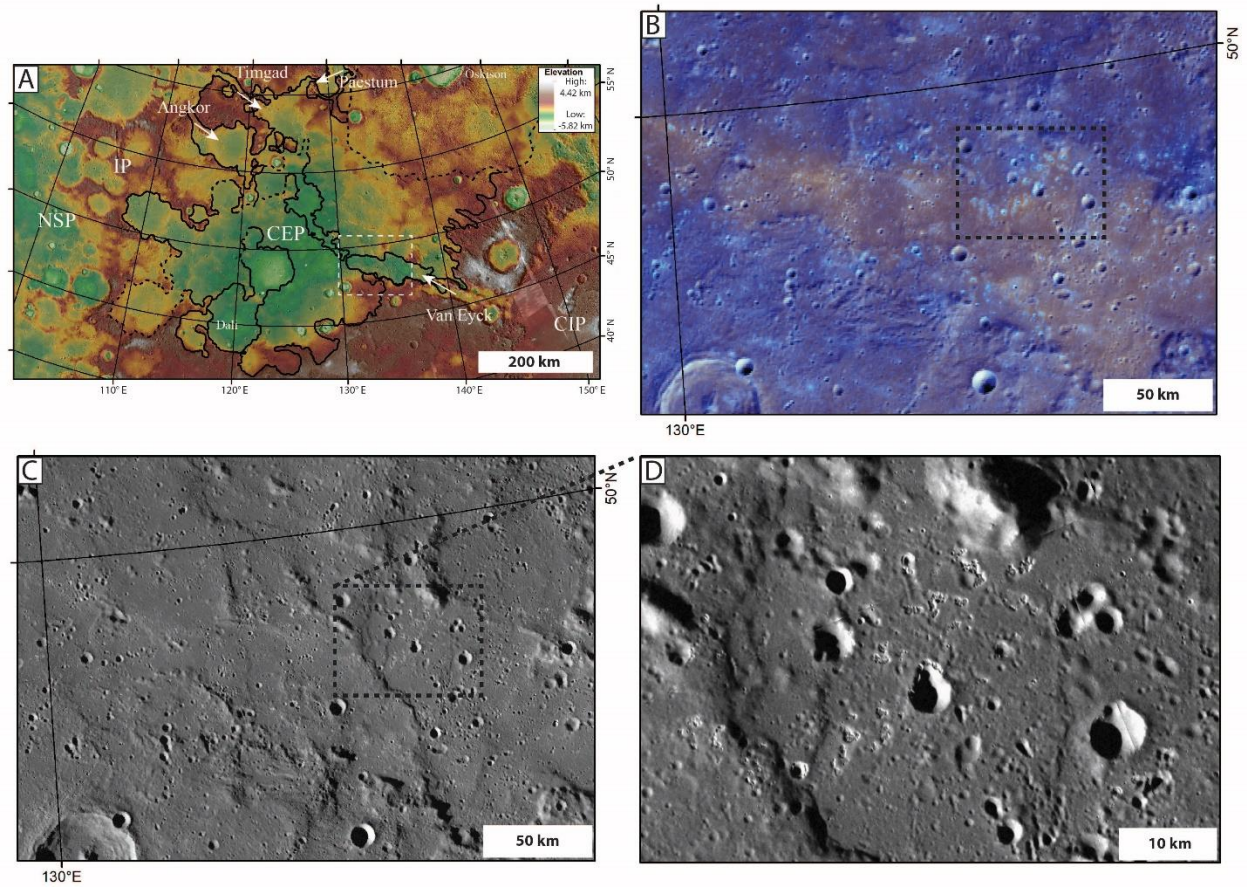

Figure 32. The hollows identified in the CEP are located on the periphery of the HRP unit that corresponds to the crater count area HRP3 and the spectral ROI #5. Some additional potential hollows may exist in other HRP units within the CEP, but high-resolution imagery is lacking and their identification would rely solely on their color characteristics that they share with the clearly identifiable hollows as shown here (B). There are other exposures of these potential hollows in the region as well, though located in the LBP units. A: Regional context of the portion of the annulus that covers my study area. The white dashed box denotes the extent of B and C. B: Enhanced color imagery showing the location of the hollows in the red-plains unit. Note the light-blue characteristics of the hollows. C: B&W image identifying the location of the observed hollows. The hollows are visible in this mosaic, but are more clearly defined in the hi-res WAC images in B. D: Hi-res WAC image covering the highest density cluster of hollows found in the red-plains unit.

al., 2014; Murchie et al., 2018). The necessary concentration of volatiles is hypothesized to have occurred due to condensation of magmatic volatiles in the subsurface, in cold traps on the surface following their eruption (Blewett et al., 2011, 2018), or beneath a capping layer of lava of pyroclastic deposits (Thomas et al., 2014; Blewett et al., 2018). Impact melts could also have differentiated and concentrated volatiles following their emplacement (Vaughn et al, 2012). Additionally, volatiles may also be concentrated and sequestered within LBP/LRM units during their formation (Blewett et al., 2016, 2018). In this sub-scenario, the localized eruption of LBP material created a veneer that completely covered the HRP material in the CEP and then was locally removed during the formation of hollows (Fig. 31). This formation of the hollows could have been triggered by activity of local faults (Fig 32C), or local impacts that exposed the volatile-bearing material to the surface (Fig. 32D).

Scenario Two

A second scenario considers the emplacement of the LBP material as ejecta (Fig. 31), perhaps from the formation of the bordering Oskison crater (120 km diameter), which is located in the northeast of the CEP (Fig. 25). The local ages derived in the CEP units preclude emplacement as ejecta or melt directly from the Caloris basin formation event, as they are younger than the model ages for the Caloris rim (e.g., Fassett et al., 2009). Nevertheless, the LBP in the CEP may be related to Oskison, other local or regional impacts. The exposure of HRP material in the CEP could be related to incomplete, diffuse deposition of this ejecta material over the HRP unit, leaving HRP material exposed and not requiring post-emplacement modification processes to removal of any overlying material (Fig. 31). Alternatively, the CEP might have been filled with the older volcanically derived LBP material, then partially filled with HRP material,

due either to limited flow into the CEP from the NSP and/or CIP or contributions from localized vents/fissures (Fig. 31).

If the potentially younger LBP material once covered the entire CEP, then post-emplacement modification would have been necessary (Fig. 31). As exposures of HRP material are limited in the CEP, or mixed with LBP material, it is reasonable to infer a once complete coating that had been modified. This modification might have been the result of flow of HRP material into the CEP from the NSP or CIP that superposed the older volcanic LBP material and younger ejecta-derived LBP. Alternatively, this modification could have been the result of small impact events or hollow formation that removed some of the overlying material, without completely resurfacing the CEP. This veneer of ejecta material could have been removed through the same processes as the volcanically emplaced LBP material in Scenario 1, although in this second scenario the ejecta material hosted the volatile material. Alternatively, "modern" hollow formation in the last ~1 Ga might have been able to remove a thin LBP veneer, exposing the ancient HRP material without altering its crater population. This scenario would lead to both the LBP and HRP material having ancient derived ages (~3.7 Ga), though the process that modified them could be far younger.

Conclusions

The results from this work support the interpretation of the smooth plains deposits within the northwestern CEP as at least one distinct lava flow, but are not conclusive, and contributions from impact ejecta cannot be entirely ruled out. These potential lava flows likely originated from the NSP and/or CIP. It is possible that the HRP materials were emplaced prior to late-stage superposition by younger LBP units. Several possible scenarios which are consistent with the observations from this work were developed to explain the prospective geologic history of CEP.

These scenarios may be tested through reinvestigation of MESSENGER data and the acquisition of new data. The understanding of this region will increase significantly with the arrival of BepiColombo and the return of higher-resolution images and spectral data, from which these proposed formation scenarios may be distinguished (see Chapter 3 Appendix). With the potential for answering these lingering questions concerning the formation of the CEP with BepiColombo data, a clearer interpretation of the thermal evolution of Mercury may be attained.

References

Ackiss, S. E., Buczkowski, D. L., Ernst, C. M., McBeck, J. A., and Seelos, K. D. (2015). Knob heights within circum-Caloris geologic units on Mercury: Interpretations of the geologic history of the region. Earth and Planetary Science Letters, 430, 542-550.

Arvidson, R.E., Boyce, J., Chapman, C., Cintala, M., Fulchignoni, M., Moore, H., Neukum, G., Schultz, P., Soderblom, L., Strom, R., Woronow, A., Young, R., (1979). Standard techniques for presentation and analysis of crater size–frequency data. Icarus 37, 467–474.

Benkhoff, J., Van Casteren, J., Hayakawa, H., Fujimoto, M., Laakso, H., Novara, M., ... & Ziethe, R. (2010). BepiColombo—Comprehensive exploration of Mercury: Mission overview and science goals. Planetary and Space Science, 58(1-2), 2-20.

Blewett, D. T., Chabot, N. L., Denevi, B. W., Ernst, C. M., Head, J. W., Izenberg, N. R., ... & Xiao, Z. (2011). Hollows on Mercury: MESSENGER evidence for geologically recent volatile-related activity. Science, 333(6051), 1856-1859.

Blewett, D. T., Vaughan, W. M., Xiao, Z., Chabot, N. L., Denevi, B. W., Ernst, C. M., ... & Solomon, S. C. (2013). Mercury's hollows: Constraints on formation and composition from analysis of geological setting and spectral reflectance. Journal of Geophysical Research: Planets, 118(5), 1013-1032.

Blewett, D. T., Stadermann, A. C., Susorney, H. C., Ernst, C. M., Xiao, Z., Chabot, N. L., Denevi, B. W., Murchie, S. L., McCubbin, F. M., Kinczyk, M. J., Gillis-Davis, J. J. and Solomon, S. C. (2016). Analysis of MESSENGER high resolution images of Mercury's hollows and implications for hollow formation. Journal of Geophysical Research: Planets, 121, 1798–1813.

Blewett, D.T., Ernst, C.M., Murchie, S.L., Vilas, F, (2018). Mercury's Hollows. In S. Solomon, L. Nittler, & B. Anderson (Eds.), Mercury: The View after MESSENGER (Cambridge Planetary Science, pp. 324-345). Cambridge: Cambridge University Press. doi:10.1017/9781316650684.013

Byrne, P. K., Klimczak, C., Williams, D. A., Hurwitz, D. M., Solomon, S. C., Head, J. W., Preusker, F., Oberst, J. (2013). An assemblage of lava flow features on Mercury. Journal of Geophysical Research: Planets, 118(6), 1303-1322.

Byrne, P.K., Ostrach, L.R., Denevi, B.W., Chapman, C.R., Fassett, C.I., Whitten, J.L., Klimczak, C., Mazarico, E., Hauck, S.A., Head, J.W. and Solomon, S.C., (2015) Near-synchronous end to global-scale effusive volcanism on Mercury. Lunar and Planetary Science Conference XLVI, Abstract # 1731.

Byrne, P. K., Ostrach, L. R., Fassett, C. I., Chapman, C. R., Denevi, B. W., Evans, A. J., et al. (2016). Widespread effusive volcanism on Mercury likely ended by about 3.5 Ga. Geophysical Research Letters, 43, 7408–7416.

Carter, L. M., Neish, C. D., Bussey, D. B. J., Spudis, P. D., Patterson, G. W., Cahill, J. T., & Raney, R. K. (2012). Initial observations of lunar impact melts and ejecta flows with the Mini-RF radar. Journal of Geophysical Research: Planets, 117(E12).

Cavanaugh, J. F., Smith, J. C., Sun, X., Bartels, A. E., Ramos-Izquierdo, L., Krebs, D. J., et al., (2007). The Mercury Laser Altimeter instrument for the MESSENGER mission. In The Messenger Mission to Mercury, pp. 451-479. Springer New York.

Charlier, B., Grove, T. L., and Zuber, M. T. (2013). Phase equilibria of ultramafic compositions on Mercury and the origin of the compositional dichotomy. Earth and Planetary Science Letters, 363, 50-60.

Christensen, P. R., Anderson, D. L., Chase, S. C., Clark, R. N., Kieffer, H. H., Malin, M. C., Pearl, J.C., Carpenter, J., Bandiera, N., Brown, F.G., Silverman, S. (1992). Thermal emission spectrometer experiment: Mars Observer mission. Journal of Geophysical Research: Planets, 97(E5), 7719-7734.

Cloutis, E. A., & Gaffey, M. J. (1991). Spectral-compositional variations in the constituent minerals of mafic and ultramafic assemblages and remote sensing implications. Earth, Moon, and Planets, 53(1), 11-53.

Dence, M. R. (1971). Impact melts. Journal of Geophysical Research, 76(23), 5552-5565.

Denevi, B. W., Robinson, M. S., Solomon, S. C., Murchie, S. L., Blewett, D. T., et al., (2009). The evolution of Mercury's crust: A global perspective from MESSENGER. Science, 324(5927), 613-618.

Denevi, B. W., Ernst, C. M., Meyer, H. M., Robinson, M. S., Murchie, S. L., Whitten, J. L., et al., (2013). The distribution and origin of smooth plains on Mercury. Journal of Geophysical Research: Planets, 118(5), 891-907.

Denevi, B. W., Seelos, F. P., Ernst, C. M., Keller, M. R., Chabot, N. L., Murchie, S. L., et al. (2016). Final Calibration and Multispectral Map Products from the Mercury Dual Imaging System Wide-Angle Camera. In Lunar and Planetary Science Conference (Vol. 47, p. 1264).

Denevi, B.W., Ernst, C.M., Prockter, L.M., Robinson, M.S., (2018) The Geologic History of Mercury. In S. Solomon, L. Nittler, & B. Anderson (Eds.), Mercury: The View after MESSENGER (Cambridge Planetary Science, pp. 144-175). Cambridge: Cambridge University Press. doi:10.1017/9781316650684.007

Domingue, D. L., Chapman, C. R., Killen, R. M., Zurbuchen, T. H., Gilbert, J. A., Sarantos, M., ... & Orlando, T. M. (2014). Mercury's weather-beaten surface: Understanding Mercury in the context of lunar and asteroidal space weathering studies. Space Science Reviews, 181(1-4), 121-214.

Ernst, C. M., Murchie, S. L., Barnouin, O. S., Robinson, M. S., Denevi, B. W., Blewett, D. T., et al. (2010). Exposure of spectrally distinct material by impact craters on Mercury: Implications for global stratigraphy. Icarus, 209(1), 210–223.

Fassett, C. I., Head, J. W., Blewett, D. T., Chapman, C. R., Dickson, J. L., Murchie, S. L., et al., (2009). Caloris impact basin: Exterior geomorphology, stratigraphy, morphometry, radial sculpture, and smooth plains deposits. Earth and Planetary Science Letters, 285(3), 297-308.

Fergason, R. L., Christensen, P. R., & Kieffer, H. H. (2006). High-resolution thermal inertia derived from the Thermal Emission Imaging System (THEMIS): Thermal model and applications. Journal of Geophysical Research: Planets, 111(E12).

Flamini, E., Capaccioni, F., Colangeli, L., Cremonese, G., Doressoundiram, A., Josset, J. L., ... & Marinangeli, L. (2010). SIMBIO-SYS: The spectrometer and imagers integrated observatory system for the BepiColombo planetary orbiter. Planetary and Space Science, 58(1-2), 125-143.

Fraser, G. W., Carpenter, J. D., Rothery, D. A., Pearson, J. F., Martindale, A., Huovelin, J., ... & Benkoff, J. (2010). The Mercury Imaging X-Ray Spectrometer (MIXS) on bepicolombo. Planetary and Space Science, 58(1-2), 79-95.

French, B. M., (2003). Traces of Catastrophe, Smithsonian Institution, 120 p.p.

Grieve, R. A., Dence, M. R., & Robertson, P. B. (1977). Cratering processes-As interpreted from the occurrence of impact melts. In Impact and explosion cratering: Planetary and terrestrial

implications (pp. 791-814).
Grieve, R. A. F., & Cintala, M. J. (1992). An analysis of differential impact melt-crater scaling and implications for the terrestrial impact record. Meteoritics, 27(5), 526-538.
Guest, J. E., and Greeley, R. (1983). Geologic Map of the Shakespeare Quadrangle of Mercury. Map I-1408, Misc. Investigations Ser. US Geological Survey, Denver, Colo.
Gunderson, K., & Thomas, N. (2010). BELA receiver performance modeling over the BepiColombo mission lifetime. Planetary and Space Science, 58(1-2), 309-318.
Gupta, R. P. (2003). Remote sensing geology. Springer.
Hawkins III, S. E., Boldt, J. D., Darlington, E. H., Espiritu, R., Gold, R. E., Gotwols, B., et al., (2007). The Mercury dual imaging system on the MESSENGER spacecraft. Space Science Reviews, 131(1-4), 247-338.
Hayne, P. O., Bandfield, J. L., Siegler, M. A., Vasavada, A. R., Ghent, R. R., Williams, J. P., ... & Paige, D. A. (2017). Global regolith thermophysical properties of the Moon from the Diviner Lunar Radiometer Experiment. Journal of Geophysical Research: Planets, 122(12), 2371-2400.
Head, J. W., Murchie, S. L., Prockter, L. M., Solomon, S. C., Chapman, C. R., Strom, R. G., Watters, T.R., Blewett, D.T., Gillis-Davis, J.J., Fassett, C.I., Dickson, J.L., Morgan, G.A., Kerber, L. (2009). Volcanism on Mercury: Evidence from the first MESSENGER flyby for extrusive and explosive activity and the volcanic origin of plains. Earth and Planetary Science Letters, 285(3), 227-242.
Head, J. W., Chapman, C. R., Strom, R. G., Fassett, C. I., Denevi, B. W., Blewett, D. T., et al., (2011). Flood volcanism in the northern high latitudes of Mercury revealed by MESSENGER. Science, 333(6051), 1853-1856.
Hiesinger, H., Helbert, J., & Team, M. C. I. (2010). The Mercury radiometer and thermal infrared spectrometer (MERTIS) for the BepiColombo mission. Planetary and Space Science, 58(1-2), 144-165.
Hurwitz, D. M., Head, J. W., Byrne, P. K., Xiao, Z., Solomon, S. C., Zuber, M. T., Smith, D.E., Neumann, G. A. (2013). Investigating the origin of candidate lava channels on Mercury with MESSENGER data: Theory and observations. Journal of Geophysical Research: Planets, 118(3), 471-486.
Kerber, L., Head, J. W., Solomon, S. C., Murchie, S. L., Blewett, D. T., & Wilson, L. (2009). Explosive volcanic eruptions on Mercury: Eruption conditions, magma volatile content, and implications for interior volatile abundances. Earth and Planetary Science Letters, 285(3-4), 263-271.
Kiefer, W. S., & Murray, B. C. (1987). The formation of Mercury's smooth plains. Icarus, 72(3), 477-491.
Klima, R. L., Denevi, B. W., Ernst, C. M., Murchie, S. L., & Peplowski, P. N. (2018). Global distribution and spectral properties of low-reflectance material on Mercury. Geophysical Research Letters, *45*(7), 2945-2953.
Kneissl, T., van Gasselt, S., & Neukum, G. (2011). Map-projection-independent crater size-frequency determination in GIS environments—New software tool for ArcGIS. Planetary and Space Science, 59(11), 1243-1254.
Kneissl, T., Michael, G. G., Platz, T., & Walter, S. H. G. (2015). Age determination of linear surface features using the Buffered Crater Counting approach–Case studies of the Sirenum and Fortuna Fossae graben systems on Mars. Icarus, 250, 384-394.
Le Feuvre, M., and Wieczorek, M. A. (2011). Nonuniform cratering of the Moon and a revised

crater chronology of the inner Solar System. Icarus, 214(1), 1-20.
Mccauley, J. F., Guest, J. E., Schaber, G. G., Trask, N. J., and Greeley, R. (1981). Stratigraphy of the Caloris basin, Mercury. Icarus, 47(2), 184-202.
McEwen, A. S., Preblich, B. S., et al. (2005). The rayed crater Zunil and interpretations of small impact craters on Mars. Icarus, 176(2), 351-381.
McCoy, T.J., Peplowski, P.N., McCubbin, F.M., Weider, S.Z., (2018). The Geochemical and Mineralogical Diversity of Mercury. In S. Solomon, L. Nittler, & B. Anderson (Eds.), Mercury: The View after MESSENGER (Cambridge Planetary Science, pp. 176-190). Cambridge: Cambridge University Press. doi:10.1017/9781316650684.008
McNutt, R.L, Benkhoff, J, Fujimoto, M., Anderson, B.J., (2018). Future Missions: Mercury after MESSENGER. In S. Solomon, L. Nittler, & B. Anderson (Eds.), Mercury: The View after MESSENGER (Cambridge Planetary Science, pp. 544-569). Cambridge: Cambridge University Press. doi:10.1017/9781316650684.021
Mellon, M. T., Jakosky, B. M., Kieffer, H. H., & Christensen, P. R. (2000). High-resolution thermal inertia mapping from the Mars global surveyor thermal emission spectrometer. Icarus, 148(2), 437-455.
Michael, G. G., & Neukum, G. (2010). Planetary surface dating from crater size–frequency distribution measurements: Partial resurfacing events and statistical age uncertainty. Earth and Planetary Science Letters, 294(3), 223-229.
Michael, G. G. (2013). Planetary surface dating from crater size–frequency distribution measurements: Multiple resurfacing episodes and differential isochron fitting. Icarus, 226(1), 885-890.
Michael, G. G., Kneissl, T., & Neesemann, A. (2016). Planetary surface dating from crater size-frequency distribution measurements: Poisson timing analysis. *Icarus*, *277*, 279-285.Michel, N. C., Hauck, S. A., Solomon, S. C., Phillips, R. J., Roberts, J. H., and Zuber, M. T. (2013). Thermal evolution of Mercury as constrained by MESSENGER observations. Journal of Geophysical Research: Planets, 118(5), 1033-1044.
Mitrofanov, I. G., Kozyrev, A. S., Konovalov, A., Litvak, M. L., Malakhov, A. A., Mokrousov, M. I., ... & Tomilina, T. M. (2010). The Mercury Gamma and Neutron Spectrometer (MGNS) on board the planetary orbiter of the BepiColombo mission. Planetary and Space Science, 58(1-2), 116-124.
Murchie, S. L., Klima, R. L., Denevi, B. W., Ernst, C. M., Keller, M. R., Domingue, D. L., et al. (2015). Orbital multispectral mapping of Mercury with the MESSENGER Mercury Dual Imaging System: Evidence for the origins of plains units and low-reflectance material. Icarus, 254, 287–305.
Murchie, S.L., Klima, R.L., Izenberg, N.R., Domingue, D.L., Blewett, D.T., Helbert, J, (2018) Spectral Reflectance Constraints on the Composition and Evolution of Mercury's Surface. In S. Solomon, L. Nittler, & B. Anderson (Eds.), Mercury: The View after MESSENGER (Cambridge Planetary Science, pp. 191-216). Cambridge: Cambridge University Press. doi:10.1017/9781316650684.009
Nittler, L. R., Starr, R. D., Weider, S. Z., McCoy, T. J., Boynton, W. V., Ebel, D. S., et al., (2011). The major-element composition of Mercury's surface from MESSENGER X-ray spectrometry. Science, 333(6051), 1847-1850.
Nittler, L.R., Chabot, N.L., Grove, T.L., Peplowski P.N., (2018) The Chemical Composition of Mercury. In S. Solomon, L. Nittler, & B. Anderson (Eds.), Mercury: The View after MESSENGER (Cambridge Planetary Science, pp. 30-51). Cambridge: Cambridge

University Press. doi:10.1017/9781316650684.003
Oberbeck, V.R. et al., 1977. Comparative studies of lunar, martian, and mercurian craters and plains. Journal of Geophysical Research 82, 1681–1698.
Oberst, J., Preusker, F., Phillips, R. J., Watters, T. R., Head, J. W., Zuber, M. T., Solomon, S. C. (2010). The morphology of Mercury's Caloris basin as seen in MESSENGER stereo topographic models. Icarus, 209(1), 230-238.
Ostrach, L. R., Robinson, M. S., Whitten, J. L., Fassett, C. I., Strom, R. G., Head, J. W., Solomon, S. C. (2015). Extent, age, and resurfacing history of the northern smooth plains on Mercury from MESSENGER observations. Icarus, 250, 602-622.
Peplowski, P. N., Lawrence, D. J., Evans, L. G., Klima, R. L., Blewett, D. T., Goldsten, J. O., Murchie, S.L., McCoy, T.J., Nittler, L.R., Solomon, S.C., Starr, R.D. and Weider, S.Z. (2015). Constraints on the abundance of carbon in near-surface materials on Mercury: Results from the MESSENGER Gamma-Ray Spectrometer. Planetary and Space Science, 108, 98-107.
Pommerol, A., Chakraborty, S., & Thomas, N. (2012). Comparative study of the surface roughness of the Moon, Mars and Mercury. Planetary and Space Science, 73(1), 287-293.
Prockter, L. M., Ernst, C. M., Denevi, B. W., Chapman, C. R., Head, J. W., Fassett, C. I., ... & Cremonese, G. (2010). Evidence for young volcanism on Mercury from the third MESSENGER flyby. Science, 329(5992), 668-671.
Robinson, M. S., Murchie, S. L., Blewett, D. T., Domingue, D. L., Hawkins, S. E., Head, J. W., et al., (2008). Reflectance and color variations on Mercury: Regolith processes and compositional heterogeneity. Science, 321(5885), 66-69.
Rothery, D., Marinangeli, L., Anand, M., Carpenter, J., Christensen, U., Crawford, I. A., ... & Fraser, G. (2010). Mercury's surface and composition to be studied by BepiColombo. Planetary and Space Science, 58(1-2), 21-39.
Rothery, D. A., Mancinelli, P., Guzzetta, L., & Wright, J. (2017). Mercury's Caloris basin: Continuity between the interior and exterior plains. Journal of Geophysical Research: Planets, 122(3), 560-576.
Schaber, G. G., and McCauley, J. F. (1980). Geologic map of the Tolstoj quadrangle of Mercury (H-8). Map I-1199, Misc. Investigations Ser. US Geological Survey, Denver, Colo.
Schlemm II, C. E., Starr, R. D., Ho, G. C., Bechtold, K. E., Hamilton, S. A., Boldt, J. D., et al. (2007). The X-Ray Spectrometer on the MESSENGER spacecraft. Space Science Reviews, 131(1-4), 393-415.
Spudis, P. D., and Guest, J. E. (1988). Stratigraphy and geologic history of Mercury. Mercury, University of Arizona Press, 1, 118-164.
Stockstill-Cahill, K. R., McCoy, T. J., Nittler, L. R., Weider, S. Z., and Hauck, S. A. (2012). Magnesium-rich crustal compositions on Mercury: Implications for magmatism from petrologic modeling. Journal of Geophysical Research: Planets, 117(E12).
Strom, R. G., Chapman, C. R., Merline, W. J., Solomon, S. C., Head, J. W. (2008). Mercury cratering record viewed from MESSENGER's first flyby. Science, 321(5885), 79-81.
Strom, R. G., Banks, M. E., Chapman, C. R., Fassett, C. I., Forde, J. A., Head, J. W., Merline, W.J., Prockter, L.M., Solomon, S. C. (2011). Mercury crater statistics from MESSENGER flybys: Implications for stratigraphy and resurfacing history. Planetary and Space Science, 59(15), 1960-1967.
Thomas, R. J., Rothery, D. A., Conway, S. J., Anand, M. (2014). Hollows on Mercury: Materials and mechanisms involved in their formation. Icarus, 229, 221-235.

Tornabene, L. L., Moersch, J. E., McSween, H. Y., McEwen, A. S., Piatek, J. L., Milam, K. A., & Christensen, P. R. (2006). Identification of large (2–10 km) rayed craters on Mars in THEMIS thermal infrared images: Implications for possible Martian meteorite source regions. Journal of Geophysical Research: Planets, 111(E10).

Tosi, N., Grott, M., Plesa, A. C., and Breuer, D. (2013). Thermochemical evolution of Mercury's interior. Journal of Geophysical Research: Planets, 118(12), 2474-2487.

Trang, D., Lucey, P. G., & Izenberg, N. R. (2017). Radiative transfer modeling of MESSENGER VIRS spectra: Detection and mapping of submicroscopic iron and carbon. Icarus, 293, 206-217.

Trask, N. J., and Guest, J. E. (1975). Preliminary geologic terrain map of Mercury. Journal of Geophysical Research, 80(17), 2461-2477.

Vaughan, W. M., Helbert, J., Blewett, D. T., Head, J. W., Murchie, S. L., Gwinner, K., McCoy, T. J. and Solomon, S. C. (2012). Hollow-forming layers in impact craters on Mercury: Massive sulfide deposits formed by impact melt differentiation? Lunar Planet. Sci., 43, abstract 1187.

Warner, N. H., Gupta, S., Calef, F., Grindrod, P., Boll, N., & Goddard, K. (2015). Minimum effective area for high resolution crater counting of martian terrains. Icarus, 245, 198-240.

Watters, T. R., Murchie, S. L., Robinson, M. S., Solomon, S. C., Denevi, B. W., André, S. L., and Head, J. W. (2009). Emplacement and tectonic deformation of smooth plains in the Caloris basin, Mercury. Earth and Planetary Science Letters, 285(3), 309-319.

Weider, S. Z., Nittler, L. R., Starr, R. D., McCoy, T. J., Stockstill-Cahill, K. R., Byrne, P. K., Denevi, B.W., Head, J.W., Solomon, S. C. (2012). Chemical heterogeneity on Mercury's surface revealed by the MESSENGER X-Ray Spectrometer. Journal of Geophysical Research: Planets (1991–2012), 117(E12).

Weider, S. Z., Nittler, L. R., Starr, R. D., Crapster-Pregont, E. J., Peplowski, P. N., Denevi, B. W., Head, J.W., Byrne, P.K., Hauck, S.S., Ebel, D.S. and Solomon, S. C. (2015). Evidence for geochemical terranes on Mercury: Global mapping of major elements with MESSENGER's X-Ray Spectrometer. Earth and Planetary Science Letters, 416, 109-120.

Whitten, J. L., Head, J. W., Denevi, B. W., Solomon, S. C. (2014). Intercrater plains on Mercury: Insights into unit definition, characterization, and origin from MESSENGER datasets. Icarus, 241, 97-113.

Wilhelms, D.E., 1976. Mercurian volcanism questioned. Icarus 28, 551–558.

Zuber, M. T., Smith, D. E., et al., (2012). Topography of the northern hemisphere of Mercury from MESSENGER laser altimetry. Science, 336(6078), 217-220.

Appendix

Future Work and BepiColombo Data

The MESSENGER mission provided the data for my observational interpretations and development of emplacement scenarios for my study area in the northwestern CEP. Additional data are required to test these explanatory scenarios. MESSENGER data may yet yield these data, and the BepiColombo mission will also offer the opportunity to test these scenarios and derive a more complete understanding of the emplacement and evolution of the CEP.

Additional Observations for Scenario One (predominantly volcanic emplacement)

A primary criterion in support of the first scenario would be the identification of flow structures. Examples of flow structures, such as kipukas ranging up to ~20 km long, are found in the CEP-bounding valleys (Byrne et al., 2013) and ~20-50 km long fan-shaped arrays are found within the Caloris basin (e.g., Rothery et al., 2017). Structures of this size have not been identified in my study area, but smaller scale features may be present. Distinguishing impact melt deposits from lavas is difficult, as they have similar morphologies. Impact melts are usually restricted to the interior of craters, or within a few crater radii beyond the rim, which are incorporated in ejecta deposits as coherent bodies and/or isolated outcrops (e.g., Dence, 1971; Grieve et al., 1977; Grieve and Cintala, 1992; Carter et al., 2012). Identification of flow structures that are not in close proximity to large impact craters would support interpretation of the CEP as surficial lava flows. Subdued tectonic structures that constrain either HRP or LBP units would also suggest emplacement of flowing materials like lava. An identification of potential source vents for filled craters would suggest a volcanic origin, similar to the apparent relationship between Dali and an unnamed crater that hosts a small vent structure (Fig. 27).

Spectral signatures consistent with volcanic compositions and with the bordering NSP and CIP, inferred to have been volcanically emplaced (Trask and Guest, 1975; Kiefer and Murray, 1987; Strom et al., 2008, 2011; Fassett et al., 2009; Head et al., 2009, 2011; Prockter et al., 2010; Byrne et al., 2013; Hurwitz et al., 2013; Ostrach et al., 2015), would also support emplacement as lava(s). More definitive spectral characterization of the CEP units, beyond differences in slope of reflectance values (e.g., Denevi et al., 2009, 2013; Watters et al., 2009; Murchie et al., 2018) would be critical in teasing out any subtle compositional differences present in the CEP, particularly any variation in the Mg/Si, Ca/Si, and Al/Si ratios. Alongside the spectral characterization, further investigation of elemental compositions could lead to the identification of source areas. Additional elemental geospatial trends, such as the Al-abundance trend between the CEP, CIP, and NSP observed in MESSENGER data (e.g., Weider et al., 2015; Peplowski et al., 2015), could be critical.

Crater counts performed in the region could be refined, which would support more robust geological interpretations through both the refinement of unit boundaries and the inclusion of additional crater count locations. Refinement and expansion of the unit boundaries, however, would allow for better constraints on crater populations which would lead to an increase in overall robustness of model age determinations for specific units. More accurate delineation of additional crater count locations, based on morphological and spectral characteristics, would increase the sample size of locations and their corresponding model ages in the CEP. Counts in HRP units related to the potential flow pathways in the Van Eyck formation and valley networks (Fassett et al., 2009; Byrne et al., 2013, respectively) and newly delineated LBP units would better constrain the regional stratigraphy. HRP unit ages that are younger than the Caloris basin and with ages consistent with the bordering NSP and CIP would be supportive of a volcanic

interpretation for their emplacement. LBP units younger than the Caloris basin formation event would be consistent with a volcanic emplacement. These potential younger ages would exclude ejecta and melt from the Caloris basin formation event having filled the CEP, but would not definitively exclude later impact events.

Additional Observations for Scenario Two (predominantly ejecta/melt emplacement)

A primary criterion for the second scenario, to distinguish whether the CEP units are predominantly ejecta and/or ballistically emplaced melt, would be strongly supported by the identification of superposing deposits that drape highstanding features. Identifying whether any mapped HRP and LBP deposits are draped on higher elevation sites, would suggest an ejecta origin. Alternatively, if those deposits are restricted to low-lying areas and topographic depressions, their presence would then support a volcanic or melt origin. The small knobs of the Odin formation that are prevalent in the region (e.g., Guest and Greeley, 1983), may be an ideal site to search for any draping deposits that might be present.

A potential further complicating factor for the identification of draping deposits relates to their composition. Draping deposits with spectra consistent with a volcanic composition might be the result of excavation of ancient magmatic material from depth (e.g., Watters et al., 2009; Denevi et al, 2009). In this case, the band centers and depths of absorption features from the spectra may be useful in distinguishing whether the observed material was emplaced on the surface as basalt or in the subsurface as gabbro (e.g., Gupta, 2003), and then subsequently incorporated into ejecta deposits during an impact event. Additionally, if draped deposits are identified, and have spectral signatures consistent with surficial lava flows, they can be interpreted as ejecta derived from the surface. These spectra might also be useful in identifying any unusual bulk compositions that may contain signatures of the impactor itself (French, 2003).

Characterization of the thermal characteristics of the surface, including the thermal inertia (TI) could yield critical distinguishing data. The TI of a surface represents its resistance to temperature change (Gupta, 2003). TI differences may be related to compositional differences between the materials, induration state, grain size, texture, and unit thickness (e.g., Mellon et al., 2000). Differences in TI might be useful in distinguishing lava flows from impact ejecta. Typically, a consolidated or crystalline material has a higher TI than a fine-grained material (e.g., Christensen et al., 1992; Mellon et al., 2000; Gupta, 2003; Fergason et al., 2006), so that TI differences might help distinguish a crystalline lava from a finer-grained ejecta deposit. Ejecta deposits on Mars, Mercury, and the Moon have often been found to have distinct TI from their surroundings (e.g., McEwen et al., 2005; Tornabene et al., 2006; Neish et al., 2013; Hayne et al., 2017). Assessing the spatial correlation of any observed TI variations with the mapped unit boundaries would help to determine whether those variations correspond to specific units or whether they are a diffuse coating. This thermal detection method might also provide a way to identify any other potential source craters for ejecta material, besides the neighboring Oskison crater, by tying any observed ejecta deposits to a distinct source crater.

Another avenue to pursue is the clarification of the age relationships in the CEP with a particular emphasis on the LBP units. Current crater count derived ages (Table 8) suggest the HRP and LBP units were emplaced within a relatively narrow time range. LBP and mixed-plains units are the most morphologically diffuse, similar to potential ejecta deposits, and better constraining their emplacement timing would be used to infer whether any are related to the formation of Caloris, or confirm that they formed well after that impact event. As a supplement to the crater count derived ages, differences in surface roughness which may be attributable to differences in ages between units (e.g., Pommerol et al., 2012) could provide an additional proxy

for dating the surface. Though any identified roughness differences may correlate to differing ages, these differences may be intrinsic to the units themselves. To avoid this potential issue, a limitation of analyses to the plains units would remove any intermingled units, to ensure comparisons are performed between similar terrains. This approach might further clarify whether adjacent LBP and HRP units are approximately the same age, or if there are distinct differences that would imply unit emplacement was separated in time. Additionally, if any of the results from these techniques identify isolated patches of material that are contemporaneous with the formation of the Caloris basin, this evidence would strongly indicate the contribution of impact ejecta to the filling of the CEP.

Potential Post-Emplacement Processes

Post-emplacement modification of the plains units might have occurred (Fig. 31). In each of my proposed scenarios, various post-plains-emplacement processes altered the main HRP and LBP units, particularly hollow formation and secondary cratering processes. Though these processes do not distinguish between the scenarios I have proposed for the plains formation mechanisms, they are still important for understanding the subsequent evolution of the plains.

Hollows

The presence of hollows, their genetic relationship to the units that host them, and their potential involvement in surface modification could explain the observed distribution of HRP and LBP units in the CEP, through the removal and/or exposure of surface material. Finding additional locations that host hollows in the CEP, beyond those already identified (Fig. 32), would be useful to spatially correlate any identified hollows to the presence of HRP deposits, which would be suggestive of surface modification. A high concentration of either fresh or subdued hollows in the HRP materials would be suggestive of post-emplacement modification

by hollows as having disrupted the surface and possibly having removed any overlying LBP material.

As volatile release (e.g., sulfur, sodium, potassium) has been suggested as the driving force leading to the formation of hollows (e.g., Blewett et al., 2013; Thomas et al., 2014), searching for volatiles might act as markers and lead to the identification of previously unrecognized hollow populations, especially older subdued hollows. Though volatiles are not exclusive to hollows, such as volatile activity related to observed pyroclastic deposits (e.g., Kerber et al., 2009; Prockter et al., 2010), their presence would be a potential indicator that hollows were/are present in the CEP.

Another consideration when investigating hollows is their age(s). Hollows are inferred to be far younger than Mercury's surface as a whole, on the basis of the preservation of undisturbed surface features, and may be < 1 Ga (e.g., Blewett et al., 2011), whereas the ages of the units in the CEP are ~3.7 Ga. Ancient hollows are not observed on Mercury, but may have existed and are no longer discernible, possibly due to their small size, they are relatively short-lived, and easily overprinted on the surface (e.g., Blewett et al., 2018). Placing age constraints on the currently observed and prospective hollows in the CEP would assist in understanding the timing of their formation and possible effect on the plains units.

Tectonic structures may offer an initiation point for hollow formation, triggering their volatile release (Thomas et al., 2014; Blewett et al., 2018). Remapping of tectonic structures in the CEP could provide data to determine whether a geospatial relationship exists with any observed hollows and/or HRP units. Spatial correlation of tectonic structures and hollows would imply that tectonism acted as a driving mechanism related to their formation in the CEP.

Cratering

The results from current mapping of the CEP units and crater counts argue against the contribution of secondary craters being responsible for exposing any surface features. However, their potential effect cannot be completely discounted. High-resolution images from BeipColombo can be used to identify any potential clusters or linear chains of small secondary craters might be identified that were previously below the limits of detection of the MDIS data. Identification of linear and clustered secondaries that are confined to within, or truncated by, HRP unit boundaries, would suggest cratering events exposed the HRP material, possibly through the disruption or removal of overlying LBP material.

BepiColombo Mission Overview and Instrumentation

The BepiColombo mission will arrive at Mercury in 2025 with a primary mission to investigate the magnetic field, magnetosphere, interior, and exterior of Mercury (e.g., Benkhoff et al., 2010). The spacecraft consist of the Mercury Transfer Module, Mercury Planetary Orbiter (MPO), and the Mercury Magnetospheric Orbiter. The MPO hosts the primary instruments that will investigate the surface of Mercury, orbiting the planet at a periapsis of 480 km and an apoapsis of 1500 km (Benkhoff et al., 2010), a far less elliptical orbit than that of MESSENGER. Over the course of a primary mission lasting one Earth year, and potential extended mission, BepiColombo's instruments aboard the MPO will generate both higher-spatial and -spectral resolution data of the surface in the visible, near-infrared, ultraviolet, X-ray, γ-ray, and neutron wavelengths, more accurate topographic models, and characterization of mineralogical and elemental compositions compared to the data collected from MESSENGER (Table 9). The VNIR and TIR spectrometers will cover a wider spectral range (0.4-2.0 and 7-14 μm). The camera systems will provide a 50-110 mpp color stereo map and 500 mpp multispectral map, along with higher-resolution global compositional maps (Table 9).

Table 9. Comparison of instrumentation aboard MESSENGER and BepiColombo. The instruments aboard BepiColombo increase the wavelength range, resolution, and data coverage over that of the MESSENGER instruments.

Instrument	Wavelength	Resolution	Data Coverage
MESSENGER			
MDIS	395-1040 nm	125-1000 mpp	250 mpp global monochrome 2 kmpp global multispectral
GRNS	Neutron	100-1000 kmpp	Northern hemisphere
XRS	x-ray	20 kmpp	Northern Hemisphere
MLA	1064 nm	0.8-1 kmpp	Northern Hemisphere
BepiColombo			
MERTIS	700-1400 nm	500 mpp	500 mpp global multispectral
SIMBIO-SYS	400-2000 nm	≥5- mpp	STC 50-110 mpp global map
MGNS	Neutron	400 kmpp	Global
MIXS	x-ray	20 kmpp	Global
BELA	1064 nm	20-50 mpp	Global

The BepiColombo Laser Altimeter (BELA) will better characterize surface elevations and lead to more accurate topographic models across the entire planet (Benkhoff et al., 2010; Gunderson and Thomas, 2010; Rothery et al., 2010). The Mercury Radiometer and Thermal Infrared Spectrometer (MERTIS) instrument will be used as a mineralogical mapper covering the 7-14 μm spectral range at 500 mpp, and investigate surface temperatures and thermal inertia (e.g., Benkhoff et al., 2010; Rothery et al., 2010; Hiesinger et al., 2010). The Mercury Gamma-ray and Neutron Spectrometer (MGNS; Benkhoff et al., 2010; Rothery et al., 2010; Mitrofanov et al., 2010) and Mercury Imaging X-Ray Spectrometer (MIXS; Benkhoff et al., 2010; Rothery et al., 2010; Fraser et al., 2010) will map elemental concentrations on the surface, supplementing the mineralogical mapping and previous elemental maps (e.g., Weider et al., 2015; Peplowski et al., 2015). The Spectrometer and Imagers for MPO BepiColombo – Integrated Observatory SYStem (SIMBIO-SYS) includes a stereo image system, high-resolution images, and VIS-IR spectrometer that will map Mercury's surface in unprecedented detail (Benkhoff et al., 2010; Rothery et al., 2010; Flamini et al., 2010). Each of these instruments and their associated data could be useful in filling any data gaps left from MESSENGER, and in clarifying which formation scenario for the CEP is most likely.

DISSERTATION CONCLUSIONS

The work outlined in the three chapters of this dissertation provide insight into the evolution, emplacement processes, and sources for lava flows found on Mercury, Earth, and Mars. From my analyses of the ages of the circum-Cerberus channelized lavas, I find that changes in the material properties during emplacement are most likely to be responsible for the observed crater-based age trends. These results are consistent with previous analyses of crater populations from comets (Holsapple and Housen, 2007), adjacent cogenetic lunar geologic units (van der Bogert et al., 2010, 2017), and within platy-ridged lava flows on Mars (Murray et al., 2005; Page et al., 2009; Chapman et al., 2010; Dundas et al., 2010). Data for terrestrial sites support the suggested influence of target properties on crater diameters on extraterrestrial bodies. Rheological changes have been observed during lava emplacement in Hawai'i and Iceland (e.g., Swanson, 1973; Wilmoth and Walker, 1993; Flóvenz and Sæmundsson, 1993; Polacci et al., 1999; Keszthelyi et al., 2004). I attribute the material property changes to increasing strength and decreasing vesicularity in the lava.

Based on my results from crater counting, scaling to reduce the counts to a single model age, and gravity data, I conclude that the possible magma source region that fed the channelized lavas in the Cerberus region is an underlying regional melt zone. My interpretation of the results best supports a sub-Cerberus magma source as the most parsimonious explanation, but contributions from multiple sources may also have occurred. The inference that the sub-Cerberus region is the apparent source region implies that the formation of magma is not confined to the large volcanic provinces, which under current martian conditions would be ideal sites for magma generation (e.g., McGovern et al., 2002, 2004; Schumacher and Breuer, 2007; Ruiz et al., 2010), but may occur in regions less obviously suitable for melt formation.

The modeling of terrestrial and martian lava flows investigated the effects of viscosities consistent with lavas that ranged in composition from basaltic-to-andesitic (e.g., Keszthelyi et al., 2000; Diniega et al., 2013). From these analyses of the bulk viscosities of the lavas in Athabasca and Grjótá Valles, I find that the lowest bulk viscosities (1-10 Pa·s) overestimate the length and areal extent of the channelized lavas. The 10 and 100 Pa·s simulations in Athabasca and the 100 Pa·s simulation in Grjótá produced the best reproductions of these flows. The highest-viscosity configurations (1000 Pa·s) resulted in shorter and thicker flows compared to the low-viscosity variants. The range of viscosity values that resulted in the best model output fits are most consistent with basaltic compositions with low phenocryst and gas bubble abundances, though komatiite-style volcanism could also explain these simulated values. This result supports previous interpretations of the surface of Mars being primarily composed of basaltic-to-andesitic lava (e.g., Bandfield et al., 2000; Wyatt et al., 2001; Hamilton et al., 2001), as well as interpretations of the Cerberus region hosting basaltic lava flows (e.g., Keszthelyi et al., 2004; Vaucher et al., 2009; Jaeger et al., 2010).

Finally, the results from the Mercury investigation support the interpretation of the smooth plains deposits within the northwestern CEP as at least one distinct lava flow, though contributions from impact ejecta cannot be entirely ruled out. This result is consistent with previous interpretations suggesting the smooth plains are predominantly volcanic (e.g., Trask and Guest, 1975; Kiefer and Murray, 1987; Strom et al., 2008, 2011; Fassett et al., 2009; Head et al., 2009, 2011; Prockter et al., 2010; Byrne et al., 2013; Hurwitz et al., 2013; Ostrach et al., 2015). These lava flows likely originated from the NSP and/or CIP. It is possible that the HRP materials were emplaced prior to late-stage superposition by younger LBP units. I developed several possible scenarios of the geologic history of CEP to describe my observations. These scenarios

can be tested by reinvestigating MESSENGER data and/or the acquisition of new data. Our understanding of this region will increase significantly with the arrival of BepiColombo and the return of higher-resolution images and spectral data, from which I would seek to distinguish between my proposed formation scenarios. With the potential for answering these lingering questions concerning the formation of the CEP with BepiColombo data, a clearer understanding of the thermal evolution of Mercury may be attained.

References

Bandfield, J. L., Hamilton, V. E., & Christensen, P. R. (2000). A global view of Martian surface compositions from MGS-TES. Science, 287(5458), 1626-1630.

Byrne, P. K., Klimczak, C., Williams, D. A., Hurwitz, D. M., Solomon, S. C., Head, J. W., Preusker, F., Oberst, J. (2013). An assemblage of lava flow features on Mercury. Journal of Geophysical Research: Planets, 118(6), 1303-1322.

Chapman, M. G., Neukum, G., Dumke, A., Michael, G., Van Gasselt, S., Kneissl, T., Zuschneid, W., Hauber, E., Mangold, N. (2010). Amazonian geologic history of the Echus Chasma and Kasei Valles system on Mars: New data and interpretations. Earth and Planetary Science Letters, 294(3), 238-255.

Diniega, S., Smrekar, S. E., Anderson, S., & Stofan, E. R. (2013). The influence of temperature-dependent viscosity on lava flow dynamics. Journal of Geophysical Research: Earth Surface, 118(3), 1516-1532.

Dundas, C. M., Keszthelyi, L. P., Bray, V. J., & McEwen, A. S. (2010). Role of material properties in the cratering record of young platy-ridged lava on Mars. Geophysical Research Letters, 37(12).

Fassett, C. I., Head, J. W., Blewett, D. T., Chapman, C. R., Dickson, J. L., Murchie, S. L., et al., (2009). Caloris impact basin: Exterior geomorphology, stratigraphy, morphometry, radial sculpture, and smooth plains deposits. Earth and Planetary Science Letters, 285(3), 297-308.

Flóvenz, Ó. G., & Saemundsson, K. (1993). Heat flow and geothermal processes in Iceland. Tectonophysics, 225(1-2), 123-138.

Hamilton, V. E., Wyatt, M. B., McSween Jr, H. Y., & Christensen, P. R. (2001). Analysis of terrestrial and Martian volcanic compositions using thermal emission spectroscopy: 2. Application to Martian surface spectra from the Mars Global Surveyor Thermal Emission Spectrometer. Journal of Geophysical Research: Planets, 106(E7), 14733-14746.

Head, J. W., Murchie, S. L., Prockter, L. M., Solomon, S. C., Chapman, C. R., Strom, R. G., Watters, T.R., Blewett, D.T., Gillis-Davis, J.J., Fassett, C.I., Dickson, J.L., Morgan, G.A., Kerber, L. (2009). Volcanism on Mercury: Evidence from the first MESSENGER flyby for extrusive and explosive activity and the volcanic origin of plains. Earth and Planetary Science Letters, 285(3), 227-242.

Head, J. W., Chapman, C. R., Strom, R. G., Fassett, C. I., Denevi, B. W., Blewett, D. T., et al., (2011). Flood volcanism in the northern high latitudes of Mercury revealed by MESSENGER. Science, 333(6051), 1853-1856.

Holsapple, K. A., & Housen, K. R. (2007). A crater and its ejecta: An interpretation of Deep Impact. Icarus, 191(2), 586-597.

Hurwitz, D. M., Head, J. W., Byrne, P. K., Xiao, Z., Solomon, S. C., Zuber, M. T., Smith, D.E., Neumann, G. A. (2013). Investigating the origin of candidate lava channels on Mercury with MESSENGER data: Theory and observations. Journal of Geophysical Research: Planets, 118(3), 471-486.

Jaeger, W. L., Keszthelyi, L. P., Skinner, J. A., Milazzo, M. P., McEwen, A. S., Titus, T. N., Rosiek, M.R., Galuszka, D.M., Howington-Kraus, E., Kirk, R. L., the HiRISE Team (2010). Emplacement of the youngest flood lava on Mars: A short, turbulent story. Icarus, 205(1), 230-243.

Keszthelyi, L., McEwen, A. S., Thordarson, T. (2000). Terrestrial analogs and thermal models for Martian flood lavas. Journal of Geophysical Research: Planets (1991–2012), 105(E6), 15027-15049.

Keszthelyi, L., Thordarson, T., McEwen, A., Haack, H., Guilbaud, M. N., Self, S., Rossi, M. J. (2004). Icelandic analogs to Martian flood lavas. Geochemistry, Geophysics, Geosystems, 5(11).

Kiefer, W. S., & Murray, B. C. (1987). The formation of Mercury's smooth plains. Icarus, 72(3), 477-491.

McGovern, P. J., Solomon, S. C., Smith, D. E., Zuber, M. T., Simons, M., Wieczorek, M. A., Phillips, R.J., Neumann, G.A., Aharonson, O., Head, J. W. (2002). Localized gravity/topography admittance and correlation spectra on Mars: Implications for regional and global evolution. Journal of Geophysical Research: Planets, 107(E12).

McGovern, P.J. et al., 2004. Correction to localized gravity/topography admittance and correlation spectra on Mars: Implications for regional and global evolution. Journal of Geophysical Research: Planets, 109, E07007.

Murray, J. B., Muller, J. P., Neukum, G., Werner, S. C., van Gasselt, S., Hauber, E., Markiewicz, W.J., Head, J.W., Foing, B.H., Page, D., Mithcell, K.L., Portyankina, G., & HRSC Co-Investigator Team. (2005). Evidence from the Mars Express High Resolution Stereo Camera for a frozen sea close to Mars' equator. Nature, 434(7031), 352-356.

Ostrach, L. R., Robinson, M. S., Whitten, J. L., Fassett, C. I., Strom, R. G., Head, J. W., Solomon, S. C. (2015). Extent, age, and resurfacing history of the northern smooth plains on Mercury from MESSENGER observations. Icarus, 250, 602-622.

Page, D. P., Balme, M. R., & Grady, M. M. (2009). Dating Martian climate change. Icarus, 203(2), 376-389.

Polacci, M., Cashman, K. V., & Kauahikaua, J. P. (1999). Textural characterization of the pāhoehoe–‘a ‘a transition in Hawai’ian basalt. Bulletin of Volcanology, 60(8), 595-609.

Prockter, L. M., Ernst, C. M., Denevi, B. W., Chapman, C. R., Head, J. W., Fassett, C. I., ... & Cremonese, G. (2010). Evidence for young volcanism on Mercury from the third MESSENGER flyby. Science, 329(5992), 668-671.

Ruiz, J., López, V., & Dohm, J. M. (2010). The present-day thermal state of Mars. Icarus, 207(2), 631-637.

Schumacher, S., & Breuer, D. (2007). An alternative mechanism for recent volcanism on Mars. Geophysical Research Letters, 34(14).

Strom, R. G., Chapman, C. R., Merline, W. J., Solomon, S. C., Head, J. W. (2008). Mercury cratering record viewed from MESSENGER's first flyby. Science, 321(5885), 79-81.

Strom, R. G., Banks, M. E., Chapman, C. R., Fassett, C. I., Forde, J. A., Head, J. W., Merline, W.J., Prockter, L.M., Solomon, S. C. (2011). Mercury crater statistics from MESSENGER flybys: Implications for stratigraphy and resurfacing history. Planetary and Space Science, 59(15), 1960-1967.

Swanson, D. A. (1973). Pahoehoe flows from the 1969–1971 Mauna Ulu eruption, Kilauea volcano, Hawai’i. Geological Society of America Bulletin, 84(2), 615-626.

Trask, N. J., and Guest, J. E. (1975). Preliminary geologic terrain map of Mercury. Journal of Geophysical Research, 80(17), 2461-2477.

van der Bogert, C. H., Hiesinger, H., McEwen, A. S., Dundas, C., Bray, V., Robinson, M. S., Plescia, J.B., Reiss, D., Klemm, K., & Team, L. (2010). Discrepancies between crater size-frequency distributions on ejecta and impact melt pools at lunar craters: An effect of

differing target properties?. In Lunar and Planetary Science Conference (Vol. 41, p. 2165).
van der Bogert, C. H., Hiesinger, H., Dundas, C. M., Krüger, T., McEwen, A. S., Zanetti, M., & Robinson, M. S. (2017). Origin of discrepancies between crater size-frequency distributions of coeval lunar geologic units via target property contrasts. Icarus, 298, 49-63.
Vaucher, J., Baratoux, D., et al. (2009). The volcanic history of central Elysium Planitia: Implications for martian magmatism. Icarus, 204(2), 418-442.
Wilmoth, R. A., & Walker, G. P. (1993). P-type and S-type pahoehoe: a study of vesicle distribution patterns in Hawai'ian lava flows. Journal of Volcanology and Geothermal Research, 55(1-2), 129-142.
Wyatt, M. B., Hamilton, V. E., McSween Jr, H. Y., Christensen, P. R., & Taylor, L. A. (2001). Analysis of terrestrial and Martian volcanic compositions using thermal emission spectroscopy: 1. Determination of mineralogy, chemistry, and classification strategies. Journal of Geophysical Research: Planets, 106(E7), 14711-14732.

VITA

Keenan Ben Golder was born in Danbury, Connecticut. Shortly thereafter he moved to upstate New York as a child, where he became an avid collector of fossils and would look up at the band of the Milky Way on clear evenings. Near the end of elementary school, he moved to Newtown, Connecticut, where he would live for the next twenty years. After completing high school, he initially attended Central Connecticut State University for a year, before taking time off to work, most notably at The Maritime Aquarium at Norwalk. Keenan then returned to CCSU, where he began his studies in geology and planetary science. There he got his first experience conducting planetary science research under the guidance of Dr. Harald Hiesinger. Keenan then performed research on ichnofossils with Dr. Michael Wizevich, which included three summers of field work in the Grand Staircase-Escalante national monument in Utah. Keenan graduated from CCSU in the spring of 2010 with a B.S. in Earth Science with a concentration in Geology and a minor in Astronomy. He then moved on to Wesleyan University, where he earned his M.A. in the spring of 2013 under the supervision of Dr. Martha Gilmore. This project involved his first extended experience mapping the surface of Mars. During the final year of his master's program, Keenan began working as an adjunct faculty member at CCSU, Southern Connecticut State University, and the University of New Haven. This experience affirmed his desire to pursue teaching. Keenan then began working towards his Ph.D. in the spring of 2014 at the University of Tennessee with his then advisor, Dr. Devon Burr. During his time at UT, Keenan has participated in numerous NASA-related outreach events, first authored 15 conference abstracts and 1 peer-reviewed article, attended the Zuni-Bandera Volcanic Field Camp in Grants, NM, and was a Mars2020 science team student collaborator, mapping portions of the landing site in Jezero Crater. Keenan completed his dissertation under the supervision of Dr. Brad Thomson.